PETROGENETIC SIGNIFICANCE OF ZIRCON IN MAFIC AND FELSIC ROCKS OF THE BUSHVELD COMPLEX: MELT INCLUSIONS, PHYSICOCHEMICAL CONDITIONS AND HF ISOTOPES

zur Erlangung des akademischen Grades eines
DOKTORS DER NATURWISSENSCHAFTEN

von der KIT-Fakultät für
Bauingenieur-, Geo- und Umweltwissenschaften
des Karlsruher Instituts für Technologie (KIT)
genehmigte

DISSERTATION

von

M. Sc. Dominik Gudelius
aus Frankfurt am Main

Tag der mündlichen Prüfung: 17.11.2020

Referent: Prof. Dr. Armin Zeh
Korreferent: Prof. Dr. Fritz Finger

Karlsruhe 2020

Acknowledgements

First, I sincerely thank my supervisor Prof. Dr. Armin Zeh who initiated this project and introduced me to the fascinating field of zircon petrology and layered intrusions. Thank you very much for giving me the opportunity to work on this exciting topic and for supporting me throughout my PhD with inspiring ideas, encouragement and never ending enthusiasm.

Further thanks are dedicated to Prof. Dr. Fritz Finger of Salzburg University for his willingness to act as an external reviewer.

A special thanks to Prof. Allan H. Wilson (University of the Witwatersrand, Johannesburg) who greatly contributed to the success of this study by assistance during fieldwork and by providing highly valuable and exiting sample material from the Bushveld Complex. Furthermore, essential for the success of this study was the support and collaboration of Dr. Renat R. Almeev (Leibniz University, Hannover), Dr. Lennart A. Fischer (Freiburg University), Dr. Axel Gerdes (Goethe University, Frankfurt) and Prof. Dr. Axel K. Schmitt (Heidelberg University).

Many thanks to my colleagues at the Institute of Applied Geosciences at Karlsruhe Institute of Technology for providing such a pleasant working atmosphere. Also thanks for many fruitful discussions during coffee and lunchtime breaks. In particular thanks to Simon Breuer, Magnus Schneider, Dr. Clifford Patten, Dr. Utz Kramar, Prof. Dr. Jochen Kolb, Dr. Christian Scheffzük, Dr. Benjamin Walter, Dr. Elisabeth Eiche, apl. Prof. Dr. Agnes Kontny, Mirja Lohkamp-Schmitz, and Dr. Ruth Haas-Nüesch. I also thank my co-supervisor apl. Prof. Dr. Kirsten Drüppel for sharing her petrological expertise and supporting me throughout my PhD with great inputs and helpful discussions.

I want to thank Dr. Axel Gerdes, Dr. Heidi Höfer, Dr. Kevin Klimm, and Dr. Richard Albert Roper and all other former colleagues at Goethe University Frankfurt for access to their analytical facilities and their great support. Also thanks to all laboratory assistants who greatly contributed to this work, in particular Linda Marko at Goethe University Frankfurt, Joe Aphane at University of the Witwatersrand and Kristian Nikoloski at Karlsruhe Institute of Technology.

I would like to thank the Deutsche Forschungsgemeinschaft (DFG) for providing financial support for this research (grants ZE 424/11-1, ZE 424/12-1).

Thank you Jenny for being there all the time and for supporting me at any time and mood.

Special thanks to my family for their unconditional support throughout my time. Also thanks to my closest friends for sharing some moments of distraction besides rocks and zircons.

I dedicate this work to my late grandfather, who has piqued my interest and enthusiasm for science in the early days of my childhood.

ABSTRACT

Zircon is a critical petrogenetic indicator for the age, magmatic evolution and physicochemical formation conditions. In this study, such information is obtained from zircons and included melts derived from mafic and felsic rocks of the Bushveld Complex (BC), and used to further constrain the formation processes of Earth's largest layered intrusion.

A detailed study of zircon trace element contents and morphologies combined with bulk rock analyses, petrography of zircon-bearing assemblages, and thermodynamic modelling reveals highly different zircon formation conditions within the BC, which comprises mafic and felsic rocks having a wide range in Zr contents (4-552 ppm). In rutile-bearing mafic cumulates of the lower Rustenburg Layered Suite (RLS), zircon was formed at 690–962 °C (Ti-in-zircon) after ≥75% fractional crystallization of B1 and B2 mafic parental magmas within quartz-rutile-biotite-bearing intercumulus domains. These zircon populations are compositionally highly variable and strongly zoned in Th/U, Nb/Ta, U and Ti following two opposing trends caused by (1) Th/U increase from core to rim due to U>Th depletion of the melt by growth of zircon ± rutile at high zircon/melt ratios, followed by (2) decreasing Th/U from core to rim due to rutile breakdown and biotite growth, causing U release. In contrast, zircons in all rutile-free felsic rocks (Lebowa Granite and Rashoop Granophyre Suites) grew at 761–935 °C after ≥20% fractional crystallization, as indicated by Ti-in-zircon temperatures (using $a\mathrm{TiO_2}$ = 0.3), in agreement with modelling results, zircon saturation temperatures and high temperature zircon morphologies dominated by {100} prisms. Low zircon/melt ratios are reflected by their weak zoning (e.g. Th/U, Nb/Ta). Zircons in rutile-free mafic rocks of the Upper Zone share identical trace element characteristics (low Ti, Th/U<0.8; high REE) with those in felsic rocks, indicating that these zircons were formed by admixing of felsic melts during ingression of mafic parental magmas, which is also required to explain zircon saturation in these rocks.

To better constrain zircon formation within the BC, zircon-forming melts are directly investigated using mineralogical and chemical data for recrystallized and homogenized melt inclusions in zircon (MIZ). Although fractional crystallization products of highly different parental magmas, entrapped melts in zircon from both mafic and felsic rocks display similar, rhyolitic major element compositions (65-78 wt.% $\mathrm{SiO_2}$) and $\mathrm{H_2O}$ contents (1.6-4.0 wt.%). In contrast, trace elements vary significantly: MIZ of the Critical Zone display higher Ti contents and Th/U ratios, but lower REE contents compared to those in Upper Zone diorites and felsic rocks. Liquidus temperatures of MIZ obtained by normative Qz-Ab-Or contents and rhyolite-MELTS modelling indicate melt entrapment mostly at 850-930 °C (at 2 kbar). For rutile-bearing

rocks, these temperatures overlap with Ti-in-zircon of respective host grains as well as TiO_2 and zircon saturation temperatures of MIZ. For all rutile-free rocks, converging results are obtained using a highly reduced $aTiO_2$ of ~0.3, consistent with the value of respective parental magmas after fractional crystallization predicted by thermodynamic modelling. Furthermore, partitioning coefficients obtained from melt inclusions and host zircons reveal no systematic dependency on rock type, melt inclusion size, composition and entrapment temperature.

To better explain zircon formation from different BC parental magmas and their origin, Hf isotopes in zircon from mafic, felsic and metasedimentary rocks were investigated. The same variation in $\varepsilon Hf_{2.055\ Ga}$ between -7.5 and -10.2 is obtained for magmatic zircons in (i) mafic cumulates throughout the RLS and in (ii) overlying granites-granophyres as well as upper Rooiberg Group volcanics, but also in (iii) metamorphic zircon grains and overgrowths on detrital zircon in quartzite and metapelitic rocks adjacent to the BC. Similar $\varepsilon Hf_{2.055\ Ga}$ are also obtained by averaging detrital zircons of the surrounding Upper Pretoria Group and by a Lu-Hf isochron from a garnet-schist of the BC contact aureole. This suggests that in the contact aureole, metamorphic zircon was precipitated from aqueous fluids and/or felsic melts at 550-900 °C, and Hf isotopes were homogenized during fluid transport. However, results of numerical modelling indicate that fluid infiltration only had a minor effect on the Zr-Hf budget and Hf isotopic composition of the RLS. Rather RLS magmas are controlled by the mixing of melts from the asthenospheric mantle (>20 %), the enriched subcontinental lithospheric mantle (<80 %) and from significant assimilation of crust (≤40%). The contribution of lower Kaapvaal Crust was minor for B1 magma (andesite), but up to 40% for B3 magma (tholeiite). Surprisingly minor variation in $\varepsilon Hf_{2.055\ Ga}$ of zircon throughout the RLS reflects (1) mantle-derived magmas having rather low Zr-Hf contents and similar $\varepsilon Hf_{2.055\ Ga}$ as upper crustal rocks surrounding the RLS; (2) significant assimilation of Zr-Hf-rich volcanic and metasedimentary rocks by RLS parental magmas and (3) mingling, mixing and/or diffusive exchange of Zr-Hf between crust and mantle-derived melts and aqueous fluids prior to late-magmatic zircon crystallization at 700-900 °C.

KURZFASSUNG

Zirkon ist ein wichtiger petrogenetischer Indikator zur Bestimmung des Alters, der magmatischen Entwicklung sowie für physikochemische Bildungsbedingungen. In dieser Studie wurden dazu Zirkone und darin eingeschlossene Schmelzen aus verschiedenen mafischen und felsischen Gesteinen des Bushveld Komplex (BK) untersucht um die Enstehungsprozesse der größten Lagenintrusion der Erde besser zu verstehen.

Aufgrund einer detaillierten Untersuchung von Spurenelementkonzentrationen und Morphologien von Zirkon, verbunden mit der Petrographie zirkon-führender Mineral-paragenesen sowie thermodynamischer Modellierung konnten sehr unterschiedliche Bildungsbedingungen von Zirkon innerhalb des BK identifiziert werden, welcher aus mafischen und felsischen Gesteinen mit sehr unterschiedlichen Zr-Gehalten (4-552 ppm) zusammengesetzt ist. In rutil-führenden, mafischen Kumulatgesteinen der basalen Rustenburg Layered Suite (RLS) wurde Zirkon bei 690–962 °C (Ti-in-Zirkon), innerhalb von quarz-, rutil- und biotit-führenden Interkumulusdomänen nach ≥75% fraktioneller Kristallisation der B1 und B2 Stammmagmen gebildet. Zirkonpopulationen in diesen Gesteinen zeichnen sich durch sehr variable Zusammensetzungen und starke Zonierungen aus, insbesondere für Th/U, Nb/Ta, U and Ti, wobei zwei gegenläufige Trends unterschieden werden können: (1) Ein Anstieg in Th/U vom Kern zum Rand verursacht durch U>Th Verarmung der Schmelze aufgrund des Wachstums von Zirkon ± Rutil bei hohen Zirkon/Schmelz-Verhältnissen, gefolgt von (2) einem Abfall von Th/U vom Kern zum Rand verursacht durch rutil-abbauende, biotit-bildende Reaktionen und dadurch frei werdendes U. Im Gegensatz dazu wurde Zirkon in rutil-freien, felsischen Gesteinen (Lebowa Granite, Rashoop Granophyre) bei 761–935 °C schon nach ≥20% fraktioneller Kristallisation gebildet, worauf Ti-in-Zirkon Temperaturen für $a\mathrm{TiO_2}$ = 0.3, Ergebnisse thermodynamischer Modellierung, Zirkon-Sättigungstemperaturen, sowie vorherrschende Hochtemperatur-Zirkonmorphologien dominiert von {100}-Prismenflächen hinweisen. Ein geringes Zirkon/Schmelz-Verhältnis ist hier zudem durch eine schwach ausgebildete Zirkon-Zonierung angezeigt. Zirkone aus rutil-freien mafischen Gesteinen der Upper Zone sind hinsichtlich ihrer Spurenelementmuster (geringes Ti und Th/U<0.8; hohe REE) und Zirkon-Morphologien identisch mit solchen in felsischen Gesteinen. Dies weist auf eine Zumischung von felsischen Schmelzen während der Intrusion der mafischen Stammmagmen hin, ohne welche auch die Zirkon-Sättigung in diesen Gesteinen nicht erklärt werden kann.

Zum besseren Verständnis der Bildungsbedingungen von Zirkon innerhalb des BK, wurden zirkon-bildende Schmelzen direkt anhand von rekristallisierten und homogenisierten Schmelzeinschlüssen im Zirkon (MIZ) untersucht. Obwohl diese Schmelzen aus der fraktionellen Kristallisation von höchst unterschiedlichen Stammmagmen hervorgingen, zeigen sie sowohl in mafischen als auch in felsischen Gesteinen des BK eine ähnliche rhyolitische Hauptelementzusammensetzung (65-78 wt.% SiO_2) sowie ähnliche H_2O Gehalte (1.6-4.0 wt.%). Spurenelemente zeigen dagegen signifikante Unterschiede innerhalb des BK, so weisen MIZ der Critical Zone deutlich höhere Ti-Gehalte, Th/U Verhältnisse sowie niedrigere REE Gehalte auf als solche aus Dioriten der Upper Zone sowie aus felsischen Gesteinen. Liquidustemperaturen der MIZ wurden durch normative Qz-Ab-Or-Gehalte und Modellierung mittels rhyolite-MELTS bestimmt und deuten auf eine Einschlusstemperatur von 850-930 °C (bei 2 kbar) hin. Für alle rutil-führenden Gesteine stimmen diese Temperaturen mit Ti-in-Zirkon Temperaturen des Zirkon-Wirtskristalls sowie mit TiO_2- und Zirkon-Sättigungstemperaturen der MIZ überein. Für alle rutil-freien felsischen und mafischen Gesteine werden konsistente Resultate nur unter Verwendung einer stark reduzierten TiO_2-Aktivität von $aTiO_2 \sim 0.3$ erreicht, was mit dem thermodynamisch modellierten Wert der jeweiligen Stammmagmen nach fraktioneller Kristallisation übereinstimmt. Des weiteren wurden Verteilungskoeffizienten zwischen Zirkon-Wirtskritall und MIZ bestimmt, welche mit experimentellen Daten überlappen und keine Abhängigkeit vom Gesteinstyp, der Einschlussgröße und –Zusammensetzung sowie der Einschlusstemperatur zeigen.

Um die Bildung von Zirkon aus den unterschiedlichen Stammmagmen des BK sowie deren Ursprung zu erklären, wurden Hf Isotopenzusammensetzungen von Zirkonen aus mafischen, felsischen und (meta-)sedimentären Gesteinen des BK untersucht. Eine identische Spanne an $\varepsilon Hf_{2.055\ Ga}$ zwischen -7.5 and -10.2 zeigen magmatische Zirkone in (i) mafischen Kumulatgesteinen der RLS, in (ii) aufliegenden Graniten-Granophyren und Vulkaniten der Rooiberg Gruppe sowie außerdem (iii) metamorphe Zirkone und Überwachsungen detritischer Zirkone in Quarziten und Metapeliten der Kontaktaureole des BK. Ein ähnlicher Durchschnittswert für $\varepsilon Hf_{2.055}$ ergibt sich zudem für detritische Zirkone aus umgebenden Sedimenten der oberen Pretoria Gruppe, welcher außerdem dem Initialwert einer Lu-Hf Isochrone für Granatschiefer der BK-Kontaktaureole entspricht. Dies weist darauf hin, dass Zirkon innerhalb der BK-Kontaktaureole aus wässrigen Fluiden und/oder felsischen Schmelzen bei 550-900 °C gebildet wurde und dabei die Hf-Isotopie homogenisiert wurde. Die Ergebnisse numerischer Modellierung zeigen jedoch, dass die Infiltration von Fluiden nur geringfügig zum Zr-Hf Budget und der Hf-Isotopenzusammensetzung der RLS beitrug. Diese wurde vielmehr durch eine Mischung von Schmelzen des asthenosphärischen Mantels (>20 %) sowie dem

angereicherten Mantel der subkontinentalen Lithosphäre (<80 %) mit großen Mengen krustalem Material (≤40%) kontrolliert. Der Beitrag der Unterkruste des Kaapvaal Kratons war hier unerheblich im Falle des B1 Stammmagmas (andesitisch), jedoch bis zu 40% in Falle des B3 Magmas (tholeiitisch). Die überraschend geringe Variation von $\varepsilon Hf_{2.055\ Ga}$ von Zirkon innerhalb der RLS lässt sich erklären durch (1) geringe Zr-Hf-Gehalte der Mantelschmelzen, welche zudem ein ähnliches $\varepsilon Hf_{2.055\ Ga}$ hatten wie die RLS umgebenden Gesteine der Oberkruste, (2) eine signifikante Assimilation von Zr-Hf-reichen Vulkaniten und Sedimenten durch die RLS Magmen, sowie (3) Mingling, Mischungen oder diffusiver Austausch von Zr-Hf zwischen Kruste und Mantelschmelzen sowie wässrigen Fluiden, vor dem spätmagmatischen Zirkonwachsum bei 700-900 °C.

CONTENTS

1. Introduction

Zircon is Earth's oldest material and one of the most useful and versatile minerals in geosciences, which derives from an outstanding combination of three properties: (1) a highly resistant crystal structure offering an unusual preservation potential, (2) an excellent suitability for geochronology based on the decay of incorporated U to Pb, and (3) an occurrence in a wide range of different sedimentary, metamorphic and magmatic rock types. Therefore, zircon has become Earth's timekeeper providing information about the major processes in Earth's history (e.g. Hoskin and Schaltegger, 2003; Harley and Kelly, 2007).

Together with U and Th used in zircon geochronology, zircon incorporates a large number of other temperature- and process-sensitive trace elements (e.g. Ti, Hf, Nb, Ta, REE, P), contents and isotopic compositions of which are frequently used as petrogenetic indicators for the origin of zircon and respective host rocks (e.g. mantle source, growth from fluid vs. melt, metamorphic vs. magmatic zircon) as well as for the physicochemical conditions during zircon crystallization (e.g. temperature, oxygen fugacity, melt composition) - (Belousova et al., 2006; Fu et al., 2008; Trail et al., 2012; Grimes et al., 2015). In particular, Ti-in-zircon is a critical geothermometer and constraints for the thermal state of Earth's earliest crust mostly rely on Ti-in-zircon thermometry of Archean and Hadean zircons (e.g. Coogan and Hinton, 2006; Harrison et al., 2007; Ickert et al., 2011). Ti-in-zircon is also one of the trace element thermometers of choice for rocks in which conventional, major element based geothermometric methods are impossible due to diffusional re-equilibration (particularly Fe-Mg), e.g. in UHT metamorphic settings (Kelsey and Hand, 2015), or if zircon is the only intact phase remaining from the initial magmatic/metamorphic assemblage, such as in case of deeply altered rocks, kimberlite megacrysts or detrital zircons.

The Bushveld Complex (BC) in South Africa is Earth's largest mafic layered intrusion and hosts morphologically and compositionally diverse zircon in a wide range of rock types ranging from (ultra-) mafic rocks (e.g. pyroxenites, norites) to felsic rocks (granites, granophyres). Here, zircon has delivered significant age constraints for the formation of the BC (Scoates and Friedman, 2008; Zeh et al., 2015), revealed a large variation in zircon trace element contents and Ti-in-zircon temperatures (Yudovskaya et al., 2013; Ver Hoeve et al., 2018; Gudelius et al., 2020), and strikingly similar Hf isotope compositions (Zirakparvar et al., 2014; VanTongeren et al., 2016; Zeh et al. 2020). As different rocks of the BC were cogenetically formed at ~2.055 Ga from different, compositionally well-constrained parental magmas (Cawthorn, 2015), the Bushveld Complex can be regarded as an ideal natural

laboratory to study processes related to zircon formation and causing systematic differences in zircon morphology, trace element compositions as well as distinct Hf isotope signatures.

The magmatic processes during zircon formation are also directly reflected by melt inclusions in zircon (MIZ), which abundantly occur in magmatic zircons from a wide range of rock types (Corfu et al., 2003; Thomas et al., 2003). Although MIZ were previously used to obtain zircon-melt partitioning coefficients and to constrain the magmatic provenance of zircons in sediments or deeply altered rocks (e.g. Chupin et al., 1998; Thomas et al., 2003; Watts and Mercer, 2020), their petrogenetic significance remains largely unexplored. Melt inclusions in zircons from the BC were never investigated, although they are highly suited to investigate how zircon-forming melts are generated from mafic parental magmas and how these melts reflect physicochemical conditions and magma differentiation processes during zircon growth.

1.2 Motivation

The magmatic processes controlling the formation and composition of zircon are still poorly understood and the genetic relationships between zircon and the respective bulk rock and parental magmas can be cryptic (Hanchar and van Westrenen, 2007; Kirkland et al., 2015). Within the Bushveld Complex (BC), zircon occurs in all major subunits within a wide range of mineral assemblages and exhibits highly variable morphologies, trace element systematics, and zoning patterns. However, it is poorly constrained if zircon formation is consistent with fractional crystallization of different parental magmas proposed for the BC (e.g. Barnes et al., 2010), and to which temperatures and degrees these magmas need to cool and differentiate, respectively, until zircon-bearing melts are generated.

The generation and composition of zircon-forming melts is scarcely investigated for any rock type, and for the BC, such information is only available from thermodynamic modelling. Melt inclusions in zircon can offer direct information about the major, trace and volatile element contents of these melts and how these differ dependent on parental magma composition, host rock, and coexistent mineral assemblage. This is particularly interesting for mafic rocks of the BC, in which zircon is a late-magmatic phase and MIZ compositions likely represent the endpoint of extensive differentiation of mafic parental magmas. Given the extremely low diffusivity of most elements in zircon, MIZ from different rock types may provide pristine compositional information of variably evolved BC magmas, including constraints for the volatile budget of the BC, which is essentially unknown.

Melt inclusions in zircon may further allow a critical evaluation whether experimentally determined zircon-melt partitioning coefficients ($D_{Zrc\text{-}melt}$) are applicable and valid for a wider range of natural rock types ranging from (ultra-) mafic to felsic. This topic is poorly investigated since $D_{Zrc\text{-}melt}$ based on MIZ are only available from a very limited range of intermediate to felsic rocks (Thomas et al., 2002, 2003). However, the knowledge whether bulk rock and/or parental magma compositions affect zircon-melt partitioning mechanisms is critical, since $D_{Zrc\text{-}melt}$ (in particular for REE) are frequently used to back-calculate the parental melt composition for out-of-context zircons (Hanchar and van Westrenen, 2007). Furthermore, as direct witnesses of the physicochemical entrapment conditions, MIZ may also provide new thermobarometric constraints for zircon crystallization and/or improve existing methods.

Zircon crystallization temperatures are commonly obtained by Ti-in-zircon thermometry. However, the present calibration of the Ti-in-zircon thermometer requires knowledge of the TiO_2 and SiO_2 activity during zircon crystallization. This is straightforward for rutile-quartz bearing rocks ($aTiO_2 = aSiO_2 = 1.0$), but challenging for rutile-free rocks ($aTiO_2 < 1.0$), which is the majority of magmatic rocks including all mafic and felsic rocks of the upper BC. This also applies to detrital zircons due to the absence of coexistent phases (host rock, Ti-bearing phases, quartz) - (Fu et al., 2008). Melt inclusions in zircon are a potentially powerful tool to constrain the incorporation mechanisms of Ti and other elements in zircon dependent on temperature and melt composition and may further provide an opportunity to intrinsically estimate the TiO_2 activity during zircon crystallization.

Together with Ti, knowledge of the processes controlling other trace element contents (e.g. Hf, Nb, Ta, REE, Th, U) and ratios (e.g. Th/U, Nb/Ta, U/Yb) in zircon is critical, given their discrimination potential for different tectono-magmatic provenances (Belousova et al., 2002; Rubatto, 2002; Grimes et al., 2015). Here, the Th/U has drawn attention because it shows significant variations between magmatic and metamorphic zircon and can be simultaneously obtained during U-Pb dating (Kirkland et al., 2015; Yakymchuk et al., 2018). However, it is poorly investigated how Th/U in zircon relates to the respective bulk rock chemistry and how it depends on the presence of other Th- and U-bearing phases (e.g. apatite, rutile, thorite). Furthermore, the processes leading to extremely high Th/U ratios in zircon as well striking zoning patterns, such as detected for zircon in intercumulus assemblages of mafic cumulates (Yudovskaya et al., 2013; Zeh et al., 2015; Ver Hoeve et al., 2018) are also unconstrained.

Furthermore, a detailed zircon systematics can also yield new constraints for the origin of parental magmas of the BC. Although their composition is well constrained (e.g. Barnes et al.

2010), it is still debated how these magmas were generated in the mantle and how they acquired their distinct major and trace element load. This also applies to the origin and distribution of Zr within the BC, which is critical to explain zircon saturation in most subunits of the BC. Since, Hf substitutes for Zr and both elements have an almost identical geochemistry, the Hf isotope composition in zircon is a critical petrogenetic indicator for the reservoirs contributing to the formation of BC parental magmas (Zirakparvar et al., 2014; VanTongeren et al., 2016). However, previous studies have largely neglected the influence of felsic rocks of the BC comprising both voluminous granitic and volcanic rocks as well as that of (meta-) sediments of the Upper Kaapvaal Craton crust, including those in the contact aureole around the BC. Both reservoirs may be critical for supplying Zr to BC parental magmas.

1.3. Thesis outline

In this study, zircon is used as a petrogenetic indicator for physicochemical conditions during zircon growth in different rock types of the Bushveld Complex, including mafic rocks of the Rustenburg Layered Suite (BC), overlying felsic rocks as well as adjacent metasediments. This information is used to better constrain the genesis and magmatic evolution of the BC. Therefore, the BC is briefly introduced in chapter 2, including an outline of its relevance in geosciences, its diversity in rock types, its geological setting and its known magmatic evolution. Subsequently, an overview of zircon petrology is presented in chapter 3, including an outline of zircon-based methods to obtain petrogenetic information, with an emphasis on those applied in this study on rocks of the BC.

The main research of this study is published in or submitted to international peer-reviewed journals. These three studies (two with Dominik Gudelius as first author) are briefly outlined in the following:

Zircon formation in mafic and felsic rocks of the Bushveld Complex, South Africa: constraints from composition, zoning, Th/U ratios, morphology, and modelling (Chapter 4)

The first study presents new zircon trace element data and respective bulk rock compositions for mafic and felsic rocks of the BC. These results are combined with thermodynamic modelling using rhyolite-MELTS and Perple_X to constrain the evolution of BC parental magmas until zircon saturation, obtain zircon crystallization temperatures and to explain different trace element systematics and zoning patterns of zircon within the BC.

Based on zircon formation processes, the BC can be subdivided into three parts: (i) rutile-free felsic rocks (Lebowa Granite, Rashoop Granophyre), zircon is an early magmatic phase and crystallized at 761-935 °C based on Ti-in-zircon thermometry using $a\mathrm{TiO_2}$ = 0.3, in agreement with temperatures derived from zircon morphology (dominated by {100} faces), zircon saturation temperatures and modelling results. (ii) rutile-free mafic rocks of the Upper Zone (RLS) containing zircon compositionally and morphologically identical to that in felsic rocks, and which was likely formed by admixing of felsic melts to mafic magma, (iii) rutile-bearing mafic cumulates (RLS base to lower Main Zone) in which zircon was formed after >75% fractional crystallization at 690–962 °C (mean: 835 °C; based on Ti-in-zircon thermometry using $a\mathrm{TiO_2}$ = 1.0) and is characterized by commonly low ΣREE and high Ti contents and Th/U ratios. Although trace element characteristics and zircon morphologies systematically vary between these different units, zircons in all felsic and mafic rocks of the BC mostly crystallized at 800-900 °C.

In rutile-bearing mafic rocks, zircon populations display highly variable zoning in Th/U, Nb/Ta and Ti, following two distinct trends. Modelling results and textural evidence indicate that these zoning patterns are mainly controlled by zircon growth in assemblage with rutile and/or biotite in small volumes of intercumulus melt at high zircon/melt ratios. Extreme Th/U ratios of up to 24, are caused by Rayleigh-like fractionation and U>Th depletion of the melt during growth of zircon ± rutile. Below ~830 °C, this trend is reversed due to rutile-breakdown during biotite-in reaction, causing U release and Th/U decrease. In contrast, zircons in felsic rocks lack pronounced Th/U zoning, which reflects zircon growth within less fractionated melts, where Th-U fractionation is compensated by coeval crystallization of abundant rock-forming minerals, all being highly incompatible for Th and U. This study was published in "*Chemical Geology*" (Gudelius et al., 2020).

Zircon melt inclusions in mafic and felsic rocks of the Bushveld Complex – constraints for zircon crystallization temperatures and partitioning coefficients (Chapter 5)

In the second study, major and trace element compositions and H_2O contents are presented for melt inclusions in zircon (MIZ) of the Bushveld Complex, which is the first dataset of this kind. Samples cover rutile-bearing cumulate rocks of the Rustenburg Layered Suite (Marginal and Critical zones) as well as rutile-free, magnetite-ilmenite-titanite-bearing diorites and granites of the Upper Zone, Rashoop Granophyre and Lebowa Granite Suites.

Within the Bushveld Complex, recrystallized MIZ assemblages always include quartz, alkali feldspar, albite-rich plagioclase and muscovite. Minor phases include fluorite, barite, apatite, monazite and magnetite, which dominate in felsic rocks, as well as amphibole, rutile, zircon daughter crystals and hydrous fluid inclusions. Homogenized MIZ of all samples display a similar rhyolitic composition and H_2O contents, but significant differences in trace element contents (e.g. Ti, Th/U, and REE). Furthermore, MIZ compositions are used to constrain the zircon crystallization temperature. For all samples, liquidus temperatures of MIZ obtained by normative Qz-Ab-Or contents and rhyolite-MELTS indicate entrapment mostly at 930-850°C (at 200 MPa), consistent with zircon saturation temperatures. For rutile-bearing rocks, these temperatures overlap with TiO_2 saturation temperatures and Ti-in-zircon temperatures of respective zircon hosts. However, in case of all rutile-free rocks, TiO_2 saturation temperatures and Ti-in-zircon temperatures only agree with temperatures from other geothermometers if a significantly reduced TiO_2 activity ~0.3 is considered, in agreement with modelling results presented in chapter 4. Furthermore, zircon-melt partitioning coefficients obtained from MIZ and host zircon compositions agree with published experimental data (for 900 °C) and show no systematic differences between mafic and felsic rocks. They also show no significant

correlations with melt inclusion size, composition and entrapment temperature. This study was submitted to "*Geochimica et Cosmochimica Acta*".

Hafnium Isotopic Composition of the Bushveld Complex requires Mantle Melt - Upper Crust Mixing: New Evidence from Zirconology of Mafic, Felsic and Metasedimentary Rocks (Chapter 6)

In the third study, zircon formation processes of the magmatic history of the Bushveld Complex are investigated using Hf isotope compositions of zircon from mafic and felsic rocks of the Bushveld Complex and adjacent metasediments. Combined with new bulk rock compositions and an investigation of zircon internal structures and morphologies, this data is used to develop a Zr-Hf budget for Bushveld Complex and to model the contribution of different mantle and crustal reservoirs to the generation of different parental magmas of the Bushveld Complex, which is still a highly debated topic.

Magmatic zircons in mafic cumulate rocks throughout the Rustenburg Layered Suite (RLS) display essentially the same Hf isotope compositions ranging between $\varepsilon Hf_{2.055\ Ga}$ of -7.5 and -10.2. Overlapping values were obtained for metamorphic zircons and overgrowths on detrital zircons in quartzites and metapelites of the BC contact aureole as well as for zircons in overlying felsic rocks (Lebowa Granite and Rashoop Granophyre suites) and Rooiberg Group volcanics. The same Hf isotope compositions are also obtained by averaging detrital zircon compositions of the surrounding Magaliesberg and Houtenbeck formations and by a six-point isochron from a garnet schist of the contact aureole. Combined with zircon core-rim relationships, this suggests that metamorphic zircon was precipitated from aqueous fluids and/or felsic melts at 550-900 °C, and that the Hf isotopic composition was homogenized by fluid transport in the contact aureole. Results of numerical modelling however indicate, that the Zr-Hf budget and Hf isotope composition of the BC is mainly controlled by mixing of mantle-derived melts with significant amounts of Kaapvaal Craton crust. Here, the B1 magma is dominated by Upper Crust, while genesis of B3 magma requires assimilation of lower crust. This study was published in "*Journal of Petrology*" (Zeh et al., 2020).

2. The Bushveld Complex

2.1 Introduction to layered intrusions

Mafic layered intrusions are solidified basaltic magma chambers that form large bodies of igneous rock having a distinct layering in bulk rock composition, mineral modes and texture. They are of particular petrological interest as they provide detailed records about the magmatic processes during the emplacement, cooling and differentiation of magma chambers in the crust and are therefore a natural laboratory to study how highly different rock types are generated from a (more or less) single parental magma (Irvine, 1982; Namur et al., 2015). Layered intrusions were found on all continents (except South America) and have a wide range in ages ranging from Archean to Oligocene (Fig 2.1). They generally occur in anorogenic settings and are frequently associated with large igneous provinces overlying mantle domains that experienced significant degrees of partial melting (O'Driscoll and VanTongeren, 2017). However, individual layered intrusions can be highly different in terms of chemical composition and size of the magmatic system, ranging from small bodies of a few kilometers in diameter (e.g. Rum in NW Scotland or Skaergaard in SE Greenland) to vast, sill-like bodies spanning hundreds of kilometers such as the Bushveld Complex in South Africa investigated in this study (Jakobsen et al., 2005; Cawthorn, 2015). Besides their scientific interest, they are further of high economic importance, as they host some world-class deposits in Cr, platinum-group elements (PGE), and V (Maier et al., 2013; Scoates and Wall, 2015).

Layered intrusions form by the intrusion and cooling of hot magma into much cooler crustal rocks. The intruded magma can reach the surface leading to a volcanic eruption or may remain stagnant within the crust, depending on the composition and temperature of the magma governing its buoyancy and viscosity as well as on the structural properties and tectonics of the surrounding crust (Namur et al., 2015). The composition of the parental magma depends on its partial melting source in Earth's mantle but can also be extensively modified during magma ascent and emplacement such as by assimilation of crustal rocks or by mixing with other, compositionally different magmas. During and/or after emplacement, the magma cools and reaches the liquidus, causing the crystallization of minerals.

In a simple model, igneous layering results from gravity-driven crystal settling and mineral sorting due to the density contrast between the crystallizing phases (cumulate phases) and the surrounding melt (Namur et al., 2015; O'Driscoll and VanTongeren, 2017). With progressive cooling, more minerals crystallize and accumulate as horizontal layers (cumulates) on a mineral substrate until the magma chamber is completely solidified. The extraction of cumulate crystals from the melt is accompanied by a change in magma composition marked by the progressive enrichment of incompatible elements (e.g. K, LILE, HFSE, H_2O) and the

depletion of compatible elements (e.g. Mg, Cr). This melt differentiation causes cumulate phases to change in composition and modal mineralogy, which finally results in compositionally and mineralogically stratified rocks. The chemical evolution of magmas can be modelled by two extreme conditions: (i) equilibrium crystallization, where the crystallizing phases stay in chemical equilibrium with the melt and (ii) fractional crystallization, in which the crystallizing phases are fractionated from the melt, e.g. due to physical separation. In reality, magmas likely evolve more complex and follow some intermediate paths in between.

Nevertheless, an ideal mafic layered intrusion should become more differentiated from base to top, as indicated by a change in (1) mineral composition (i.e. decreasing Mg# in olivine or pyroxenes; decreasing An% in plagioclase) and (2) cumulus assemblage showing a transition from a base rich in heavy, mafic minerals (e.g. olivine, orthopyroxene) to a top enriched in light, felsic minerals (e.g. plagioclase, quartz, alkali feldspar) and hydrous phases (e.g. amphibole). Thus, bulk-rock compositions of cumulates should become increasingly Fe- and Si-rich with stratigraphic height. Indeed, many layered intrusions generally show these differentiation trends from base to top (Jakobsen et al., 2010; Cawthorn, 2015) (Fig. 2.1), and further display cumulate layers with cross-bedding, scour textures and dropstones, suggesting a sedimentary-style deposition and supporting the crystal settling theory (O'Driscoll and VanTongeren, 2017). During settling of cumulate crystals, variable amounts of intercumulus melt can be trapped, and respective cumulate rocks are termed adcumulate (<7 % melt), mesocumulate (7-25 % melt) or orthocumulate (25-50 % melt). After entrapment, intercumulus melts may further differentiate and crystallize intercumulus mineral assemblages that can be highly different from that of the bulk rock and frequently include minerals rich in incompatible elements (HFSE, LILE) and H_2O – i.e. are the preferential place to look for zircon within mafic cumulates of layered intrusions (e.g. Zeh et al. 2015; Ver Hoeve et al., 2018; Wall et al. 2018).

The formation of cumulate rocks by crystal settling, however, cannot explain all phenomena and characteristics of igneous layering observed in layered intrusions, which also include repetition of layers with similar composition, reverse layering (less differentiated from base to top) or discordant layer contacts. Furthermore, cumulus plagioclase occurs at the base of some layered intrusions, which is in conflict with its slight buoyancy in basaltic melts (e.g. Campbell et al., 1978; Namur et al., 2011). Therefore, an alternative model was proposed in which basaltic magma chambers mostly crystallize in situ from slightly undercooled boundary layers formed at the floor and walls of the magma chamber (Campbell, 1978; McBirney and Noyes, 1979). Other studies suggested that post-cumulus processes like recrystallization or metasomatism also account for some igneous layering features (Sparks et al., 1985; Boudreau, 1995). Today, the debates about the formation of igneous layering continue and mainly concern the question, to which extent mineral compositions in layered cumulates may be used to extract

information about the parental magma (O'Driscoll and VanTongeren, 2017). The only consensus is that not a single layer-forming process can account for all phenomena observed in layered intrusions. Instead, layered intrusions result from a complex interplay between (1) dynamic layer forming processes involving large-scale internal movement of melt, mush or crystals (crystal settling, magma injection/mixing, liquid immiscibility, melt percolation through crystal mush) and (2) non-dynamic processes during crystallization, such as fluctuations in crystal growth rates (due to oscillatory nucleation along cotectic lines and/or a change in intensive parameters) and processes of re-equilibration in the crystal mush, like mush compaction, dissolution-precipitation, grain coarsening and chemical diffusion (Namur et al., 2015).

In summary, layered intrusions such as the Bushveld Complex are a product of a large number of magmatic processes, which can interfere and interact with each other, forming complex mineralogical and geochemical phenomena on multiple scales. They provide deep insights into some fundamental processes shaping and altering Earth's crust, such as magma differentiation, emplacement of large plutonic bodies and element fractionation processes.

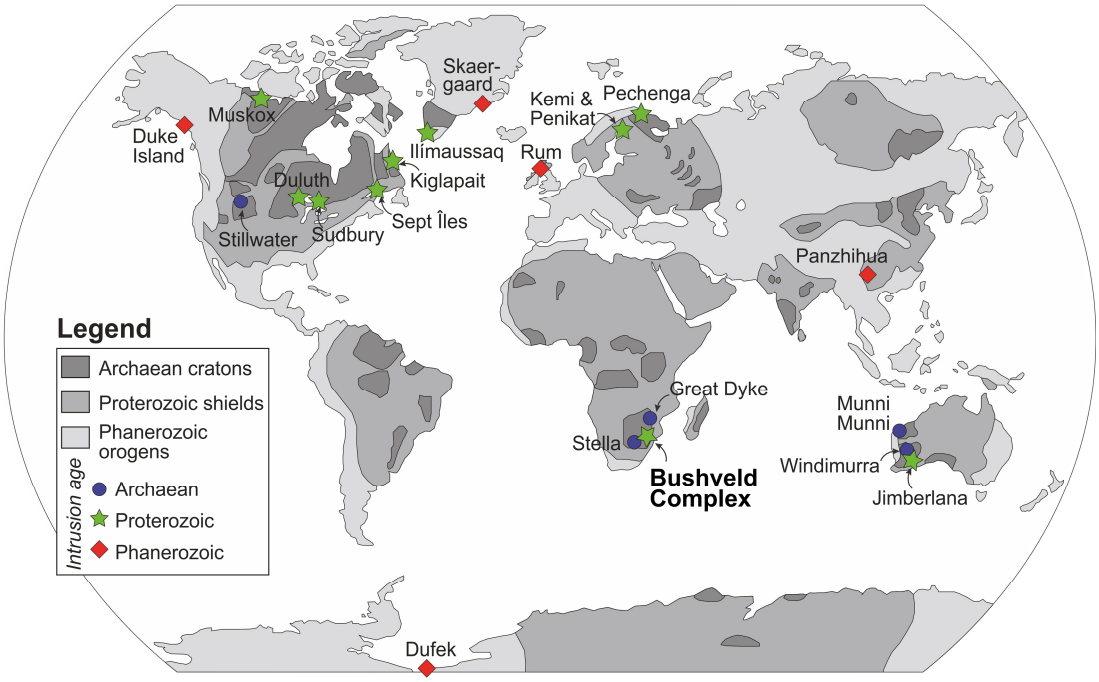

Figure 2.1 - World map showing the locations of Earth's most important layered intrusions, broadly subdivided after intrusion age (after O'Driscoll and VanTongeren, 2017).

2.2 Geology of the Bushveld Complex

The Bushveld Complex (BC) shares some general features outlined above with other layered intrusions, but it is unique in terms of size, complexity and economic importance which is the reason for its high scientific interest and relevance in petrology and geochemistry. It is a major

bimodal large igneous province (LIP) comprising by far Earth's largest mafic layered intrusion (outcrop size >65.000 km^2), Earth's largest A-type granite and vast volumes of felsic volcanic rocks. In total, the complex constitutes one of Earth's most valuable mineral provinces hosting the bulk of global resources in PGE, Cr and V, significant resources in Cu, Ni, Au, Sn, fluorite and Fe, as well as the world's largest andalusite resources in the contact metamorphic aureole (Maier et al., 2013; Cawthorn, 2015). Although subject to intense research spanning decades, its magmatic origin, emplacement and dynamic evolution is still incompletely understood, which is also due to the complexity of observed magmatic and mineralogical phenomena. In the following, some general features of the BC relevant in this study are briefly introduced.

2.2.1 Tectonic Setting and emplacement

The Bushveld Complex (N South Africa) is located in the northern part of the Kaapvaal Craton, which is the oldest subunit of the Kalahari Craton. The granitoid basement of the Kaapvaal Craton beneath the Bushveld Complex comprises the Witwatersrand Block (3.4 – 3.1 Ga) underlying most of the BC, and the slightly younger Pietersburg Block to the North (mostly 3.0 – 2.7 Ga) - (Poujol et al., 2003; Zeh et al., 2009) – (Fig. 2.2a). Both Blocks represent terranes which amalgamated during the Archean and are now separated by the Thabazimbi-Murchison lineament (TML), a prominent, crustal scale fault zone. Since its consolidation at ~3.0 Ga, the Kaapvaal Craton remained a highly stabilized, largely undeformed block of crust which was intermittently submerged, accompanied by the formation of large volcano-sedimentary basins comprising (with decreasing age): Witwatersrand, Ventersdorp, Transvaal, Waterberg, and Karoo. These included a series of large-scale magmatic events, the earliest of which was the eruption of voluminous flood basalts of the Ventersdorp large igneous province at ca. 2.7 Ga. Subsequently, the Bushveld magmatism occurred at ca. 2.06 Ga in a similar area of the Kaapvaal Craton, thus a genetic relationship is suggested by some authors (e.g. Olsson et al., 2011). Magmas of the Bushveld Complex were emplaced within the Transvaal Basin into clastic (meta-) sediments of the Transvaal Supergroup. This extensive, ca. 15 km thick sedimentary unit mostly comprises sandstones, shales and carbonates, having deposition ages between 2642 and 2055 Ma (Eriksson et al., 1995; Zeh et al., 2016, 2020 and references therein). Its uppermost part, the Pretoria Group (e.g. quartzites of the Magaliesburg formation), forms the direct wall rocks to most of the Bushveld Complex, while north of the TML, the Bushveld Complex magmas are directly underlain by granitoid rocks of the cratonic basement.

Large volumes of melt as those forming the Bushveld Complex are generated in the mantle either by (1) adiabatic decompression melting associated with lithospheric thinning or (2) by elevated temperatures associated with mantle plumes. The Bushveld Complex is underlain by an subcratonic lithospheric mantle (SCLM) characterized by 0.5-1.0 % lower P-

wave velocities at ~150 km depth as well as by Re-Os systematics in mantle xenoliths reset at ~2.05 Ga, indicating significant chemical modification of the mantle coeval to Bushveld magmatism (Carlson et al., 2000; James et al., 2001). Therefore, like for most large igneous provinces, a mantle plume origin for the BC is considered by most studies (e.g. Hatton, 1995, Richardson and Shirey, 2008, Zeh et al., 2015). Alternatively, the BC magmas were emplaced in an extensional stress field within a back-arc setting, possibly related to the NW-SE directed collision of the Kaapvaal and Zimbabwe cratons recorded in the Limpopo belt N of the Bushveld Complex (see Fig. 2.2a) - (Clarke et al., 2009; Maier et al., 2013).

Magma ascent through an up to 250 km thick SCLM keel seems unlikely, therefore previous studies suggested that BC magmas were emplaced due to localized transpressional extension along reactivated major crustal lineaments, in particular the Thabazimbi–Murchison lineament (TML) or possibly also along the Crocodile River and Steelpoort faults (Silver, 2004; Clarke et al., 2009; Maier et al., 2013). Indeed, early intruded, basal ultramafic rocks of the RLS display the greatest thickness and some of the highest Mg# in orthopyroxene close to the TML (Kruger, 2005; Clarke et al., 2009; Wilson, 2012). However, no vertical feeders having the right age, size or composition have been found in the field close to the TML or anywhere else within the BC. However, a proposed feeder is the Uitkomst Complex to the SE (Fig. 2.2b), which is a Ni-Cu-Cr-PGE-rich, tubular mafic-ultramafic layered body coeval and cogenetic to the BC (Maier et al., 2018).

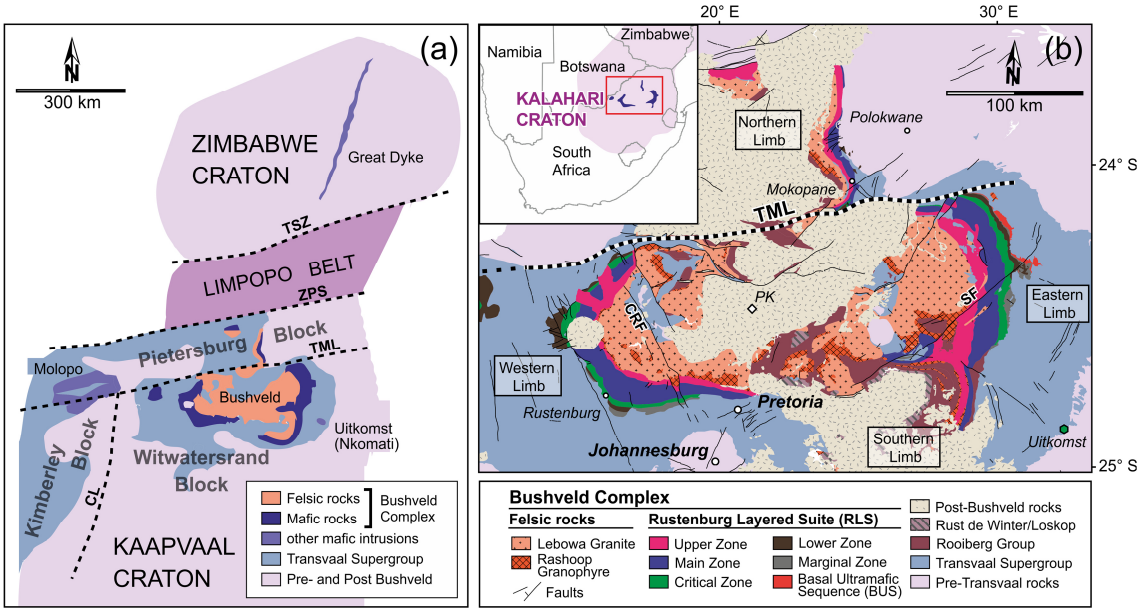

Figure 2.2 - (a) Simplified map showing the tectonic setting of the Bushveld Complex (modified after Zeh et al., 2015 and Viljoen, 2016). Shown are some major features of the northern Kalahari Craton. CL = Colesberg lineament; TML = Thabazimbi Murchison lineament; ZPS = Zoetfontein-Palala shear zone, TSZ = Triangle shear zone. (b) Geological map of the Bushveld Complex modified after the Council of Geoscience of South Africa (Johnson and Wolmarans, 2008); Wilson (2015) and Mungall et al. (2016) and references therein. Shown are the main units of the BC and surrounding rocks; SF = Steelpoort fault; CRF = Crocodile River Fault; PK = Palmietgat kimberlite.

2.2.2 Structure and main rock types

The Bushveld Complex is a bimodal large igneous province comprising three major subunits that were emplaced successively: (1) The mostly felsic volcanic rocks of the Rooiberg Group, (2) mafic-ultramafic cumulate rocks of the Rustenburg Layered Suite (RLS), and (3) overlying granitic rocks of the Lebowa Granite and Rashoop Granophyre Suites (Fig. 2.2b). The RLS and related granitic rocks intruded at a shallow crustal level between 1.5 and 3.0 ± 0.5 kbar (Kaneko and Miyano, 1990; Waters and Lovegrove, 2002), crystallized at ~2055 Ga and cooled rapidly below 650 °C within 1 Million years (Zeh et al., 2015; Setera et al., 2020). All three units have complicated field relationships to each other and their genetic relationship is subject to ongoing research (VanTongeren et al., 2010; Mathez et al., 2013). The RLS crops out at the surface as five distinct limbs having a curved shape and dipping towards the center: Northern, Eastern, Southern (mostly covered), Western and Far Western (Fig. 2.2b). Most Rooiberg Group volcanics and all granitic rocks occupy the center of the Bushveld Complex and are enclosed by RLS units. As most of the central Bushveld Complex is submerged by post-Bushveld rocks (e.g. volcanic rocks and sediments of the Karoo Group), it is still debated if and how the exposed limbs are connected at depth. However, a connectivity is supported by the occurrence of chromite-bearing pyroxenite xenoliths in the Palmietgat kimberlite showing chromite and pyroxene compositions overlapping with those of the BC (Webb et al., 2011) as well as by gravity data consistent with a 6-8 km thick sheet of dense, mafic rocks within an isostatically depressed crust (Cawthorn and Webb, 2001; Webb, 2004).

The first magmatic stage of the BC event was the eruption of voluminous felsic lavas of the Rooiberg Group, having an initial volume of ~300,000 km^3 (Twist and French, 1983; Günther et al., 2018). Lavas of the Rooiberg Group form an up to 5 km thick sheet of mostly glassy/ fine-grained rocks comprising from base to top: the basaltic to rhyolitic Dullstroom formation (located below the southeastern RLS) and the dacitic-rhyolitic Damwal, Kwaggasnek and Schrikkloof formations (Buchanan et al., 1999; Schweitzer et al., 1995; Buchanan, 2006). The Rooiberg lavas overly rocks of the Transvaal Supergroup and are intercalated with sedimentary strata (Eriksson et al., 1994; Günther et al., 2018). Although an eruption synchronous to the intrusion of the RLS was proposed (VanTongeren et al., 2010; VanTongeren and Mathez, 2012), field relationships and recent U-Pb zircon ages of 2057.3 ±2.8 Ma clearly support a formation prior to the RLS (Walraven, 1997; Martini, 1998; Harmer and Armstrong, 2000).

The RLS intrudes volcanic rocks of the Rooiberg Group (especially in the southern part) and is by far Earth's largest mafic layered intrusion. It was formed by the intrusion of ~1 Million km^3 magma, is 7-9 km thick and covers at least 65,000 km^2 (Cawthorn, 2015), dwarfing Earth's second largest layered intrusion, which is likely Dufek (Antartica) covering only 6600

km^2 (see compilation by Namur et al., 2010). The original size of the RLS was likely even bigger, if the coeval Molopo Farms Complex (~17,000 km^2, but mostly unexposed) in SE Botswana is included as a massive W-directed extension and considering that a large fraction of the RLS has been eroded (Prendergast, 2012; Maier et al., 2013; Kaavera et al., 2018). Since its discovery by Carl Mauch in 1921, the RLS became one of Earth's major mining areas, especially after discovery of the platiniferous Merensky Reef in 1924 (or associated Pt-rich iron-rich ultramafic pegmatite pipes ("IRUP") cross-cutting the layering as exemplified in Fig. 2.4a). Today, the RLS hosts about 75 % of the world's platinum-group element deposits (Cawthorn, 2015).

The stratigraphic subdivision of the RLS is mostly based on the occurrence of cumulus phases and includes from base to top: the Basal Ultramafic Sequence (BUS; recently discovered by Wilson, 2012, 2015), Marginal Zone, Lower Zone, Critical Zone, Main Zone and Upper Zone (Hall, 1932). In Fig. 2.3, the general order of appearance and disappearance of cumulus minerals as well as their changing mineral composition is illustrated: Most notably, a general differentiation trend of decreasing Mg# in olivine and pyroxenes and An% in plagioclase can be observed from base to top. However, the RLS stratigraphy is more complicated in detail due to multiple injections of parental magmas and lateral facies variations (Cawthorn et al., 2006).

The BUS consists of a ~750 m thick succession of chromite-bearing highly magnesian pyroxenites, harzburgites and dunites, which represents the first stage of filling of precursor magma compartments separated by basement highs, which developed prior to the formation of a coherent RLS magma chamber (Wilson, 2015) (see approximate field relationships in Fig. 2.4e). Mostly unlayered, noritic rocks of the Marginal Zone (ca. 800 m thick) were likely generated by multiple intrusion of variably contaminated and/or differentiated magmas and also occur as fine-grained chilled rocks at the contact to metasedimentary country rocks (Figs. 2.4d, 2.6g-h) - (Cawthorn et al., 2006; Wilson, 2015). The overlying Lower Zone (up to 1300 m thick) mostly consists of harzburgite and pyroxenite showing poor layering. In contrast, rocks of the Critical Zone above (~1800 m thick) are characterized by a spectacular layering of pyroxenite, chromitite, anorthosite and norite on all scales ranging from millimeters to tens of meters (e.g. Cawthorn et al., 2006; Maier et al., 2013; Scoon and Viljoen, 2019) (Figs. 2.4b-c, 2.6a-f). It hosts huge chromite deposits (LG, MG and UG layers) and the world's largest PGE deposits within the UG-2 chromitite and the Merensky Reef. The Merensky and Bastard Reef units are transitional to the overlying Main Zone (up to 3100 m thick), which consists of a vast sequence of gabbronorites and norites sometimes showing prominent textural layering (Fig. 2.5d). Its upper part is separated by the Pyroxenite Marker, which likely results from a change in parental magma composition (see below). The Upper Zone (~2000 m thick) is the laterally most extensive RLS unit and is characterized by cumulus magnetite, fayalitic olivine and apatite

(at the top) as well as by the lowest Mg# and An% within the RLS. Upper Zone rocks comprise gabbronorites and ferrodiorites intercalated with massive magnetitite layers (Figs. 2.5c, 2.7e-f), which host massive V deposits (Scoon and Mitchell, 2012). Complex emplacement mechanisms are indicated by several compositional reversals and the presence of coeval, pegmatitic diorite dykes (Figs. 2.5c, 2.7g-h) - (Ashwal, 2005; Scoon and Mitchell, 2012; Yuan et al., 2017).

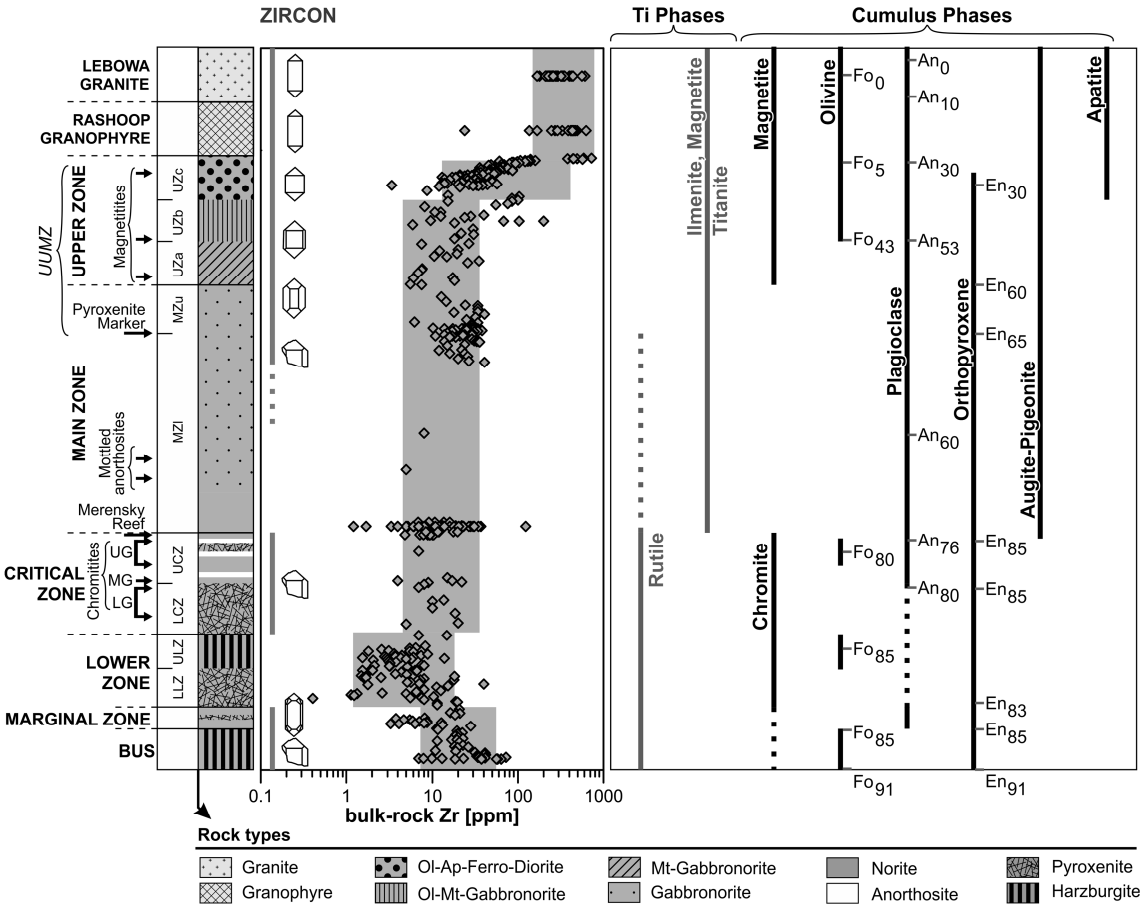

Figure 2.3 - Generalized stratigraphic profile of the Bushveld Complex including main rock types, bulk-rock Zr contents as well as main Ti-phase and cumulus phase assemblage with mean anorthite (An), forsterite (Fo) and enstatite (En) contents given for plagioclase, olivine and orthopyroxene, respectively (modified after Cawthorn and Walraven, 1998 and Wilson, 2015 and references therein). Compilation of bulk-rock Zr contents taken from Gudelius et al. (2020). Also shown are the occurrence and simplified crystal shapes of zircon within the BC.

Together with a change in cumulus phase assemblage and mineral composition from base to top, the RLS is characterized by a prominent change in the occurrence of Ti-bearing phases. Mafic cumulates of the lower RLS (BUS to lower Main Zone) are rutile-bearing (Fig. 2.6c,d), while mafic rocks of the central and upper RLS (Main and Upper Zones) are rutile-free and titanite-magnetite-ilmenite-bearing (Figs. 2.5e,f). Similar Ti-bearing phase assemblages continue in overlying granitic rocks (Kleemann and Twist, 1989). This main shift in Ti-bearing phases is critical for zircon-based thermometry of the whole Bushveld Complex as it determines the prevalent TiO_2 activity, knowledge of which is necessary to obtain accurate Ti-in-zircon

temperatures (see 3.4.2). Although the RLS comprises a large number of different rock types and displays highly different Zr contents (Fig. 2.3), all units excluding the Lower Zone and most of the Main Zone are zircon-bearing. However, the abundance of zircon is highly variable and it occurs in highly different shapes, crystal morphologies and assemblages, suggesting highly different physicochemical conditions during zircon formation, the investigation of which is one of the main topics of this study (see chapters 4 and 5).

Granitic rocks forming the roof of the BC are characterized by broadly overlapping major element compositions, but display textural and genetic differences. Rocks characterized by micrographic intergrowths of quartz and alkali feldspar accompanied by only minor amounts of plagioclase are combined as the Rashoop Granophyre Suite. These granophyres occur as sill-like bodies and several subtypes were recognized in an extensive study by Walraven (1987), the petrogenetic relations between which are still incompletely understood. By far the most voluminous unit is the Stavoren granophyre, which occurs as sheets up to several hundreds of meters thick above the RLS and below the Rooiberg Group. It was interpreted to represent intrusive, time-equivalent magmas to some Rooiberg Group volcanics (Walraven, 1987) or accumulated residual felsic melts derived from fractional crystallization within the RLS magma chamber (Mathez et al., 2013). Furthermore, metamorphic granophyres were identified, which were likely formed by contact metamorphism between mafic rocks of the RLS and overlying metasedimentary rocks (illustrated in Fig. 2.3b), or by re-melting of overlying Rooiberg Group volcanics (Walraven, 1987; Mathez et al., 2013; VanTongeren and Mathez, 2015).

The Lebowa Granite Suite is the youngest intrusive event of the BC and forms the largest exposure (65.000-70.000 km^2) of anorogenic A-type granite on Earth having a thickness of ~3 km and a volume of ~200.000 km^3 (Kleemann and Twist, 1989; Hill et al., 1996). The main intrusion comprises a lens-like body which dips towards the center of the intrusion with a shallow angle (~15°). Lebowa Granite rocks also occur as dykes penetrating RLS rocks and Rooiberg Group volcanics in some areas (Walraven, 1997; Wilson et al., 2000; Günther et al., 2018). The Lebowa Granite Suite mainly outcrops as two semicircular lobes within the Eastern and Western limbs of the RLS, which almost meet N of Pretoria (Cawthorn et al., 2006). It mainly consists of the voluminous Nebo Granite overlying the mafic layered rocks of the RLS in most parts of the BC. It is coarse-grained, pink to grey in colour (Figs. 2.5a, 2.7a-b) and mainly consists of alkali feldspar (perthitic), quartz, fayalitic olivine, hornblende and minor biotite and primary plagioclase. It is absent SE of Steelpoort Fault, where mafic rocks are mostly overlain by felsic rocks of the Rashoop Granophyre Suite and Rooiberg Group suggesting that this fault was active during granite emplacement and possibly acted as a magmatic feeder (Cawthorn et al. 2006). Further granites of the BC include the Sn-rich Bobbejaankop granite comprising endogenetic Sn mineralization suitable for mining, as well as

the vein- and dyke-like Klipkloof (closely related to Nebo granite) and Makhutso granites, which are youngest and form stocks and dykes in the other granites (Kleemann and Twist, 1989; Cawthorn et al., 2006).

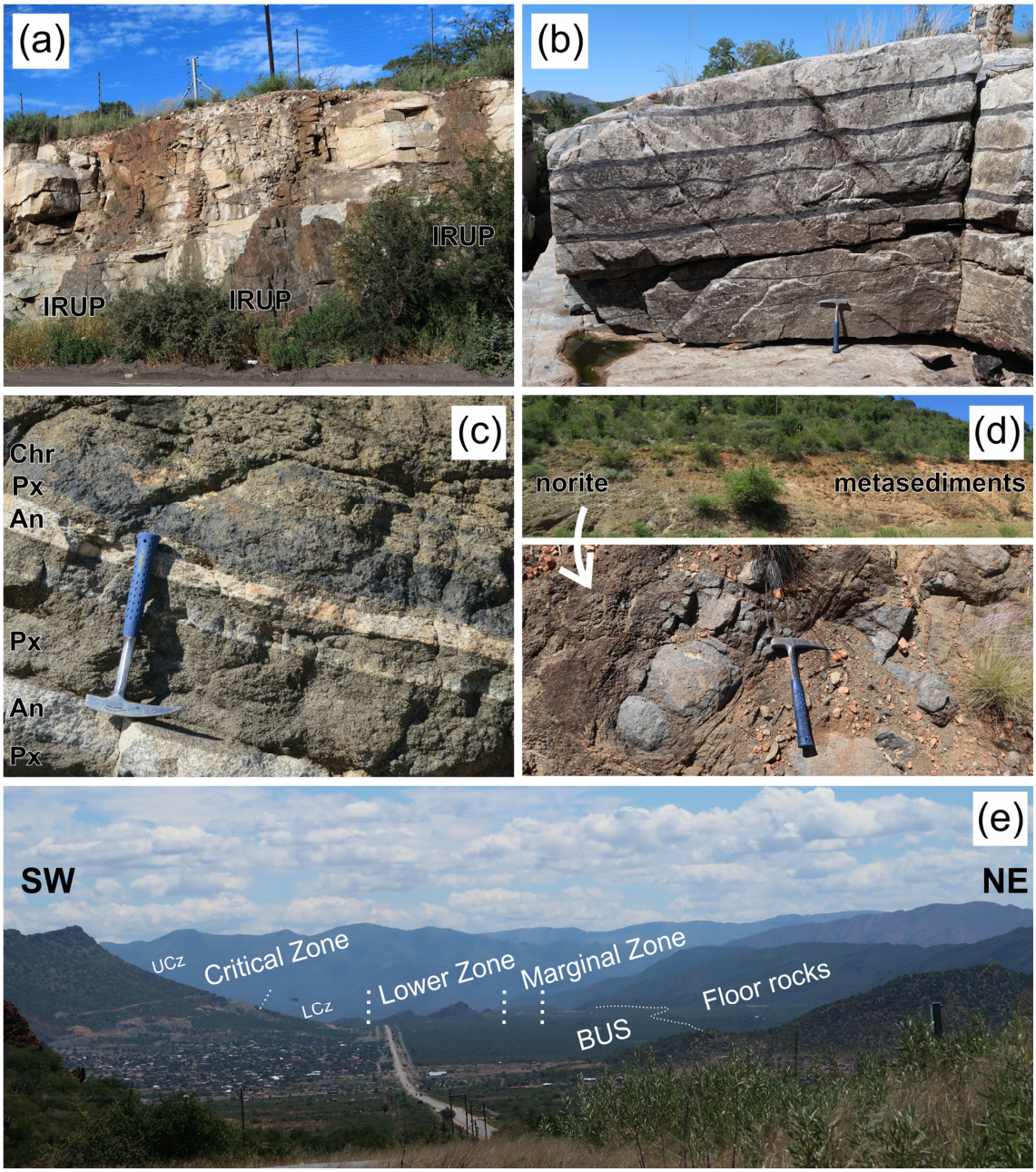

Figure 2.4 – Outcrop images of mafic rocks of the lower Bushveld Complex (rutile-bearing). (a) Outcrop of IRUP (Iron-rich ultramafic pegmatite) cutting cumulate rocks of the Upper Critical Zone near Tweefontein Mine. Wall height = 4 m. (b) Anorthosite (bright) intercalated with chromitite (dark grey) below UG-1 layer (Upper Critical Zone) at Dwars River outcrop. (c) Alternating chromite (Chr), pyroxenite (Px) and anorthosite (An) below UG-2 layer (Upper Critical Zone) at Bokoni Mine. (d) Outcrop of fine-grained, norites of the Marginal Zone near Schwerin Fold (E Limb) at the basal contact of the RLS towards metasediments of the Pretoria Group (Magaliesberg Quartzite). Boulders of fresh norite occur within the altered matrix. (e) Profile from the BC floor rocks to the Critical Zone in the Olifants River Trough at the Eastern Limb of the Bushveld Complex (so-called "Cameron Section"). Shown are approximate borders of SW-dipping RLS subunits. Note illegal chromite mining activity within the Critical Zone.

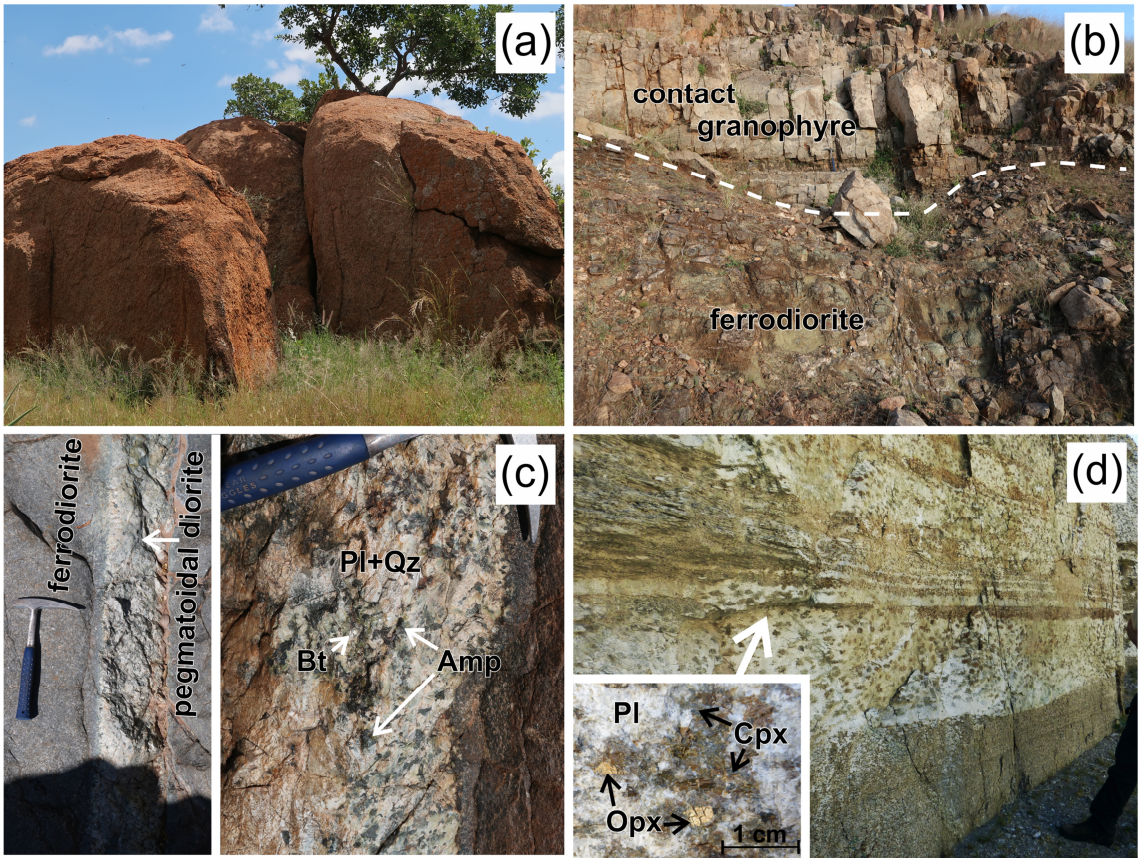

Figure 2.5 - Outcrop images of granitic and mafic rocks of the upper Bushveld Complex (rutile-free). (a) Typical outcrop of Lebowa Granite in the Eastern Limb (Nebo Granite), W Jane Furse. (b) Roof of the RLS showing the contact of ferrogabbro of the Upper Zone with overlying contact granophyre; Eastern Limb near Jane Furse (c) pegmatoidal diorite cross-cutting ferrodiorites of the Upper Zone, Eastern Limb near Magnet Heights. (d) Gabbronorites of the Main Zone showing prominent textural layering, Eastern Limb. Wall height = 2.5 m. Bt = biotite, Pl = plagioclase, Qz = quartz, Amp = amphibole, Cpx = clinopyroxene, Opx = orthopyroxene.

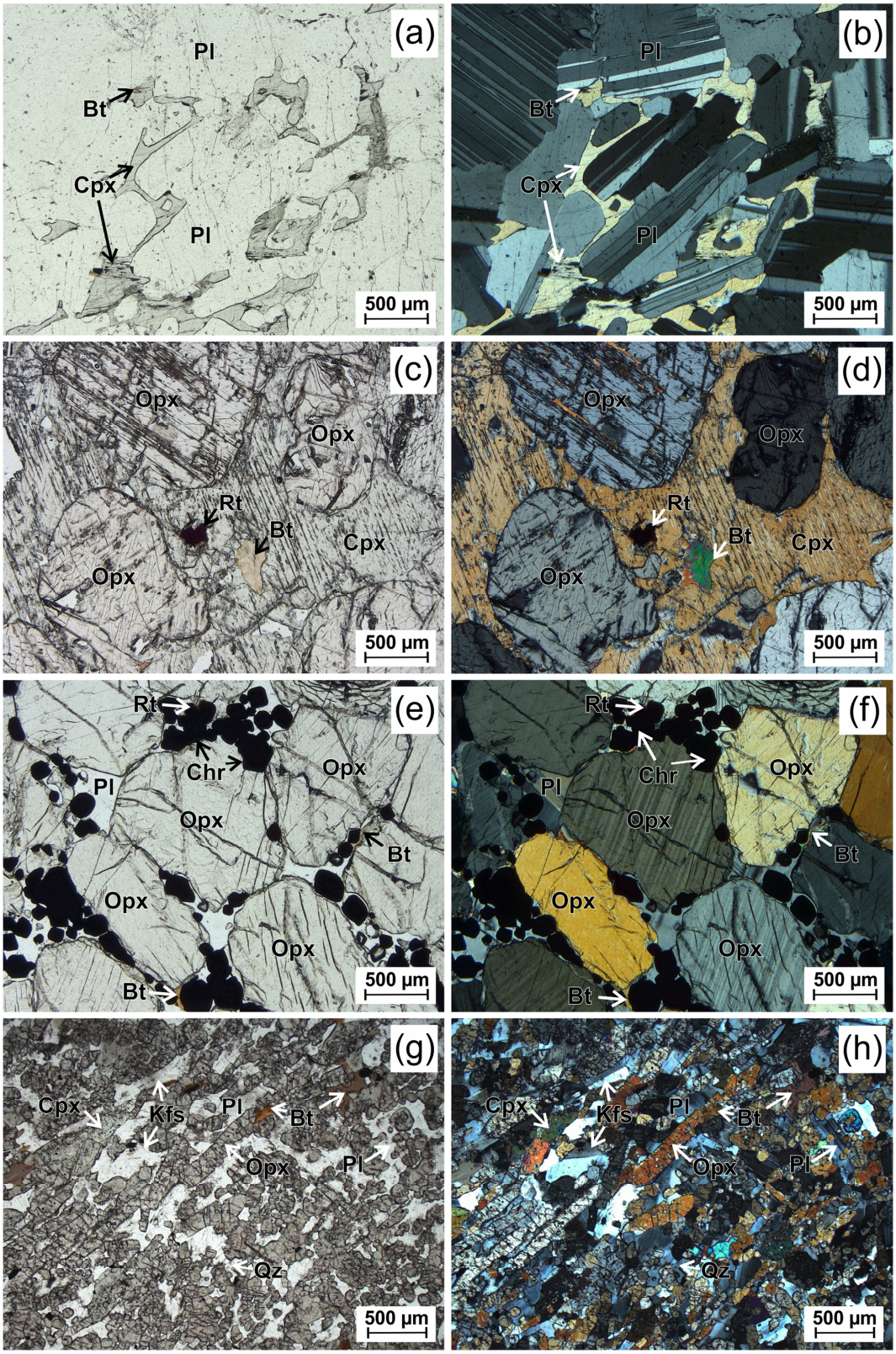

Figure 2.6 - Representative photomicrographs (left: plane-polarized light; right: cross-polarized light) of mafic rocks of the lower BC (rutile-bearing). (a-b) Pl cumulate with intercumulus Cpx and Bt (Upper Critical Zone). (c-d) Opx cumulate with intercumulus Rt and Bt (Merensky Reef), within a Cpx oikocryst. (e-f) Opx-Chr cumulate with intercumulus Pl, Bt and Rt (Lower Critical Zone). (g-h) Fine-grained, chilled norite of the Marginal Zone close to the RLS floor composed of elongated Opx, Cpx and Pl with intercumulus Bt, Qz and Kfs. Rt = rutile, Chr = chromite. Other mineral abbreviations as in Fig. 2.5.

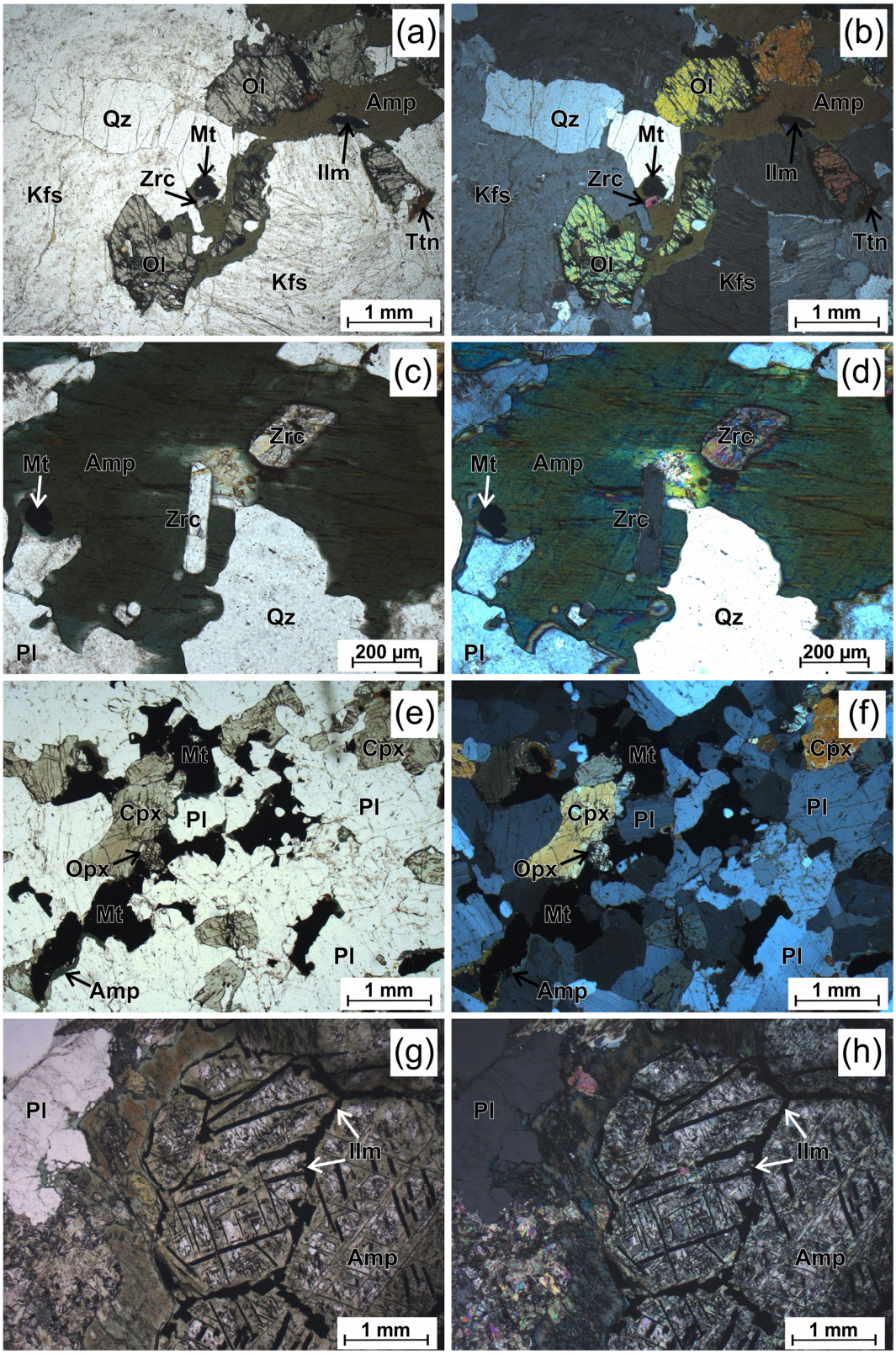

Figure 2.7 - Representative photomicrographs (left: plane-polarized light; right: cross-polarized light) of granitic and mafic rocks of the upper BC (rutile-free). (a-d) Rocks of the Lebowa Granite are mainly composed of Qz, Kfs, fayalitic Ol, Pl, Bt, and Amp. Here, euhedral zircon is abundant and frequently surrounded by Amp or Bt. Ti-phases comprise Ilm, Mt and Ttn. (e-f) Ferrodiorites of the Upper Zone are composed of Pl, Opx, Cpx and are commonly rich in Mt and Ilm. (g-h) Pegmatoidal diorite cross-cutting Upper Zone ferrodiorites showing coarse-grained intergrowths of mainly Pl and Amp (containing exsolved Ilm). Amp = amphibole, Mt= magnetite. Other mineral abbreviations as in Figs. 2.5 and 2.6.

2.2.3 Parental magmas

Parental magma compositions of the RLS were previously estimated from the composition of chilled rocks at the contact of the RLS and from the composition of mafic and ultramafic sills intruding the sedimentary country rocks (Sharpe, 1981; Cawthorn and Davies, 1983; Sharpe and Hulbert, 1985; Barnes and Maier, 2002). These studies revealed that the RLS was formed by two principal parental magmas: a Mg-rich (basaltic) andesite and a tholeiitic basalt. In a detailed study, Barnes et al. (2010) presented an extensive dataset of major and trace element compositions of RLS marginal rocks, which revealed a further subdivision of the tholeiitic basalt magma type: Following the terminology introduced by Barnes et al. (2010), the marginal rocks of the Lower and Lower Critical Zones indicate a Mg-andesitic magma B1, those of the upper Critical Zone a tholeiitic basalt magma B2 and those of the Main Zone a tholeiitic basalt magma B3, having higher average Mg# and lower contents in Ti, K, P and most incompatible trace elements compared to B2. For the Upper Critical Zone, only mixtures of B1 and B2 (at a ratio of ~60:40) satisfy the observed crystallization order and mineral compositions (Barnes et al., 2010). Notably, trace element analysis revealed that B1 magma is richest in most incompatible elements, Cr, Zr, all PGE and Ni. More recently, the discovery of an extensive succession of ultramafic rocks characterized by Mg# > 0.91 in olivine and orthopyroxene at the very base of the RLS required the contribution of a fourth, ultramafic parental magma UM (Wilson, 2012; Wilson, 2015) – (Table 2.1).

The Upper Main and Upper Zone (UUMZ) is considered as a coherent magmatic unit formed by the last major injection of mafic magma into the RLS chamber. Its base is marked by the Pyroxenite Marker, which is a massive, ~ 3 m thick orthopyroxenite layer about 650 m below the first appearance of cumulus magnetite (i.e. the base of the Upper Zone). Previous studies suggested that the Pyroxenite Marker was formed by abundant orthopyroxene crystallization due to a compositional change of the resident magma within the RLS chamber caused by the injection of new UUMZ magma (VanTongeren et al., 2010). Initial Sr isotope compositions significantly drop at the Pyroxenite Marker and stay generally constant in all units stratigraphically above, suggesting that the entire UUMZ resulted from closed-system fractional crystallization of a single batch of magma (Kruger, 2005; VanTongeren et al., 2010). However, previous studies documented several compositional reversals within the UUMZ stratigraphy, indicating that this unit was not an entirely closed system but rather reflects a magma chamber intermittently replenished by new inputs of magma (Ashwal, 2005; Yuan et al., 2017). Furthermore, it was suggested that significant amounts of exsolved felsic melt escaped from the UUMZ and may have contributed to the formation of felsic roof rocks of the BC (VanTongeren et al., 2010; VanTongeren and Mathez, 2012). This challenged previous estimations of the UUMZ parental magma, which were simply based on averaging bulk rock compositions of the

UUMZ which revealed a basalt-basaltic andesite composition (Tegner et al., 2006; VanTongeren et al., 2010). Since UUMZ rocks lack marginal sills, their parental magma composition is still unconstrained and the role of exsolved and/or admixed felsic melts during UUMZ formation is further discussed in chapters 4 and 5.

The parental magma composition of granitic rocks of the BC (Rashoop Granophyre and Lebowa Granite Suite) is essentially unknown and their genetic relationship with mafic rocks of the RLS is controversially discussed in literature (e.g. Twist and French, 1983; Walraven, 1985; Hill et al., 1996; Mathez et al., 2013). Commonly, their bulk rock composition is used as an approximation for the parental magma. However, granitic rocks of the BC are differentiated and display systematic variations in major and trace element compositions from base to top. These are characterized by a decrease in modal contents of mafic minerals, an increase in modal quartz and perthite, decreasing An% of plagioclase, increasing contents of Si, K, and Rb, decreasing contents of Fe, Ti, Ca, P, Ba, Sr, and Zr, as well as by a decrease in (Sr×Ba)/Rb (Kleemann and Twist, 1989; Hill et al., 1996; Cawthorn et al., 2006). The definition of a parental magma composition for volcanic rocks of the Rooiberg Group is similarly challenging, since they also show significant compositional fractionation trends with stratigraphic height (Buchanan et al., 2002; Buchanan, 2006; Günther et al., 2018).

Table 2.1 Proposed parental magma compositions for the Rustenburg Layered Suite

magma	**UM**	**B1**	**B2**	**B1+B2 (60:40)**	**B3**	**Bulk UUMZ**	**Bulk UUMZ**	**UUMZ + 25% Rashoop**
parent to	BUS	LZ, LCz	UCz	UCz	Mz	UUMZ	UUMZ	UUMZ (exsolved)
reference	[1]	[2]	[2]	[2]	[2]	[3]	[4]	[4]
P_2O_5	0.08	0.08	0.16	0.11	0.03	0.40	0.38	0.29
SiO_2	53.38	55.74	50.79	53.76	51.33	51.40	47.03	53.75
TiO_2	0.39	0.34	0.76	0.51	0.37	1.00	1.74	1.36
Al_2O_3	9.73	11.82	15.70	13.37	16.14	16.60	16.37	15.27
Cr_2O_3	0.24							
Fe_2O_3	1.13	10.50	12.54	11.32	10.45	13.00	17.33	13.96
MnO	0.17	10.50	0.19	6.38	0.18	0.10	0.20	0.17
MgO	19.00	11.85	6.91	9.87	7.69	4.60	6.48	4.99
CaO	5.36	6.50	10.70	8.18	11.25	9.70	9.39	7.11
NiO	0.09							
Na_2O	1.34	1.63	1.94	1.75	1.91	2.90	2.46	2.62
K_2O	0.54	0.98	0.25	0.69	0.28	0.70	0.36	1.6
Cr		1874	201	1205	408		92	70
Ni		368	106	263	133		84	63
Cu		32	76	50			132	99
Rb		41	4	26	8.9		5	76
Sr		198	348	258	337		260	215
Y		11.4	19.4	14.6	9.9		10	35
Zr		71	54	64	22.9		22	173
Nb		4.5	3.9	4.3	1.4		1.0	10
Ba		293	192	253	139		117	299
La		18	15	17	5.7			
Ce		35	32	34	11.5			
Pr		4.2	4.0	4.1	1.5			
Nd		15.5	17.2	16.2	6.3			
Sm		2.8	3.8	3.2	1.5			
Eu		0.82	1.31	1.02	0.76			
Gd		2.4	3.6	2.9	1.6			
Tb		0.34	0.55	0.42	0.26			
Dy		1.9	3.2	2.4	1.6			
Ho		0.38	0.66	0.49	0.35			
Er		1.1	1.8	1.3	0.96			
Tm		0.16	0.26	0.20	0.15			
Yb		1.1	1.7	1.4	0.98			
Lu		0.18	0.27	0.21	0.15			
Hf		1.9	1.3	1.7	0.66			
Ta		0.48	0.34	0.42	0.17			
Pb		13.9	4.3	10.0	2.8			
Th		3.5	0.7	2.3	0.63			
U		0.99	0.23	0.68	0.18			
Pt		0.0194	0.0095	0.0154	0.0127			

[1] Wilson (2015), [2] Barnes et al. (2010), [3] Tegner et al. (2006), [4] VanTongeren et al. (2010); LZ = Lower Zone, LCz = Lower Critical Zone, UCz = Upper Critical Zone, Mz = Main Zone, UUMZ = Upper Main and Upper Zone
major elements: wt.%; trace elements: ppm

3. Overview of zircon petrology

Zircon is a common accessory mineral in a wide range of magmatic, sedimentary and metamorphic rocks and occurs having highly different shapes, morphologies and compositions (Corfu et al., 2003; Hoskin and Schaltegger, 2003). The significance of zircon in geosciences derives from its exceptional suitability for U-(Th-)Pb geochronology and its mineralogical properties, characterized by a high physical and chemical resistivity and the incorporation of a large number of process-sensitive trace elements (e.g. Ti, U, Th, REE) - (Grimes et al., 2015; Kirkland et al., 2015). Thus, zircon provides a large number of geochemical and petrological applications, the ones relevant for this study are briefly outlined in the following.

3.1 Mineralogical properties of zircon

The physical and chemical properties of zircon and its ability to incorporate and retain trace elements are determined by its crystal structure (Finch and Hanchar, 2003). Zircon ($ZrSiO_4$) is an orthosilicate having a tetragonal crystal structure (space group $I4_1/amd$). The zircon structure is dominated by chains of edge-sharing SiO_4 tetrahedra and ZrO_8 dodecahedra parallel to the c axis, separated by channels or voids unoccupied in pure zircon (Fig. 3.1). This results in a relatively open structure characterized by a moderate density of 4.66 g/cm^3 and a very low thermal expansion which is mostly accommodated along the c-axis by an increase in the Zr-O bond length. This makes zircon extremely resistant to physical modification related to changes in pressure or temperature (Finch and Hanchar, 2003; Harley and Kelly, 2007). Zircon readily incorporates U, Th, Hf, P and the REE, and frequently accounts for significant fractions of the bulk-rock abundances of these elements (Hoskin and Schaltegger, 2003 and references therein).

Within the zircon lattice, impurity cations are mostly incorporated by substitution at either the Zr or Si sites, and only to a minor extent on interstitial sites. While Hf^{4+} can substitute for Zr^{4+} forming a complete solid solution with the hafnon component (natural zircons commonly contain <4 wt.% Hf), incorporation of REE^{3+} requires more complex coupled substitution mechanisms in which REE^{3+} replaces Zr^{4+} and charge balance is kept by P^{5+} replacing Si^{4+} (xenotime substitution) or by OH^- replacing O^{2-} (Finch and Hanchar, 2003; Hoskin and Schaltegger, 2003). The compatibility and abundance of REE in zircon increases with atomic number, and natural zircons frequently display positive Ce anomalies (expressed as Ce/Ce*N) and negative Eu anomalies (expressed as Eu/Eu*N). This is due to Ce^{4+} more readily substitutes for Zr^{4+} than Ce^{3+}, while Eu^{2+} is less compatible on the Zr site than Eu^{3+}. As Ce^{3+}/Ce^{4+} and Eu^{2+}/Eu^{3+} ratios are a function of oxygen fugacity, the magnitude of Ce- and Eu-anomalies (expressed as Ce/Ce*N and Eu/Eu*N) in zircon can be utilized as a sensor for redox conditions (Trail et al., 2012).

Commonly high contents of U and Th in zircon result from simple substitution of U^{4+} and Th^{4+} for Zr^{4+}, and are responsible for radiation damage in many natural zircons. Because zircon is characterized by sluggish diffusion for most elements (e.g. REE, Th, U, Hf, O), a low solubility in crustal fluids and melts and a general resistance to chemical and physical breakdown, coupled dissolution-precipitation processes of structurally damaged, self-irradiated zircons are the only way to effectively break down zircon (Cherniak and Watson, 2003; Geisler et al., 2007). Due to its structural stability, there is also a high chance for melt inclusions entrapped in zircon to remain compositionally pristine without suffering from post-entrapment alteration or diffusional re-equilibration (further discussed in 3.5).

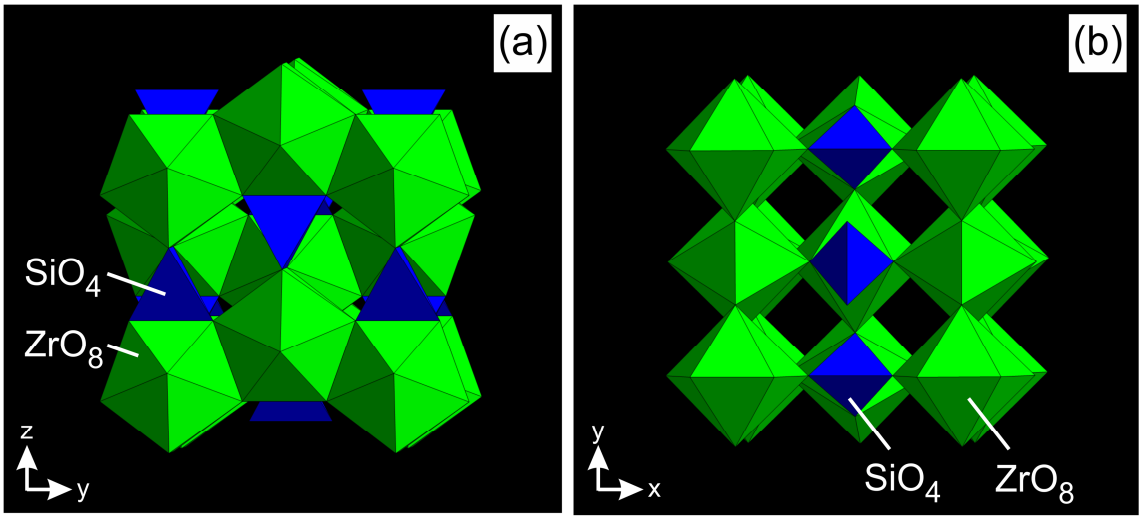

Figure 3.1 – (a) Zircon structure projected on (100) with z vertical, showing chains of alternating edge-sharing SiO_4 tetrahedra (blue) and ZrO_8 dodecahedra (green) linked laterally by edge-sharing dodecahedra (Crystal Maker image after Deer et al. (2013)). (b) Zircon structure projected on (001), showing view down the [001] channels (Finch and Hanchar, 2003).

3.2 U-Pb geochronology and Hf isotopes

The crystal structure of zircon incorporates U and Th but essentially excludes Pb, which is particularly useful since ^{238}U, ^{235}U, and ^{232}Th follow long-lived decay series towards ^{206}Pb, ^{207}Pb and ^{208}Pb, having half-lives of 4468, 704 and 14050 Ma, respectively, long enough to cover all of Earth's history but short enough, so that radiogenic Pb can be also measured in comparatively young zircons down to ~1 Ma (Parrish and Noble, 2003). Derivation of the decay equation and isochron equations in the U–Th–Pb system results in the following isochron equations:

$$\left(\frac{^{206}Pb}{^{204}Pb}\right) = \left(\frac{^{206}Pb}{^{204}Pb}\right)_0 + \left(\frac{^{238}U}{^{204}Pb}\right)\left(e^{\lambda_{238}t} - 1\right) \quad (3.1)$$

$$\left(\frac{^{207}Pb}{^{204}Pb}\right) = \left(\frac{^{207}Pb}{^{204}Pb}\right)_0 + \left(\frac{^{235}U}{^{204}Pb}\right)\left(e^{\lambda_{235}t} - 1\right) \quad (3.2)$$

$$\left(\frac{^{208}Pb}{^{204}Pb}\right) = \left(\frac{^{208}Pb}{^{204}Pb}\right)_0 + \left(\frac{^{232}Th}{^{204}Pb}\right)\left(e^{\lambda_{232}t} - 1\right) \quad (3.3)$$

where subscripts 0 denotes the initial isotope ratios, t the time since last equilibrium (e.g. crystallization of the mineral) and λ_{238}, λ_{235} and λ_{232} the decay constants for ^{238}U, ^{235}U and ^{232}Th, respectively (Schoene, 2014). Normalization is done using the stable isotope ^{204}Pb, which has no radioactive parent and the abundance of which remained effectively unchanged during Earth's history (Parrish and Noble, 2003). Initial Pb in equations 3.1-3.3 is also termed "common lead", which in case of zircon is mostly negligible compared to the radiogenic component. Thus, these equations simplify to:

$$\left(\frac{^{206}Pb^*}{^{238}U}\right) = \left(e^{\lambda_{238}t} - 1\right) \quad (3.4)$$

$$\left(\frac{^{207}Pb^*}{^{235}U}\right) = \left(e^{\lambda_{235}t} - 1\right) \quad (3.5)$$

$$\left(\frac{^{208}Pb^*}{^{232}Th}\right) = \left(e^{\lambda_{232}t} - 1\right) \quad (3.6)$$

where * denotes radiogenic Pb. The Th-Pb decay is commonly not utilized in zircon geochronology due to its significantly longer half-live and because the U-Pb dual decay system permits the construction of another isochron equation:

$$\frac{\left(\frac{^{207}Pb}{^{204}Pb}\right) - \left(\frac{^{207}Pb}{^{204}Pb}\right)_0}{\left(\frac{^{206}Pb}{^{204}Pb}\right) - \left(\frac{^{206}Pb}{^{204}Pb}\right)_0} = \left(\frac{^{235}U}{^{238}U}\right)\left(\frac{e^{\lambda_{235}t} - 1}{e^{\lambda_{238}t} - 1}\right) = \left(\frac{^{207}Pb^*}{^{206}Pb^*}\right) \quad (3.7)$$

Since present day $^{235}U/^{238}U$ is constant in most terrestrial systems, there is no need to measure U. Solving equation 3.7 iteratively, an Pb-Pb age can be obtained by linear fitting in the $^{206}Pb/^{204}Pb$ vs. $^{207}Pb/^{204}Pb$ space or, if common lead can be neglected, directly from the measured $^{207}Pb^*/^{206}Pb^*$. Thus, by analysis of U and Pb isotopes in zircon, three ages can be obtained which should all agree, provided closed system conditions. There are several numerical and graphical methods to test the assumption of a closed-system and to extract further geological information. In zircon U-Pb geochronology, data are usually shown after common lead correction in Concordia diagrams which plots $^{206}Pb^*/^{238}U$ versus $^{207}Pb^*/^{235}U$ and which was introduced by Wetherill (1956) - (Schoene, 2014). Here, the concordia curve is the locus where

both systems yield the same age, indicating closed system conditions since last equilibrium. If analyses are discordant (i.e. off the concordia) but are linearly correlated, the upper intercept with the concordia curve should give the crystallization age while the lower intercept should yield the age of isotopic disturbance (Davis, 2003). There are numerous reasons for discordance, including Pb loss, mixing of different age domains and intermediate daughter product disequilibrium in case of young zircons (extensively reviewed by Schoene, 2014).

Together with U and Th, zircon is a significant carrier of heavy REE and Hf, which provides Lu-Hf, another long-lived radioactive isotope system, making zircon the most versatile mineral in geochronology. Zircon incorporates ^{176}Lu which decays to ^{176}Hf with a half live of 35.6 Ga. Using the stable isotope ^{177}Hf for normalization, this decay system can be expressed by the following age equation:

$$\left(\frac{^{176}\mathrm{Hf}}{^{177}\mathrm{Hf}}\right) = \left(\frac{^{176}\mathrm{Hf}}{^{177}\mathrm{Hf}}\right)_0 + \left(\frac{^{176}\mathrm{Lu}}{^{177}\mathrm{Hf}}\right)\left(e^{\lambda t} - 1\right) \qquad (3.8)$$

where subscript 0 denotes the initial isotope ratio, t the time since last equilibrium and λ the decay constant of ^{176}Lu (Kinny and Maas, 2003). Zircon commonly contains Lu at the ppm level and up to several wt.% Hf, which substitutes for Zr and has a largely identical geochemistry as Zr. Thus, most zircons display extremely low Lu/Hf (mostly ~0.002) causing that radiogenic ingrowth of ^{176}Hf is only minor and the measured ^{176}Hf/^{177}Hf ratio of zircon largely represents the initial value during zircon crystallization. During partial melting, Lu/Hf of a rock changes because Lu is slightly more compatible than Hf, causing that rocks of the residual mantle evolve towards more radiogenic ^{176}Hf/^{177}Hf compared to crustal rocks. Thus, Hf isotopes in zircon can track the chemical differentiation and evolution of Earth's crust and mantle, including partial melting events, magma mixing or recycling of crust. They can be used to calculate model ages (e.g. with respect to the depleted mantle) and are highly resistant against overprint, even for zircons having highly discordant U-Pb ages (Kinny and Maas, 2003). In combination with (concordant) U-Pb ages, Hf isotopes in zircon are particularly powerful geochemical tracers and can reveal an integrated image of the tectono-magmatic history of entire continents (e.g. Griffin et al., 2004; Gerdes and Zeh, 2006).

3.3 Zircon trace element systematics

Trace element contents and ratios in zircon are frequently employed as a petrogenetic indicator for the growth mechanism and tectono-magmatic provenance of zircon and can yield answers to a wide range in petrological-geochemical problems. For example, previous studies have demonstrated that magmatic zircon populations revealed systematic variations in Hf, REE, Ti, U

and Th contents as well as in Eu/Eu*N, Ce/Ce*N, Yb/Gd, Zr/Hf and Th/U ratios which were interpreted to reflect zircon crystallization within an evolving magma chamber (Claiborne et al., 2006; Claiborne et al., 2010; Miles et al., 2013). Furthermore, the investigation of large zircon populations revealed that zircon trace element systematics consistently differ between rocks from MOR-settings, ocean islands and continental arcs (Grimes et al., 2007; Grimes et al., 2015) as well as between granitoids, mafic rocks, syenites, carbonatites and kimberlites (Belousova et al., 2002). This was employed to construct zircon discrimination diagrams for different rock types and tectono-magmatic settings which has gained significant attention, since they allow to estimate the likely geochemical source of out-of-context zircons, including detrital zircons preserved from the Hadean and Archean (e.g. Whitehouse and Kamber, 2002; Nutman and Hiess, 2009; Carley et al., 2014).

However, while the discrimination for zircon populations based on their trace element systematics mainly relies on comparison with published discrimination diagrams (e.g. U/Yb vs. Nb/Yb; Ti vs. Sc/Yb) obtained from the statistical evaluation of large datasets of zircon compositions from various rock types (e.g. Grimes et al., 2015), the magmatic processes causing trace element variation in zircon remain poorly investigated. This also applies to the Th/U ratio of zircon, which is frequently used as a petrogenetic indicator, because it can be simultaneously obtained during U-Pb dating and may be helpful to discriminate between different zircon domains. Previous studies have detected large differences for natural zircons, which sometimes systematically differ between different rock types and zircon age populations (Kirkland et al., 2015; Yakymchuk et al., 2018). It was frequently observed that metamorphic zircon displays lower Th/U (<0.1) compared to magmatic zircon (>0.1) - (Williams and Claesson, 1987; Rubatto, 2002). However, subsequent studies have shown that this discrimination is not straightforward, since high Th/U above 0.1 were also observed in metamorphic zircon, in particular from (ultra-) high temperature rocks. However, the reasons for variations in Th/U in zircon are poorly constrained, and some variability in Th/U was attributed to coeval growth and/or breakdown of Th-rich phases like allanite and monazite (Kirkland et al. 2015; Yakymchuk et al., 2018 and references therein). Several attempts have been made to relate Th/U of magmatic zircon with that of the respective bulk rock in order to detect inherited zircon domains which likely display a non-equilibrium in Th/U (Kirkland et al., 2015). However, the potential of Th/U in zircon as a petrogenetic indicator for magmatic rocks and how it depends on cogenetic mineral assemblages and fractionation processes of U and Th during zircon growth are incompletely understood and further addressed in chapter 4.

3.4 Zircon-based geothermometers

3.4.1 Zircon saturation models

Although zircon occurs widespread in different rock types, some crustal rocks lack zircon, which led to the question, which physicochemical magma conditions (chemical composition, temperature, pressure, oxygen fugacity) control zircon saturation. In a landmark study, Watson and Harrison (1983) experimentally determined zircon saturation as a function of both melt composition and temperature and established a widely used thermometer of zircon formation:

$$\ln D_{Zr}^{zircon/melt} = \{-3.8 - [0.85(M - 1)]\} + 12900/T \quad (3.9)$$

where $D_{Zr}^{zircon/melt}$ is the concentration ratio of Zr in zircon to Zr in the melt, T is the absolute temperature (in K), and M the compositional parameter given by the cation ratio (Na + K + 2Ca)/(Al - Si). Thus, the temperature at which zircon (having stoichiometric 497600 ppm Zr) saturates (TZr-WH83) is given by:

$$\text{TZr-WH83 (°C)} = \frac{12900}{\ln\frac{497600}{Zr(ppm)} + 3.8 + 0.85(M - 1)} - 273.15 \quad (3.10)$$

where Zr (ppm) is the Zr concentration of the melt. The zircon saturation experiments by Watson and Harrison (1983) were performed at temperatures of 800-1020 °C, pressures of 1.2-6.0 kbar and resulted in melts having M values of 1.01-2.00 and Zr contents of 180-3420 ppm, setting the calibration limits for which their formulation is valid. More recently, Gervasoni et al. (2016) provided a zircon saturation thermometer calibrated for more alkaline rocks having M of 1.7-3.1. Furthermore, Boehnke et al. (2013) used improved analytical methods and experimental designs to refine the zircon saturation model, yielding the zircon saturation thermometer (TZr-B13):

$$\text{TZr-B13 (°C)} = \frac{10108}{\ln\frac{497600}{Zr(ppm)} + 1.48 + 1.16(M-1)} - 273.15 \quad (3.11)$$

where the compositional parameter M is the same as in Watson and Harrison (1983) and Zr (ppm) is the Zr concentration of the melt. The thermometer of Boehnke et al. (2013) as well as the most recent calibration by Borisov and Aranovich (2019) yield largely similar results to that of Watson and Harrison (1983), but tend to produce slightly lower zircon saturation temperatures below ~900 °C (Marxer and Ulmer, 2019).

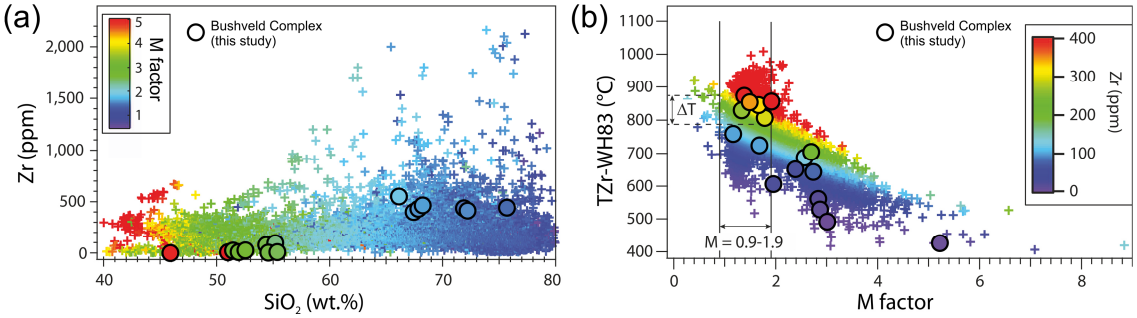

Figure 3.2 - Covariation between bulk-rock contents of (a) Zr and SiO_2 and between (b) the zircon saturation temperature of Watson and Harrison (1983) (TZr-WH83) and the M factor used for its calculation, which is the cation ratio (Na + K + 2Ca)/(Al-Si). Shown is data for 11,705 igneous rocks from Queensland, Australia (modified after Siégel et al., 2018), and for samples of the Bushveld Complex investigated in this study. Note that the M factor mostly depends on bulk-rock SiO_2, while TZr-WH83 decreases with increasing M factor and with decreasing Zr content. Also note, that TZr-WH83 is only applicable for a narrow range of bulk-rock compositions between M = 0.9-1.9 (indicated in b).

It is important to note, that zircon saturation temperatures are theoretical temperatures for the onset of zircon crystallization and are only relevant as a magmatic geothermometer, if the investigated bulk rock closely resembles that of the actual melt from which zircon grew from (Hanchar and Watson, 2003; Siégel et al., 2018). This may apply to unaltered, crystal poor volcanic rocks but is likely not the case for most plutonic rocks. Using compositionally different mafic and felsic samples from the Bushveld Complex (Fig. 3.2) combined with a detailed thermometric investigation of zircon crystallization, the validity of zircon saturation thermometry for different rock types is further tested in chapters 4 and 5.

3.4.2 Ti-in-zircon geothermometry

Titanium-in-zircon is one of the most frequently used mineral thermometers and was applied to zircons from a wide range of rock types. Within the zircon lattice, Ti^{4+} can substitute for both Si^{4+} and Zr^{4+}, which can be expressed as two equations using endmember components:

$$\text{Si-Substitution:} \quad ZrSiO_4 + TiO_2 = ZrTiO_4 + SiO_2 \qquad (3.12)$$

$$\text{Zr-Substitution:} \quad ZrSiO_4 + TiO_2 = TiSiO_4 + ZrO_2 \qquad (3.13)$$

Recent experiments involving zircon crystallization in the presence of SiO_2 and TiO_2 as well as computational models suggest that Ti substitution for Si dominates at pressures <3.5 GPa (Ferry and Watson, 2007; Ferriss et al., 2008). Thus, the basis of Ti-in-zircon thermometry is equilibrium 3.12, thermodynamic analysis of which predicts a linear correlation of [log(ppm Ti-Zrc) + log($a$$SiO_2$) - log($a$$TiO_2$)] with T^{-1} (Ferry and Watson, 2007). Using data of Watson et al.

(2006) and new experiments, this relationship was quantitatively calibrated by Ferry and Watson (2007) resulting in the most recent and frequently used Ti-in-zircon thermometer:

$$\log(\text{ppm Ti-Zrc}) = 5.711 \pm 0.072 - \frac{4800 \pm 86}{T(K)} - \log(a\text{SiO}_2) + \log(a\text{TiO}_2) \qquad (3.14)$$

or rearranged to:

$$\text{T}(°\text{C}) = \frac{4800 \pm 86}{5.711 \pm 0.072 - \log(\text{ppm Ti-Zrc}) - \log(a\text{SiO}_2) + \log(a\text{TiO}_2)} - 273.15 \qquad (3.15)$$

Titanium-in-zircon thermometry is ideally suited for rocks, in which zircon occurs in textural and chemical equilibrium with both rutile and quartz, indicating $a\text{SiO}_2 = a\text{TiO}_2 = 1$. While quartz commonly occurs together with zircon, rutile is absent in most magmatic rocks, which rather contain other Ti-bearing phases such as ilmenite, Ti-magnetite or titanite, suggesting $a\text{TiO}_2 < 1$. While zircon commonly occurs together with quartz (indicating $a\text{SiO}_2 = 1$), this requires independent estimates of $a\text{TiO}_2$ during zircon crystallization, which can be estimated using phase equilibria (e.g. $\text{TiO}_2 + \text{FeTiO}_3 = \text{SiO}_2 + \text{MgSiO}_3$ as in Ickert et al. (2011)), rutile saturation models (Hayden and Watson, 2007; Xiong et al., 2009) or thermodynamic modelling (Schiller and Finger, 2019). However, all these methods cannot be applied if investigated zircons occur out of their petrologic context, which is the case for most detrital zircons (Fu et al., 2008). Inherent constraints for $a\text{TiO}_2$ based on zircon alone are only possible if zircon grains include the cogenetic Ti phase assemblage or directly using TiO_2 saturation thermometry of zircon-forming melts obtained from melt inclusions analysis combined with other independent thermometers (see chapter 5).

Besides the need for $a\text{TiO}_2$ estimates for rutile-free rocks, another drawback of the Ti-in-zircon thermometer is its largely unconstrained dependency on pressure. Based on the calculated ΔV of reaction 3.12, Ferry and Watson (2007) stated that the Ti content in zircon coexisting with quartz and rutile decreases with increasing pressure at a rate of ~50°/GPa at constant temperature, $a\text{TiO}_2$ and $a\text{TiO}_2$. Even higher rates of up to 100°C/GPa are predicted by computational modelling (Ferriss et al., 2008). Therefore, the Ti-in-zircon thermometer is most appropriate for pressures similar to ~1 GPa corresponding to the experiments used for its calibration (Ferry and Watson, 2007). On the other hand, the incorporation of Ti in the zircon lattice is likely compensated by elastic lattice dilation without a change in unit cell volume, suggesting that the pressure effect is rather minor (Blundy and Wood, 1994; Schiller and Finger, 2019). Furthermore, previous studies concluded that only at pressures >2 GPa, more Ti substitutes for Zr instead of Si, compromising Ti-in-zircon thermometry based on the calibration

of Ferry and Watson (2007) using equilibrium 3.12, while at lower pressure (such as 0.2 GPa estimated for the Bushveld Complex), no pressure correction is necessary. However, the pressure dependency of Ti-in-zircon has never been rigorously tested for natural samples and remains a persisting uncertainty of the method (Fu et al., 2008).

Once incorporated into the zircon lattice by reaction 3.12, Ti displays an extremely low diffusivity, suggesting that zircon is highly retentive of Ti chemical signatures and corresponding Ti-in-zircon temperatures. Although Ti diffusion is slightly faster than that of U and Th, it is significantly below that of Pb, REE and O, suggesting that zircon can retain its crystallization temperature even if radiometric ages are lost (Cherniak and Watson, 2003; 2007).

3.4.3 Zircon morphology

Natural zircon occurs in a wide range of crystal shapes and morphologies showing highly different fractions of pyramid faces {101}, {211} and {301} as well as prism faces {100} and {110}. With the aim to distinguish different granite types based on the morphology of zircon populations, Pupin (1980) introduced a classification scheme comprising 64 subtypes (Fig. 3.3). Here, classification on the x-axis (so-called “index A”) is done by the occurrence of the three pyramid faces {101}, {211} or {301}, or the combination of {101} and {211} at variable ratios. Shown on the y-axis (so-called “index T” or temperature) are zircons classified based on the occurrence of no prism faces, {100}, or {110} prisms faces, or the combination of {100} and {110} at variable ratios. Here, the S-type habitus (likely most abundant in endo- and exogenous rocks) forms the diagram’s core and the other main types were logically arranged around (Pupin, 1980). It must be noted, that some main types, including the entire column C, I, R, F, are purely theoretical.

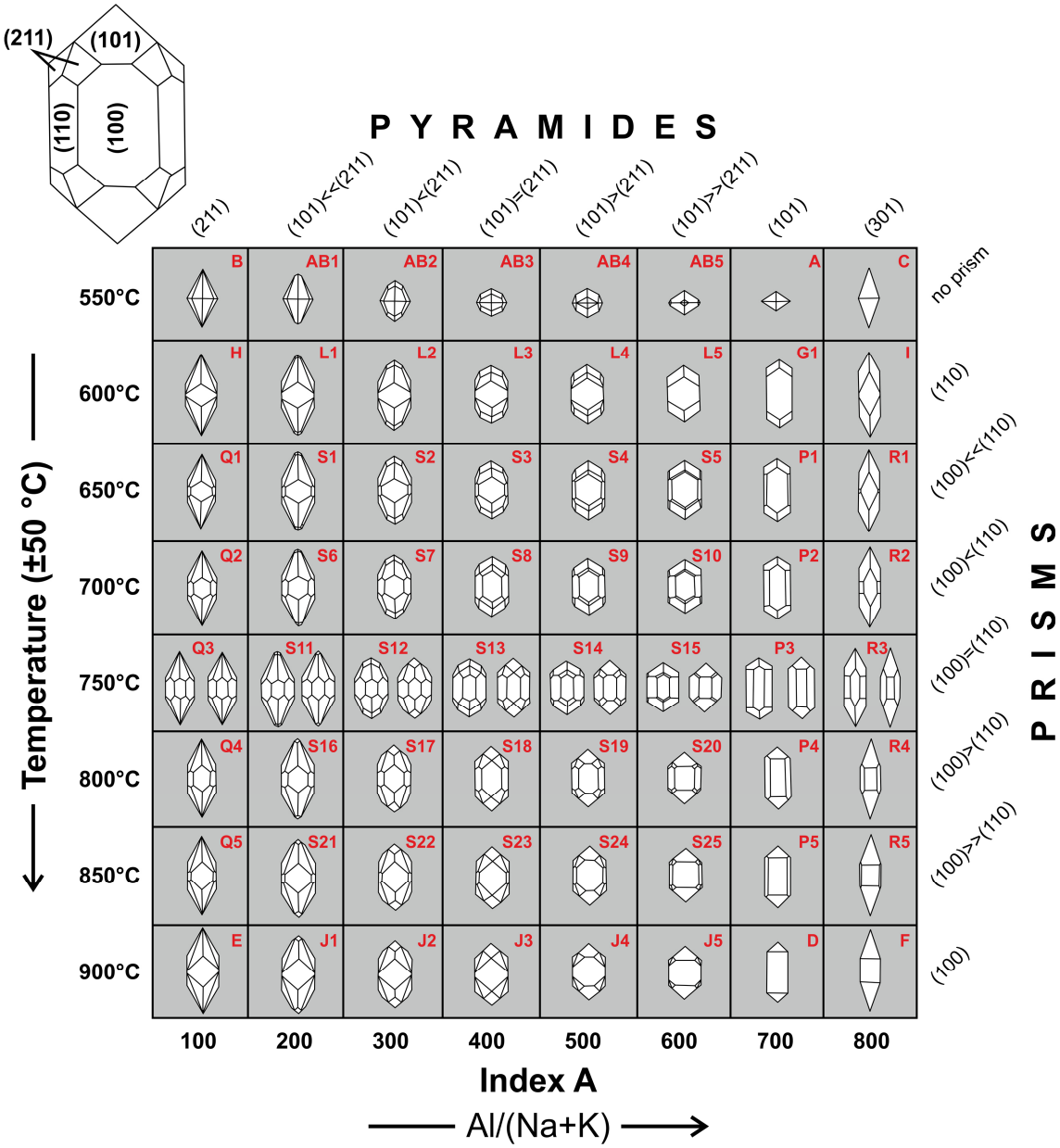

Figure 3.3 - Zircon morphology classification scheme after Pupin (1980), modified after Belousova et al. (2006). Classification is based on the proportion of zircon pyramid and prisms faces, which according to Pupin (1980) reflect the alkalinity of the host magma (i.e. Al/(Na+K)) and the crystallization temperature, respectively.

Based on empirical comparison with geochemical data of 300 samples, Pupin (1980) proposed that the distribution of zircon pyramid faces (index A) reflects the Al/(Na+K) ratio of the melt and can be used to discriminate between (1) crust-derived granites (aluminous, S-Type) having A ~ 300, (2) granites of mixed crust and mantle origin (calc-alkaline and sub-alkaline series) having A ~ 300-600 and (3) granites of mantle origin (alkaline, tholeiitic) having A ~ 500-700. The distribution of zircon prisms faces, however, was linked to the crystallization temperature, and was calibrated by Pupin (1980) using several temperature constraints: (i) the stability limits of igneous minerals (e.g. muscovite), (ii) geothermometric data (pyroxenes; vitreous melt inclusions, not specified), (iii) the temperature ranges for gneiss anatexy, (iv) the

temperature ranges for the beginning and end of magmatic crystallization in granites, diorites, gabbros and effusive equivalents, as well as on (v) formation temperatures of minerals syn-crystallized with zircon (i.e. fluorite, late-magmatic quartz). Vavra (1990) additionally proposed that the {100}/{110} ratio increases with increasing zircon-supersaturation of the melt, because growth of {100} faces becomes kinetically less favorable. Furthermore, Benisek and Finger (1993), suggested that the {100}/{110} increases with increasing contents of U, Th, REE and P in the melt (relative to Zr). Nevertheless, several studies emphasized that temperatures obtained from zircon morphology generally agree with other temperature constraints such as bulk rock zircon saturation temperatures. Thus, a careful investigation of zircon morphologies provides an overview of the physicochemical conditions during zircon formation and, in combination with respective zircon compositions (trace elements, Hf isotopes, U-Pb), is a powerful tool to constrain the magmatic evolution of igneous rocks (e.g. Corfu et al., 2003; Belousova et al., 2006; Köksal et al., 2008; Akin et al., 2019).

3.5 Melt inclusions in zircon

Melt inclusions are small droplets of melt that are trapped during crystal growth and which can preserve information about the composition of the melt and the P-T conditions during entrapment. Therefore, melt inclusions allow reconstructing the thermal and compositional evolution of a magma (Thomas et al., 2003; Audétat and Lowenstern, 2014). Studying melt inclusions is highly informative for intrusive rocks, which are coarse-grained, holocrystalline and do not contain quenched, glassy remnants of the respective parental melt as in case of some volcanic rocks. This particularly holds for layered intrusions such as the Bushveld Complex, which mostly consist of cumulate rocks having a bulk rock composition which can be highly disparate from the parental magma (Namur et al., 2015). Thus, many constraints for the processes during formation of layered intrusions derive from melt inclusion studies of cumulus and intercumulus minerals, representing different stages of the magma evolution (e.g. Spandler et al., 2005; Jakobsen et al., 2011; Fischer et al., 2016). In this context, melt inclusions in zircon (MIZ) are advantageous in that chemical information about the magma can be combined with geochronological (U-Pb) and thermometric data (e.g. Ti-in-zircon of host). However, MIZ derived from any setting are still poorly investigated, although they are common in magmatic zircon and may provide valuable insights into the generation of zircon-forming melts, which is still incompletely understood but has a high significance, nonetheless because Hadean zircons are the only preserved material of Earth’s earliest crust (Thomas et al., 2003; Trail et al., 2007; Nutman and Hiess, 2009).

Igneous minerals commonly include silicate melts, although inclusions of other melts may also occur, e.g. sulfide or salt melts or carbonatites. Melt inclusions differ from fluid inclusions, which are mostly composed of liquid and gaseous phases at room temperature. The phase relationships between fluids and silicate melts entrapped in magmatic minerals are complex, and dependent on pressure, temperature and composition, immiscible aqueous fluids and melts or a single phase may be included (Kamenetsky and Kamenetsky, 2011; Audétat and Lowenstern, 2014). The entrapment of melt inclusions occurs at the interface between melt and the crystallizing solid phase in regions of relatively slow and/or disturbed crystal growth creating a melt-filled cavity. Here, a number of mechanisms are suggested, of which the most relevant to zircon are localized slow crystal growth rates associated with defects or the presence of other phases as well as entrapment of melt pockets due to rapid skeletal or dendritic growth, which was already described for zircon of the Bushveld Complex (Zeh et al., 2015). Furthermore, streaks of small melt inclusions may also form after annealing of melt-filled fractures (Fig. 3.4), which may be secondary and not represent the actual zircon-forming melt (Roedder, 1979; Kent, 2008 and references therein).

It is key for the petrological interpretation of melt inclusion data to constrain, whether the measured composition of the melt inclusion represents that of the bulk melt or was changed during and/or after the entrapment process (Kent, 2008). During crystal growth, compatible elements are depleted from the melt near the crystal-melt interface while incompatible elements accumulate in the boundary layer surrounding the growing crystal (Thomas et al., 2003) – (Fig 3.4). Thus, if a substantial fraction of this differentiated boundary layer melt is incorporated, the melt inclusion composition may not be representative for the bulk melt. Likely, this effect becomes more severe as the melt inclusion size approaches the width of the boundary layer, which is controlled by the crystal growth rate, the rate of diffusive transport of the involved elements towards or away from the growing crystal as well as mineral-melt distribution coefficients (Thomas et al., 2003). Another process shifting the melt inclusion composition away from that of the bulk melt is diffusional re-equilibration with the host phase. For example, gains in water contents of up to 2.5 wt.% in melt inclusions due to hydrogen diffusion and equilibrated major element contents (mostly Fe, Mg) are reported for olivine (Gaetani and Watson, 2000; Portnyagin et al., 2008). To what extent boundary layer effects and re-equilibration compromise melt inclusions in zircon was discussed by Thomas et al. (2003) and is further addressed in this study (see 3.5.1 and chapter 5, respectively). After entrapment, melt inclusions may recrystallize including growth of daughter phases and sidewall crystallization, and may be affected by alteration including fracturing, replacement of the original phase assemblage by secondary phases, and leakage of elements previously stored in the inclusion (Fig 3.4).

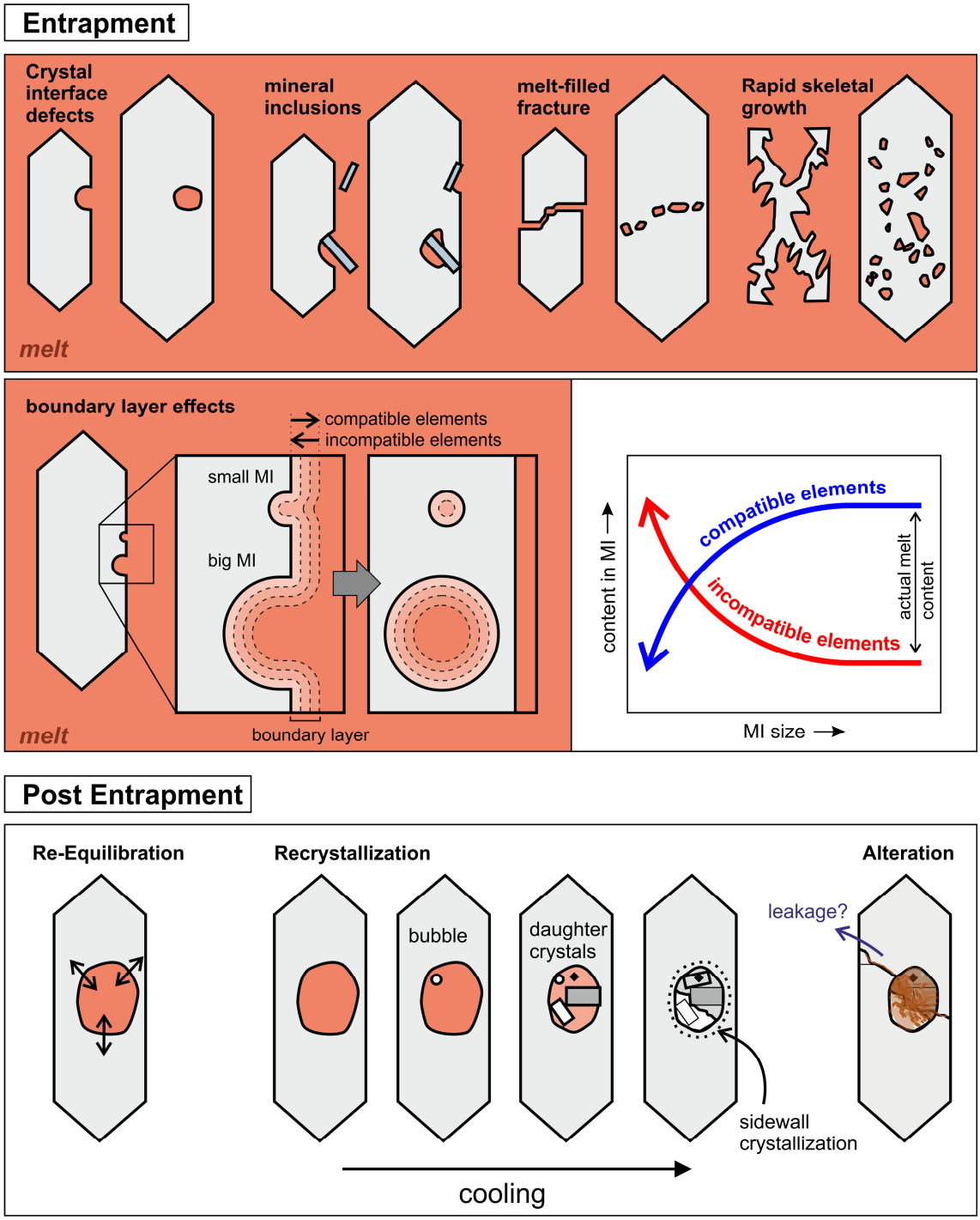

Figure 3.4 - Simple cartoon illustrating the principle mechanisms of melt inclusion (MI) entrapment relevant for zircon as well as post-entrapment processes including re-equilibration of MI with host phase, recrystallization and alteration. Modified after Roedder (1979) and Thomas et al. (2003).

3.5.1 Previous studies

Many studies have investigated melt inclusions in major, rock-forming minerals (e.g. quartz, olivine, plagioclase), while studies on melt inclusions in accessory minerals are still scarce. Melt inclusions in zircon (MIZ) were investigated for the first time by Chupin et al. (1992) for orthogneisses of the Anbar and Aldan Shields in Siberia. Subsequently, Li (1994) reported MIZ

from different igneous rocks spanning the compositional range from diorite to alkali syenite. Furthermore, Li (1994) conducted homogenization experiments at atmospheric pressure, resulting in homogenization temperatures of 950-1100 °C. However, high Zr contents (1-5 wt.%) in EPMA analyses reported by Li (1994) suggest analytical artefacts and/or significant host zircon dissolution. Chupin et al. (1998) reported small (mostly 3-7 µm), recrystallized melt inclusions in detrital zircons separated from Archean quartzitic rocks of the Witwatersrand Supergroup. After homogenization at 1200 °C at atmospheric pressure, these MIZ revealed two compositional groups having different average K_2O and Cl contents. This was interpreted to reflect the emplacement of both granitic (>2.5 wt.% K_2O) and tonalitic-trondhjemitic magmas (<2.5 wt.% K_2O) in the sediment source.

In a pioneering study, Thomas et al. (2002) presented zircon-melt partitioning coefficients ($D_{Zrc\text{-}melt}$) for the REE and other trace elements (Ba, Rb, B, Sr, Ti, Y and Nb) based on MIZ – zircon host pairs from quartz diorite of the Quottoon Igneous Complex in British Columbia. Furthermore, Thomas et al. (2002) introduced an analytical method in which MIZ were re-heated under pressure (up to 1.6 kbar), minimizing the problem of decrepitation reported in earlier studies (Li, 1994; Chupin et al., 1998). Subsequently, Thomas et al. (2003) comprehensively reviewed MIZ and presented new $D_{Zrc\text{-}melt}$ obtained from glassy MIZ separated from rhyolites of Toba volcano, which were remarkably similar to those obtained from re-homogenized MIZ of quartz diorite presented by Thomas et al. (2002). Furthermore, MIZ populations investigated by Thomas et al. (2003) revealed no decrease in the La content of MIZ (La = incompatible in zircon) with increasing MIZ size and with increasing $D_{Zrc\text{-}melt}$ for La, determined using respective MIZ – host zircon pairs. Therefore, Thomas et al. (2003) concluded that the effect of boundary layers on MIZ composition was minor. However, currently available $D_{Zrc\text{-}melt}$ determined from both MIZ studies and from experiments commonly show a range over several orders of magnitude (e.g. for the REE), the reasons for which still remain largely unconstrained. This also limits the utility of this method to calculate the parent melt composition for zircons with unknown source rock composition, e.g. detrital zircons. Thus, to better understand which processes control zircon-melt partitioning, there is a need for more experimental data as well as MIZ studies using well-characterized natural samples encompassing chemically and texturally different rock types (Hanchar and van Westrenen, 2007).

Following the work of Thomas et al. (2003), the number of MIZ studies increased. Chupin et al. (2006) presented more MIZ data for Archean gneisses from the Kola Superdeep Borehole, and reported a change in MIZ composition from core (trondhjemitic) to rim (granitic). In a subsequent study, Nutman and Hiess (2009), investigated MIZ from a 3.8 Ga tonalite of W Greenland, which are recrystallized to quartz, plagioclase, alkali feldspar, hornblende, biotite,

ilmenite and apatite. Although no re-homogenization was performed, Nutman and Hiess (2009) stated that broadly equal amounts of alkali feldspar and plagioclase in recrystallized MIZ indicate that these zircons crystallized from granitic melts at 700-800 °C (obtained by Ti-in-zircon thermometry using $aTiO_2 = 0.6$), which remained after >50% fractional crystallization of an initially hot (1000 °C) Eoarchean tonalitic magma. Nutman and Hiess (2009) further concluded that low Ti-in-zircon temperatures and granitic inclusion assemblages found in Hadean detrital zircons could be generated by a similar process, and do not necessarily indicate the presence of low temperature granitic melts (Watson and Harrison, 2005; Harrison et al., 2007; Hopkins et al., 2008).

More recently, both glassy and re-homogenized MIZ were investigated for intermediate to silicic volcanic rocks. In Watts and Mercer (2020), MIZ were employed to reconstruct the primary composition and P-T-conditions of the magma for deeply altered rhyolites of the mesoproterozoic St. Francois Mountains terrane (Missouri), which are the host rocks for the Pea Ridge iron oxide-apatite (IOA) deposit. The MIZ investigated in their study display normative quartz, albite and orthoclase contents which in the haplogranite ternary lie on cotectic curves between 0.5 and 10 kbar (average 2-3 kbar), which was interpreted to reflect entrapment mostly at 7-12 km depth. The chemical composition of MIZ revealed a trachydacitic-rhyolitic parental magma consistent with a metasomatized mantle source (e.g. back-arc or rifted segment of a volcanic arc) imparting the generated magmas with distinct geochemical features, like a high alkalinity and high Cl contents, which facilitated the transport and concentration of Fe and REE in the shallow crust (Watts and Mercer, 2020). Most recently, glassy melt inclusions were investigated from a 4,382 Ma old zircon fragment separated from a lunar meteorite (Zeng et al., 2020). These MIZ display a Si-rich, Fe-poor composition (~80–90 wt.% SiO_2; <0.5 wt.% FeO) similar to immiscible silica-rich melts reported in Apollo rocks, suggesting entrapment during an early phase of magmatism on the Moon.

In summary, MIZ combine the compelling advantages of (1) providing compositional information about some of Earth's earliest periods of magmatism, (2) linking zircon U-Pb age data with magma compositions and temperatures, and (3) revealing zircon formation conditions and parental melt compositions in cases where the host matrix is deeply altered or not present due to erosion. The wide range of geochemical and petrological applications for MIZ studies outlined above underscores their importance in deciphering complex problems ins geosciences, which will likely increase along with further progress in microanalytical methods.

4. Zircon formation in mafic and felsic rocks of the Bushveld Complex, South Africa: Constraints from composition, zoning, Th/U ratios, morphology, and modelling

Dominik Gudelius[a], Armin Zeh[a], Allan H. Wilson[b]

[a] Karlsruhe Institute for Technology, Institute for Applied Geosciences, Adenauerring 20b, 76131 Karlsruhe, Germany

[b] University of the Witwatersrand, School of Geosciences, South Africa, 2050 Johannesburg, South Africa

Chemical Geology Volume 546, pages 1-26, DOI: 10.1016/j.chemgeo.2020.119647

Abstract

Zircon is a potential petrogenetic indicator that can be used to derive physicochemical conditions during magma crystallization. In this study, such conditions are obtained from zircon of both felsic and mafic rocks of the Bushveld Complex (BC), which are characterized by a wide range in bulk-rock Zr contents (4-552 ppm). For that, information from bulk-rock compositions, petrography, zircon trace element data and morphologies are combined with results of thermodynamic modelling using the software packages rhyolite-MELTS and Perple_X. In felsic rocks (Lebowa Granite, Rashoop Granophyre), zircon is formed in rutile-free assemblages together with olivine-clinopyroxene-amphibole-biotite-ilmenite-titanite-apatite after ≥20% fractional crystallization at 761-935 °C (mean: 860 °C), based on Ti-in-zircon thermometry using $a\mathrm{TiO_2} = 0.3$, in agreement with independent geothermometers and modelling results. The resulting zircon populations show {100}- and {101}-dominated morphologies as well as high ΣREE (mean: 651 ppm) and low Ti contents (mean: 9.5 ppm), and only minor zoning in Th/U (0.3-0.8) and Nb/Ta (1.2-4.4). Identical zircon characteristics in gabbros and diorites of the Upper Zone within the Rustenburg Layered Suite (RLS) suggest admixing of felsic melts during ingression of mafic parental magmas. In contrast, zircons in mafic rocks of the lower RLS (Basal Ultramafic Sequence to lower Main Zone) show significantly lower ΣREE (mean: 324 ppm), commonly higher Ti contents (8-60 ppm), as well as large variations in Ti, U, Th contents, Th/U (0.2-24) and Nb/Ta ratios (0.15-18) as well as in zircon morphology. These zircons mostly occur in rutile-bearing intercumulus domains associated with orthopyroxene-biotite-amphibole-plagioclase-quartz-rutile and are formed at 690-962°C (mean: 835 °C; $a\mathrm{TiO_2} = 1.0$) based on Ti-in-zircon thermometry. These temperatures are in good agreement with zircon morphologies, but mostly higher than those obtained by rhyolite-MELTS modelling, suggesting zircon growth at <810 °C after >75% fractional crystallization of high Mg andesitic (B1) and tholeiitic parental magma (B2). These lower temperatures perhaps result from oversimplified modelling parameters or may reflect variable mixing of parental magma with evolved resident magma. Zircon populations in rutile-bearing mafic rocks of the lower

RLS reveal two distinct zoning trends: an early trend at high Ti (>20 ppm), characterized by increasing Th/U (0.5 to 18) at decreasing U (175 to 10 ppm) from core to rim and a reverse trend at lower Ti contents. Both trends require zircon formation in intercumulus melt pockets at high zircon/melt ratios. The high-Ti trend can be explained by Rayleigh-like fractionation due to zircon growth together with rutile, both having highly different partition coefficients for U>>Th. The low-Ti trend results from zircon growth after onset of the biotite-in reaction, causing breakdown of previously formed rutile, thereby releasing U but no Th. The absence of pronounced Th/U zoning of zircon in felsic rocks reflects zircon growth in less fractionated melts, resulting in Th-U fractionation compensated by coeval crystallization of abundant rock-forming minerals, all being highly incompatible for Th and U.

4.1 Introduction

Zircon is commonly used as a geochronometer, but also as a petrogenetic indicator to constrain physicochemical conditions during magma crystallization. In recent studies, trace element (TE) contents in zircon were used to determine zircon crystallization temperatures by Ti-in-zircon thermometry (Ferry and Watson, 2007; Fu et al., 2008), and the redox state of the host magma using Ce- and Eu-anomalies (Trail et al., 2012). Furthermore, trace elements were applied to monitor magmatic differentiation processes (Miles et al., 2013) using experimentally calibrated zircon/melt partition coefficients (Rubatto and Hermann, 2007), to assess the amount of fractional vs. equilibrium crystallization during zircon growth (Kirkland et al., 2015), and to fingerprint tectono-magmatic provenances (Belousova et al., 2002; Carley et al., 2014; Grimes et al., 2015). The results of these studies indicate that incorporation of TE into zircon is complex and controlled by several factors, comprising P-T conditions, oxygen fugacities and bulk rock compositions. These parameters in combination determine in which mineral assemblage zircon is likely to be formed, and consequently the bulk distribution coefficient during magma crystallization.

In a thermodynamic context, zircon starts crystallizing when an evolving melt becomes zircon-saturated, whereby the saturation temperature is dependent on bulk-rock composition and can be calculated by applying calibrated zircon saturation geothermometers (Watson and Harrison 1983; Boehnke et al., 2013). During subsequent magma cooling, zircon growth commonly continues within changing mineral assemblages, melt fractions, and melt compositions, resulting in zircon grains with different morphologies, compositions and zoning patterns. The successive change in mineral assemblage during magma crystallization can be traced by petrographic observations and thermodynamic modelling, such as by using the software packages rhyolite-MELTS (Gualda et al., 2012) and Perple_X (Conolly, 2009). Zircon formation temperatures can be obtained either by applying Ti-in-zircon thermometry (Ferry and

Watson, 2007; Fu et al., 2008) or by using the classification scheme of Pupin (1980), based on zircon {100}:{110} prism ratios.

However, each of the aforementioned thermometric methods has several disadvantages, which make them more or less useful in obtaining reliable zircon formation temperatures. For example, temperatures estimated by using Pupin's classification scheme are imprecise (50 °C steps) and might be biased due to enhanced and/or suppressed growth of certain crystal faces dependent on U, Th and REE contents and/or the degree of zircon supersaturation of the melt, as discussed by Benisek and Finger (1993) and Vavra (1990). Titanium-in-zircon thermometry only yields precise and accurate zircon crystallization temperatures if zircon was formed in equilibrium with quartz and rutile (indicating $a\mathrm{SiO_2} = a\mathrm{TiO_2} = 1$), a prerequisite that is rarely fulfilled for magmatic rocks (Fu et al., 2008). Most magmatic rocks commonly contain Ti-bearing phases like titanite, ilmenite, titanomagnetite and biotite, requiring the use of $a\mathrm{TiO_2}<1$ for Ti-in-zircon thermometry, which otherwise produces minimum temperatures (Ferry and Watson, 2007; Fu et al., 2008; Siégel et al., 2018; Schiller and Finger, 2019). Zircon saturation geothermometry has the advantage that it is independent on mineral assemblages. However, it only yields reliable temperatures if the measured bulk rock composition is close to the melt composition at the time of zircon growth. This is not the case for mafic cumulate rocks, where zircon crystallization occurs late during the fractionation history, if at all (Siégel et al., 2018). This illustrates that the different zircon-based thermometers cannot be used without limitation for all rock types.

In this study, the consistency between different zircon-based thermometers and their reliability will be tested by applying them to a wide range of geochemically and petrologically well-characterized rocks of the BC. This complex is an ideal testing ground as it contains zircon in a wide range of rock types comprising both mafic cumulates and felsic rocks, all being essentially coeval but having formed from different parental magmas. Furthermore, we will place new constraints on the formation or absence of spectacular zoning patterns, in particular of Th/U ratios of zircon in felsic and mafic rocks. Finally, implications of the observed zircon systematics for the BC magma chamber evolution will be discussed.

4.1.1 Geological setting

The Bushveld Complex (BC) in South Africa is the Earth's largest mafic layered intrusion and hosts the world's largest resources for platinum group elements, Cr, V and Ni (Cawthorn and Walraven, 1998; Cawthorn, 2015). It comprises three large igneous provinces which were formed successively: (1) Rooiberg Group volcanics (mostly felsic), (2) mafic cumulate rocks of the RLS, and (3) granitic rocks of the Lebowa Granite and the Rashoop Granophyre Suites (Fig. 4.1) (Molyneux, 1970; Von Gruenewaldt, 1972; Molyneux, 1974; Twist and French, 1983; Walraven, 1987; Schweitzer et al., 1997; Mathez et al., 2013; VanTongeren and Mathez, 2015).

The RLS and related granites crystallized between 1.5 and 3.0 ± 0.5 kbar (Kaneko and Miyano, 1990; Pitra and De Waal, 2001; Waters and Lovegrove, 2002), and the parental magmas of the RLS intruded at 1150-1300 °C (Cawthorn and Walraven, 1998). The felsic rocks of the Rooiberg Group and Lebowa Granite Suite had liquidus temperatures >1100 °C (Günther et al., 2018).

The Rooiberg Group consists of an up to 5 km thick pile of mostly very fine-grained to glassy lava flows (felsites) and minor pyroclastic rocks (Twist and French, 1983; Twist and Harmer 1987; Buchanan et al., 1999; Buchanan et al., 2002, 2004; Lenhardt and Eriksson, 2012). It comprises from bottom to the top the Dullstroom, Damwal, Kwaggasnek and Schrikkloof Formations.

The RLS is made up of a 7500-9000 m thick stack of mafic cumulate rocks. Based on stratigraphy, gravimetric data, and xenoliths in kimberlites, it is concluded that the RLS developed in a continuous magma chamber of at least 400 km extent in an E-W direction (Cawthorn and Walraven, 1998). Presently, it is exposed in five distinct limbs: Northern, Eastern, Southern (mostly under cover), Western and Far Western (Fig. 4.1), and subdivided from bottom to top into 6 stratigraphic units: Basal Ultramafic Sequence (BUS), Marginal Zone, Lower Zone, Critical Zone, Main Zone and Upper Zone (for details see Hall, 1932 and Wilson, 2012, 2015). The BUS represents relics of a sill complex, which developed in three distinct compartments prior to formation of a coherent magma chamber, hosting the other 5 units (Wilson, 2015). The RLS stratigraphy is further subdivided by several prominent marker horizons comprising prominent chromitite and magnetite layers, the Merensky Reef, and the Pyroxenite Marker (see Fig. 4.1; and summary in Cawthorn et al., 2005; Wilson et al., 2017).

Geochemical and petrological data suggest that the cumulate rocks of the RLS result from crystallization of different parental magmas (UM, B1, B2, B3; e.g. Barnes et al., 2010, Wilson 2012), which intruded the RLS magma chamber periodically, and led to the formation of cyclic units, which are most spectacular in the Upper Critical Zone (Eales and Costin, 2012; Latypov et al., 2017). It is suggested that UM (ultramafic) and B1 (high-Mg andesite) magmas played a major role during formation of the BUS, Marginal Zone, and Lower Zone, mixed B1 and B2 (tholeiite) magmas for the Critical and lower Main zones, and the B3 (aluminous basalt) magma for the Main Zone below the Pyroxenite Marker. For the rocks above the Pyroxenite Marker, comprising the uppermost Main Zone and Upper Zone (UUMZ), two parental magmas are suggested. The first magma is represented by the average bulk rock composition of the UUMZ rocks (Tegner et al., 2006), and the second magma by a mixture of UUMZ with a felsic component, which after unmixing led to the formation of the overlying Rashoop granophyres (VanTongeren et al., 2010). Results of high-precision U-Pb dating suggest that accretion of the RLS (from Marginal Zone to Upper Zone) and subsequent cooling below 700 °C lasted less than 1 million years, between 2055.91 ± 0.26 Ma and 2054.89 ± 0.37 Ma (Zeh et al., 2015) and

is in accord with the modelled emplacement duration of ca. 70,000 years (Cawthorn and Walraven, 1998).

The Lebowa Granite Suite is the largest exposure (ca. 65.000 km^2) of anorogenic granite on Earth with a ferroan (A-type) composition (Hill et al., 1996). It is intrusive into mafic cumulate rocks of the RLS, volcanic rocks of the Rooiberg Group, and Rashoop granophyres (Von Gruenewaldt, 1972; Walraven 1985, 1987; VanTongeren and Mathez, 2015). Its major and trace element compositions overlap with those of the Rashoop granophyres and rhyolites of the Rooiberg Group (Fig. 4.2), as noted by several authors (Twist and French, 1983; Twist and Harmer, 1987; Hatton and Schweitzer, 1995; Hill et al., 1996; Schweitzer et al., 1997; Buchanan et al., 2002, 2004; Mathez et al., 2013).

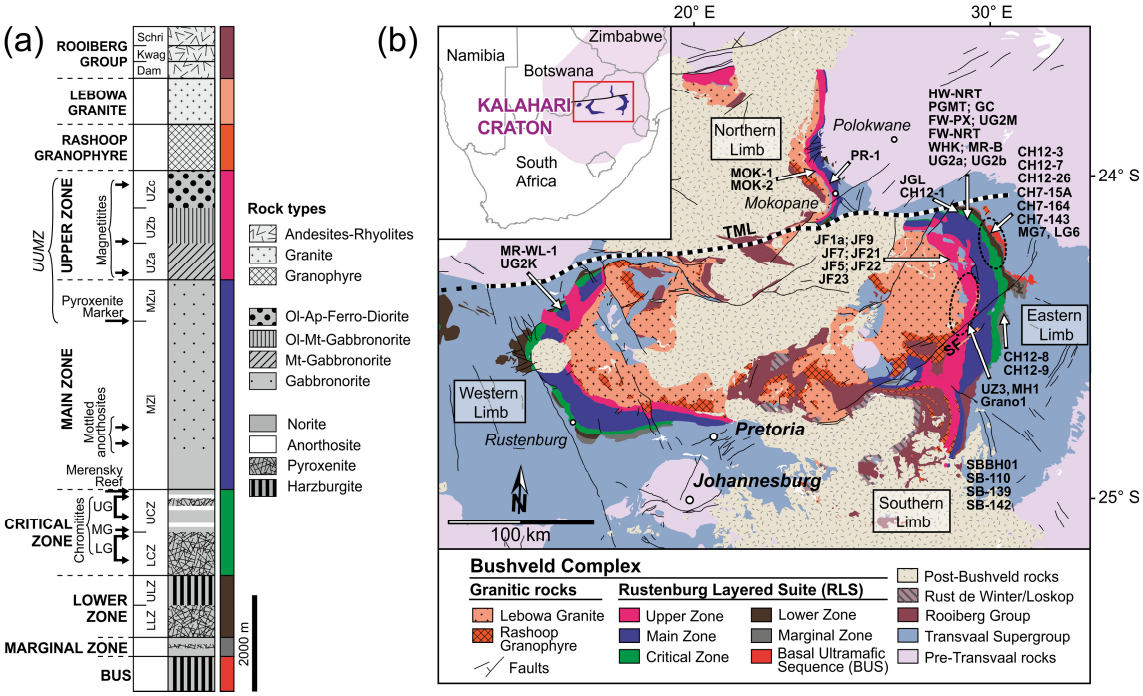

Figure 4.1 - (a) Generalized stratigraphic profile and (b) geological map of the Bushveld Complex (BC), modified after the Council of Geoscience of South Africa (Johnson and Wolmarans 2008); Wilson (2015) and Mungall et al. (2016) and references therein. Shown are the main units of the BC and surrounding rocks and sample locations. Sample coordinates and stratigraphic positions are given in Table 4.1 and Figure 4.6, respectively. UUMZ = Upper Main and Upper Zone; Chromitites: LG = Lower Group; MG = Middle Group; UG = Upper Group. Rooiberg Group formations: Schri = Schrikkloof; Kwag = Kwaggasnek; Dam = Damwal; TML = Thabazimbi-Murchison lineament; SF = Steelpoort fault.

4.1.2 Previous studies on Bushveld zircon

In previous studies, zircon of the BC was used for high-precision U-Pb dating (Scoates and Friedman, 2008; Zeh et al., 2015; Mungall et al., 2016) and Hf isotope analyses to obtain information about magma sources (Zirakparvar et al., 2014; VanTongeren et al., 2016; Zeh et al., 2020). The first systematic TE study on zircon was carried out by Yudovskaya et al., (2013) on intercumulus rocks of the Critical Zone, revealing significant variation in Ti-in-zircon temperatures (760-930 °C), and zircon trace element contents (Hf, U, REE). An observed decrease in Th/U ratio (from 4 to 0.5) and Ti content at increasing U content from core to rim

was interpreted in that study to result from zircon growth during cooling accompanied by intercumulus percolation of U-rich melts. Zeh et al. (2015) additionally reported zircon grains with increasing Th/U from core to rim, which they interpreted to result from early Rayleigh fractionation during zircon growth. Zircon populations with even more extreme variations in Th/U (from 0.5 to 77) in Critical Zone rocks were recently reported by Ver Hoeve et al. (2018) but detailed core-rim systematics of the investigated zircons was not provided. These authors speculate that high Th/U ratios result from the selective loss of U from the intercumulus melt, caused by the migration of oxidized, chlorine-rich fluids. Ver Hoeve et al. (2018) presented the first TE systematics of zircon in both mafic and felsic rocks of the BC. Furthermore, based on Ti-in-zircon geothermometry they suggested that zircon in Rt-bearing mafic rocks of the Lower and Critical Zone of the RLS were formed on average at 60 °C higher temperatures than in Rt-free mafic rocks of the Upper Zone and overlying granites thereby having important petrogenetic implications for the emplacement of the BC and associated rock units.

4.2 Samples and analytical methods

In this study, zircon populations were investigated from 41 samples with different bulk rock compositions. Most samples were taken from the Eastern Limb of the BC, and a few from the Northern, Western and Southern limbs (for sample locations and coordinates see Fig. 4.1 and Table 4.1). The samples comprise cumulate rocks from all stratigraphic units of the RLS (except for the Lower Zone), as well as from the overlying Lebowa Granite Suite, Rashoop Granophyre Suite, and Rooiberg Group. Furthermore, three samples were taken from drillcore CH7 covering the Basal Ultramafic Sequence (for details see Wilson, 2015) as well as four samples from a drillcore through the Main Zone of the Southern Limb.

Table 4.1 Sample list and coordinates

sample	rock type	limb	latitude (S)	longitude (E)	location
Lebowa Granite					
JF9	granite	E	24°34'22.9"	29°52'41.3"	N Jane Furse
MOK-1	granite	N	24°03'44.7"	28°48'40.7"	25 km NW Mokopane (village Ga-Pila)
MOK-2	granite	N	24°02'59.0"	28°46'24.3"	27 km NW Mokopane (rd. to Sterkrivier)
Rashoop Granophyre & Rooiberg felsite					
JF7	contact granophyre	E	24°37'62.3''	29°55'80.7''	10 km NE Jane Furse (rd. to Chuniespoort)
Grano1	granophyre	E	24°56'33.3''	29°54'11.0''	20 km S Jane Furse (near Lehlakong)
JF22	microgranite	E	24°15'58.2''	29°08'56.9''	17 km N Jane Furse (village Mphanama)
JF21	felsite	E	24°15'58.2''	29°08'56.9''	17 km N Jane Furse (village Mphanama)
Contact quartzite					
JF1a	quartzite wall rock	E	24°37'62.3"	29°55'80.7"	10 km NE Jane Furse (rd. to Chuniespoort)
RLS - Upper Zone					
JF5	ferrodiorite	E	24°37'62.3''	29°55'80.7''	10 km NE Jane Furse (rd. to Chuniespoort)
JF23	ferrodiorite	E	24°37'62.3''	29°55'80.7''	10 km NE Jane Furse (rd. to Chuniespoort)
UZ3	pegmatoidal diorite	E	24°49'60.8"	29°58'18.9"	3 km S Magnet Heights
MH1	Mt-rich gabbro	E	24°49'60.8''	29.58'18.9''	3 km S Magnet Heights
RLS - Main Zone					
SB-139	gabbronorite	S	na	na	drillcore (Bethal)
SB-110	gabbronorite	S	na	na	drillcore (Bethal)
SB-142	gabbronorite	S	na	na	drillcore (Bethal)
SBBH01	gabbronorite	S	na	na	drillcore (Bethal)
GC	mottled anorthosite	E	24°17'55.0"	29°52'10.0"	Bokoni Mine
PR-1	pyroxenite (Platreef)	N	24°00'39.0"	28°54'44.0"	N Mokopane (Platreef Mine)
RLS - Critical Zone					
HW-NRT	hanging wall norite (MR)	E	24°17'55.0"	29°52'10.0"	Bokoni Mine
MR-B	pgmt. pyroxenite (MR)	E	24°17'55.0"	29°52'10.0"	Bokoni Mine
MR-WL-1	pgmt. pyroxenite (MR)	W	24°27'00.0"	27°09'20.0"	Union Mine
PGMT	pgmt. pyroxenite (MR)	E	24°17'55.0"	29°52'10.0"	Bokoni Mine
FW-PX	footwall pyroxenite (MR)	E	24°17'55.0"	29°52'10.0"	Bokoni Mine
FW-NRT	footwall norite (MR)	E	24°17'55.0"	29°52'10.0"	Bokoni Mine
WHK	pyroxenite	E	24°17'55.0"	29°52'10.0"	Bokoni Mine
UG2K	pgmt. pyroxenite (MR)	W	24°27'00.0"	27°09'20.0"	Union Mine
UG2a	chromitite (UG2)	E	24°17'55.0"	29°52'10.0"	Bokoni Mine
UG2b	chromitite (UG2)	E	24°17'55.0"	29°52'10.0"	Bokoni Mine
UG2M	pgmt. pyroxenite (MR)	E	24°17'55.0"	29°52'10.0"	Bokoni Mine
MG7	chromitite (MG)	E	24°52'46.8"	30°07'25.6"	Tweefontein Mine
LG6	chromitite (LG)	E	24°39'34.0"	30°10'03.0"	Doornbosch Mine
JGL	pyroxenite (LG)	E	24°16'08.0"	29°53'17.0"	Jagdlust farm
CH-12-1	pyroxenite (LG)	E	24°39'34.0"	30°10'03.0"	Doornbosch Mine
RLS - Marginal Zone					
CH12-3	norite (chilled)	E	24°18'15.1''	30°00'05.6''	Schwerin fold
CH12-7	norite (chilled)	E	24°18'15.1''	30°00'05.6''	Schwerin fold
CH12-26	norite (chilled)	E	24°18'15.1''	30°00'05.6''	Schwerin fold
CH12-8	norite (chilled)	E	24°56'58.9''	30°10'39.3''	Schwerin fold
CH12-9	pyroxenite	E	24°56'58.9''	30°10'39.3''	Steelport-Lydenburg (rd.-cut)
RLS - Basal Ultramafic Sequence (BUS)					
CH7-15A	norite; drill core	E	24°26'44.0''	30°07.47.0''	drillcore CH7 (Wilson 2015)
CH7-143A	pyroxenite; drill core	E	24°26'44.0''	30°07.47.0''	drillcore CH7 (Wilson 2015)
CH7-164	pyroxenite; drill core	E	24°26'44.0''	30°07.47.0''	drillcore CH7 (Wilson 2015)

RLS=Rustenburg Layered Suite; MR=Merensky Reef cyclic unit, UG-2=upper group chromitite unit (UG-2), MG=middle group chromitite unit, LG=lower group chromitite unit, pgmt.=pegmatoidal, rd.=road

4.2.1 Bulk rock major and trace element analysis

Major and trace element compositions of selected samples were obtained at the Earth Lab of the University of the Witwatersrand in Johannesburg (South Africa). The analytical method of trace element analysis by solution-ICP-MS (inductively coupled plasma mass spectrometry) and bulk rock major element analysis by WD-XRF (wavelength dispersive X-ray fluorescence analysis) is described in Wilson et al. (2017) and Wilson (2015), respectively. Additionally, trace element contents of samples MG7 and JGL were obtained by laser ablation ICP-MS of fused disks at Erlangen University (Germany) using the method of Brätz and Klemd (2002). Fused disks were prepared using *X-Ray Flux* of *XRF-Scientific* (66:34 ratio of lithium tetraborate to lithium metaborate) having blank concentrations of 4-96 ppm for Ba, Mn, Cr, P; 0.35-4 ppm for Ni, Co, Sc, Ti, V, Rb, Sr, Zr; 0.1-0.35 ppm for La-Nd, Y, Hf, Ta, Th and <0.1 ppm for Sm-Lu, Nb, U.

4.2.2 Zircon imaging

Zircon grains were separated from heavy mineral concentrates. For morphology studies, a large number of euhedral zircon grains was selected and mounted on conductive adhesive pads, coated with Pt, and investigated with *JEOL JSM 6490* and *TESCAN VEGA*2 scanning electron microscopes, at Goethe University Frankfurt (Germany) and KIT Karlsruhe (Germany), respectively. Imaging of internal structures and trace element analysis were carried out on zircon grains embedded in epoxy resin mounts and ground to expose crystal cores. Internal zonation was identified by back scattered electron (BSE) and cathodoluminescence (CL) imaging using a *Gatan miniCL* detector.

4.2.3 In-situ trace element analyses of zircon

Trace element compositions of zircon were obtained by laser ablation inductively coupled plasma mass spectrometry (LA-ICP-MS) using a *RESOlution M-50* ArF Excimer laser ablation system coupled to a *Thermo-Finnigan Element2* sector field mass spectrometer, at Goethe University Frankfurt (Germany). For zircon analysis, a laser spot size of 43 µm (small grains: 33 µm), a laser pulse rate of 7 Hz and an energy density of 5.6 J/cm^2 was used. Following blocks of 50-100 analyses, NIST612 glass standard as well as GJ1 and 91500 zircon reference materials were analyzed. All data were processed using the GLITTER data reduction software. NIST612 standard was used for external sensitivity calibration using the stoichiometric Si content of zircon (32.7 wt.% SiO_2) as an internal standard. The zircon standards GJ1 and 91500 yielded Ti concentrations of 3.63 ± 0.33 ppm (2σ, n = 24) and 4.91 ± 0.44 ppm (2σ, n = 20), respectively, which are in agreement with published values (Szymanowski et al., (2018): GJ1: 3.55 ± 0.06 ppm, 91-500: 4.73 ± 0.15 ppm; average values of data provided in Liu et al. (2010): GJ1: 3.75 ppm, 91-500: 4.71 ppm). Contents of other trace elements determined for GJ1 and

91500 were generally in accordance with published values within analytical errors (Wiedenbeck et al., 2004; Liu et al., 2010).

BSE and CL images were used to avoid LA-ICP-MS analysis of altered zircon domains. Nevertheless, some analyses of visually unaltered domains yield elevated contents of Sr, Ca and light rare earth elements (LREE). As these elements do not fit in the zircon lattice (Hoskin and Schaltegger, 2003; Geisler et al., 2007), these analyses were considered as derived from altered material and discarded. In this study, the following criteria were used to distinguish pristine from altered zircon domains: Sr >5 ppm, Ca >500 ppm, positive Eu anomaly and La_N/Sm_N >1.

4.2.4 Thermodynamic modelling

Thermodynamic modelling was carried out with the software packages rhyolite-MELTS v.1.02 (Gualda et al., 2012; Ghiorso and Gualda, 2015) and Perple_X (Connolly, 2009). Rhyolite-MELTS modelling was performed to calculate fractional crystallization ("fractionate solids" mode with 1 °C intervals) for different BC parental magmas B1, B2, and B3 and mixtures of them (B1 + B2 = 60 : 40), using data of Barnes et al. (2010). For calculation of magmatic processes in the Upper and Upper Main Zone (UUMZ) we used the parental magma composition suggested by VanTongeren et al. (2010), and for all felsic rocks the composition of Rooiberg Group felsite sample JF21, with an initial H_2O content of 2.2 wt.%, in agreement with the data set of Kleemann and Twist (1989). For all mafic parental magmas an initial H_2O content of 1 wt.% and the fractional crystallization mode was used, but the effect of different initial H_2O contents (0.2, 1.0, and 2.0 wt.%) and of equilibrium crystallization on modelling results was tested (see section 4.3.7. 'Results of thermodynamic modelling'). All calculations were done at 2 kbar in accordance with pressure estimates of BC crystallization (Kaneko and Miyano, 1990; Pitra and De Waal, 2001; Waters and Lovegrove, 2002). In contrast to previous modelling carried out by Ver Hoeve et al. (2018), no suppression of any solid phase was applied, except for whitlockite and leucite, minor amounts of which were occasionally predicted by the model but were never observed in our samples. Most calculations were performed using fO_2 = FMQ, in agreement with the results summarized in Naldrett et al. (2012), but the effects of higher and lower fO_2 (FMQ ± 2) on phase compositions and amounts were tested (Fig. 1 in S5). For modelling of zircon saturation and zircon zoning, concentrations of Zr, U, Th, Nb and Ta of the evolving melt were calculated using melt and mineral modal fractions computed by rhyolite-MELTS along with mineral/melt partition coefficients (Kd) from the literature (for values used see Table S4, supplementary materials). For rutile-free rocks (granites, UUMZ), the temperature-dependent evolution of $aTiO_2$ was also calculated by rhyolite-MELTS between 700 and 1100 °C. For Ti-in-zircon thermometry we used $aTiO_2$ at the temperature of 50 % zircon crystallization derived from an ideal zircon crystallization temperature distribution curve

(ZCTD) based on the zircon saturation model of Watson and Harrison (1983) using the method of Schiller and Finger (2019).

The software package Perple_X was used to calculate P-T pseudosections, with the aim to constrain the crystallization processes that occurred in the late-magmatic stage in closed intercumulus melt pockets. Modelling was carried out with the internally consistent thermodynamic dataset HP98 (Holland and Powell 1998), using the following activity models for solid-solutions: Biotite [Bio(TCC)]: Tajčmanová et al. (2009); olivine [O(HP)]: Holland and Powell (1998); melt [melt(HP)]: Holland and Powell (2001); alkali feldspar [OrFsp(C1)]: Holland and Powell (2003); plagioclase [Pl(h)]: Fuhrman and Lindsley (1988); clinopyroxene [Cpx(HP)] and orthopyroxene [Opx(HP)]: Holland and Powell (1996); spinel [Sp(WPC)]: White et al. (2002); amphibole [cAmph(DP)]: Diener et al. (2007). Bulk rock compositions used for modelling were calculated from mineral modes and compositions, estimated by point counting and EDX analyses of minerals in restricted zircon-bearing intercumulus domains, observed in cumulate rocks of the Critical Zone (sample PGMT) and Marginal Zone (CH12-3) – (for examples see Fig. 4.3). The H_2O contents used range between 1.25 and 4.0 wt.%. The lower limit for H_2O content was obtained from mineral modes and compositions of biotite and amphibole in intercumulus domains. The upper limit results from rhyolite-MELTS modelling after ~75 % fractional crystallization of B1 and B2 parental magmas.

4.3 Results

4.3.1 Bulk rock composition

The investigated samples comprise magmatic rocks of very different composition, as is reflected by highly variable bulk-rock SiO_2 and Zr contents ranging from 51 to 76 wt.%, and from 4 to 552 ppm, respectively (Table 4.2, Fig. 4.2a). The compositions of the investigated magmatic rocks overlap with those analyzed in previous studies of the RLS, Rooiberg Group, Lebowa Granite and Rashoop Granophyres (Fig. 4.2a-d). We note that mafic rocks of the RLS commonly show much lower Zr contents (4-204 ppm; average: 34 ppm, n = 502) than felsic rocks of the Rashoop Granophyre Suite (Zr = 24-628 ppm; average: 367 ppm, n = 20), Lebowa Granite Suite (Zr = 169-607 ppm; average: 327 ppm, n = 30) and Rooiberg Group (Zr = 75-714 ppm; average: 298 ppm, n = 290). Within the RLS, the highest Zr contents were observed in Fe-rich diorites and gabbros of the Upper Zone, where they systematically increase from 20 up to 200 ppm from the floor toward the top contact (see compilation in VanTongeren et al. (2010)), and also in the BUS, where they decrease from about 73 ppm (chilled rocks) to 5 ppm (cumulate rocks) from the floor contact towards the Marginal Zone (Wilson et al., 2017). Volcanic rocks of the Rooiberg Group reveal a correlated increase of Zr and SiO_2 contents from the oldest (Dullstroom lavas) towards the youngest rocks (Schrikkloof rhyolites), interpreted to result from fractional crystallization (without zircon removal) in an evolving magma chamber

(Buchanan et al., 2002; Günther et al., 2018), whereas samples from the Lebowa Granite and Rashoop Granophyre Suites show a negative correlation, likely pointing to successive zircon fractionation (Fig. 4.2a).

The Zr contents are positively correlated with the total rare earth element contents (ΣREE) - (Fig. 4.2b). Felsic rocks of the BC mostly display much higher ΣREE (70-648 ppm; average: 358 ppm, n = 41) than mafic rocks of the RLS (ΣREE = 1.3-159 ppm; average: 18 ppm, n = 202). Furthermore, they show higher average Th/U of 4.1, compared to the RLS rocks (average: 2.9) - (Fig. 4.2d). The TiO_2 contents are also highly variable (0.03- 4.5 wt.%) and are highest in mafic rocks of the Upper Zone (0.8-4.5 wt.%), and much lower in all mafic rocks beneath the Pyroxenite Marker (0.03-0.80 wt.%), and in all felsic rocks (0.05-1. 0 wt.%) - (Fig. 4.2c). Mafic rocks beneath the Pyroxenite Marker reveal a positive correlation between TiO_2 and Zr contents (Fig. 4.2c).

Chondrite-normalized REE patterns of felsic rocks (Fig. 4.2e) point to different degrees of fractionation, which increase from sample JF9 (La_N/Lu_N = 3.2, Eu/Eu^*_N = 2.2) to MOK1 (La_N/Lu_N = 6.4, Eu/Eu^*_N = 1.2) and MOK2 (La_N/Lu_N = 6.5, Eu/Eu^*_N = 0.2) - (subscript N denotes normalization to chondrite). Similar fractionation trends are also indicated by the data set of Hill et al. (1996). Some Lebowa Granite samples show pronounced positive Eu-anomalies (JF9 and MOK1), pointing to feldspar accumulation, whereas most others reveal negative Eu anomalies, suggesting feldspar fractionation (MOK2). All Rooiberg Group felsites as well as a few granophyres and granites only show weak Eu-anomalies. The REE contents and patterns of the investigated ferrodiorites of the Upper Zone (JF5, JF23) overlap with those of the felsic rocks (Fig. 4.2e), whereas REE contents in mafic rocks of the Critical Zone are much lower. Their REE patterns reveal variable LREE enrichment and variable Eu anomalies (La_N/Lu_N = 0.8-5.2, Eu/Eu^*_N = 0.5-1.3). Rocks from the Marginal Zone and BUS show highly variable REE patterns, ranging from unfractionated, B1-like patterns (CH12-3) to samples with low REE contents and positive Eu anomalies (e.g. CH12-8).

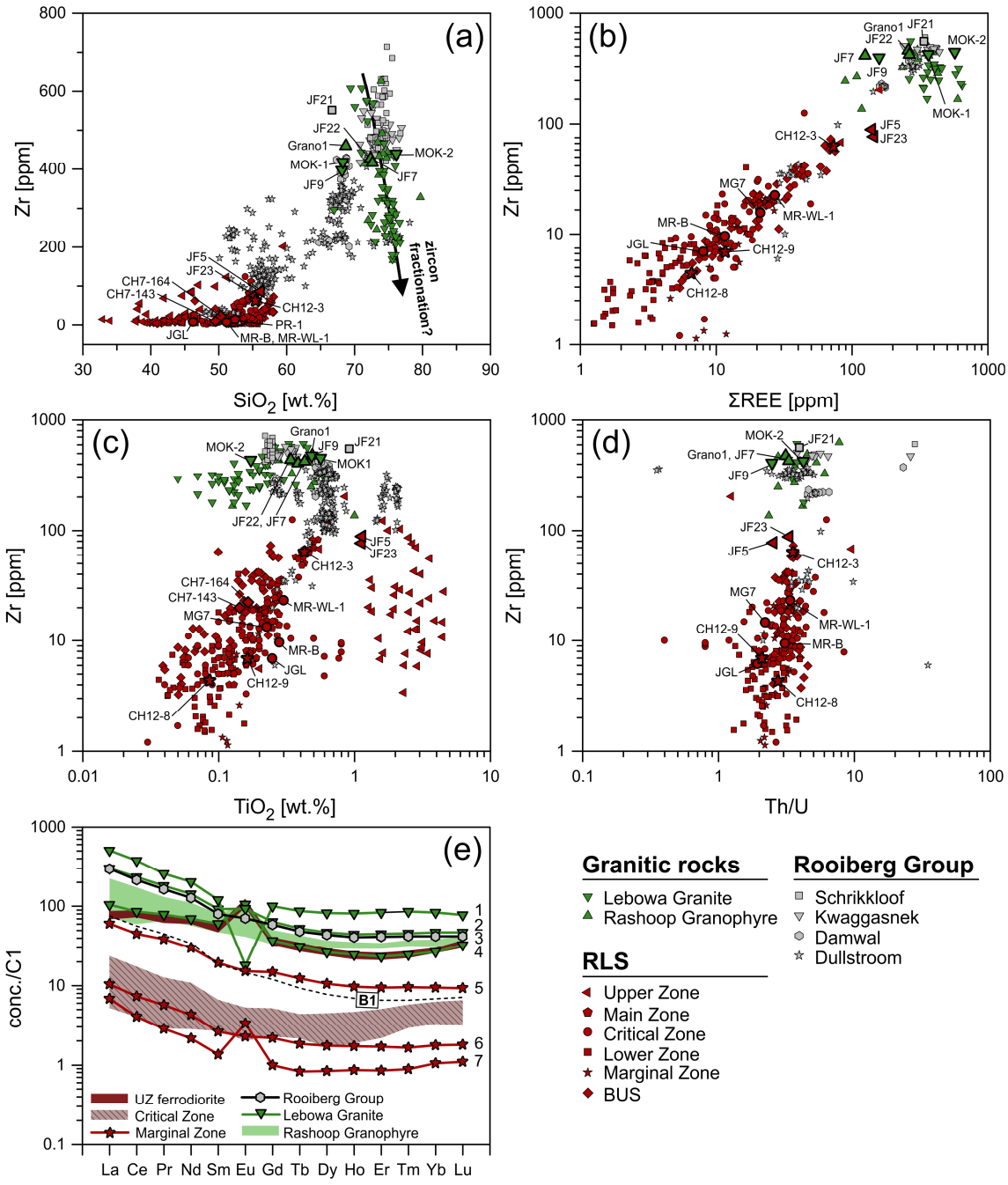

Figure 4.2 - Bulk rock composition of felsic and mafic rocks of the BC - compiled (small symbols) and new data (large symbols). Covariation diagrams (a) Zr vs. SiO_2, (b) Zr vs. ΣREE, (c) Zr vs. TiO_2, and (d) Zr vs. Th/U comprising mafic cumulate rocks of different units of the Rustenburg Layered Suite (RLS), granitic rocks (Lebowa Granite and Rashoop Granophyre) and volcanic rocks of the Rooiberg Group. Complete database and reference list for compiled data are given in supplementary materials S2. (e) Rare earth element (REE) patterns of samples investigated in this study, normalized to chondrite after McDonough and Sun (1995). Samples: (1) MOK-2, (2) MOK-1, (3) JF21, (4) JF9, (5) CH12-3, (6) CH12-9, (7) CH12-8. Other samples are summarized as compositional fields: green field - Rashoop Granophyre (JF7, JF22, Grano1); brown field - Upper Zone (UZ) ferrodiorite (JF5, JF23); red, hatched field - Critical Zone (MR-B, MR-WL-1, MG7, JGL, PR-1). B1 parental magma composition (Barnes et al. 2010) is shown for comparison. Note similarity with sample CH12-3.

Table 4.2 Whole rock major and trace element compositions

	Felsic Rocks							Rustenburg Layered Suite (RLS)											
	Lebowa Granite			Rashoop Grp & Rooiberg				Upper Zone		Critical Zone & Platreef					Marginal Zone			BUS**	
sample	JF9	MOK1	MOK2	Grano1	JF7	JF22	JF21	JF23	JF5	PR-1	MR-WL-1	MR-B	MG7	JGL	CH12/3	CH12/8	CH12/9	CH7-143A	CH7-164
SiO_2	67.66	67.83	75.89	68.32	72.10	72.22	66.21	55.30	54.46	52.26	51.48	51.14	52.44	45.95	55.45	52.09	54.70	55.36	55.42
Al_2O_3	13.50	12.87	11.55	13.43	13.66	11.56	13.46	14.78	14.86	6.78	5.79	3.49	4.31	4.74	11.21	14.53	3.85	4.39	5.29
Fe_2O_3 (t)	6.70	6.88	3.05	6.19	4.31	6.23	8.15	15.89	16.59	12.73	12.01	17.51	13.66	14.23	10.5	7.61	11.25	9.62	9.10
MnO	0.13	0.12	0.05	0.10	0.07	0.10	0.13	0.31	0.33	0.21	0.19	0.27	0.32	1.06	0.16	0.14	0.22	0.19	0.17
MgO	0.06	0.08	0.1	0.08	0.26	0.09	0.10	0.10	0.11	21.64	24.39	21.88	23.38	23.33	13.5	16.99	26.26	26.05	25.37
CaO	2.02	1.99	0.54	1.83	2.83	1.83	2.82	7.07	7.16	4.33	3.61	4.53	3.72	2.45	6.55	7.84	2.97	3.17	3.05
Na_2O	3.62	3.61	3.15	3.71	4.25	3.33	4.25	4.63	4.57	0.77	0.52	0.24	0.81	0.45	1.92	0.89	0.35	0.46	0.76
K_2O	5.47	4.90	4.99	5.26	2.75	4.21	3.73	0.98	0.90	0.24	0.30	0.07	0.14	0.07	0.78	0.09	0.11	0.26	0.39
TiO_2	0.57	0.49	0.17	0.48	0.42	0.39	0.91	1.11	1.12	0.17	0.30	0.28	0.26	0.25	0.423	0.09	0.16	0.14	0.16
P_2O_5	0.05	0.05	0.02	0.04	0.07	0.06	0.07	0.16	0.17	0.02	0.05	0.02	0.01	0.01	0.09	0.01	0.02	0.02	0.04
LOI	0.10	0.82	0.86	0.31	0.39	0.01	0.11	0.05	0.09	1.22	2.2	0.55	na	na	0.19	0.20	0.25		
Total	99.88	99.64	100.37	99.75	101.12	100.02	99.93	100.37	100.35	100.37	100.84	99.99	99.04	99.95	99.91	100.48	100.13	99.66	99.76
Li	8.3	19	14	14	19	5.7	16	6.2	6.3	11.1	3.2	4.4	na	na	10	0.69	0.33		
P	175	158	28	146	221	182	224	566	597	50	148	35	65	52	359	34	56		
Sc	4.2	3.3	0.86	4.0	6.3	5.7	4.2	12	16	19	15	32	32	32	31	15	19		
Ti	3386	2937	1019	2841	2812	2329	5498	6780	7468	1019	1798	1679	1861	2014	2360	581	865		
V	1.6	0.80	0.45	1.4	8.8	0.51	2.7	0.72	3.6	111	100	227	192	503	152	62	80		
Cr	2.1	1.6	2.2	2.3	24	1.5	2.3	2.1	3.7	1631	3134	4346	5180	53394	1088	681	1620		
Co	0.86	0.77	0.53	1.5	2.5	1.9	1.7	2.3	2.9	126	91	152	118	152	59	29	90		
Ni	2.2	1.8	2.0	4.5	10	3.3	2.4	2.6	5.3	3703	1113	3534	521	590	239	196	557		
Cu	7.4	5.6	10	12	24	2.7	34	15	34	2196	208	2232	na	na	26	11	6.6		
Zn	113	235	89	105	63	90	140	165	189	70	61	96	na	na	81	51	81		
Ga	22	22	23	22	19	17	21	20	24	5.4	5.8	4.8	na	na	11	4.8	2.8		
As	na	0.54	2.1	na	0.63	0.19	0.51	0.38	0.65	0.29	0.20	0.15	na	na	0.47	0.18	0.20		
Rb	124	195	345	197	60	114	143	14	10	12	14	2.5	2.8	0.40	26	1.1	3.2	9.1	12
Sr	186	126	12	171	317	110	184	438	503	98	86	28	68	47	168	152	44	47	91
Y	36	72	142	56	49	48	54	33	32	4.4	6.5	7.2	4.9	2.7	16	1.3	2.6		
Zr	397	418	439	461	429	418	552	87	77	15	23	9.6	15	6.8	63	4.4	6.9	20	23
Nb	32	28	39	30	22	13	38	22	23	0.50	2.3	0.4	0.91	0.24	4.5	0.60	0.82		

(continued on next page)

Table 4.2 (continued)

	Felsic Rocks							Rustenburg Layered Suite (RLS)											
	Lebowa Granite			Rashoop Grp & Rooiberg				Upper Zone		Critical Zone & Platreef					Marginal Zone			BUS**	
sample	**JF9**	**MOK1**	**MOK2**	**Grano1**	**JF7**	**JF22**	**JF21**	**JF23**	**JF5**	**PR-1**	**MR-WL-1**	**MR-B**	**MG7**	**JGL**	**CH12/3**	**CH12/8**	**CH12/9**	**CH7-143A**	**CH7-164**
Ba	2872	2455	296	2837	1600	1066	1685	995	1113	63	87	18	48	41	255	28	22	0.78	1.6
Sn	0.92	14	13	3.6	2.2	0.91	8.4	0.37	0.52	0.70	0.70	0.60	na	na	0.77	0.28	0.24		
Cs	1.6	3.2	2.0	5.8	0.48	1.4	8.7	0.48	0.32	1.28	0.47	0.13	0.31	0.06	1.00	0.064	0.28		
La	25	72	121	48	17	53	71	20	17	2.8	5.6	1.2	3.5	1.4	14.4	1.6	2.5	3.8	5.4
Ce	53	143	231	98	37	105	132	48	50	5.4	11	3.0	9.1	2.4	28	2.5	4.5	8.4	12
Pr	7.4	17	24	12	6.1	12	15	6.1	6.8	0.60	1.2	0.43	1.04	0.26	3.6	0.27	0.53	0.99	1.4
Nd	32	66	93	47	26	51	58	29	31	2.4	5.0	2.0	3.7	1.3	14	0.98	2.0	3.7	5.0
Sm	9.0	14	18	11	7.0	10	12	7.3	8.0	0.53	0.98	0.58	0.85	0.57	2.9	0.20	0.39	0.68	0.89
Eu	6.0	5.3	1.02	6.0	3.8	2.3	4.0	5.7	6.5	0.21	0.23	0.11	0.30	0.23	0.85	0.19	0.13	0.17	0.25
Gd	7.4	13	20	10	6.6	10	12	6.9	7.4	0.57	1.03	0.74	0.85	0.46	2.9	0.20	0.44	0.63	0.85
Tb	1.1	1.9	3.1	1.6	1.1	1.4	1.8	1.05	1.2	0.094	0.15	0.14	0.14	0.078	0.45	0.030	0.067	0.080	0.11
Dy	6.5	12	20	9.1	7.3	8.6	11	6.2	6.8	0.62	0.99	1.1	0.84	0.41	2.6	0.21	0.43	0.40	0.54
Ho	1.3	2.4	4.5	1.9	1.6	1.7	2.2	1.2	1.4	0.14	0.21	0.25	0.21	0.102	0.53	0.047	0.094	0.076	0.10
Er	3.7	7.2	14	5.5	4.7	5.0	6.6	3.7	3.8	0.42	0.66	0.78	0.58	0.34	1.52	0.14	0.27	0.22	0.28
Tm	0.61	1.1	2.1	0.91	0.80	0.76	1.03	0.59	0.62	0.073	0.105	0.14	0.11	0.09	0.24	0.022	0.041	0.032	0.039
Yb	4.3	7.5	14	6.1	5.2	4.8	6.8	4.5	4.6	0.51	0.74	1.01	0.68	0.5	1.5	0.17	0.28	0.21	0.25
Lu	0.80	1.2	1.9	1.02	0.83	0.73	1.03	0.80	0.87	0.078	0.11	0.16	0.095	0.092	0.23	0.027	0.044	0.033	0.041
Hf	7.9	9.2	15	9.9	11.2	9.9	14	2.5	2.0	0.37	0.74	0.32	0.38	0.31	1.6	0.13	0.22	0.77	1.02
Ta	1.4	1.4	2.4	1.9	1.2	0.58	2.3	1.01	0.74	0.048	0.16	0.02	0.26	0.30	0.29	0.038	0.056	0.26	0.36
W	0.47	0.90	3.1	0.92	0.39	0.15	2.0	0.21	0.28	0.26	0.18	0.048	na	na	0.52	0.052	0.075		
Pb	18	27	27	29	12	19	34	5.0	6.7	3.7	4.3	4.5	na	na	4.2	3.3	1.7		
Th	2.5	16	41	17	8.0	8.5	33	2.1	0.72	0.63	1.35	0.30	0.30	0.14	2.2	0.055	0.29	0.77	1.02
U	1.0	4.2	12	5.2	2.0	2.0	8.4	0.63	0.29	0.23	0.40	0.096	0.15	0.070	0.64	0.020	0.14	0.26	0.36
ΣREE	158	362	566	259	125	266	335	141	146	14	28	12	22	8.2	73	6.6	12	19	27
Eu/Eu*N	2.2	1.2	0.2	1.7	1.7	0.7	1.0	2.4	2.5	1.2	0.68	0.53	1.06	1.3	0.89	2.9	0.95	0.79	0.85
Zrc-Sat (°C)*	838	845	882	858	858	853	861	653	644	542	568	434	497	521	629	506	491	548	571

Major elements given in wt.%, trace elements given in ppm. na=not available; Grp=Granophyre; BUS=Basal Ultramafic Sequence

* Zircon saturation temperature after Watson and Harrison (1983)

** data of Wilson et al. (2017)

4.3.2 Petrography

The different bulk-rock compositions of the investigated samples are reflected by distinct mineral assemblages, as illustrated in Figure 4.3 and summarized in Table 4.3. The felsic rocks (Lebowa Granite, Rashoop Granophyre and Rooiberg Group) are dominated by quartz (Qz), perthitic alkali feldspar (Kfs) and plagioclase (Pl), with Kfs > Pl, closely intergrown with clinopyroxene (Cpx), fayalitic olivine (Ol), amphibole (Amp), and biotite (Bt). Furthermore, they contain substantial amounts of apatite (Ap), magnetite (Mt), ilmenite (Ilm) and titanite (Tit), and accessory zircon (Zrc), sulfides (mostly pyrrhotite and sphalerite) and occasionally thorite (Thr). Zircon grains of euhedral shape are commonly intergrown and/or surrounded by fayalitic Ol, Cpx, Amp, Bt and Ilm, and occur in contact with Qz, Pl, Kfs, Tit and Ap (Fig. 4.3a-d. Several grains contain inclusions of Ap-needles, Ilm, sulfides, and recrystallized melt inclusions, consisting of Qz, Pl, Kfs ± Bt.

Mafic rocks of the Upper Zone contain assemblages of Pl, Cpx, Opx, Amp, Mt, Ilm, Qz, and accessory Ap, Tit, Thr, monazite (Mnz), Zrc, and sulfides. Zircon grains are less abundant than in felsic rocks and mostly subhedral. In ferrodiorites and -gabbros, zircon grains commonly form euhedral crystal faces towards plagioclase and quartz, and anhedral faces in contact with Cpx, Opx, Ilm, and Mt (Fig. 4.3e). Furthermore, zircons contain mineral inclusions of Ap, Ilm and Mt, as well as recrystallized melt inclusions of Qz, Pl, Kfs ± Bt. In pegmatoidal diorite (UZ3), zircon mostly occurs in Amp- and Qz-rich domains and rarely contains inclusions of Ap, Ilm and sulfides.

In the lower RLS, from the BUS towards the lower Main Zone, zircon mainly occurs in cumulate rocks dominated by Opx, mostly zoned Pl, Chromite (Chr) and subordinate Cpx as well as variable amounts of Bt, Amp, Pl, Kfs, Qz and rutile (Rt) in intercumulus melt pockets (see Table 4.3). Typical mineral assemblages observed in such melt pockets are illustrated in Figure 4.3g-i. Here, zircon grains are commonly anhedral and contain recrystallized melt inclusions mostly comprising Qz, Pl, and Kfs. In thin sections and heavy mineral concentrates zircon is observed closely intergrown with Bt, Amp, Qz Pl, Kfs, Chr and Rt (Figs. 4.3, 4.4, 4.5; Table 4.3).

Table 4.3 Mineral assemblages observed in the investigated samples and in textural contact with zircon

Sample	assemblage[a]	observed phases in textural contact with zircon*												
	main	melt	Qz	Kfs	Pl	Bt	Ap	Ilm	Rt	Opx	Cpx	Ol	Amp	Sf
Lebowa Granite														
JF9	Qz+Kfs+Pl+Cpx+Ol+Ilm+Mt+Bt+Ap	I	O	O	O	X	X	X			X	X		
MOK-1	*na*	I	O	I			X	X				I		I
MOK-2	*na*	I	X				I	I						I
Rashoop Granophyre & Rooiberg felsite														
JF7	Kfs+Qz+Pl+Amp+Cpx+Bt+Ap	I	O	O	O	O	X	X			I		O	I
Grano1	Kfs+Qz+Pl+Amp+Ol+Ap+Ilm	I	X	O	O		X	X					O	
JF22	Qz+Kfs+Pl+Cpx+Ol+Mt+Amp+Ap+Ilm	I	O	O	O		I	I						I
JF21	Qz+Kfs+Pl+Cpx+Ol+Mt+Amp+Ap+Ilm	I	O	O	O		X					O		
Contact quartzite														
JF1a	Qz+Amp	I	O				I							
RLS - Upper Zone														
JF5	Pl+Cpx+Opx+Amp+Mt+Ilm+Qz+Ap	I	O		O		I	X			O			
JF23	Pl+Cpx+Opx+Amp+Mt+Ilm+Qz+Ap	I	O		O		I	I						
UZ3	Pl+Qz+Amp+Ilm+Ap+Tit	I	O				I	I					O	I
MH1	Pl+Mt+Kfs+Cpx+Amp+Bt	I					I							
RLS - Main Zone														
SB-139	*na*	I	O	O	O								O	
SBBH01	*na*	I	O		O		I			O				
GC	Pl+Opx+Cpx+Qz+Rt	I	I	I	I					I	I			
PR-1	Opx+Cpx+Pl+Chr+Sf+Rt	I												
RLS - Critical Zone														
HW-NRT	Pl+Opx+Cpx+Amp+Sf	I	I		I									
MR-B	Opx+Cpx+Pl+Sf+Bt+Qz+Chr+Rt	I	O						O					
MR-WL-1	Opx+Cpx+Pl+Sf+Chr+Rt+Qz	I	O						O					
PGMT	Opx+Pl+Cpx+Bt+Amp+Sf+Chr+Qz	I	X	X	X	X				I	I			
FW-PX	Opx+Pl+Cpx+Rt	I	I			I				I				
FW-NRT	Pl+Opx+Cpx+Chr+Rt	I												
WHK	Opx+Pl+Cpx+Bt	I	I											
UG2K	Opx+Chr+Pl+Bt+Rt	I	I	I		I			X	I				
UG2a	Opx+Cpx+Pl+Bt+Kfs+Qz+Ap	I	O			O								
UG2b	*na*	I	O	O	O	O								
UG2M	Opx+Cpx+Chr+Pl+Kfs+Qz+Bt+Rt	I	O	O		O			X					
MG7	Opx+Cpx+Bt+Chr+Sf+Ap	I	I			O				O	O		O	
LG6	Chr+Cpx+Pl+Opx+Qz+Rt	I	I				I							
JGL	Opx+Chr+Pl+Cpx+Bt+Rt	I	I	I	I	I								
CH-12-1	Chr+Opx+Pl+Rt	I	I	I						I				
RLS - Marginal Zone														
CH12-3	Pl+Cpx+Opx+Kfs+Bt+Qz+Amp+Chr+Rt	I	X	O	O	X	O	O	I	O	X			
CH12-26	Opx+Pl+Cpx+Qz+Rt	I	X	I										
CH12-9	Opx+Cpx+Pl+Bt+Qz+Rt	I												
RLS - Basal Ultramafic Sequence (BUS)														
CH7-164	Opx+Cpx+Pl	I	I											

RLS=Rustenburg Layered Suite; Qz=quartz, Kfs=alkali feldspar, Pl=plagioclase, Bt=biotite, Amp=amphibole, Ap=apatite, Mt=magnetite, Chr=chromite, Tit=titanite Rt=rutile, Ilm=ilmenite, Opx=orthopyroxene, Cpx=clinopyroxene, Ol=olivine, Amp=amphibole, Sf=sulfides

[a] mineral assemblages observed in thin sections (where available), ordered after decreasing modal proportion

* O=attached to zircon, I=included in zircon, X=both attached to and included in zircon

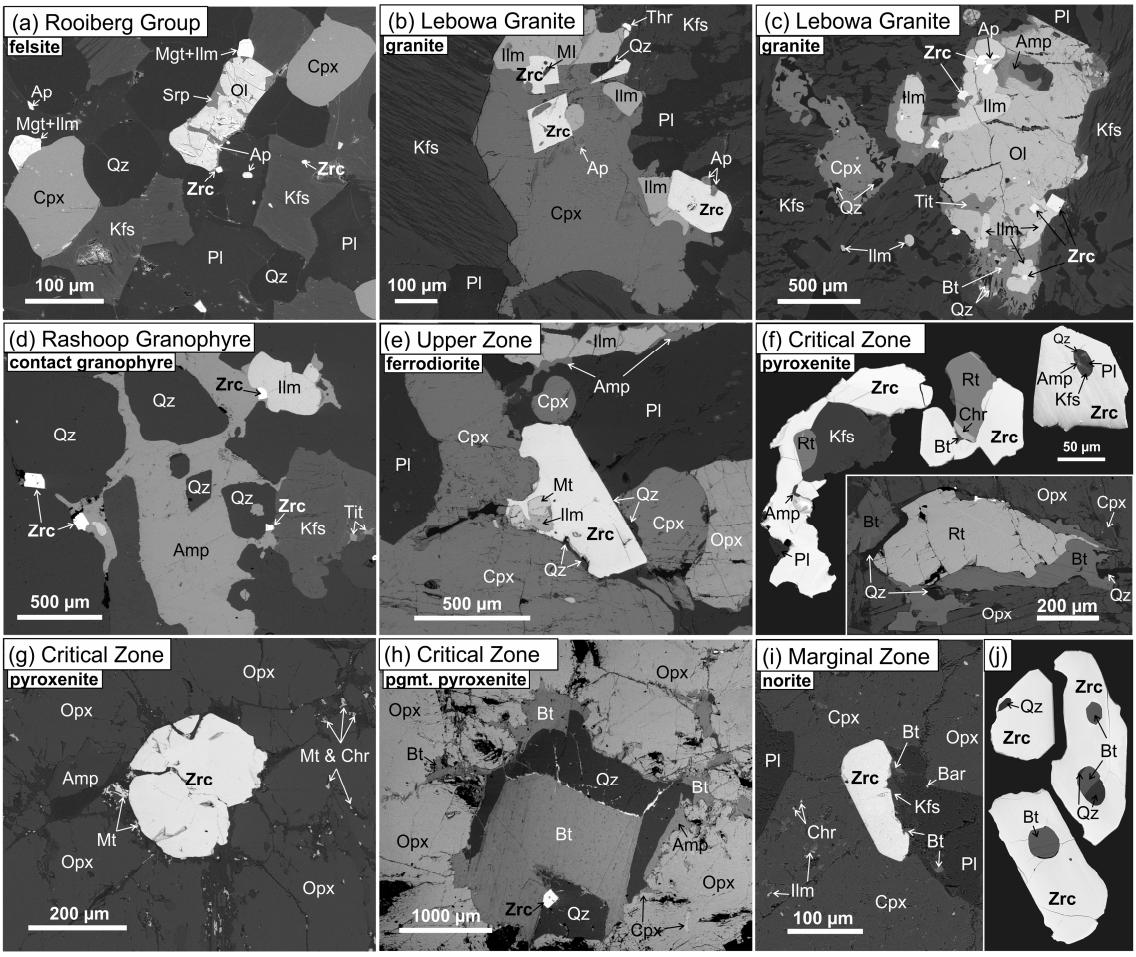

Figure 4.3 - Back scattered electron images (BSE) showing zircon-bearing assemblages in felsic (a-d) and mafic rocks (e-j) of the BC. Zircon in (a) felsites of the Rooiberg Group (JF21), (b, c) Lebowa granite (JF9), (d) contact granophyre (JF7), (e) Upper Zone ferrodiorite (JF5), (f, g, h) Critical Zone pyroxenites (UG2M, MG7, PGMT), and (i, j) in chilled norite of the Marginal Zone (CH12-3). Within Critical Zone rocks, rutile occurs intergrown with zircon (f) and is locally replaced by biotite (inset in f). (j) Zircons in Marginal Zone rocks contain quartz and biotite inclusions. Zircons shown in (f) and (j) are from grain mounts, all other images are from thin sections. Zrc = zircon, Cpx = clinopyroxene, Opx = orthopyroxene, Ol = olivine, Pl = plagioclase, Kfs = alkali feldspar, Qz = quartz, Mt = magnetite, Amp = amphibole, Chr = chromite, Rt = rutile, Ilm = ilmenite, Bt = biotite, Cal = calcite, Bar = baryte, Srp = serpentine, Thr = thorite, Tit = titanite, Ap = apatite, MI = melt inclusion.

4.3.3 Zircon morphology

Euhedral zircon is abundant in all felsic rocks, but also in some mafic rocks of the Upper Zone (JF23, UZ3), Main Zone (SB-110), and the Marginal Zone (CH12-3). Zircon populations of felsic rocks and ferrodiorites of the Upper Zone (JF5, JF23) show identical morphologies, dominated by {100} prisms and {101} pyramids, corresponding to J5 and D types in the classification scheme of Pupin (1980) - (Fig. 4.4a-d). In contrast, morphologies of zircon populations in samples UZ3 (pegmatoidal diorite of the Upper Zone), SB-110 (Main Zone gabbro) and CH12-3 (chilled Marginal Zone) are more diverse, characterized by higher fractions of {110} prisms and {211} pyramids of variable size (Fig. 4.4e-g). This also holds true for euhedral zircon grains rarely found in several other rocks of the Critical Zone, e.g. Merensky Reef pyroxenite (Fig. 4.4h).

According to the classification scheme of Pupin (1980), the morphologies of zircons in felsic rocks and in ferrodiorites of the Upper Zone (JF5, JF23) reflect zircon growth at mainly 850-900 °C, whereas zircon populations in pegmatoidal diorite of the Upper Zone, in Main Zone gabbros, and in cumulate rocks of the Marginal Zone point to a wide range of crystallization temperatures between 750 and 900 °C (Fig. 4.4, Table 4.4).

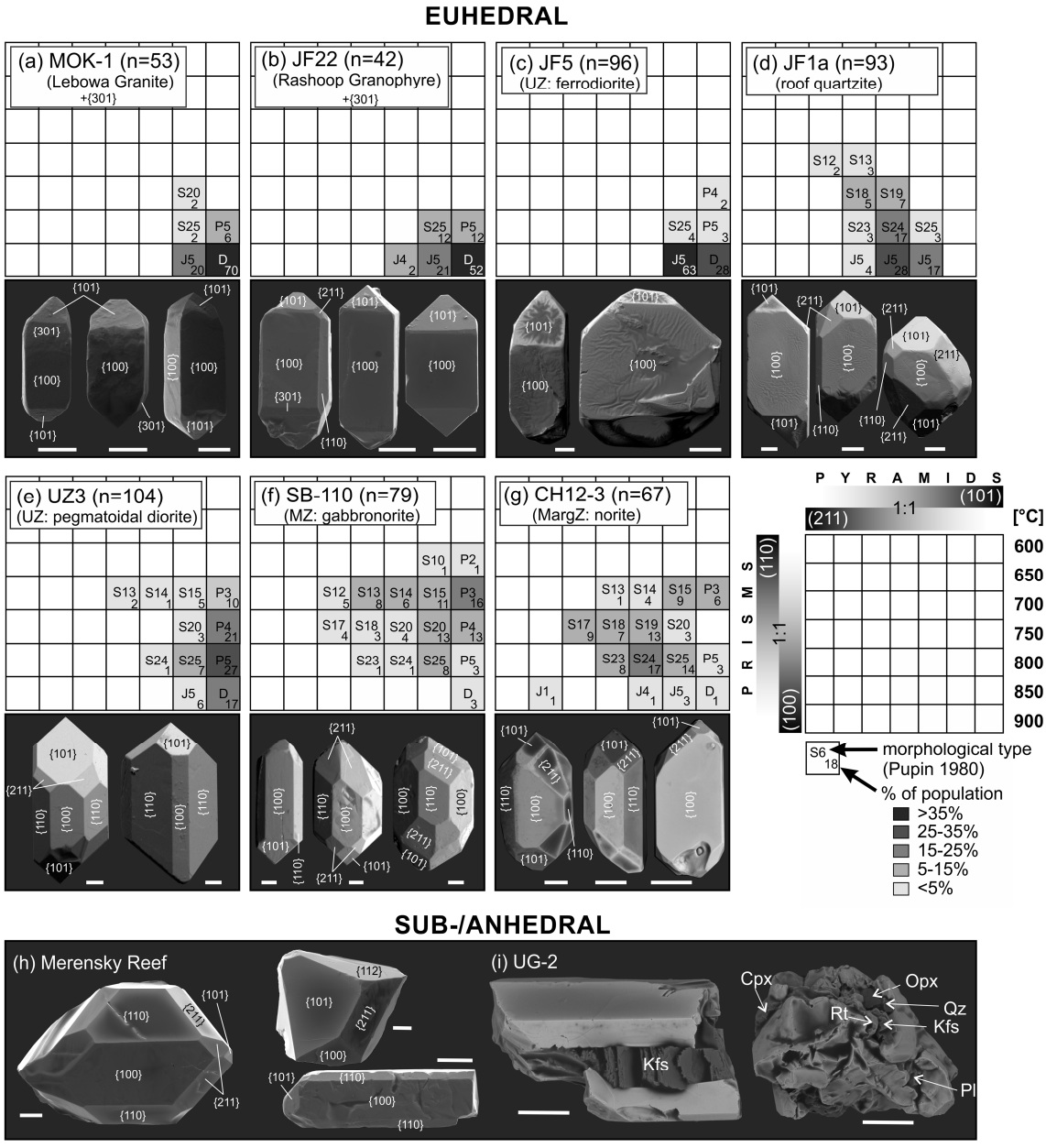

Figure 4.4 - Zircon morphologies in different felsic (a, b) and mafic rocks (c, e-i) of the BC, and in contact metamorphic quartzite (d). Shown are representative secondary electron images, as well as morphological diversities quantified using the classification scheme of Pupin (1980). (a-d) Zircon in felsic, mafic and contact metamorphic quartzites all located at the roof of the BC are dominated by {100} prisms and {101} pyramids, suggesting crystallization temperatures of 850-900 °C, whereas zircon in (e) pegmatitic diorite of the Upper Zone, (f) Main Zone gabbronorite and (g) Marginal Zone norite is morphologically more diverse, pointing to crystallization temperatures of 700-900 °C. (h) Rare examples of euhedral zircon in Merensky Reef sample (MR-WL-1) reveal wide variations in morphology, corresponding to temperatures between 700 and 850 °C. (i) Zircons in sample UG-2 are always sub- to anhedral, and are commonly intergrown with Rt, Kfs, Qz, Pl and pyroxenes. White bars indicate 50 µm in all images.

4.3.4 Internal zircon textures

Zircon in samples of the Lebowa Granite (JF9, MOK-1, MOK-2) and Rashoop Granophyre Suites (JF7, Grano1, JF22) show very similar zoning patterns, characterized by three zones, (i) a core dominated by sector zoning surrounded by, (ii) a zone with oscillatory zoning, grading (iii) into a CL-dark/BSE-bright rim with weak zoning (Fig. 4.5a). In all granite and granophyre samples, alteration is indicated by porous domains which in most cases transect the primary growth zoning as revealed by CL-BSE images. These porous domains most likely result from a coupled dissolution-precipitation processes causing a pseudomorphic alteration (Geisler et al., 2007).

Zircons of the Upper Zone of the RLS commonly display a combination of oscillatory and sector zoning (JF5, JF23, UZ3, MH1). The populations of individual samples show little variation in CL-brightness and zoning patterns, and are less altered compared to the granitic rocks (Fig. 4.5b). Zircon populations in mafic rocks of the Main Zone (SB-110, SB-139, SB-142 and SBBH-01) mostly show coarse zoning, highlighted by large angular domains of even BSE-brightness. However, in many grains, growth zoning is disturbed by alteration, highlighted by porous domains and reaction zones along fractures (Fig. 4.5f).

Zircons in pegmatoidal pyroxenites of the Merensky Reef (PGMT, MR-B, MR-WL-1), Platreef (PR-1) and in other samples of the Critical Zone (e.g. UG2K, UG2a), Marginal Zone (CH12-3) and BUS (CH7/143) display sector and/or oscillatory zoning and a large variety of CL intensities between individual grains (Fig. 4.5d-g). Zircon populations in some samples show coherent CL-intensities for all grains (e.g. CH12-3 in Fig. 4.5g), whereas pronounced core-rim zoning is observed in others. Two types of zoning can be distinguished: zircon populations showing a systematic increase in CL-brightness from core to rim, even within the same sector of crystallographic orientation (Trend 1 in Fig. 4.5d) , and those with reverse zoning (Trend 2: e.g. samples PGMT, MG7, CH7/143) which is more common. In some samples (e.g. UG2K, MR-B), zircon populations with both trends were observed (Fig. 4.5d).

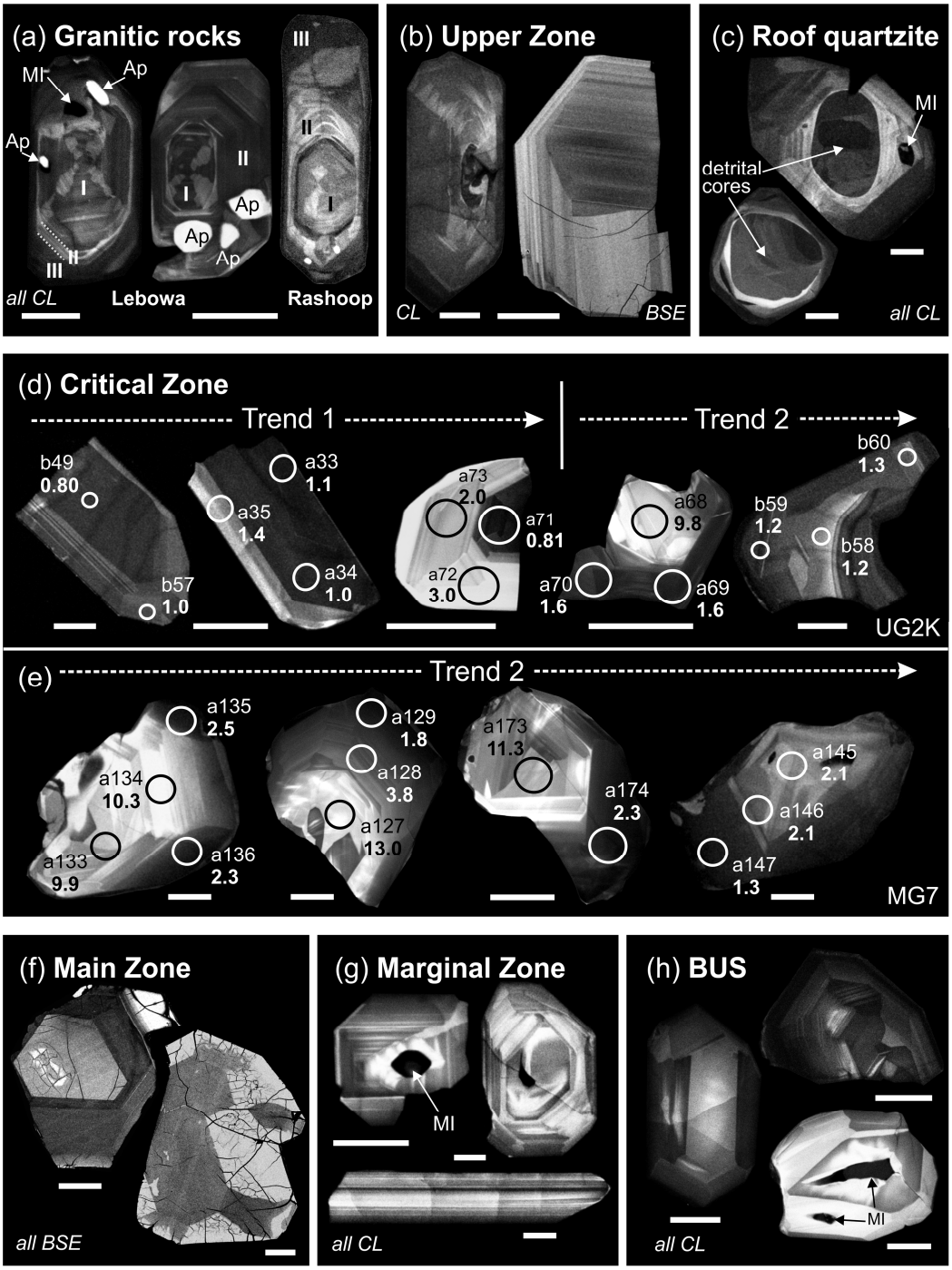

Figure 4.5 - Representative zoning patterns of zircon in (a) felsic and (b, d-h) mafic rocks of the BC and in (c) associated quartzite derived from the roof contact revealed by back scattered electron (BSE) and cathodoluminescence (CL) images. (a) Zircons in granitic rocks comprising Lebowa Granite (sample JF9; left & middle) and Rashoop Granophyre (sample JF22; right) commonly show three, texturally distinct zones: (I) sector-zoned core, (II) intermediate domain with oscillatory zoning, and (III) weakly-zoned, CL-dark rim. (b) Zircons in Upper Zone mafic rocks (left: JF23; right: UZ3) reveal oscillatory sector zoning, and those in (c) roof quartzite (JF1a) display detrital zircon cores surrounded by metamorphic rims with weak oscillatory zoning. (d, e) Typical zoning patterns of zircon in mafic cumulate rocks of the Critical Zone. Two zoning trends can be distinguished: Trend 1 is characterized by CL-dark cores surrounded by CL-bright rims, whereas Trend 2 is opposite. The zircon population in sample UG2K (d) reveals both trends, and that in sample MG7 (e) only Trend 2. Circles and related numbers represent laser spot positions and analysis numbers (corresponding to Table S1), and Th/U ratios (bold). (f) In Main Zone sample SB-142, zircons display coarse zoning marked by large domains of even BSE-brightness and strong alteration/fracturing in BSE-bright areas. (g) Zircons in Marginal Zone norite (CH12-3) display similar CL intensitites and well-developed oscillatory zoning, whereas CL intensitites of zircon in (h) BUS pyroxenites (CH7-164) are highly variable, and zoning commonly follows Trend 2. Ap = apatite, MI = melt inclusion. White bars indicate 50 µm in all images.

4.3.5 Zircon composition

Zircon populations show clear variations in trace element contents and ratios that can be related to the BC stratigraphy. Some general patterns are summarized in Fig. 4.6, Fig. 4.7 and Table 4.5, and the complete dataset is presented in Table S1. From base to top of the BC, zircon populations show a general decrease in Ti contents and Th/U ratios, and increasing rare earth element contents. Based on ΣREE and Th/U ratios, the stratigraphic profile is subdivided into two major sections (Figs. 4.6 and 4.7). Zircons in all felsic and mafic rocks above the Pyroxenite Marker show higher ΣREE (average 651 ppm) and lower Th/U (<1), compared to those in the mafic rocks beneath (average ΣREE <300 ppm, Th/U = 0.5 to 24), corresponding to the variations reflected by bulk rock compositions (Fig. 4.2b). Furthermore, they mostly display lower Ti contents (<10 ppm), compared to zircons in mafic cumulate rocks beneath the Pyroxenite Marker (Ti >10-60 ppm), and their variations in Th/U (0.3-0.8) and Nb/Ta (1.2-4.4) are minor. In contrast, Th/U and Nb/Ta ratios of zircon in Rt-bearing mafic rocks of the BUS and Critical Zone are mostly much higher and variable (Nb/Ta = 0.15-18, Th/U = 0.2-24). In some samples, Th/U values reach up to 24 (Fig. 4.6), which is extremely high for igneous zircon (Yakymchuk et al., 2018). As shown in Fig. 4.7, the distinction between the base and top of the Stillwater Intrusion based on zircon TE compositions is very similar to the BC (Wall et al., 2018).

Chondrite-normalized REE patterns of pristine zircon grains/domains are marked by positive Ce and negative Eu anomalies, whereas altered zircon domains show much higher contents in LREE, minor or even no Ce-anomalies, and in some samples positive Eu-anomalies (Fig. 4.8). Negative Eu anomalies (Eu/Eu*N) in zircon are similar in all samples independent on respective bulk rock REE patterns, which are characterized by negative (MOK-2, MR-B), positive (JF9, JF5), or absent Eu-anomalies (CH12-3), suggesting different degrees of feldspar fractionation and/or accumulation prior to zircon growth (Fig. 4.8).

Titanium-in-zircon temperatures ($T_{Ti\text{-}Zrc}$) of Rt-Qz-bearing cumulate rocks of the RLS range between $T_{Ti\text{-}Zrc}$ = 690 and 962 °C (average: 835 °C), using the calibration of Ferry and Watson (2007) and $a TiO_2 = a SiO_2 = 1$. There are large differences among the samples (Table 4.5): Average values range from 743 °C in sample CH7-164 (n = 23) to 920 °C in sample UG2b (n = 13). In some samples, zircon populations show a wide range in Ti-in-zircon temperature (e.g. UG2K and MR-B in Fig. 4.6), whereas others only show minor variations (e.g. samples WHK and CH12-8).

For zircon populations in Rt-free, Ilm-Tit-Mt-bearing mafic rocks of the Main and Upper Zones (UUMZ) and in felsic rocks, Ti-in-zircon temperatures were calculated using $a SiO_2 = 1$ and a reduced Ti activity of $a TiO_2 = 0.3$ ($T_{Ti\text{-}Zrc}$*), which is the value calculated by rhyolite-MELTS for granitic rocks and the UUMZ during zircon crystallization (see section ‘4.3.7. Results of thermodynamic modelling’). For felsic rocks $T_{Ti\text{-}Zrc}$* range between 761 and 935 °C

(average: 859 °C) and for the UUMZ, $T_{Ti\text{-}Zrc}$* are very similar and range between 742 and 968 °C (average: 846 °C).

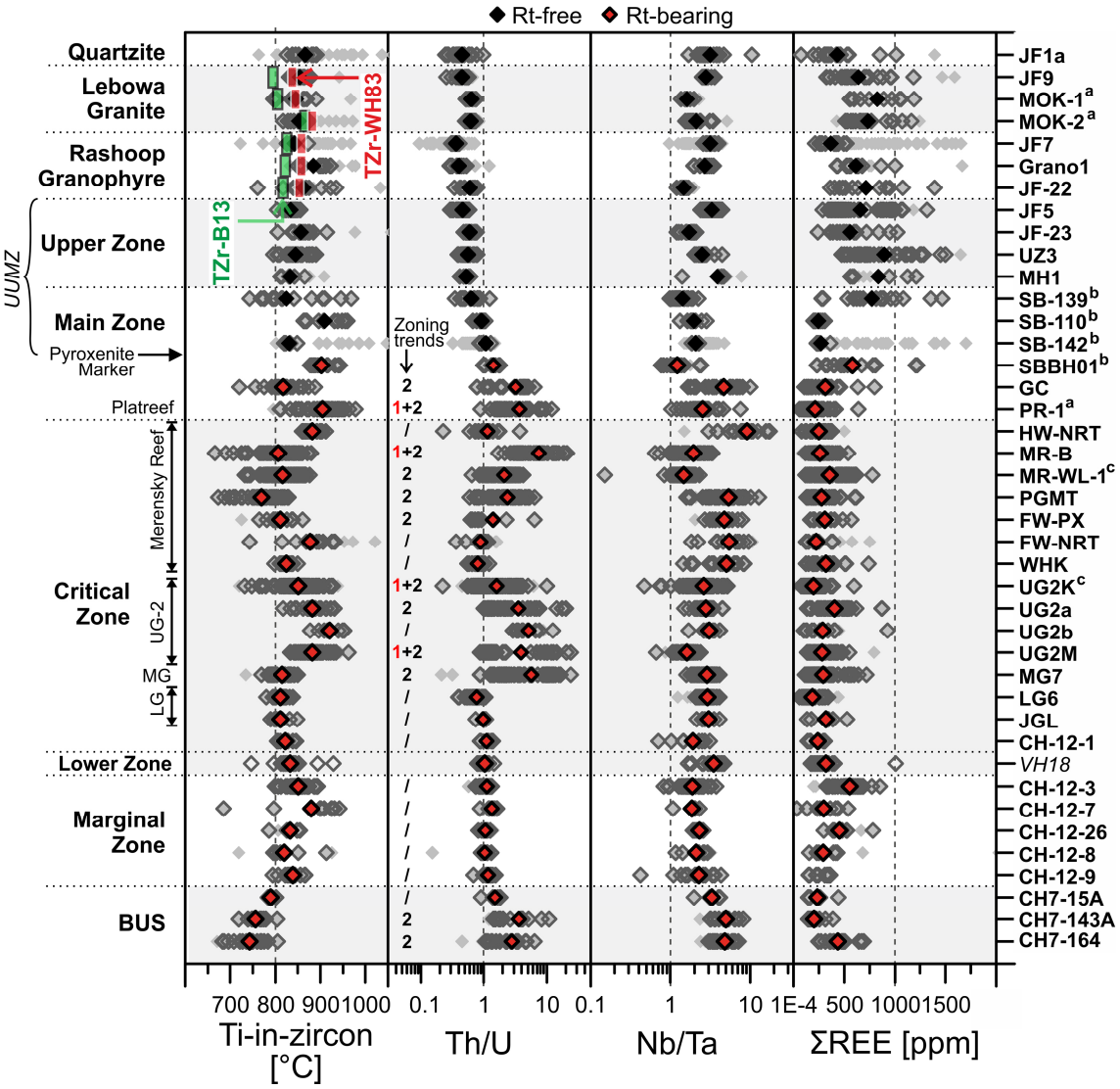

Figure 4.6 - Trace element systematics of zircon throughout the BC stratigraphy and results of Ti-in-zircon and zircon saturation geothermometry. For quartzite sample JF1a, only data of metamorphic overgrowths are presented, and for the Lower Zone, data of Ver Hoeve et al. (2018) is shown for comparison ('VH18'). Note that zircons in Rt-free felsic and mafic rocks above the Pyroxenite Marker (black solid diamonds) show significantly higher REE contents, lower average Th/U ratios and Ti-in-zircon temperatures compared to Rt-bearing mafic cumulate rocks below (red diamonds). Zircons in many mafic rocks from the BUS to the Lower Main Zone show highly variable Th/U and Nb/Ta ratios, as well as Ti-in-zircon temperatures, pointing to different physicochemical conditions during zircon growth. Ti-in-zircon temperatures for rutile-bearing rocks were calculated using $a\mathrm{TiO_2}$ = 1.0, and for rutile-free rocks with $a\mathrm{TiO_2}$ = 0.3 (modelled by using the method of Schiller and Finger (2019); for explanation see text). Vertical red and green bars mark the bulk-rock zircon saturation temperature obtained with the models of Watson and Harrison (1983; TZr-WH83), and Boehnke et al. (2013; TZr-B13), respectively. Open grey diamonds = values of pristine zircons; black solid diamonds = average values for Rt-free samples, red diamonds = average values for Rt-bearing samples, light grey solid diamonds = altered zircons. For Th/U, distinct zircon zoning trends are indicated which are discussed in the main text: Trend 1 (increasing Th/U at decreasing U from core to rim), Trend 2 (decreasing Th/U at increasing U from core to rim) or absent/indistinct zoning trends (/); [a]Northern Limb, [b]Southern Limb, [c]Western Limb, all other samples are derived from the Eastern Limb.

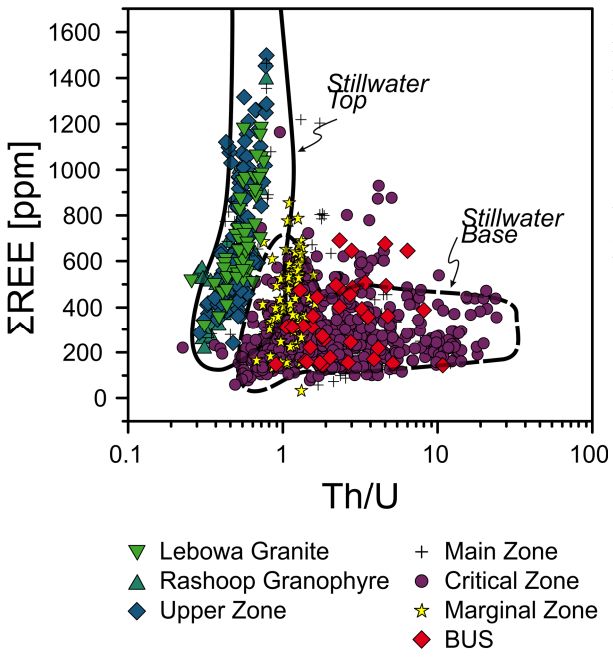

Figure 4.7 - Covariation diagram of ΣREE vs. Th/U ratios revealing that zircons in Rt-free felsic and mafic rocks above the Pyroxenite Marker (Lebowa Granite, Rashoop Granophyre and Upper Zone) define a different trend (similar to Stillwater Top) than zircons in Rt-bearing mafic cumulate rocks below (overlapping with Stillwater base), suggesting distinct trace element fractionation processes (detailed in the discussion). Fields for Stillwater Top (Middle and Upper Banded Series) and Stillwater Base (Ultramafic and Basal Series) were drawn using data of Wall et al. (2018).

4.3.6 Zircon zoning

Zircon grains in all granitic rocks (e.g. samples JF22, JF9) show increasing U and Nb contents with decreasing Ti contents from core to rim, whereas Th/U and Nb/Ta ratios remain nearly constant (Fig. 4.9a-d). This zoning trend is commonly highlighted by decreasing CL intensities from zone i (core) towards zone iii (rim; Fig. 4.5a). The compositional zoning of zircon in Upper Zone mafic rocks (UZ3, JF23, JF5, MH1) is very similar, although less pronounced. In contrast, zircons found in Rt-bearing samples beneath the Pyroxenite Marker (from the BUS to the lower Main Zone), are commonly characterized by pronounced Th/U and Nb/Ta zoning. In these rocks, zircon grains with two distinct zoning trends can be distinguished. Zircon grains with Trend 1 are characterized by increasing CL-brightness from core to rim, and show a correlated decrease in Ti (60 to 20 ppm), U (175 to 10 ppm), and increase in Th/U ratio from about 0.5 up to 24 (Fig. 4.9e-l). In contrast, zircon grains with Trend 2 mostly have lower Ti contents (30 to 8 ppm), and are characterized by a correlated decrease in Ti with increasing U, Th, Nb, Ta contents from core to rim, accompanied by a decrease in both Th/U and Nb/Ta ratios (Fig. 4.9e-p). Here we note that in U vs. Th/U diagrams both trends (1 and 2) have a very similar curvature (Fig. 4.9f, j, n), making them indistinguishable without considering additional parameters (e.g. core-rim relationships reflected by BSE/CL images and/or Ti contents). The observed core-rim systematics and Ti contents suggest that Trend 1 is typical for zircon formed at temperatures above ~825 °C, and Trend 2 for zircon formed at lower temperatures down to 690 °C. Reasons for the development of the two trends will be discussed in detail below (section 4.4.2. ‘Reasons for zircon zoning’).

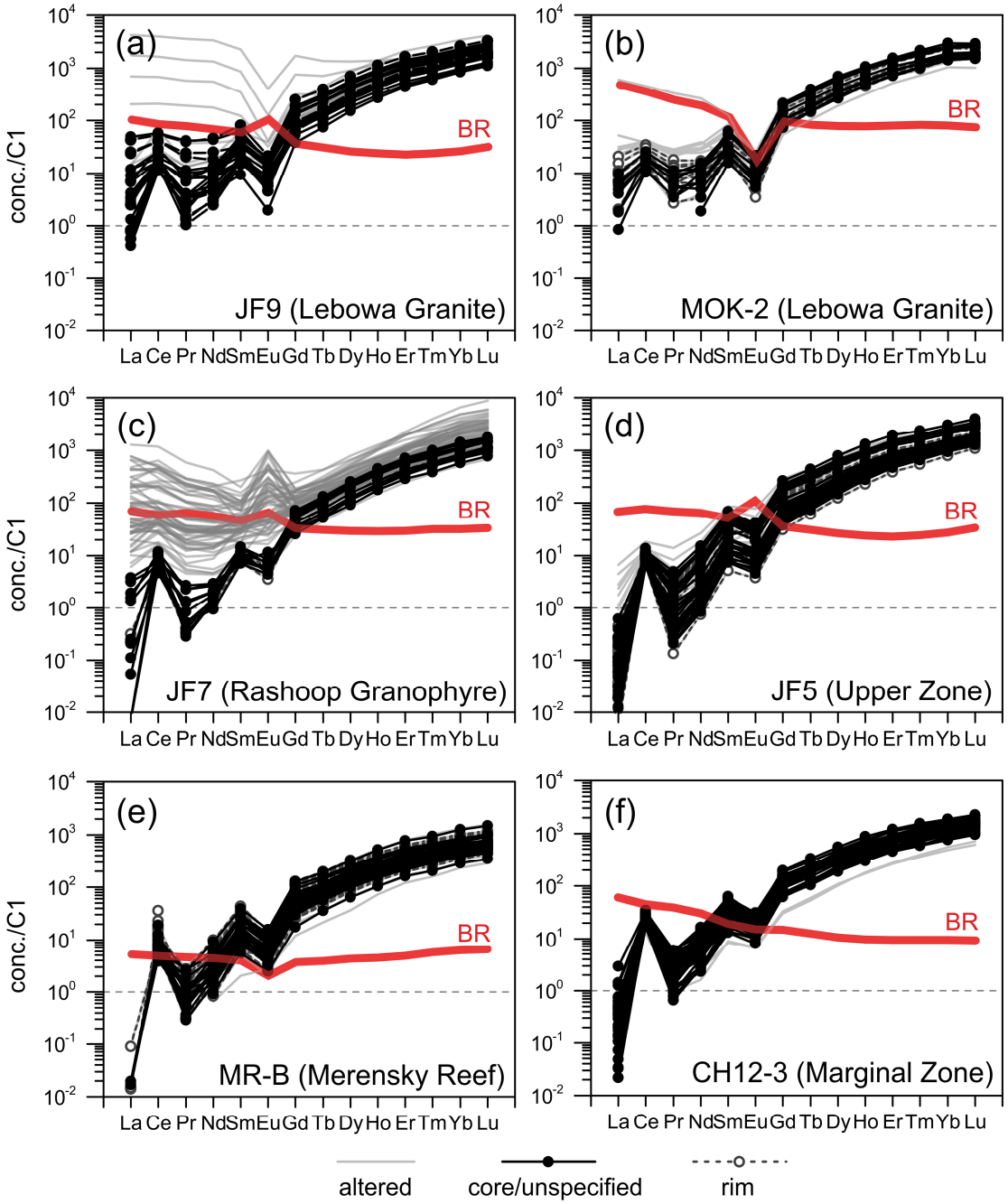

Figure 4.8 - Chondrite-normalized rare earth element patterns of pristine and altered zircon grains, and of bulk rocks (BR) of representative samples of Lebowa Granite (JF-9, MOK-2), Rashoop Granophyre (JF-7), Upper Zone diorite (JF-5), Merensky Reef pyroxenite (MR-B) and Marginal Zone norite (CH12-3). Chondrite normalization according to McDonough and Sun (1995).

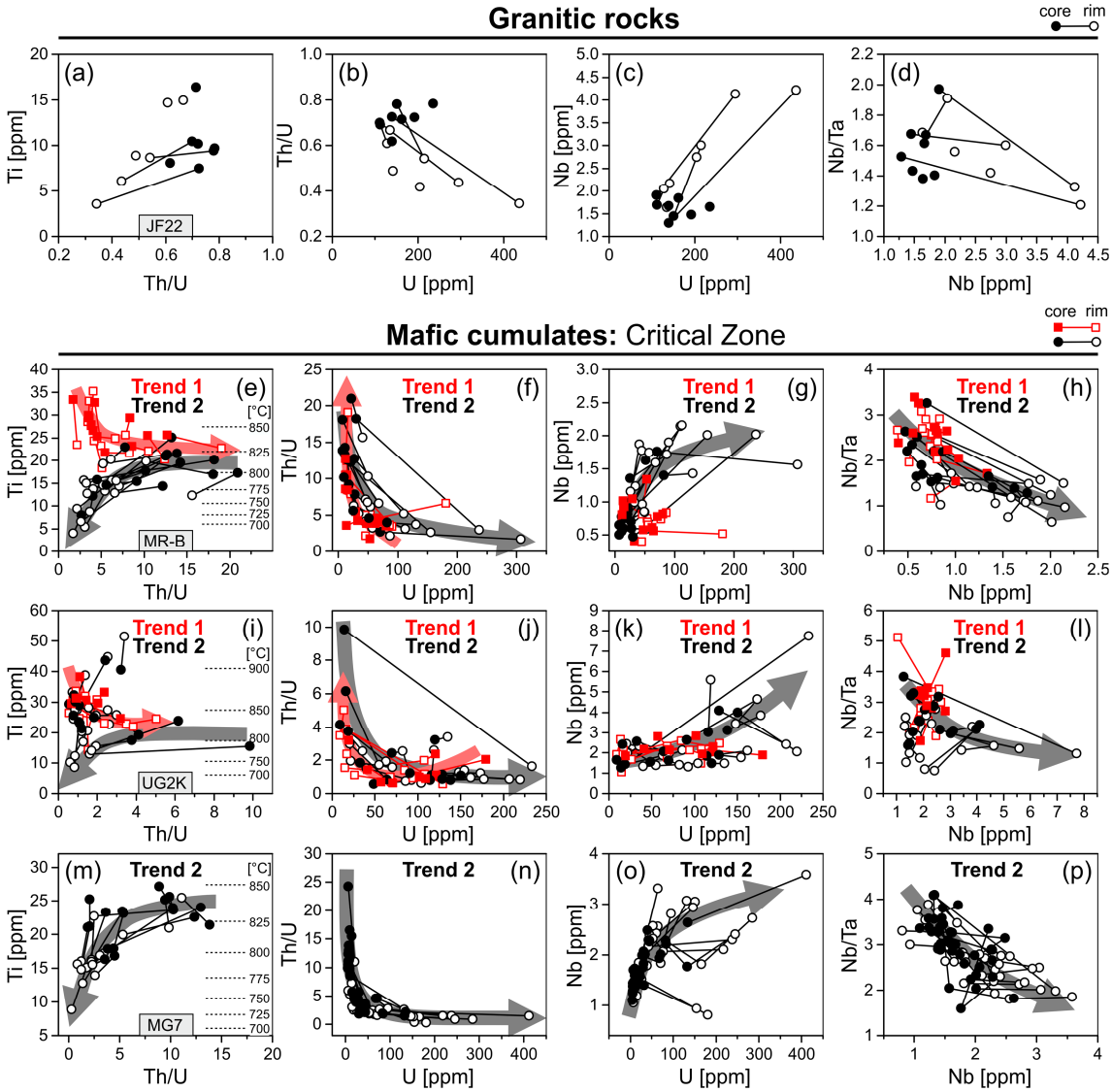

Figure 4.9 - Covariation diagrams illustrating trace element zoning patterns of zircon in (a-d) typical felsic rock (sample JF22), and (e-p) in three mafic cumulate rocks of the Critical Zone (e-h: sample MR-B; i-l: sample UG2K; m-p: sample MG7). Core and rim analyses are indicated by filled and open symbols, respectively. Analyses of single grains are connected by black tie lines. Note that zircon grains and populations in felsic rocks show weak zoning in Th/U and Nb/Ta from core to rim, while those in Rt-bearing mafic cumulate rocks are strongly zoned, whereby two zoning trends can be distinguished, even within individual samples (MR-B, UG2K). Trend 1 (red boxes) is typically characterized by increasing Th/U at decreasing U from core to rim and Trend 2 (black circles) by the opposite behavior. Trend 1 occurs at higher temperatures (commonly >825 °C) than Trend 2, which is further characterized by a correlated increase in Nb, U and a decrease in Nb/Ta towards zircon rims.

4.3.7 Results of thermodynamic modelling

The effect of fractional crystallization on different BC parental magmas is investigated by forward modelling using rhyolite-MELTS (Gualda et al., 2012) - (all data tables given in Table S3, supplementary materials). Modelling results show that during fractional crystallization of felsic parental magmas of the BC, zircon saturation is reached at 881 °C, applying the zircon saturation model of Watson and Harrison (1983) (referred in the following as TZr-WH'83), or at 836 °C by using the model of Boehnke et al. (2013) – (referred in the following as TZr-B'13). Zircon formation will occur after ca. 20% of fractional crystallization for a melt composition approximated by the felsite sample JF21, having a Zr content of 552 ppm (Fig. 4.10a). A

slightly higher degree of fractionation (~30 %) is required if felsic melts with lower Zr contents are used (e.g. sample JF9). In the model, magnetite-rich spinel (Mt) is the liquidus phase that starts to crystallize at 1026 °C followed by Pl at 962 °C and Qz, Kfs and Cpx at ~810 °C. At zircon saturation, the composition of the melt is (in wt.%): 71.8 SiO_2, 11.6 Al_2O_3, 2.2 CaO, 3.9 Na_2O and 4.6 K_2O (Fig. 4.10a).

For mafic rocks of the Upper and Upper Main Zones (UUMZ), no zircon saturation is predicted to occur before the model ends at 735 °C, if the calculations are done by using a pure UUMZ parental magma. However, by adding 15% of average Rashoop Granophyre to UUMZ, as suggested by VanTongeren et al. (2010), zircon crystallization occurs at ≤810 °C (TZr-W&H'83) or at ≤744 °C (TZr-B'13) (Fig. 4.10b), in assemblage with Cpx, Opx, Mt, Pl, Ap, Kfs and Qz. At zircon saturation, the magma composition is (in wt.%): 70.4 SiO_2, 11.0 Al_2O_3, 2.8 CaO, 3.6 Na_2O and 4.3 K_2O. If 25% Rashoop Granophyre is added to UUMZ, the fractional crystallization history is similar, but zircon saturation already occurs at 840 °C ((TZr-W&H'83) or at 790 °C (TZr-B'13).

Rhyolite-MELTS modelling was further used to obtain the TiO_2 activity ($a$$TiO_2$) at the time of zircon growth in the Rt-free felsic and mafic rocks of the BC (JF21, UUMZ), by applying the method proposed by Schiller and Finger (2019). By this method the TiO_2 activity is derived from the intersection of the TiO_2 activity evolution curve calculated with rhyolite-MELTS and the ideal zircon crystallization temperature distribution (ZCTD) curve at 50% (for example see Fig. 4.10c), which is calculated for a certain rock based on bulk rock composition and zircon saturation modelling (for more details see Schiller and Finger, 2019). For the Rt-free felsic and mafic rocks of the BC this intersection is mainly at $a$$TiO_2$ ~0.3 (see Figs. 4.10c and d). We note that for the felsic magmas of the BC, the modelled ideal ZCTD is nearly identical to the temperature distribution obtained by applying the Ti-in-zircon geothermometer of Ferry and Watson (2007) for $a$$TiO_2$ = 0.3 - (compare Fig. 4.10a and 4.10c). However, for UUMZ rocks, the ZCTD lies ~50 °C below the calculated Ti-in-zircon temperatures (Fig. 4.10b and d). This discrepancy can be explained by the complexity of the considered system, which apart from temperature, bulk rock composition, and Zr-content is also dependent on fractionation progress, activity models, and initial H_2O content. As shown in Figure 4.10b and d, $a$$TiO_2$ in both felsic and UUMZ magmas increases significantly during cooling from 950 °C ($a$$TiO_2$=0.23-0.25) to 750 °C ($a$$TiO_2$=0.41-0.45) at constant initial H_2O. However, both $a$$TiO_2$ and the ideal ZCTD will shift to higher values at decreasing initial H_2O content. This is exemplified for UUMZ magma (+25% felsic component) in Figure 4.10d, showing that $a$$TiO_2$ increases from 0.30 to 0.42 (at 50% ZCTD) if the initial H_2O content of the melt is reduced from 1.0 to 0.3%, while the ZCTD shifts to ca. 40 °C higher temperatures. Convergence between the calculated Ti-in-zircon temperature curve and the ideal ZCTD curve (for UUMZ +25% felsic) is achieved for initial H_2O ~0.7 wt.% and $a$$TiO_2$ = 0.39.

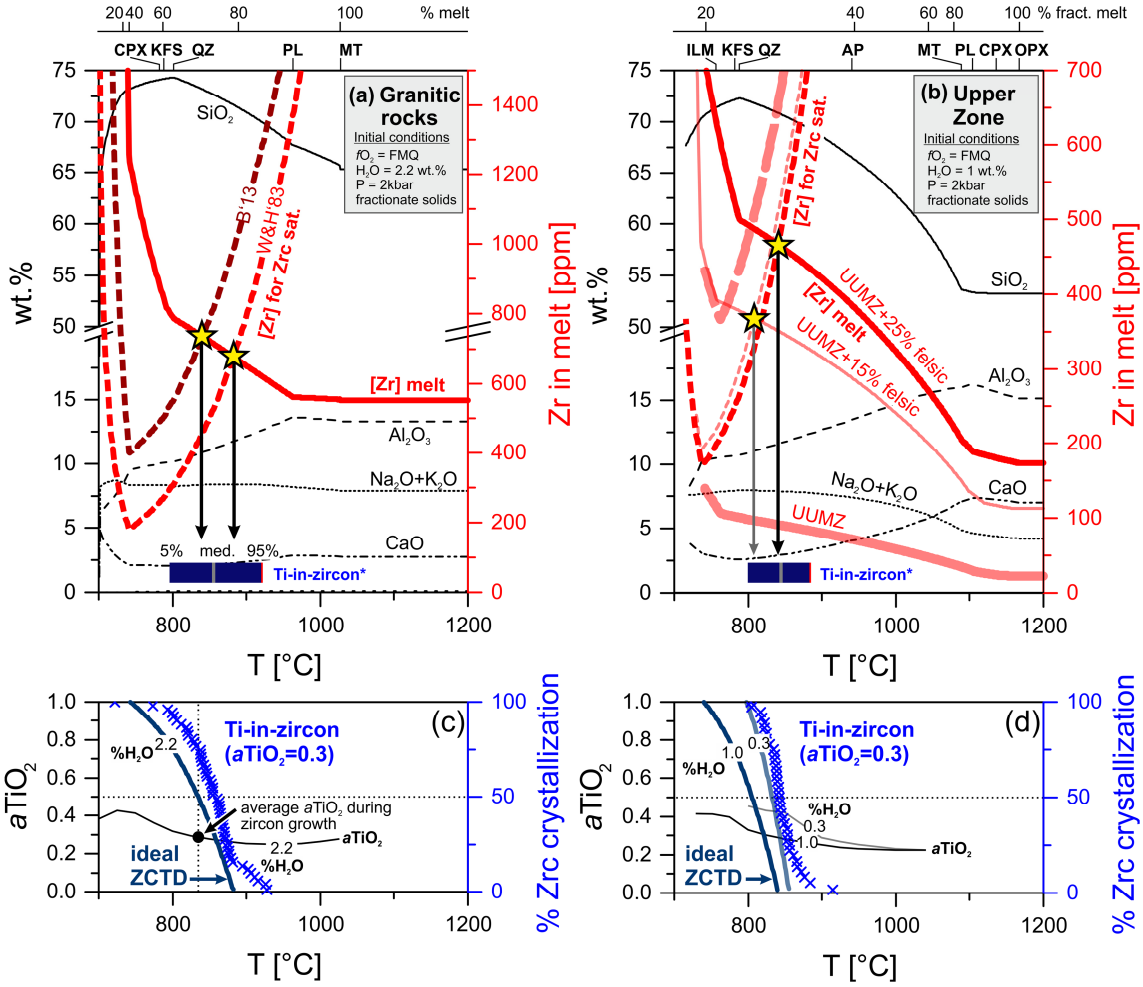

Figure 4.10 - Zircon saturation temperatures calculated for (a) granitic rocks and (b) Upper Zone mafic rocks of the BC using rhyolite-MELTS (Gualda et al., 2012) in combination with zircon saturation geothermometers calibrated by Watson and Harrison (1983) ("W&H'83") and Boehnke et al. (2013) ("B'13"). Results of Ti-in-zircon thermometry shown for comparison (Ferry and Watson, 2007), with indicated median (med.), 5% and 95% percentiles (labelled as in a). (a) Zircon saturation in granitic rocks is reached after 20-30% of fractional crystallization at 836-881 °C (yellow stars). (b) In Upper Zone mafic rocks, zircon saturation is not reached by crystallization of pure UUMZ parental magma (VanTongeren et al., 2010), but only by admixing a significant amount of felsic melt represented by Rashoop Granophyre composition (810 °C at +15% felsic, 841 °C at +25% felsic). For modelling details see text. Mineral abbreviations as in Fig. 4.3. For Ti-in-zircon thermometry in (a) and (b), $a\mathrm{TiO_2}$ = 0.3 was used, estimated by using the method of Schiller and Finger (2019), which is based on the intersection of the $\mathrm{TiO_2}$ activity ($a\mathrm{TiO_2}$) evolution curve (calculated with software rhyolite-MELTS; Gualda et al., 2012), with the ideal zircon crystallization temperature distribution (ZCTD) curve at 50% (calculated by using the zircon saturation model of Watson and Harrison (1983)). This method was applied for (c) granitic rocks and (d) Upper Zone mafic rocks (UUMZ parental magma +25% felsic melt). Exemplified for the Upper Zone in (d), the resulting $a\mathrm{TiO_2}$ increase with decreasing initial $\mathrm{H_2O}$ contents (1.0 to 0.3 wt.%).

For B3, the proposed parental magma to the Main Zone (Barnes et al., 2010), modelling does not predict zircon saturation. However, it has to be noted that quadratic minimization of rhyolite-MELTS fails to produce results at ≤773 °C (Fig. 4.11a).

For both pure B2 magma (Fig. 4.11b) and mixtures of B1and B2 magmas (B1:B2 = 60:40; see Fig. 4.11d), representing the proposed parental magmas for the Upper Critical Zone, modelling results indicate zircon saturation at ≤803 °C, after ca. 75 % fractional crystallization (using TZr-W&H'83), or at ≤760 °C (using Zr-B'13), following the crystallization of Opx (1138-1276 °C), Cpx (1150-1165 °C), chromite-rich spinel (Chr:1003-1224 °C), Ap (only B2:

885 °C) and Pl (1127-1153 °C). The minerals Qz (799-796 °C) and Ol (753-778 °C) either form together with or later than zircon. The melt compositions at zircon saturation are (in wt.%): 70.2-71.8 SiO_2, 9.7-11.1 Al_2O_3, 2.9-3.5 CaO, 2.9-4.1 Na_2O and 1.6-3.0 K_2O. We note that a change of the initial H_2O content has a great impact on the melt composition, but only slightly affects the zircon saturation temperature. This is illustrated in Fig. 4.11d for the B1 + B2 magma mixture, where initial H_2O contents of 0.2, 1 and 2 wt.% all result in similar zircon saturation temperatures (812 °C, 800 °C and 802 °C, respectively). We further note, that lower initial H_2O contents result in higher SiO_2 contents and Qz-in at higher temperatures (0.2 wt.% initial H_2O: Qz-in at 949 °C) compared to magmas with high initial H_2O contents (2 wt.% initial H_2O: Qz-in at 786 °C; see Fig. 4.11d). The dependency of other parameters (fO_2 and pressure) in addition to initial H_2O contents on the modelling results is presented in supplementary materials S5.

For the B1 magma composition (Fig. 4.11c), the proposed parental magma to the BUS, Marginal, Lower and Lower Critical Zones, zircon saturation is predicted to occur at 809 °C (TZr-W&H'83) or at 772 °C (TZr-B'13) after ca. 75% fractional crystallization of Opx (at <1338 °C), Chr (<1266 °C), Cpx (<1127 °C) and Pl (<1102 °C). Quartz (800 °C), Kfs and Ol (both 742 °C) either form together with zircon or afterwards. The resulting magma composition at zircon-in is (in wt.%): 73.75 SiO_2, 9.57 Al_2O_3, 2.7 CaO, 2.3 Na_2O and 4.5 K_2O. We note that modelling of equilibrium crystallization of B1 magma (but also all other magmas, not shown) results in zircon saturation at a higher temperature of 853 °C, but in a melt with a significantly lower SiO_2 content (SiO_2 = 68 wt.% at 800 °C); compared to fractional crystallization modelling (SiO_2 = 72 wt.% at 800 °C) – (see Fig. 4.11c).

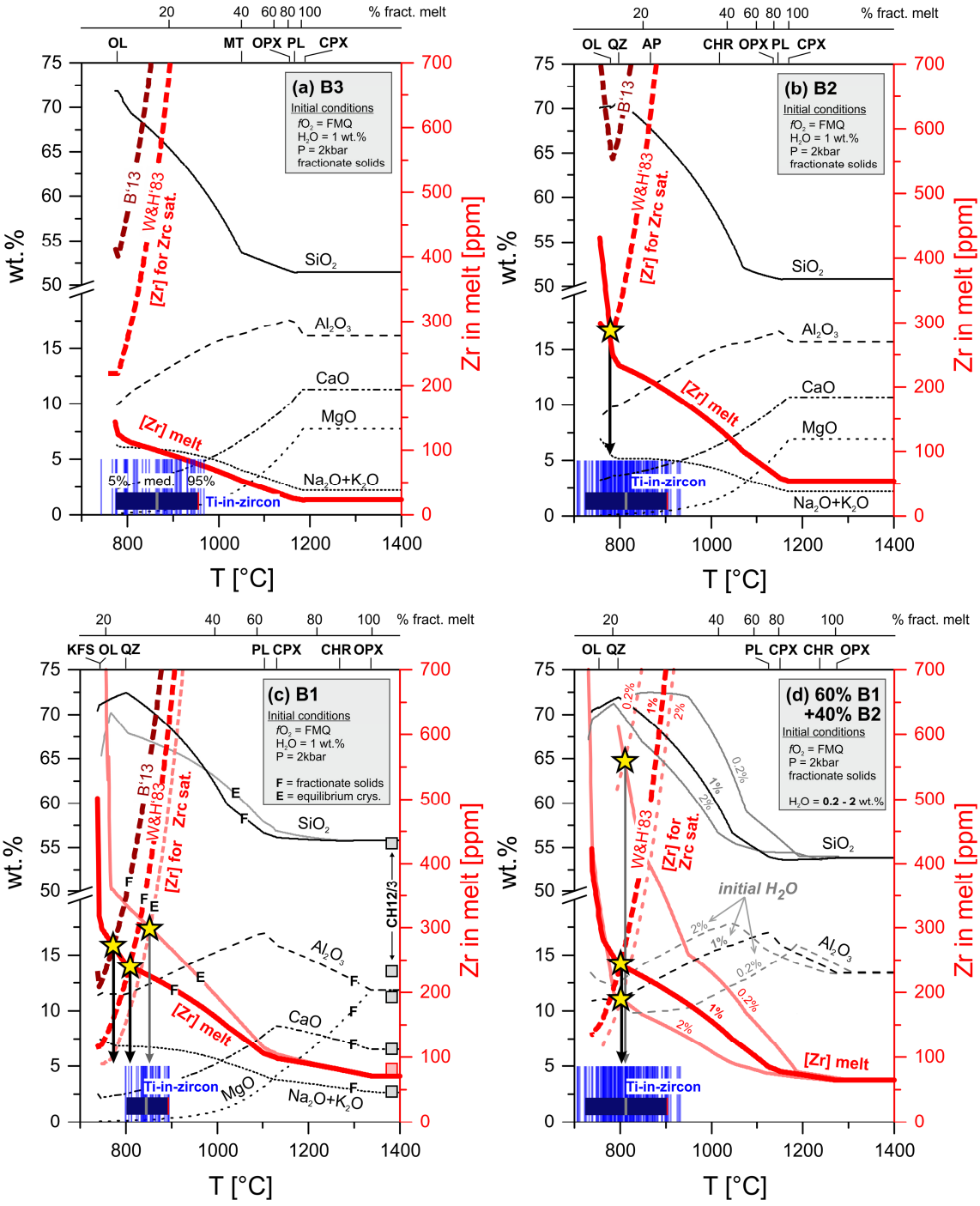

Figure 4.11 - Zircon saturation temperatures calculated for mafic cumulate rocks of the Rustenburg Layered Suite crystallized from parental magmas (a) B3, (b) B2 and (c) B1, as well as for (d) B1+B2 mixture (60:40) using rhyolite-MELTS (Gualda et al., 2012) in combination with zircon saturation geothermometers calibrated by Watson and Harrison (1983) ("W&H'83") and Boehnke et al. (2013) ("B'13"). Results of Ti-in-zircon thermometry calculated for $aTiO_2$ = 1.0 are shown for comparison (Ferry and Watson, 2007) with indicated median (med.), 5% and 95% percentiles (labelling as in a). (a) For B3 magma, which is typical for the Main Zone, no zircon saturation is modelled. (b-d) For parental magmas B1 and B2, and for B1+B2 mixtures, zircon saturation is achieved at >75% of fractional crystallization and at 800-820°C. Note that these temperatures are significantly lower than most obtained by Ti-in-zircon geothermometry on zircon grains from mafic rocks of the Marginal (in c), Critical (in b, d) and lower Main Zones (in a). Shown in (c) are modelling results carried out for equilibrium crystallization (labelled "E") and fractional crystallization (labelled "F") for comparison. Note that equilibrium crystallization causes zircon saturation at ca. 50 °C higher temperatures and a melt with ca. 5 wt.% lower SiO_2 contents compared to fractional crystallization modelling. In (d), the effect of different initial H_2O contents (0.2, 1.0 and 2.0 wt.%) on zircon saturation temperatures and melt evolution (exemplified by SiO_2 and Al_2O_3) is illustrated. The results indicate that variations in initial H_2O content have only little effect on zircon saturation temperature, but a major effect on melt composition. Mineral abbreviations as in Fig. 4.3.

P-T pseudosections were calculated with the aim to place constraints on the mineralogical evolution in intercumulus domains, which formed after a high degree of fractional crystallization (>75%), and commonly contain abundant amphibole and biotite, two hydrous minerals which are not well represented by rhyolite-MELTS. In addition, zircon-bearing phase assemblages were calculated for test purposes for felsic rocks, where zircon growth occurs at low degrees of fractional crystallization (≥20%). The P-T pseudosection calculated for felsic rocks explains the formation of zircon in assemblage with Ol-Cpx-Bt-Pl-Kfs-Qz-Mt-Ilm at 2 kbar and H_2O = 2.2 wt.% (Fig. 4.12a). Parity between observed and calculated Ol-bearing assemblages requires zircon formation at temperatures ≤860 °C (Fig. 4.12a), which is consistent with the results obtained above with rhyolite-MELTS (Fig. 4.10a).

Reasonable results were also obtained for felsic intercumulus domains formed in mafic rocks after ca. 75% of fractional crystallization of B1+B2 parental magmas. For sample PGMT (pegmatoidal pyroxenite from Merensky Reef), the P-T pseudosection indicates formation of Ti-rich Bt (TiO_2 = 3.89 mol.%) in an assemblage with Opx, Cpx, Amp, Qz, Rt and Mt (as observed together with zircon; see Fig. 4.3f-j) at ≤836 °C and 2 kbar (Fig. 4.12c-d), from a melt having 4% H_2O. At lower H_2O contents, the biotite-in reaction will occur at a somewhat higher temperature of 869 °C (for comparison see Figs. 4.12c and d). Notably, the position of the biotite-in reaction not only depends on H_2O content but also on bulk-rock composition. For example, biotite-in in sample CH12-3 occurs at 883 °C, compared to 836 °C in PGMT, both calculated for 2 kbar and 4% H_2O (Fig. 4.12b, d). The modelling results also reveal that Rt always represents an early phase during magma crystallization, that becomes partially or completely consumed after biotite-in (Fig. 4.12b-d). This is in agreement with petrographic observations, showing resorbed rutile surrounded by biotite (Fig. 4.3f).

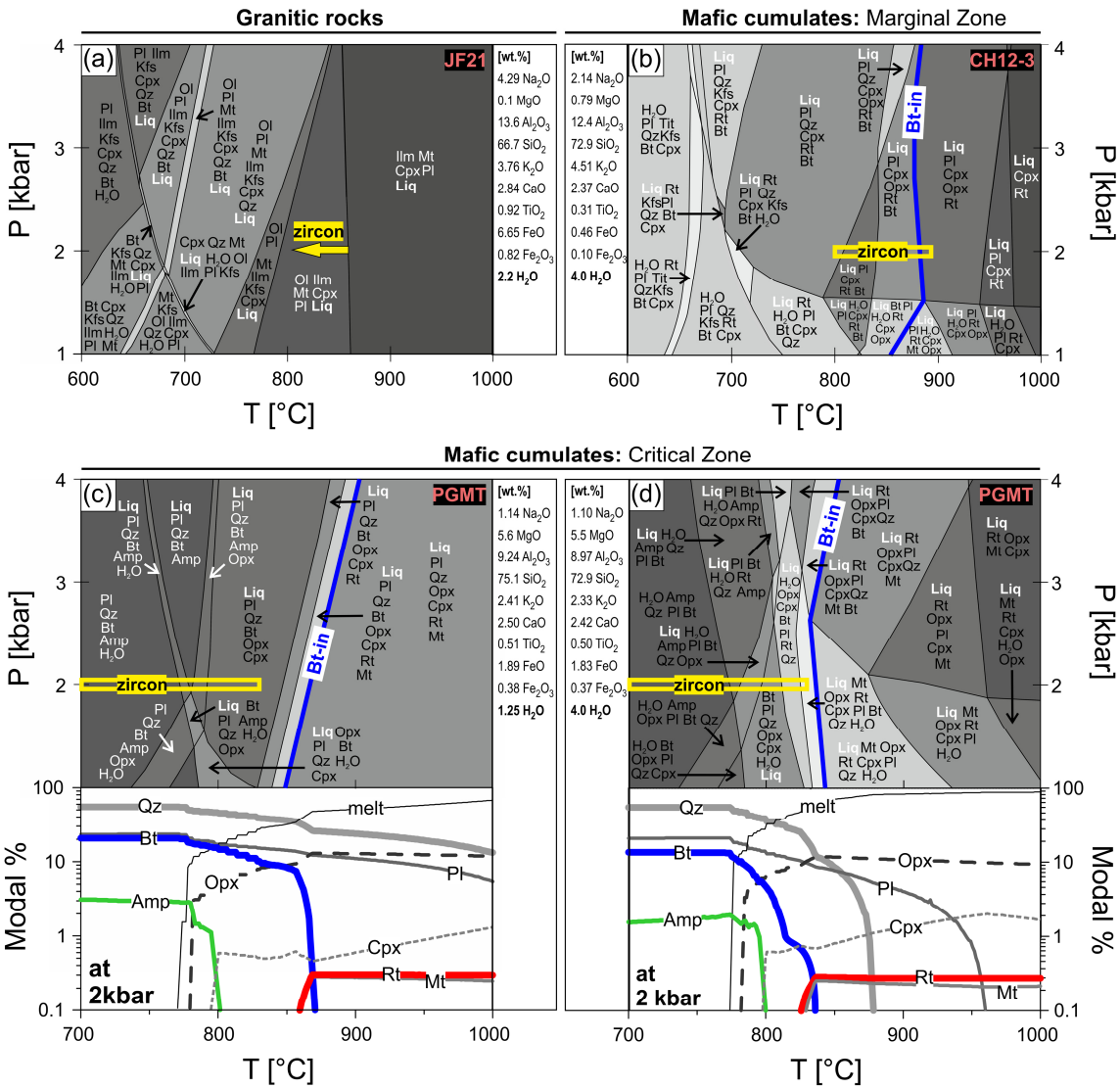

Figure 4.12 - P-T pseudosections calculated for (a) felsic rocks of the BC, and for (b-d) late magmatic intercumulus domains in Marginal Zone norite (b) and Critical Zone pyroxenite (c-d) using Perple_X (Conolly, 2009). For felsic rocks, agreement between modelled and observed mineral assemblages (Ol-Cpx-Pl-Mt-Ilm-Zrc; Fig. 4.3a) requires zircon crystallization at ≤860 °C at 1-3 kbar (yellow arrow). In Marginal Zone norite, zircon formation occurred at ≤881 °C at 2 kbar, as suggested by the position of the calculated Bt-in reaction and Bt inclusions observed in zircon grains of sample CH12-3 (Fig. 4.3j). These results are consistent with respective Ti-in-zircon temperatures (yellow bar). (c, d) P-T pseudosection calculated for sample PGMT at different H_2O contents of (c) 1.25 wt.% and (d) 4.0 wt.%. Both diagrams illustrate that Rt forms a stable phase at high temperatures, but becomes consumed during Bt-in reaction, which occurs at 840-880 °C dependent on the H_2O content. The position of the Bt-in reaction overlaps with the range of zircon crystallization temperatures obtained for all Critical Zone samples (667-962 °C) by Ti-in-zircon geothermometry, with sample PGMT (yellow bars in c and d) being an example where zircon growth exclusively occurred at temperatures below Bt-in, resulting in Trend 2 zoning. Rutile consumption during Bt growth is in agreement with petrographic observation (Fig. 4.3)

Table 4.4: Zircon crystallization temperature in different units of the BC derived by different methods

parental magma	TZr-WH83 [a] rMELTS [°C]	TZr-B13 [a] rMELTS [°C]		TZr-WH83 [b] BR [°C]	TZr-B13 [b] BR [°C]	T-Pupin [c] [°C]	Ti-in-zircon [d] [°C]
Felsic rocks							
JF21 felsic magma	880	836	**avg**	**856**	**822**	**900**	**859**
			max	882	865	900	935
			min	838	796	800	761
			n	*7*	*7*	*95*	*87*
Contact quartzite (metamorphic zircon rim)							
			avg			**850**	**865**
			max			900	891
			min			750	821
			n			*93*	*11*
UUMZ							
B3 *	no	no	**avg**	(648)	(559)	**850**	**846**
UUMZ **	no	no	max			900	968
UUMZ +15% felsic **	810	744	min			750	742
UUMZ +25% felsic **	841	790	*n*			*279*	*148*
Critical Zone							
B1+B2 mix (60:40) *	800	760	**avg**	(505)	(404)	**800**	**850**
B2 *	779	no	max			700	962
			min			850	666
			n			*10*	*610*
Marginal Zone							
B1 *	808	772	**avg**	(542)	(451)	**850**	**847**
			max			900	941
			min			750	686
			n			*67*	*83*
BUS							
B1 *	808	772	**avg**	(559)	(465)	sub-/anhedral	**752**
UM ***	754	no	max				805
			min				683
			n				*41*

avg=average; max=maximum value; min=minimum value; n=number. Parental magmas and magma mixtures suggested by
* Barnes et al. (2010), **VanTongeren et al. (2010) and *** Wilson (2015).
[a] Zircon saturation temperatures obtained by fractional crystallization modelling using rhyolite-MELTS (rMELTS) in combination with the zircon saturation models after Watson and Harrison (1983) (TZr-WH83) and Boehnke et al. (2013) (TZr-B13)
[b] Zircon saturation temperatures calculated from bulk rock compositions (BR) using TZr-WH83 and TZr-B13
[c] Temperature obtained from crystal morphology using the classification scheme of Pupin (1980)
[d] Ti-in-zircon temperature after Ferry and Watson (2007), values for felsic rocks, contact quartzite and UUMZ calculated using $a\mathrm{TiO_2}$ = 0.3 (obtained by rhyolite-MELTS).

Table 4.5: Average zircon trace element composition and Ti-in-zircon temperatures

Sample	*n*	Ti	La	Lu	Nb	Hf	Th	U	ΣREE	Nb/Ta	Th/U	Ti-in-Zrc [°C] [b]		
		[ppm]	[ppm]	[ppm]	[ppm]	[ppm]	[ppm]	[ppm]	[ppm]			med	min	max
Lebowa Granite														
JF9	21	8.6	2.33	48.7	3.6	8123	83	187	642	2.8	0.45	854*	831*	879*
MOK-1	10	8.1	1.26	56.6	2.2	11410	122	194	828	1.6	0.63	852*	796*	890*
MOK-2	19	10.7	1.67	48.8	2.9	8297	105	171	735	2.1	0.62	859*	816*	874*
Rashoop Granophyre														
JF7	13	7.8	0.24	31.8	2.2	8190	41	111	367	3.2	0.36	838*	825*	872*
Grano1	12	12.2	4.14	45.7	4.2	8720	99	269	615	2.7	0.40	900*	849*	923*
JF22	12	9.8	1.09	48.6	2.3	10041	113	201	717	1.5	0.60	867*	761*	935*
Contact quartzite														
JF1a (rim) [c]	11	10.7	0.74	34.2	2.0	9288	45	113	409	3.3	0.50	871*	821*	891*
RLS - Upper Zone														
JF5	53	7.2	0.03	51.8	1.9	8177	77	164	662	3.3	0.46	837*	804*	856*
JF23	18	11.2	0.35	39.5	1.3	7696	87	140	560	1.7	0.60	859*	805*	915*
UZ3	35	8.0	0.19	72.4	4.8	9411	133	228	894	2.5	0.57	844*	796*	891*
MH1	6	7.1	0.10	55.8	5.6	7840	90	169	836	3.9	0.53	832*	811*	865*
RLS - Main Zone														
SB-139	21	9.1	1.41	62.9	1.0	11249	189	303	773	1.4	0.64	799*	742*	968*
SB-110	11	13.9	0.25	19.6	0.5	9536	285	318	247	2.0	0.91	908*	863*	960*
SB-142	4	7.0	0.12	22.8	0.4	9694	479	454	273	2.1	1.08	828*	819*	848*
SBBH01	18	39.3	0.27	29.4	1.2	10633	441	303	580	1.2	1.41	895	877	943
GC	23	21.3	0.01	20.3	4.1	8141	171	107	313	4.7	3.21	820	720	888
PR-1	48	44.6	0.06	12.4	0.7	10381	329	108	213	2.5	3.64	910	809	978
RLS - Critical Zone														
HW-NRT	21	35.1	0.04	16.7	2.8	8206	305	301	252	9.1	1.14	877	859	912
MR-B	58	19.5	0.01	17.6	1.0	9845	265	53	261	1.9	7.55	815	666	879
MR-WL-1	75	21.1	0.06	21.7	1.1	9562	167	89	358	1.5	2.11	817	732	876
PGMT	47	13.6	0.02	21.0	3.3	8844	187	118	276	5.4	2.36	767	673	830
FW-PX	12	19.6	0.03	23.4	3.3	8211	236	262	311	4.7	1.40	809	764	861
FW-NRT	12	37.1	0.04	15.4	2.3	8083	274	308	225	5.5	0.89	894	743	932
WHK	20	21.2	0.02	23.8	3.0	7736	285	369	321	5.0	0.80	825	798	850
UG2K	95	28.6	0.02	11.6	2.3	10090	119	87	198	2.6	1.60	856	732	927
UG2a	53	36.7	0.08	19.5	2.9	9481	230	109	407	2.8	3.50	885	818	931
UG2b	13	50.0	0.03	15.6	2.3	9076	250	53	291	3.0	5.09	916	877	953
UG2M	52	36.6	0.15	14.5	2.4	10240	279	145	285	1.6	3.91	878	833	962
MG7	70	20.1	0.06	20.2	1.9	9570	136	56	295	2.9	5.71	820	769	849
LG6	37	19.4	0.06	12.6	2.1	8036	105	134	188	2.9	0.77	812	780	839
JGL	9	19.6	0.14	15.5	8.0	8258	370	361	322	3.0	0.99	808	789	849
CH-12-1	8	21.4	0.23	12.8	2.0	9440	325	293	242	1.9	1.10	821	804	846
RLS - Marginal Zone														
CH12-3	42	28.1	0.11	37.4	1.0	10400	120	107	555	1.9	1.13	846	799	894
CH12-7	9	40.2	0.05	17.7	0.9	7467	107	88	300	1.9	1.34	909	686	941
CH12-26	10	23.8	0.05	31.0	1.2	8945	131	125	455	2.3	1.05	833	786	854
CH12-8	7	22.3	0.76	20.3	1.6	8066	390	386	293	2.1	1.04	803	761	913
CH12-9	15	25.0	0.05	16.4	1.0	8483	144	122	276	2.3	1.16	842	794	866
RLS - Basal Ultramafic Sequence drillcore (BUS)														
CH7-15A	5	13.8	0.09	15.7	2.7	6134	202	132	232	3.3	1.52	788	783	801
CH7-143A	13	11.4	0.03	13.8	1.9	9135	185	83	204	5.0	3.59	755	719	804
CH7-164	23	10.1	0.12	26.5	2.0	8050	394	172	438	4.8	2.76	744	683	805

Given are mean trace element contents and ratios. The complete dataset is given in the supplementary materials

[a] normalization to chondrite using values of McDonough and Sun (1995)

[b] Ti-in-zircon temperatures after Ferry and Watson (2007); *calculated using $a\mathrm{TiO_2}$=0.3 for rutile-free samples, med=median; min=minimum value; max=maximum value

[c] only trace element compositions of metamorphic overgrowths on detrital zircon cores

4.4 Discussion

4.4.1 Zircon crystallization temperatures

The results of this study indicate that zircon crystallization temperatures for different rock types throughout the BC stratigraphy are very similar and average at ca. 850 ±30 °C, irrespective of applying different thermometric methods. These methods are either based on bulk rock compositions (i.e. zircon saturation temperatures and thermodynamic modelling) or on the composition and shapes of individual zircon grains (i.e. Ti-in-zircon and zircon morphology geothermometry) - (Table 4.4).

For Rt-Qz-bearing mafic rocks below the Pyroxenite Marker of the BC (BUS to lower Main Zone), Ti-in-zircon thermometry provides a robust method to obtain zircon crystallization temperatures, as SiO_2 and TiO_2 are both buffered during zircon growth ($a SiO_2 = a TiO_2 = 1$). However, for Rt-free, Ilm-Mt-Ttn-bearing granites and mafic rocks of the upper Main and Upper Zones, $a TiO_2$ is significantly lower than 1.0. During this study, an average of $a TiO_2 = 0.3$ was obtained for these rocks by using the method proposed by Schiller and Finger (2019) resulting in temperatures of 742-962 °C (mean: 851 °C) when applied to the Ti-in-zircon geothermometer of Ferry and Watson (2007). These temperatures overlap with those obtained for Rt-bearing mafic rocks below the Pyroxenite Marker (743-920 °C; mean: 835 °C), but are ca. 70 °C higher (on average) than those previously calculated by Ver Hoeve et al. (2018) for zircons in the Rt-free rocks of the BC. This discrepancy mainly arises from the fact that Ver Hoeve et al. (2018) calculated all temperatures with $a TiO_2 = 0.7$, a value that is commonly used in the literature for Rt-free igneous rocks (for detailed discussions see Hayden and Watson, 2007, Fu et al., 2008, Grimes et al., 2009). However, this value is obviously much too high, in particular for zircon in Rt-free granites, as has been demonstrated recently by Schiller and Finger (2019). We note, that by applying the method of Schiller and Finger (2019) to the rocks of the BC, we not only get overlapping Ti-in-zircon temperatures throughout the stratigraphy of the BC (comprising all Rt-bearing and Rt-free rocks), but also consistent results by applying different independent geothermometric methods to individual rocks (Table 4.4).

For felsic rocks of the BC, we get Ti-in-zircon temperatures of 742-962 °C (mean: 851 °C; all calculated for $a TiO_2 = 0.3$), which overlap with those obtained by (i) bulk-rock zircon saturation thermometry (838-882 °C using TZr-WH'83; 786-867 °C using TZr-B'13), (ii) zircon morphology thermometry (900-800 °C; see Pupin scheme in Fig. 4.4), as well as by (iii) rhyolite-MELTS modelling, suggesting start of zircon crystallization at <881 °C (TZr-WH83) or at <836 °C (TZr-B13; Fig. 4.10), and (iv) by Perple_X modelling pointing to zircon growth in assemblages with Ol-Ilm-Mt-Cpx-Pl at ≤860 °C (Fig. 4.12a). The results further suggest that temperatures obtained from zircon morphologies according to Pupin's scheme are accurate (within error of method), and that the zircon prism ratio {100} : {110} is mainly controlled by temperature, as suggested by Pupin (1980), and to much less extent by other parameters such as

zircon supersaturation and/or the HFSE concentration of the melt, as postulated by Vavra (1990) and Benisek and Finger (1993), respectively. This conclusion is supported by the observation that zircon populations with identical morphologies are found in rocks of highly different bulk rock compositions within a single outcrop of a few meters size at the roof of the RLS, comprising the samples JF5 and JF23 (ferrodiorites), JF1a (quartzite) and JF7 (Rashoop granophyre) - (Fig. 4.4).

In mafic rocks beneath the Pyroxenite Marker, zircon is formed together with both Qz and Rt (locally forming inclusions in zircon). For these rocks, Ti-in-zircon thermometry yields a wide range in temperatures from 690 to 962 °C, indicating zircon growth during an extensive period of magma cooling. This is also reflected by pronounced compositional zoning, e.g. systematic changes in Ti, U, Th contents from core to rim (Fig. 4.9e-p), as well as by great diversity in zircon morphology (Fig. 4.4f-i). For example, zircon morphologies in sample CH12-3 (Fig. 4.4g) point to a wide range in temperature from 750 to 900 °C, overlapping with the results obtained by Ti-in-zircon thermometry ranging from 799 to 894 °C (Fig. 4.6, Table 4.5). In contrast, zircon crystallization temperatures modelled using rhyolite-MELTS for B1 and B2 magmas (and mixtures between them) never exceed 810 °C and therefore are about 100 °C lower than the highest temperatures obtained by Ti-in-zircon thermometry (Fig. 4.11b-d). There are two possible explanations to account for this discrepancy. The first considers that the used modelling parameters, including activity models for solid-solutions are oversimplified. As mentioned by Gualda et al. (2012), rhyolite-MELTS lacks appropriate activity models for hydrous phases like amphibole and biotite. These phases occur abundantly intergrown with zircon (Fig. 4.3), and have relatively high partition coefficients for Zr (Table S4). However, in modelling results obtained by rhyolite-MELTS, amphibole is always absent and biotite modes are much lower than observed. Furthermore, some assumptions have to be made for fO_2 and initial H_2O contents of the parental magma. In particular, the amount of H_2O is crucial and has a great influence on the composition of the evolving melt, e.g. a higher amount of H_2O causes a higher SiO_2 content at a given temperature, as is illustrated in Figure 4.11d. We also note that pure fractional crystallization, as considered in our models, may not represent reality during crystallization of the BC. Although fractional crystallization is indicated by the cumulate character of all investigated rocks and by the occurrence of zoned plagioclase (e.g. in Marginal Zone norite CH12-3), some equilibrium crystallization component was possibly present, as is reflected by the fact that mafic minerals (Opx, Cpx, Ol) in most rocks of the BC are unzoned (except in the deepest part of the BUS: see Wilson et al., 2017). We note, that for the B1 parental magma (Fig. 4.11c), but also for B1 + B2 mixture (not shown), equilibrium crystallization results in zircon saturation at ca. 50 °C higher temperatures (853 °C) compared to fractional crystallization (810 °C), and agree better with calculated Ti-in-zircon temperatures of $T_{Ti\text{-}Zrc}$ = 799-894 °C.The second explanation is related to the evolution of the BC magma

chamber, which was not formed by single-stage fractional crystallization of parental magma (B1 or B2), but by the development of cyclic units resulting from ingression of repeated pulses of parental magma into an evolving magma chamber (for example see Wilson et al., 2017), already containing resident magma enriched in incompatible trace elements like Zr. Consequently, the mixed magma will have higher Zr contents than the parental magma, and therefore will reach zircon saturation at higher temperatures. In order to achieve parity between Ti-in-zircon and modelled zircon saturation temperatures, the Zr content of the (parental-resident) magma mix must have been ca. 150 ppm. In case of incomplete mixing, perhaps due to viscosity differences of compositionally different magmas, the situation would be even more complex. In evolved magma domains, zircon growth would occur earlier (i.e. at higher temperatures) than in more primitive domains. Furthermore, it is possible that zircon grains were formed in unconnected intercumulus melt pockets, which evolved independently from each other, in a similar way to that described for titanite in a granodiorite cumulate from the Matok Pluton (South Africa) by Laurent et al. (2017).

According to our modelling results, cumulate rocks formed from B3 or UUMZ parental magmas (i.e. all rocks above the Pyroxenite Marker) should be devoid of zircon. Their abundant occurrence can be explained by three different processes, which can interfere with each other. First, zircon formation can result from mixing between parental and evolved resident magma, as discussed in the previous section. Second, it was achieved by unmixing of UUMZ parental magma, into a Zr-poor mafic magma, which contributed to the formation of the Fe-rich cumulate rocks of the Upper Zone, and a Zr-rich felsic magma, which segregated and lead to the formation of the Rashoop Granophyres (see detailed discussion in VanTongeren et al. (2010) and Fischer et al. (2016)). Unmixing, however, cannot account for zircon growth in the Main Zone gabbronorites, which were likely formed from B3 parental magma. It must be noted that no zircons were found to date in Main Zone rocks of the Eastern and Western limbs of the BC, but in those of the Southern limb (samples SB-139, SB-110, SB-142, SBBH01 in this study). These gabbros have relatively high Zr contents which are explained by Lundgaard et al. (2006) to result from a higher amount of trapped intercumulus melt. Third, it is likely that zircon grains crystallized from assimilated felsic melts, which became admixed during periodic (turbulent) ingression of parental mafic magma into the roof zone of the BC. These felsic melts perhaps formed a permanent layer on top of the evolving RLS magma chamber resulting originally from re-melting of overlying Rooiberg Group felsites (see Walraven (1985, 1987). The third process could also provide a reasonable explanation for the striking similarity in zircon morphology, trace element contents (Ti, ΣREE, Th/U), and melt inclusion assemblages (Qz, Kfs, Pl, Bt), of all zircon populations found in mafic cumulate rocks above the Pyroxenite Marker and in overlying granitic rocks (Figs. 4.4, 4.6), requiring similar physicochemical conditions during

zircon crystallization. The third process is also consistent with the observation that the bulk rock compositions of Upper Zone rocks plot closest to felsic rocks in a Zr vs. ΣREE plot (Fig. 4.2b).

4.4.2 Reasons for zircon zoning

Zircons in Rt-bearing cumulate rocks of the BC commonly show pronounced zoning in Ti (8-60 ppm), U (5-300 ppm), Th/U (0.5-24) and Nb/Ta (0.15-18), but only minor zoning in all felsic and Rt-free mafic rocks (UUMZ). While Ti zoning reflects changing temperatures during zircon growth, the other trace elements are mainly controlled by mineral/melt partition coefficients of zircon and other coexistent phases. Based on our modelling, fundamental differences between felsic and Rt-bearing mafic rocks mainly result from two overlapping effects: (i) the degree of fractional crystallization of the parental magma, and (ii) changing mineral assemblages during zircon growth. Both effects control the zircon/melt and zircon/solid ratios (solid = sum of all phases crystallizing together with zircon), as well as the amount and local distribution of TE in the melt at each stage of differentiation. In this context, it must be considered that zircon preferentially incorporates elements like Hf, U, Th, Nb, Ta (Table S4), which are incompatible in most rock-forming minerals (Ol, Opx, Cpx, Amp, Pl, Kfs, Chr, Mt, Qz), which were formed either prior to, or in competition with zircon. The only exceptions are biotite, which can fractionate Nb from Ta (Stepanov and Hermann, 2013), and accessory phases like Tit, Thr, monazite (Mnz), Ap, and Rt, which occur in variable amounts in some of the investigated samples (Table 4.3).

For felsic rocks of the BC, thermodynamic modelling indicates zircon formation started at a relatively low degree of fractional crystallization of ≥20%, i.e. at low zircon/melt and during a period of strongly changing zircon/solid ratio. Therefore, depletion of U, Th, Nb and Ta in the evolving melt due to zircon growth was largely compensated by the contemporaneous crystallization of abundant rock-forming minerals (Rubatto and Hermann, 2007). This interpretation is supported by observed mineral assemblages in the investigated felsic rocks (Fig. 4.3a-d), inclusions in zircon (Table 4.3), as well as by modelling results, showing that at low zircon/solid ratios, U, Th contents as well as Th/U and Nb/Ta ratios remain relatively constant during the entire period of zircon crystallization between 935 and 700 °C (Fig. 4.13a-e). The modelling also shows that the absolute amount of trace elements and the Th/U ratio in zircon can vary among samples and domains, depending on the (i) initial magma composition, (ii) zircon/solid and zircon/melt ratios (Fig. 4.13), and (iii) the amount of other accessory phases like Thr, Mnz, Tit, and/or Ap. The effect of competitive Zrc + Thr formation on the Th/U ratio is shown in Figure 4.13a-e, where Th/U ratios slightly decrease towards zircon rims in Thr-bearing assemblages, but increase in the absence of Thr. Early formation of Ap and Tit, as suggested by petrographic observations (e.g. Fig. 4.3b, c), causes a decrease of U and Th contents in the melt, but only has a very minor effect on Th/U and Nb/Ta ratios (Fig. 4.13a,b, c).

Both phases are however required to account for the observed U contents of ca. 100-200 ppm in zircon cores in granitic rocks crystallizing from a parental magma with ~6 ppm U (Fig. 4.13c).

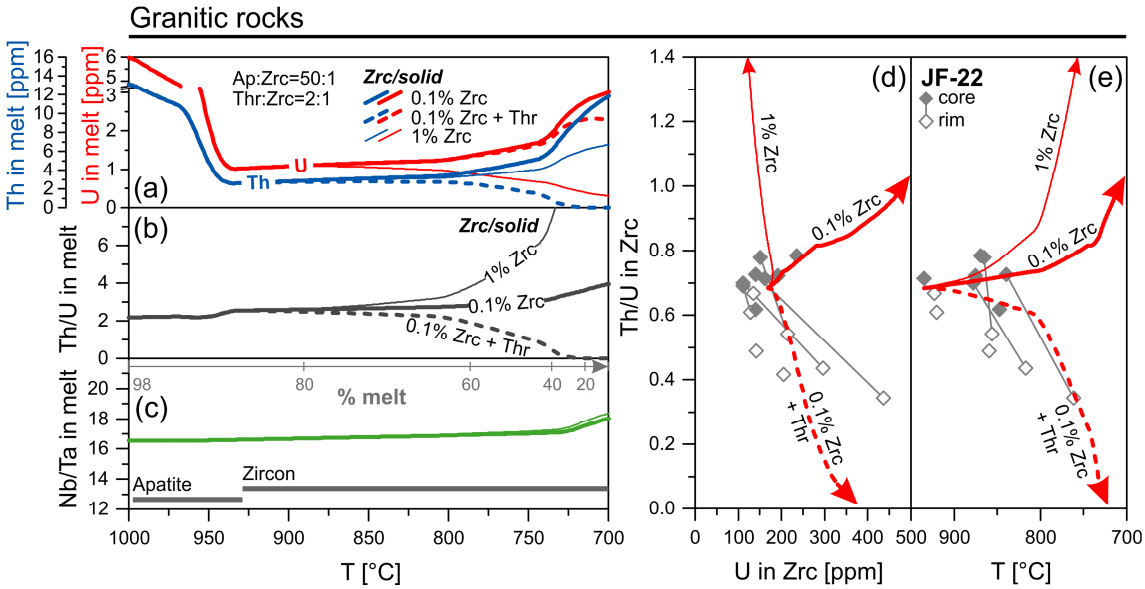

Figure 4.13 - Evolution of Th, U contents and Nb/Ta in melt and corresponding zircon during fractional crystallization of felsic magmas of the BC between 1000 and 700°C modelled with rhyolite-MELTS (for details see Fig. 4.10a). The modelling considers different fractions of zircon relative to other solid phases predicted by rhyolite-MELTS (range of zircon/solid ratio: 0.1-1 %), and the incremental crystallization of accessory Ap and Thr, at fixed Ap:Zrc (50:1) and Thr:Zrc (2:1) ratios. Th, U, Nb and Ta concentrations were calculated using published partition coefficients (Table S4). The modelling results indicate that zircon with high Th/U ratios and pronounced Th/U zoning can be formed only if the zircon/solid ratio is >>1%, and that the Nb/Ta ratio of melt (and zircon) remains nearly constant. Parity between modelled and observed zircon zoning (grey diamonds and dotted arrow in c-d) is reached if abundant apatite is formed prior to zircon crystallization, which occurs between 935 and 700°C at a low zircon/solid ratio <0.1 %, and in equilibrium with thorite. These results are in agreement with observed apatite inclusions in zircon and matrix thorite (Fig. 4.3).

Zircon in Rt-bearing mafic cumulate rocks below the Pyroxenite Marker was formed after high degrees of fractional crystallization of >75%, causing high zircon/melt and zircon/solid ratios. Under such conditions, competitive crystallization of rock-forming minerals will be unable to compensate the TE-depletion caused by zircon growth, with the consequence that the evolving melt becomes successively depleted in zircon-compatible TE (similar to Rayleigh fractionation). Consequently, the degree of depletion is mainly controlled by zircon/melt partition coefficients, which are significantly different for the zircon-compatible trace elements (Table S4). In this context, it must be noted that all investigated cumulate rocks contain Rt, which can incorporate high contents of U, Nb and Ta, but expels Th (Klemme et al., 2005; Rubatto and Hermann, 2007). Furthermore, our textural observations and modelling results indicate that Rt was formed prior to, but also together with zircon and became consumed during the formation of Ti-rich Bt at T < 900 °C (Figs. 4.3f, 4.12b-c). In summary, the results of modelling and petrographic observations suggest that zircon zoning in Rt-Bt-bearing mafic cumulate rocks is strongly dependent on zircon/solid ratios and the crystallization sequence of the three minerals Rt, Zrc, and Bt during cooling.

The high-Ti zoning trend (Trend 1 in Fig. 4.9), which is characterized by a significant decrease in Th and U contents at increasing Th/U ratios (from 0.5 to 24) from core to rim, can be explained by TE fractionation due to zircon growth without Rt and Bt. As shown in Fig. 4.14 a-d, the strongly curved increase in Th/U during U decrease (Fig. 4.9f, j) results from the ca. 7-fold higher zircon/melt partition coefficient of U compared to Th (Table S4). Here we note that very similar zircon zoning trends will also be formed, if zircon is formed together with Rt. Here, the zircon zoning trend would essentially be the same up to Rt/Zrc = 5.

The low-Ti zoning trend (Trend 2 in Fig. 4.9), which is characterized by increasing U and Nb contents at decreasing Th/U (24 to 1) and Nb/Ta ratios (18 to 0.15) from core to rim, requires that abundant Rt was formed prior to Zrc and Bt, but consumed during subsequent Zrc growth in the assemblage with Bt, i.e. after the onset of the Bt-in reaction. Early Rt formation caused a significant U depletion of the melt, resulting in high Th/U. This process can account for the high Th/U ratios up to 24 in zircon cores observed in samples PGMT and MG7, which only reveal Trend 2 (Fig. 4.9n, Table S1). Subsequent Rt breakdown during Zrc and Bt formation, causes the release of abundant U, Nb and Ta (in addition to Zr), leading to the observed increase in these elements towards zircon rims, and the significant decrease in Th/U (Fig. 4.14 e-h). The decrease in Nb/Ta can be explained by the higher compatibility of Nb compared to Ta in Bt (see partition coefficients in Table S4).

The occurrence of both Trend 1 and Trend 2 in a few samples, e.g. UG2K and MR-B (Fig. 4.9e-l) can be explained by continuous zircon growth in sequential assemblages (i) Zrc + Rt + melt followed by (ii) Zrc + Rt +Bt + melt. The prevalence of samples with Trend 2 in the BC (Fig. 4.6) suggests that zircon growth mostly occurred in biotite-bearing assemblages at T<880 °C (e.g. Fig. 4.12d). The lack of any pronounced zircon Th/U zoning in some samples (e.g. WHK, JGL) is most likely caused by (i) mass balance constraints, comprising low amounts of Rt and Zrc prior to Bt-in reaction, or (ii) by the early appearance of Bt causing abundant Rt consumption prior to Zrc growth. As shown in the P-T pseudosections in Figure 4.12b-d, the Bt-in reaction does not occur at a fixed temperature, but varies between ca. 880 and 820 °C (at 2 kbar), dependent on bulk-rock composition and H_2O content.

In summary, our results show that zircon grains with very different zoning trends, (from unzoned to highly zoned), can all be formed in restricted intercumulus domains, at nearly closed-system conditions. They further demonstrate that the development of extreme Th/U ratios, and of opposite zoning trends requires neither the influx of melts from external sources (Yudovskaya et al., 2013; Zeh et al., 2015), nor the selective removal of U by oxidized, chlorine-rich fluids as suggested by Ver Hoeve et al. (2018). Instead, it can result from the complex interaction of the minerals Zrc, Rt and Bt during magma cooling within small intercumulus melt domains.

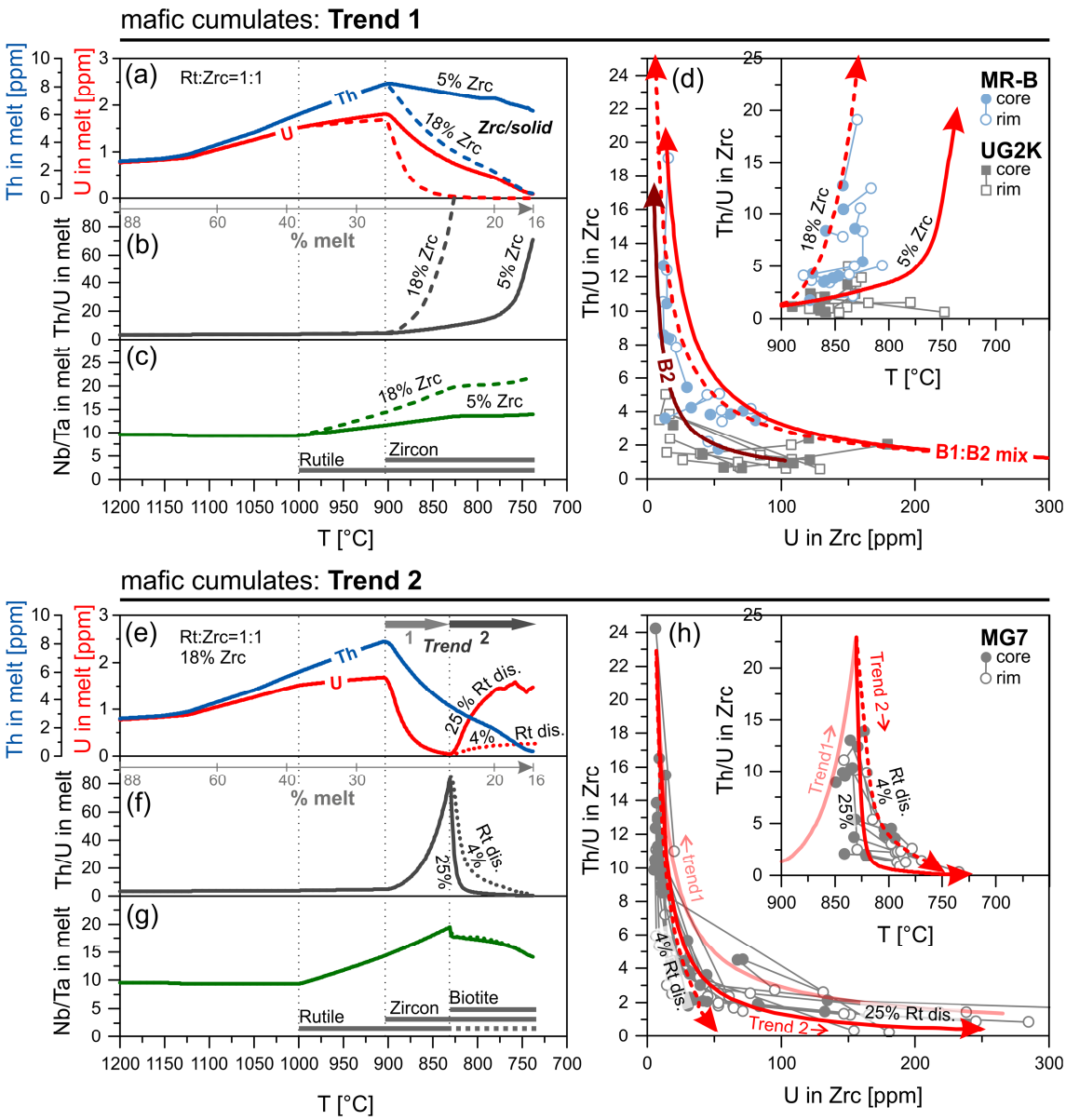

Figure 4.14 - Evolution of Th, U contents and Th/U and Nb/Ta ratios in melt and corresponding zircon during fractional crystallization of mafic parental magmas of the BC between 1200 and 700 °C modelled with rhyolite-MELTS (for details see Fig. 4.11), and designed to explain zoning Trends1(a-d) and Trend 2 (e-h) shown in Fig. 4.9. The modelling considers different fractions of zircon relative to other solid phases predicted by rhyolite-MELTS (range of zircon/solid ratio: 5-18 %), the incremental crystallization of accessory Rt + Zrc (in a-d), and of Zrc + Rt + Bt (in e-h) at fixed Rt : Zrc (1:1), and different degrees of Rt dissolution (4-25 % Rt dis.) during biotite growth (dotted lines in e-h). In (d) variations resulting from different parental magmas (pure B2 and 60:40 B1 + B2 mixture) on zircon zoning is additionally illustrated. (a-d) Zircon with zoning Trend 1 can be formed in intercumulus domains characterized by high zircon/solid ratios (>5%), where zircon crystallizes either alone (not shown) or in assemblage with rutile, causing successive depletion of the melt in U and Th, accompanied by a significant increase in Th/U and Nb/Ta ratios, independent on the parental magma composition. (e-h) With Bt-in reaction, the zircon zoning Trend 1 becomes reversed (Trend 2), due to the breakdown of early rutile accompanied by the release of abundant U, Nb and Ta, resulting in a decrease in Th/U towards zircon rims (h), along with increasing Nb, Ta contents (see Fig. 4.9) and decreasing Nb/Ta ratios (g). The composition of assimilated rutile (0.023 ppm Th; 35 ppm U, 8200 ppm Nb, 465 ppm Ta) is the average for high-T rutile of the Merensky Reef presented by Ver Hoeve et al. (2018).

4.5 Conclusions

1) Zircon occurs abundantly in felsic and mafic rocks of all stratigraphic units of the BC, including mafic rocks of the Main and Upper Zones which, according to thermodynamic modelling based on B3 and UUMZ parental magma compositions, should be zircon-free.

2) The occurrence of zircon in mafic rocks of the Main and Upper Zones most likely results from admixing of felsic melts during periodic parental magma ingression into a stratified magma chamber, as suggested by zircon morphologies and TE contents (ΣREE, Ti), and ratios (Th/U), which are identical to those in overlying granitic rocks (Rashoop Granophyre and Lebowa Granite), as well as by bulk rock compositions.

3) Zircons in Rt-bearing mafic cumulates below the Pyroxenite Marker, show significantly lower ΣREE, higher Ti, and commonly higher and more variable Th/U ratios than in Rt-free mafic and felsic rocks above it. Based on petrographic observations in conjunction with thermodynamic modelling, these zircons were formed in intercumulus domains after high degrees of fractional crystallization of ≥75% formed from B1 and B2 parental magmas. This is in contrast to zircon in all felsic rocks, which was formed after relatively low degrees of fractional crystallization of ≥20%.

4) Zircon in Rt-bearing mafic cumulates was formed during cooling from 962 to 690 °C peaking at 850 °C, as indicated by Ti-in-zircon temperatures and zircon morphologies. These temperatures are commonly much higher than those obtained by rhyolite-MELTS modelling (≤810 °C), either due to oversimplified system parameters and/or the effect that the cumulate rocks did not form directly from B1 or B2 magmas, but from variable mixtures of parental magmas with evolved resident magma.

5) Zircon formation temperatures estimated for all felsic rocks by zircon saturation thermometry, zircon morphology classification and rhyolite-MELTS modelling, are at 900-800 °C, and agree well with those obtained by Ti-in-zircon thermometry (averaging between 838 and 900 °C) using a very reduced $a\mathrm{TiO_2}$ of 0.3, estimated by using the method of Schiller and Finger (2019).

6) Significant differences in compositional zoning of zircon (Ti, Th, U, Nb, Ta) in mafic and felsic rocks mainly result from (i) distinct zircon/melt ratios, (ii) changes in mineral assemblage during cooling, and (iii) different zircon/melt partition coefficients.

7) The absence of any pronounced Th/U and Nb/Ta zoning of zircon in felsic rocks can be explained by low zircon/melt ratios, causing that fractionation due to zircon growth is compensated by coeval crystallization of abundant rock-forming minerals having all very low partition coefficients for Th, U, Nb and Ta.

8) Highly variable Th/U and Nb/Ta zoning of zircon in many mafic rocks derived from B1 and B2 parental magmas is mainly controlled by zircon growth in assemblage with rutile and/or biotite in restricted intercumulus domains at high zircon/melt ratios.

9) Extreme Th/U ratios, and increasing Th/U with decreasing U contents from core to rim (zoning trend 1), can be explained by Rayleigh-like fractionation during zircon growth, with or without Rt. This trend is reversed after Rt-breakdown during biotite-in reaction, causing U release, but also the fractionation of Nb from Ta during biotite growth (zoning trend 2).

Acknowledgements

DG and AZ thank the Deutsche Forschungsgemeinschaft (DFG grant ZE 424/12-1), and Linda Marko (University Frankfurt am Main, Germany) for support with sample preparation and LA-ICP-MS analyses. All authors are also indebted to late Joe Aphanane (University of the Witwatersrand) for zircon separation and preparation, David Schiller (Salzburg University, Austria) for support during thermodynamic modelling as well as to Samancor Chrome and Bokoni Platinum Mine Proprietary Ltd. for support during sampling.

5. Zircon melt inclusions in mafic and felsic rocks of the Bushveld Complex - constraints for zircon crystallization temperatures and partitioning coefficients

Dominik Gudelius[1], Armin Zeh[1,2], Renat. R. Almeev[3], Allan. H. Wilson[4], Lennart A. Fischer[5], Axel. K. Schmitt[6]

[1] Karlsruhe Institute for Technology, Institute for Applied Geosciences, Adenauerring 20b, 76131 Karlsruhe, Germany

[2] Frankfurt Isotope and Element Research Center (FIERCE), Altenhöferallee 1, D-60438 Frankfurt, Germany

[3] Leibniz University Hannover, Institute of Mineralogy, Callinstraße 3, 30167 Hannover, Germany

[4] University of the Witwatersrand, School of Geosciences, South Africa, 2050 Johannesburg, South Africa

[5] Albert-Ludwig University, Institute of Earth and Environmental Sciences, Albertstraße 23b, 79104 Freiburg, Germany

[6] Heidelberg University, Institute of Earth Sciences, Im Neuenheimer Feld 236, 69120 Heidelberg, Germany

Geochimica et Cosmochimica Acta (submitted 05/2020)

Abstract

Melt inclusions in zircon represent time capsules, which allow detailed information about the physicochemical conditions during magma crystallization. In this study, new mineralogical and chemical data are presented from recrystallized and homogenized melt inclusions and host zircon from different mafic and felsic rocks of the Bushveld Complex (BC), South Africa. Samples cover rutile-bearing cumulate rocks of the Marginal and Critical zones, as well as rutile-free, magnetite-ilmenite-titanite-bearing diorites and granites of the Upper Zone, Rashoop Granophyre and Lebowa Granite Suite. Mineral assemblages in recrystallized melt inclusions in all samples comprise quartz, alkali feldspar, albite-rich plagioclase and muscovite, and more rarely amphibole, rutile, fluorite, barite, apatite, monazite, zircon daughter crystals and hydrous fluid inclusions. All melt inclusions have rhyolitic compositions with SiO_2 contents ranging from 65 to 78 wt.%, and H_2O from 1.6 to 4.0 wt.%, whereas trace element contents vary significantly with rock type. In Critical Zone rocks, melt inclusions commonly show higher Ti contents (>800 ppm), higher Th/U ratios (up to 38), and lower REE contents (ΣREE <150 ppm) compared to those in diorites and granites (Ti <800 ppm; Th/U <5; ΣREE >150 ppm). Normative Qz-Ab-Or of melt inclusions and liquidus temperatures modelled with rhyolite-MELTS indicate melt entrapment at 930-850°C (at 200 MPa), tailing down in some samples to 700°C. For rutile-bearing rocks, these temperatures overlap with those obtained by TiO_2-in-melt and Ti-in-zircon geothermometry. For all rutile-free mafic and felsic rocks, reduced TiO_2 activities of $a\mathrm{TiO_2}$ ~0.3 are required for Ti-in-zircon geothermometry, and TiO_2^{rutile} ~30 wt.% for TiO_2 saturation geothermometry, to match temperatures from other geothermometers. Partitioning coefficients obtained from melt inclusions and host zircon of both mafic and felsic

rocks are within error identical and reveal no systematic variations with melt inclusion size, composition and entrapment temperature. In summary, melt inclusions in zircon are a powerful tool for zircon geothermometry and can be used to constrain the composition and TiO_2 activity of zircon-forming melts.

5.1 Introduction

Melt inclusions in minerals allow studying the physicochemical evolution of magmatic systems and may provide instantaneous snapshots of evolving melt compositions. Melt inclusions in zircon (MIZ) are of particular interest, since zircon occurs in most magmatic rocks, from mafic to felsic, and is widely used as a petrogenetic indicator, for geothermometry, and for U-Pb dating (Hoskin and Schaltegger, 2003). In most studies, physicochemical conditions during zircon crystallization (temperature, magma composition, degree of melt fractionation) are derived indirectly, either by using zircon trace element compositions (Fu et al., 2008; Trail et al., 2012) or by applying thermodynamic melt modelling in combination with zircon saturation thermometry (e.g. Ver Hoeve et al., 2018; Gudelius et al., 2020). In contrast, MIZ are rarely used, even though they can provide direct information about melt composition (major element, trace element and volatile contents), and entrapment temperature during zircon growth (Thomas et al., 2003). Furthermore, they allow estimation of zircon-melt partitioning coefficients ($D_{Zrc\text{-}melt}$) by analyzing both MIZ and host zircon (Thomas et al., 2002). Previous results indicate that zircon is a well-suited mineral for melt inclusion studies due to its high structural stability which commonly prevents post-entrapment alteration by leakage and diffusion (Thomas et al., 2003). Nevertheless, the extraction of high-quality physicochemical data from MIZ is challenging due to the commonly small size of MIZ, and post-entrapment recrystallization in slowly cooled rocks, which requires re-homogenization prior to chemical analysis, e.g. by electron microprobe (EPMA), secondary ion mass spectrometry (SIMS), and laser ablation inductively coupled plasma mass spectrometry (LA-ICP-MS). In previous studies, homogenization was done by controlled re-melting of melt inclusions using a heating stage attached to a microscope (Sobolev and Kostyuk, 1975; Roedder, 1984) which allows precise determination of homogenization temperatures. However, this method commonly suffers from decrepitation of melt inclusions prior to complete homogenization, a problem which particularly affects large melt inclusions (>20 µm) surrounded by tiny host zircon. In order to avoid decrepitation, MIZ in some studies were homogenized stepwise (~20°C steps) in pressurized metal vessels (for details see Thomas et al. 2002). This method allows bracketing the entrapment temperature of a large number of MIZ.

Previous studies mainly focused on MIZ sampled from felsic-to-intermediate magmatic rocks comprising granites, rhyolites and quartz diorites (Thomas et al., 2003; Watts and Mercer, 2020), as well as from quartzite (Chupin et al., 1998), whereas MIZ in mafic rocks like norites

and pyroxenites have never been studied. However, such studies are of particular interest, as they can provide direct information about physicochemical conditions during late-magmatic processes in intercumulus domains, which are very difficult to access by other methods. This is possible since zircon crystallization in mafic rocks commonly starts at a much higher degree of fractional crystallization (>70%) compared to felsic rocks (<25%) as has been demonstrated by thermodynamic modelling (e.g. Ver Hoeve et al., 2018; this study), but is also shown by zircon saturation experiments (Watson and Harrison, 1983; Boehnke et al., 2013; Borisov and Aranovich, 2019). Therefore, studying MIZ has a great potential to investigate the influence of bulk-rock composition and temperature on zircon-melt partitioning. Presently, $D_{Zrc\text{-}melt}$ of trace elements (U, Th, REE) are only available from a few experiments carried out using granitic compositions in the temperature range between 800 and 1050°C (Rubatto and Hermann, 2007), and from a MIZ study of a quartz diorite from the Quottoon Igneous Complex in southern Alaska (Thomas et al., 2003). Thomas et al. (2003) showed that the interpretation of $D_{Zrc\text{-}melt}$ derived from MIZ can be challenging and might be biased by several effects, comprising boundary layer effects and re-equilibration with host zircon.

In this study, we provide a new comprehensive dataset of MIZ and coexisting host zircon derived from felsic and mafic rocks of the Bushveld Complex (BC). In these rocks, zircon occurs in both rutile-bearing and rutile-free, magnetite-ilmenite-titanite-bearing assemblages, which allow cross-checking of temperatures obtained by a number of different independent geothermometers based on both MIZ and host zircon compositions. In detail, our dataset allows comparison of liquidus temperatures resulting from normative Qz-Ab-Or contents (Tuttle and Bowen, 1958) and rhyolite-MELTS modelling (Gualda et al., 2012), from TiO_2 and zircon saturation temperatures (Watson and Harrison, 1983; Xiong et al., 2009; Boehnke et al., 2013), and from Ti-in-zircon geothermometry (Ferry and Watson, 2007). Based on these results, we explore the influence of the mineral assemblages (Rt-bearing vs. Rt-free) and H_2O contents on the geothermometric results. Finally, we elucidate the dependency of $D_{Zrc\text{-}melt}$ on MIZ sizes, compositions and entrapment temperatures. Furthermore, we discuss the consequences of our results for BC parental magma evolution.

5.2 Geological outline

The Bushveld Complex in South Africa is Earth's largest mafic layered intrusion and comprises mafic cumulate rocks of the Rustenburg Layered Suite (RLS) which are overlain by felsic rocks of the Rashoop Granophyre and the Lebowa Granite Suites (Fig. 5.1). The BC was intruded at approximately 2.055 Ga at shallow crustal level (~200 MPa) mostly into sediments of the Transvaal Supergroup (Pitra and De Waal, 2001; Cawthorn, 2015; Zeh et al., 2015). The RLS is subdivided into six main subunits comprising from bottom to top the Basal Ultramafic Sequence (BUS), Marginal, Lower, Critical, Main, and Upper Zone (Wilson et al., 2017). Rocks of the

lower RLS from the BUS to the lowermost Main Zone are commonly rutile-bearing (Zeh et al., 2015; Gudelius et al., 2020), whereas rocks of the upper Main and Upper Zones (UUMZ) as well as all overlying granitic rocks are rutile-free but contain ilmenite, magnetite and titanite (Ver Hoeve et al., 2018; Gudelius et al., 2020). The RLS reveals a general differentiation trend from base to top characterized by decreasing An% in plagioclase and decreasing Mg# in olivine and pyroxenes (Cawthorn, 2015).

Previous studies suggested that the cumulate rocks of the RLS result from (at least) four parental magmas. Rocks from the BUS to the lower Critical Zone mainly formed by the crystallization of Mg-rich andesitic magma (B1), Critical Zone rocks from tholeiitic magma (B2) variably mixed with B1 (Barnes et al. (2010) suggested B1:B2 = 60:40), and Main Zone rocks from tholeiitic magma B3 (Barnes et al., 2010; Wilson, 2015). Iron-rich cumulate rocks of the Upper Main and Upper Zones (UUMZ) are suggested to have formed from a Si-rich tholeiitic magma unmixed into felsic and Fe-rich melts (VanTongeren et al., 2010; Fischer et al., 2016). The origin of the ferroan (A-type) granites and granophyres at the top of the RLS is still debated. Present models consider re-melting of felsic Rooiberg volcanics and/or unmixing from UUMZ parental magma (for a detailed discussion see Hill et al., 1996; VanTongeren et al. (2010); Mathez et al., 2013 and references therein).

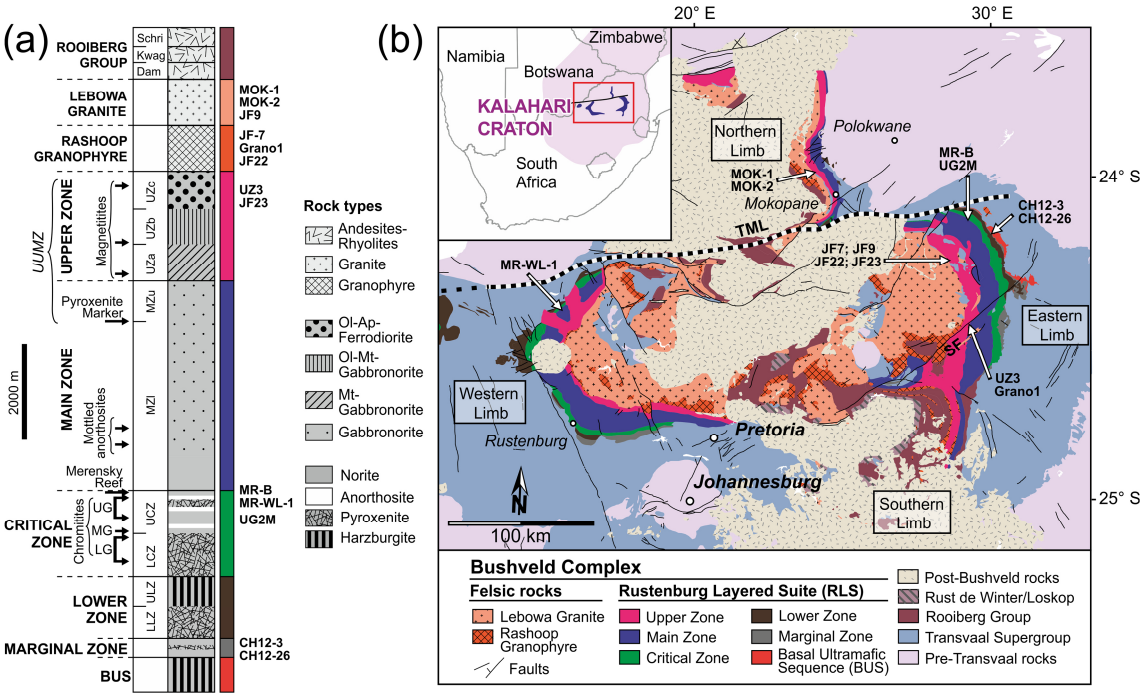

Figure 5.1 - (a) Generalized stratigraphic profile and (b) geological map of the Bushveld Complex (BC), modified after the Council of Geoscience of South Africa (Johnson et al., 2006); Wilson (2015) and Mungall et al. (2016) and references therein. Shown are the main rock units of the BC and surrounding rocks as well as locations of investigated samples and their position within the BC stratigraphy. UUMZ = Upper Main and Upper Zone; Chromitites: LG = Lower Group; MG = Middle Group; UG = Upper Group. Rooiberg Group formations: Schri = Schrikkloof; Kwag = Kwaggasnek; Dam = Damwal; TML = Thabazimbi-Murchison lineament; SF = Steelpoort fault. Mineral abbreviations used here and below are from Whitney and Evans (2009).

5.3 Sample description

In this study, MIZ were investigated from mafic cumulate rocks of the RLS and overlying granites (for sample positions see Figure 5.1 and Table 5.1). Samples from the RLS comprise chilled norites of the Marginal Zone (CH12-3, CH12-26), pegmatoidal pyroxenites of the Critical Zone (UG2-chromitite: sample UG2M; Merensky Reef: samples MR-B, MR-WL-1), as well as ferrodiorite (JF23) and pegmatoidal diorite (UZ3) of the Upper Zone. Studied felsic rocks are from the Rashoop Granophyre Suite (JF7, Grano1, JF22) and from Lebowa Granite (JF9, MOK-1, MOK-2). All mineral abbreviations in this study are according to Whitney and Evans (2009).

Petrographic observations indicate that zircon in the investigated samples occurs in two fundamentally different mineral assemblages. In rocks of the lower RLS (Marginal Zone to Merensky Reef), zircon is present mainly in intercumulus melt pockets of Opx-Pl-Chr-dominated cumulates, and is commonly intergrown with Qz, Pl, Kfs, Bt, Amp, and in some samples directly with Rt (UG2M, MR-B and MR-WL-1). In contrast, zircon in mafic rocks of the Upper Zone and in overlying granites occurs in assemblages with Ol-Cpx-Hbl-Pl-Qz in addition to Ilm, Mt, Ttn and Ap (for details see Zeh et al. 2015, 2020; Gudelius et al. 2020). Granites and granophyres additionally contain abundant perthitic Kfs. The different mineralogy is also reflected by different bulk-rock compositions (data for all samples given in Gudelius et al., 2020). The investigated rocks comprise a wide range in SiO_2, (51.5-72.1 wt.%), TiO_2 (0.28-1.1 wt.%), ΣREE (12-566 ppm) and Zr contents (10-461 ppm). Bulk-rock zircon saturation temperatures derived from the granite and granophyre samples range from 838 to 858°C (using the calibration of Watson and Harrison 1983).

5.4 Analytical methods

5.4.1 Re-homogenization of melt inclusions in zircon

Zircon crystals with recrystallized melt inclusions were selected under ethanol from heavy mineral concentrates, and the MIZ imaged by using a ZEISS polarization microscope. Subsequently, zircons were embedded in epoxy resin and ground to expose the MIZ. Imaging and mineral identification of recrystallized MIZ was performed at Goethe University Frankfurt and Karlsruhe Institute of Technology using a scanning electron microscope attached to an EDX system (*JEOL JSM 6490* and *TESCAN VEGA*2).

Homogenization of the MIZ was performed using an internally heated pressure vessel (IHPV) at Institute of Mineralogy, Leibniz University Hannover, for which only zircon crystals without any visible fractures were selected. Zircon crystals were loaded in open Pt capsules and run in the IHPV pressurized with Argon at 200 MPa. During each experiment, capsules were initially heated to 600°C with a ramp of 50°C/min followed by slower heating at 10°C/min to a peak temperature of 1100 °C. This run temperature was held for 6 h prior to quenching (cooling rate ~150 °C/s). This experimental treatment resulted in completely homogenized MIZ. Preliminary tests showed that a shorter heating duration (3h at 1100 °C) and a lower peak temperature (1050 °C for 6h) resulted in incomplete homogenization, whereas a longer heating (24 h at 1100 °C) and faster heating rates (50°C/min to 1100 °C) resulted in decrepitation of most MIZ.

5.4.2 Chemical analysis of melt inclusions and host zircon

Major element compositions of melt inclusions were determined by electron microprobe (EPMA) using a *JEOL JXA8900* at Goethe University Frankfurt and a *CAMECA SX100* at Freiburg University. For analysis, an accelerating voltage of 15 kV, a beam current of 5 nA and a beam diameter of 2 µm was used. The counting times for individual elements ranged between 10s and 30s. Calibration was performed using the following standards: wollastonite for Si and Ca, Al_2O_3 for Al, albite for Na, orthoclase for K, fayalite (Freiburg: hematite) for Fe, Cr_2O_3 for Cr, forsterite (Freiburg: MgO) for Mg, $KTiOPO_4$ (Freiburg: rutile, apatite) for Ti and P, $MnTiO_3$ (Freiburg: spessartine) for Mn, fluorapatite for F, and scapolite for Cl.

Trace element compositions of MIZ and host zircon were determined by LA-ICP-MS at Goethe University Frankfurt using a *RESOlution M-50* ArF excimer laser ablation system coupled to a *Thermo-Fisher Scientific Element XR* sector field mass spectrometer. Melt inclusions were ablated using a laser pulse rate of 6 Hz, an energy density of 4.8 J/cm^2 and laser spot diameters of 10 or 15 µm. Ablation was performed in a 0.36 L min^{-1} He stream, which was mixed directly after the ablation cell with 0.009 L min^{-1} N_2 and 1.051 L min^{-1} Ar. For analysis, the following masses were used: ^{7}Li, ^{29}Si, ^{44}Ca, ^{49}Ti, ^{85}Rb, ^{88}Sr, ^{89}Y, ^{90}Zr, ^{93}Nb, ^{137}Ba, ^{139}La, ^{140}Ce,

^{141}Pr, ^{146}Nd, ^{147}Sm, ^{151}Eu, ^{158}Gd, ^{159}Tb, ^{161}Dy, ^{165}Ho, ^{167}Er, ^{169}Tm, ^{172}Yb, ^{175}Lu, ^{178}Hf, ^{181}Ta, ^{208}Pb, ^{232}Th and ^{238}U. The oxide production, monitored as ^{254}UO/^{238}U on the standard glass NIST612 was below 0.2%. For standardization, the glass standards NIST612 and the basalt glass standards BHVO-2G, BIR-1G and BCR-2G were used, which were ablated using a spot size of 33 µm. Data processing was performed with GLITTER software, using NIST612 as the primary standard, and the SiO_2 content of the MIZ as an internal standard. Host zircon was analyzed close to the respective melt inclusions using a laser spot size of 33 µm, a laser pulse rate of 7 Hz and an energy density of 5.6 J/cm^2. Data processing was carried out with GLITTER software, using NIST612 as external standard and the stoichiometric Si content of zircon (32.7 wt.% SiO_2) as an internal standard. Accuracy of the method was checked by analyzing reference zircons GJ1 and 91-500. The results of standard analyses are in agreement with published data (supplementary materials 1).

5.4.3 Analysis of H_2O in melt inclusions

Water contents of MIZ embedded in epoxy resin were determined by SIMS using the *CAMECA IMS 1280-HR* at Heidelberg University. For analysis, a 1 nA primary beam of $^{16}O^-$ ions was used at an impact energy of 22905 eV; high energy ions with -100 eV offset and an energy bandpass of 40 eV were detected. To improve vacuum in the sample chamber, a liquid N_2 cooling trap was applied. Before analysis, measurement areas were presputtered for 300 s using a rastered ion beam covering approximately 25 × 25 µm. For the measurement, a stationary beam ~8 µm in diameter was centered in the presputtered area. Water contents were quantified by using measured $H^+/^{30}Si^+$ ratios, the SiO_2 contents of the MIZ, and a calibration line based on five rhyolitic glass standards which cover H_2O contents between 0.09 and 4.44 wt.% H_2O (Schmitt, 2001). A background of ~0.05 wt.% H_2O was determined by analyzing H_2O-free NIST610 glass and host zircon.

5.5 Results

5.5.1 Petrography of recrystallized melt inclusions

Assemblages observed in recrystallized MIZ are summarized in Table 5.1 and shown in Figs. 5.2 and 5.3. In all samples, MIZ assemblages are dominated by Qz, Pl, and Kfs, but also contain Ms and more rarely Ca-Amp and Bt. Recrystallized MIZ are mostly colorless and transparent, although big MIZ may appear dark-colored due to fine-grained intergrowths of daughter crystals. In contrast, altered MIZ (e.g. such in fractured zircon domains) always look brownish and were not considered in this study.

Felsic rocks (Lebowa Granite, Rashoop Granophyre) contain abundant MIZ, which commonly display round or negative crystal shapes of variable size (mostly 5-30 µm in diameter). They also occur as melt pockets attached to mineral inclusions in zircon of needle-like Ap, Ilm and sulfides, mostly pyrrhotite (Fig. 5.2a, b). Accessory phases in MIZ comprise daughter crystals of zircon, magnetite, ilmenite, titanite, apatite, monazite and fluorite. Barite was only found in Rashoop Granophyre samples.

In mafic rocks of the RLS, MIZ reveal different assemblages, sizes and shapes dependent on their stratigraphic position. The MIZ in ferrodiorite of the Upper Zone (JF23) are very similar to those in granitic rocks, but lack fluorite, apatite, monazite and ilmenite. In pegmatoidal diorite sample UZ3, MIZ are rare, but commonly big (up to 70 µm diameter), spherical, and never form melt pockets intergrown with apatite and/or ilmenite. A few contain titanite and monazite. In Critical Zone pyroxenites MIZ are rare. They are commonly spherical with diameters <50 µm and contain accessory titanite, daughter crystals of zircon, and rare fluorite. In chilled norite of the Marginal Zone, MIZ shapes range from spherical (most common) to extremely tubular (aspect ratios >20), and accessory daughter crystals include Ca-amphibole, zircon, rutile, titanite, calcite, barite and tiny grains of iron oxide.

Fluid inclusions with vibrating gas bubbles were observed in a few MIZ of the samples UZ3, MR-WL-1 and CH12-3 (Fig. 5.2c). These inclusions are up to 5 µm in diameter and the gas bubbles appear mono-phase resembling pure aqueous fluid inclusions as described by van den Kerkhof and Hein (2001). Unfortunately, they were too small to obtain a reliable Raman spectrum. Micro-porous textures observed in quartz and feldspars in MIZ of most samples (Fig. 5.3) perhaps also originate from fluid inclusions.

After successful re-homogenization by IHPV, MIZ appear as colorless, transparent glasses which sometimes contain shrinkage bubbles (Fig. 5.4a, b). We note that decrepitated MIZ always contain incompletely dissolved daughter crystals, are strongly fractured and dark colored.

Table 5.1 Mineral assemblages of recrystallized melt inclusions in zircon of the Bushveld Complex

Sample	rock type	Ti phase in matrix	*n*	minor phases in recrystallized melt inclusions [a]													
				Ms	Bt	Amp	Rt	Ttn	Mt	Ilm	Flt	Brt	Ap	Mnz	Cal	Zrc	fluid
Felsic Rocks (Rt-free)																	
JF9	Lebowa Granite	Ilm, Mt	*23*	X	X	X		X	X	X	X		X	X	X	X	
MOK-1	Lebowa Granite	Ilm, Mt	*5*								X					X	
MOK-2	Lebowa Granite	Ilm, Mt	*2*	X	X				X		X			X			
JF7	Rashoop Granophyre	Ilm, Ttn	*20*	X	X	X		X	X		X	X			X	X	
Grano1	Rashoop Granophyre	Ilm, Ttn	*12*	X				X	X		X	X		X		X	
JF22	Rashoop Granophyre	Ilm, Mt	*19*	X		X			X	X	X	X	X	X		X	
Rt-free mafic rocks - RLS				X													
JF23	UZ: ferrodiorite	Ilm, Mt	*14*	X		X			X			X				X	
UZ3	UZ: pgmt. diorite	Ilm, Mt, Ttn	*8*	X		X		X	X					X		X	X
Rt-bearing mafic rocks - RLS																	
MR-B	CZ: pgmt. pyroxenite	Rt	*3*	X							X						
MR-WL-1	CZ: pgmt. pyroxenite	Rt	*5*	X				X									X
UG2M	CZ: pgmt. pyroxenite	Rt	*6*	X	X	X											
CH12-3	MrZ: chilled norite	Ilm, Ttn, Rt	*20*	X	X	X	X	X	X						X	X	X
CH12-26	MrZ: chilled norite	Rt	*5*	X		X	X		X			X	X				

UZ=Upper Zone, CZ=Critical Zone, MrZ=Marginal Zone, pgmt.=pegmatoidal. Mineral abbreviations: Ms=muscovite, Amp=amphibole, Rt=rutile, Ttn=titanite, Mt=magnetite, Ilm=ilmenite, Flt=fluorite, Brt=baryte, Ap=apatite, Mnz=monazite, Cal=calcite, Zrc=zircon, fluid=aqueous fluid inclusions.

[a] main phases in all melt inclusions are quartz, plagioclase and alkali feldspar

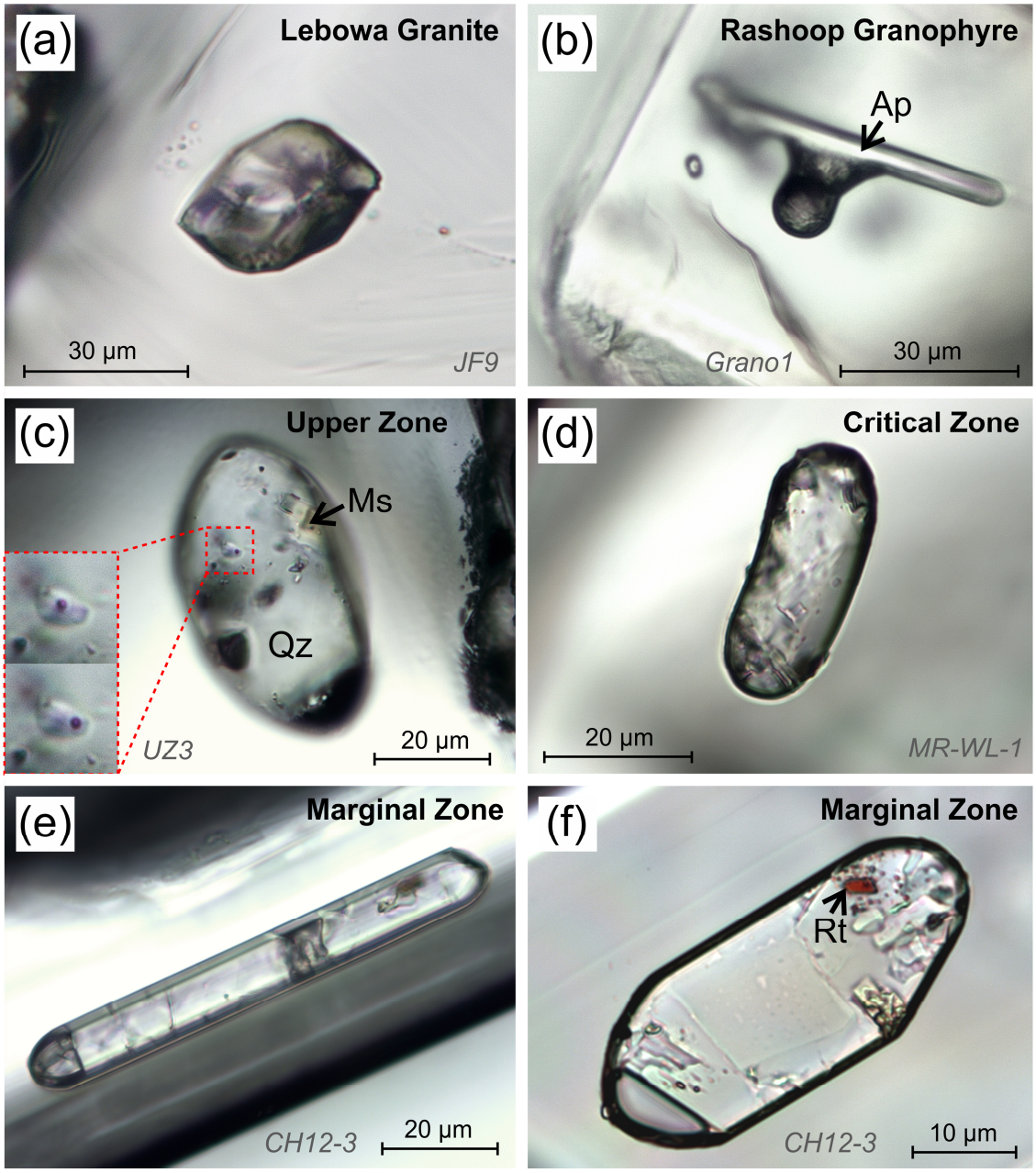

Figure 5.2 - Transmitted light photomicrographs of recrystallized melt inclusions in zircon (MIZ) from felsic and mafic rocks of the BC. (a, b) In felsic rocks (Lebowa Granite, Rashoop Granophyre), MIZ commonly display (a) negative crystal shapes or (b) are attached to needle-like apatite; (c) In Rt-free mafic rocks (Upper Zone), MIZ are mostly round and some contain aqueous fluid inclusions with visible vibrating gas bubbles (see inset) within quartz and feldspars. (d) In Rt-bearing mafic cumulates of the Critical Zone, MIZ are generally rare and mostly display round shapes. In contrast, MIZ in chilled norites of the Marginal Zone (d, f) are abundant and show variable shapes including tubular (d), round and negative crystal shapes (f). Some MIZ also contain Rt (f).

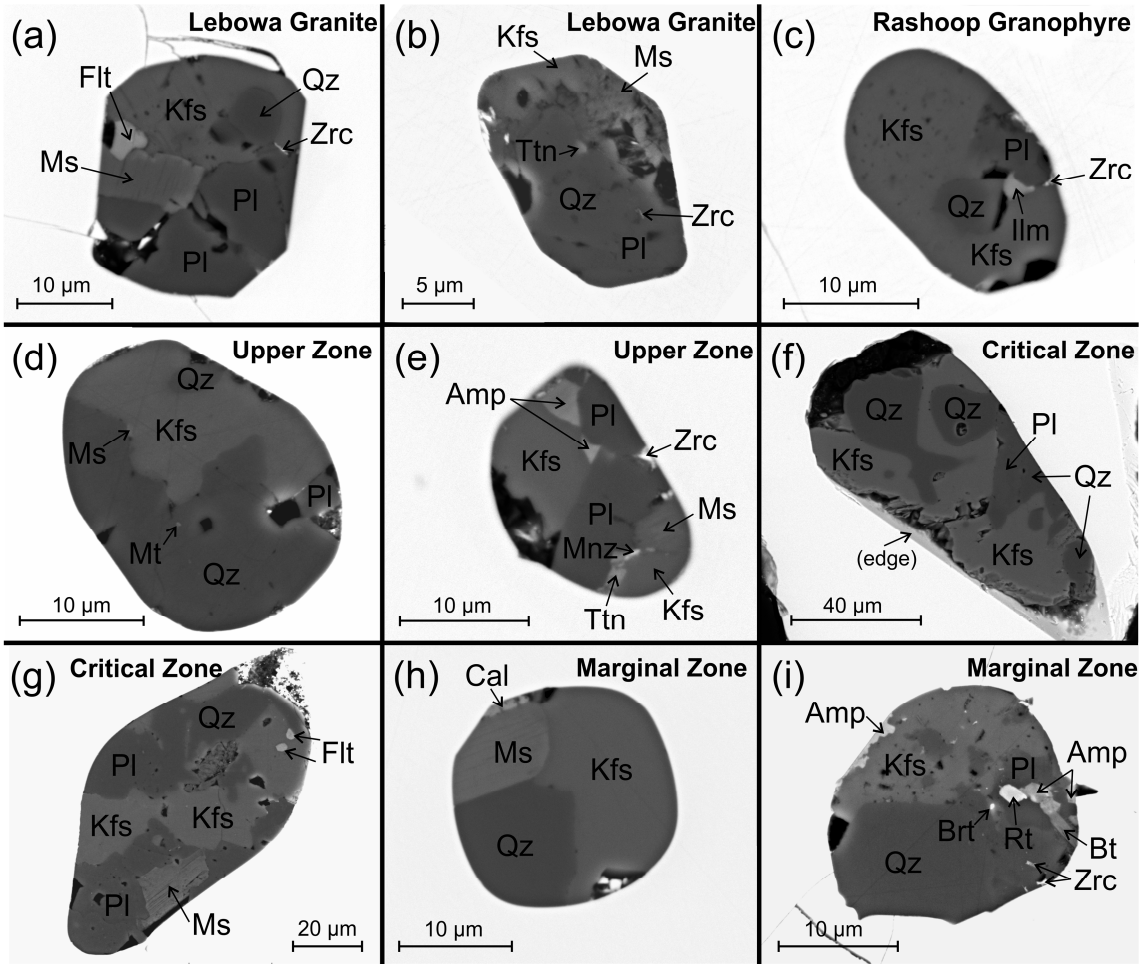

Figure 5.3 - Back-scattered electron images of recrystallized MIZ from felsic and mafic rocks of the BC. All MIZ contain quartz, plagioclase, alkali feldspar and a hydrous phase, mostly muscovite, biotite or amphibole. In most samples, MIZ also contain small daughter crystals of zircon (a, c, f). (a-c) In felsic rocks, MIZ additionally contain fluorite, ilmenite, magnetite, titanite, monazite and barite. (d, e) Assemblages in MIZ of the Upper Zone diorite are similar to those in felsic rocks but lack fluorite and ilmenite. (f, g) MIZ in Critical Zone pyroxenites rarely contain fluorite and titanite (not shown), and (h, i) in Marginal Zone norites commonly rutile and rarely calcite and barite.

5.5.2 Major and trace element composition of melt inclusions

5.5.2.1 Major element compositions

The MIZ of all samples (n = 250) have rhyolitic compositions characterized by high SiO_2 (65.3-77.8 wt.%; average: 75.0), and low CaO (0.3-1.1 wt.%; average: 0.9), FeO_T (0.08-1.9 wt.%; average: 0.5) and MgO (mostly <0.5 wt.%) contents (Fig. 5.5). The Cl concentrations vary from 0.06-0.84 (average: 0.46) – (all data given in supplementary materials 1). MIZ from felsic rocks show slightly higher F contents (>0.15 wt.%), higher F/Cl and Na_2O/CaO (>0.3 and >2.5, respectively), as well as lower MgO and FeO_t contents (mostly below detection and <0.35 wt.%, respectively), compared to those from the mafic rocks. However, a clear discrimination between felsic and mafic samples is hardly possible. All other elements (Na_2O, K_2O, Al_2O_3, SiO_2, TiO_2 and CaO) show significant overlap. The MIZ of mafic rocks show large differences in TiO_2 and Al_2O_3 contents which are generally higher and more variable in rocks of the Critical Zone (MR-WL-1, MR-B, UG2M) compared to the Upper and Marginal zones (Fig. 5.5c). The CaO

contents are higher in MIZ from the Upper and Critical Zones, compared to those from the Marginal Zone and granites. The Na_2O and K_2O contents of all samples define two clusters, a first at about 2 wt.% Na_2O/3.5 wt.% K_2O, and a second at 1 wt.% Na_2O/5.3 wt.% K_2O (Fig. 5.5). These clusters are also reflected by normative Qz, Ab and Or contents (Fig. 5.6).

5.5.2.2 H_2O contents

The H_2O contents of the MIZ measured by SIMS (all data given in supplementary materials 1) range between 1.64 and 4.07 wt.% (average = 2.4 wt.%; n = 18). Values are essentially the same for mafic rocks of the Critical Zone (1.91-2.35 wt.% H_2O), Upper Zone (1.64-4.07 wt.% H_2O) and granites (2.19-2.58 wt.% H_2O). The highest H_2O content of 4.07 wt.% was measured in a MIZ containing a shrinkage bubble. Significantly lower H_2O contents of 0.10-0.35 wt.% were only analyzed in two MIZ clearly connected with the zircon surface by minute fractures, along which H_2O was probably released prior to or during homogenization.

5.5.2.3 Trace element compositions

The MIZ of all Rt-free felsic and mafic rocks show similar trace element compositions and ratios and are significantly different to MIZ of Rt-bearing mafic rocks (Figs. 5.7, 5.8 and supplementary materials 1). They mostly have higher Li (avg: 74 ppm), LREE (average La = 48 ppm), HREE (average Yb = 4.8 ppm), ΣREE (average = 208 ppm), and lower Ti contents (average = 554 ppm) compared to Rt-bearing mafic rocks (Fig. 5.7). Furthermore, they show lower Ti/Yb (<300), Lu/Hf (<0.02) and Nb/Yb (<5) ratios. Most MIZ have Th/U = 3.4, except a few in the Rt-bearing mafic rocks of the Critical Zone with Th/U ratios up to 38, also showing the lowest U contents (<1.5 ppm). Furthermore, the REE patterns of some MIZ from the Critical Zone are HREE-depleted showing Dy_N/Yb_N >1.3. Zirconium contents measured on MIZ of all samples range from 280 to 719 ppm (average: 517 ppm) and are not correlated with MIZ diameter or surface/volume ratio (Fig. 5.9).

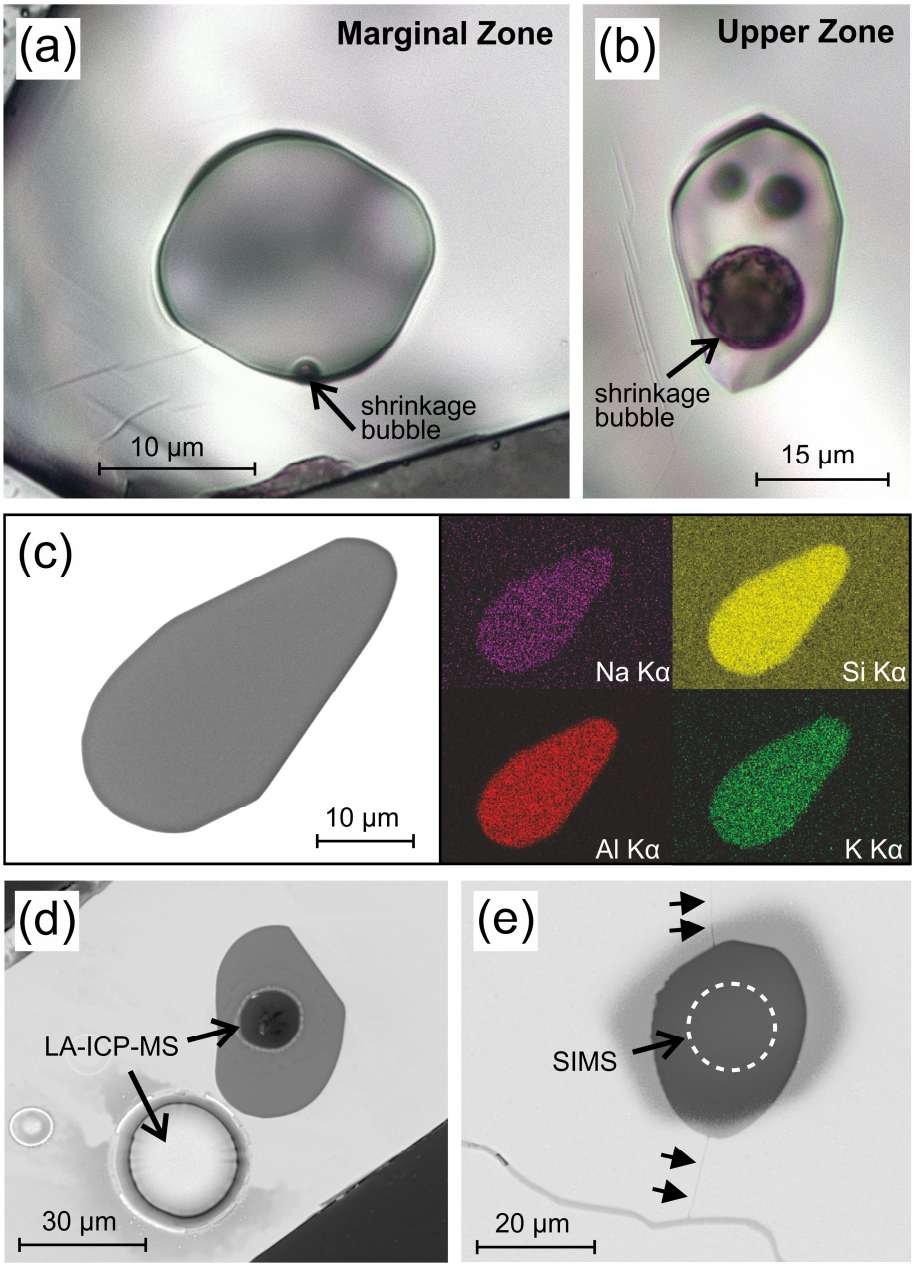

Figure 5.4 - Re-homogenized MIZ of different samples of the BC. (a) and (b) transmitted light photomicrographs of re-homogenized MIZ of the Marginal Zone and Upper Zone, respectively, showing shrinkage bubbles. (c) Back-scattered electron image (left) and element distribution maps for Na, Si, K and Al (right) for a re-homogenized MIZ illustrating a homogeneous glass composition. (d) Laser spot positions for LA-ICP-MS analysis in re-homogenized MIZ (big spot) and surrounding host zircon (small spot). (e) SIMS spot (dashed circle) within a re-homogenized MIZ connected by minute fractures with the zircon surface (arrows). Note, that the fractured MIZ has a very low H_2O content of 0.1 wt.%, compared to H_2O contents of 1.5-4.0 wt.% (average: 2.4 wt.%) obtained from non-fractured, pristine MIZ during this study.

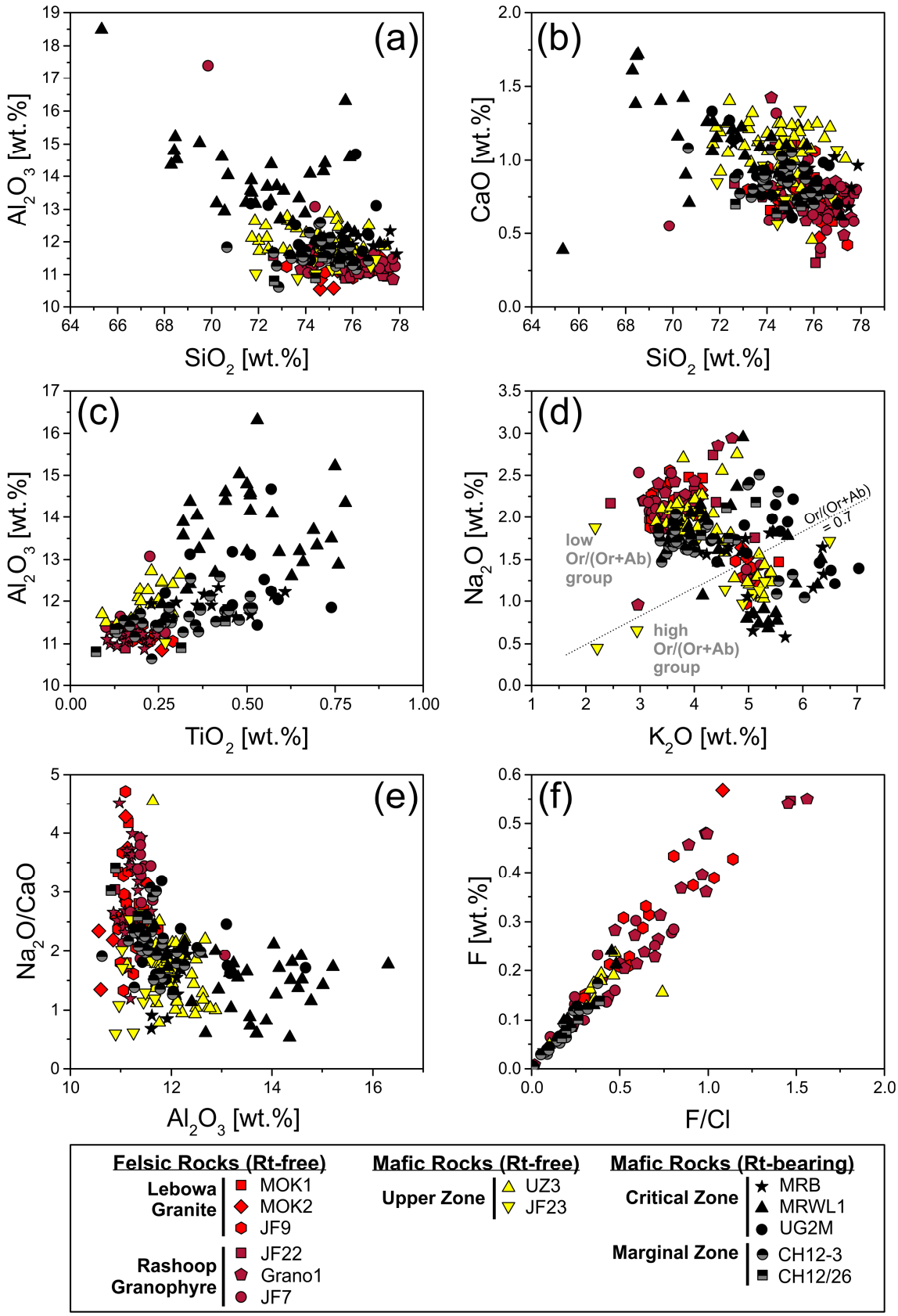

Figure 5.5 - (a-f) Major element composition of MIZ from different felsic and mafic rocks of the BC, shown in covariation diagrams. Note that MIZ compositions of all samples overlap, irrespective of rock type, except for F and Na_2O/CaO ratios. These are commonly higher in MIZ of the felsic compared to mafic rocks (e, f). (c) MIZ of the Critical Zone rocks show the widest range in major element compositions, and the highest Al_2O_3 and TiO_2 contents of all samples investigated. (d) MIZ of all samples reveal two clusters in K_2O vs. Na_2O diagram, one at high normative Or/(Or+Ab) >0.7 and one at low normative Or/(Or+Ab) <0.7. These clusters are also present as two linear trends in normative Qz-Ab-Or diagrams (Fig. 5.6).

5.5.3 Trace element composition of host zircon

Zircon in all granites and Rt-free mafic rocks of the Upper Zone shows similar trace element compositions and ratios, which are significantly different to those of the Rt-bearing mafic rocks of the RLS. Zircon in granites and Rt-free mafic rocks has higher REE (ΣREE: average 638 ppm) and lower Ti contents (average 10 ppm) compared to the Rt-bearing mafic rocks (average: ΣREE = 299 ppm; Ti = 30 ppm) - (Fig. 5.8). Zircon Th/U in Rt-free rocks is always <1, whereas zircon Th/U in the Rt-bearing mafic rocks is 3 (on average) and more variable (Th/U = 1-20).

5.5.4 Results of geothermometry

5.5.4.1 Liquidus temperatures of MIZ

The MIZ of all samples have normative Qz >50 %, and 20-30% normative Ab and Or (Fig. 5.6). The normative mineral contents correspond to liquidus temperatures ($T_{Liq\text{-}QAO}$) between 700 and 930 °C (mainly at 850-900 °C), when plotted in the Qz-Ab-Or diagram of Tuttle and Bowen (1958) valid for 200 MPa and aH_2O = 1. The data of all samples define two linear cooling trends, which follow tie lines connecting the Qz apex with the cotectic line, indicating that quartz crystallized prior to feldspars. The two linear cooling trends are observed in all samples, the first at Or/(Or+Ab) = 0.5-0.6 (comprising most data), and the second at higher Or/(Or+Ab) ratios of >0.7 (Fig. 5.6).

Liquidus temperatures of MIZ were additionally calculated with rhyolite-MELTS v.10.2 (Gualda et al., 2012) ($T_{Liq\text{-}rM}$), which, in contrast to the Qz-Ab-Or diagram of Tuttle and Bowen (1958), considers additional system parameters (CaO, FeO, MgO, TiO_2) and variable volatile contents (H_2O, Cl, F). The calculations were carried out using the composition of each MIZ and a pressure of 200 MPa. Oxygen fugacity was held constant at fO_2 = FMQ. Variation of fO_2 by FMQ±2 had no significant effect on the results. Most calculations were performed using a H_2O content of 2.4 wt.%, which is the average of all MIZ measured by SIMS, but the influence of higher H_2O contents (up to 5 wt.%) was also tested. For most MIZ, the resulting $T_{Liq\text{-}rM}$ at 2.4 wt.% H_2O are 50-100 °C higher than respective $T_{Liq\text{-}QAO}$, which are based on aH_2O = 1, corresponding to ca. 5 wt.% H_2O in the melt (Figs. 5.10, 5.11a; Table 5.2).

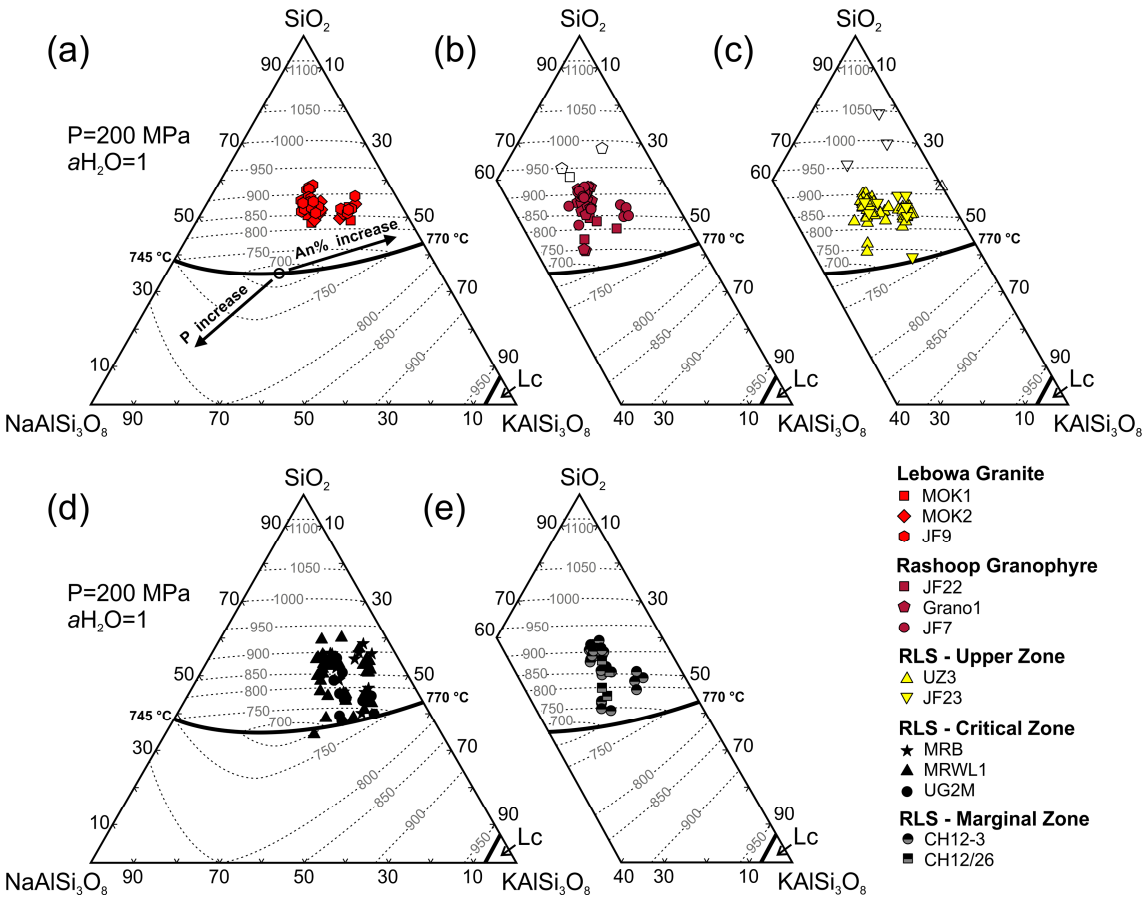

Figure 5.6 - Ternary plots showing the normative Qz (SiO2), Or (KAlSi3O8) and Ab (NaAlSi3O8) contents of MIZ in felsic rocks of the (a) Lebowa Granite, and (b) Rashoop Granophyre, as well as in mafic rocks of the (c) Upper Zone, (d) Critical Zone and (d) Marginal Zone. Contour lines for liquidus temperatures and phase relations are after Tuttle and Bowen (1958) obtained for 200 MPa and water-saturated conditions (aH2O = 1). Note, that MIZ compositions of all samples reveal two parallel cooling trends, which always start in the field of quartz at 890-920 °C and develop towards the cotectic line. Black arrows in (a) indicate the effects of increasing anorthite contents (An%) and pressure (P) on the position of the ternary minimum (for details, see Wilke et al. (2017)). Lc = leucite. Empty symbols indicate outliers, resulting from MIZ alteration.

5.5.4.2 TiO_2 saturation temperatures of MIZ

The TiO_2 saturation temperatures (T_{TiSat}) were calculated with the geothermometer of Xiong et al. (2009):

$$\ln(TiO_2)^{melt} = \ln(TiO_2)^{rutile} + 1.701 - (9041/T) - 0.173P + 0.348FM + 0.016H_2O$$

In this formula, the TiO_2 content of the melt $[(TiO_2)^{melt}]$ is a function of T (in K), P (in GPa), the TiO_2 content of rutile $[(TiO_2)^{rutile}]$, and the H_2O content of the melt. The major element composition of the melt is considered by the compositional parameter FM = (1/Si)×[Na + K + 2(Ca + Fe + Mn + Mg)]/Al, calculated by using cation fractions. In this study, T_{TiSat} were calculated by using the MIZ compositions, the average H_2O contents of 2.4 wt.%, a pressure of 200 MPa, and TiO_2^{rutile} = 100%, i.e. pure rutile. The average H_2O content was used, because it was not possible to measure H_2O contents (by SIMS) and TiO_2 contents (by LA-ICP-MS) on the same MIZ. We note that variations in H_2O content only had a minor effect on T_{TiSat}. The

calculated temperatures decreased by <5 °C for H_2O increasing from 2 to 4 wt.%. Based on T_{TiSat}, the investigated samples can be subdivided into three groups. The highest T_{TiSat} of 777-916 °C (average = 843 °C, n = 12) were obtained for Rt-rich mafic cumulate rocks of the Critical Zone, whereas Rt-poor mafic rocks of the Marginal Zone yield lower and more variable T_{TiSat} of 671-829 °C (average = 760 °C, n = 8). The lowest T_{TiSat} of <760 °C (average = 709 °C, n = 27) were calculated for Rt-free mafic and felsic rocks (Fig. 5.10, Table 5.2).

5.5.4.3 Zircon saturation temperatures of MIZ

Zircon saturation temperatures were calculated by applying the calibrations of Watson and Harrison (1983) = $T_{ZrcSat-W}$, and Boehnke et al. (2013) = $T_{ZrcSat-B}$, using the MIZ composition. Zirconium contents measured on MIZ of all samples correspond to $T_{ZrcSat-W}$ = 856-982 °C (average = 926 °C) and $T_{ZrcSat-B}$ = 841-1023 °C (average = 933 °C) – (Fig. 5.10, Table 5.2). Temperatures obtained by using the most recent zircon saturation model of Borisov and Aranovich (2019) are very similar to $T_{ZrcSat-W}$ and $T_{ZrcSat-B}$ (average deviation: 5 °C). In contrast, the model of Gervasoni et al. (2016) yields ~60 °C higher and more variable temperatures. It is noted that variations in Zr abundance are independent of MIZ size (Fig. 5.9) and resulting zircon saturation temperatures are significantly lower than 1100 °C used for MIZ homogenization. Reasons for that are discussed in chapter "6.2 Zircon saturation thermometry of MIZ".

5.5.4.4 Titanium-in-zircon thermometry

For host zircon, temperatures were calculated by applying the Ti-in-zircon geothermometer of (Ferry and Watson, 2007) - (T_{Ti-Zrc}). Zircon from Rt-Qz-bearing cumulate rocks of the RLS (Marginal Zone and Critical zones) yields variable T_{Ti-Zrc} between 738 and 933 °C (average: 856 °C, n = 70), in agreement with results of previous studies (Zeh et al., 2015; Ver Hoeve et al., 2018; Gudelius et al., 2020) – (Fig. 5.10; Table 5.2). Zircon populations in Rt-free, Ilm-Ttn-Mt-bearing felsic and mafic rocks mostly yield lower T_{Ti-Zrc} between 700 and 824 °C (average: 772 °C, n = 103), even by applying a reduced $a\mathrm{TiO_2}$ = 0.7, a value that is commonly used for Rt-free rocks in the literature (Hayden and Watson, 2007; Fu et al., 2008). The problem of TiO_2 activity during zircon growth in Rt-free magmatic rocks is further discussed in chapter: 6.1 "Entrapment temperatures of MIZ".

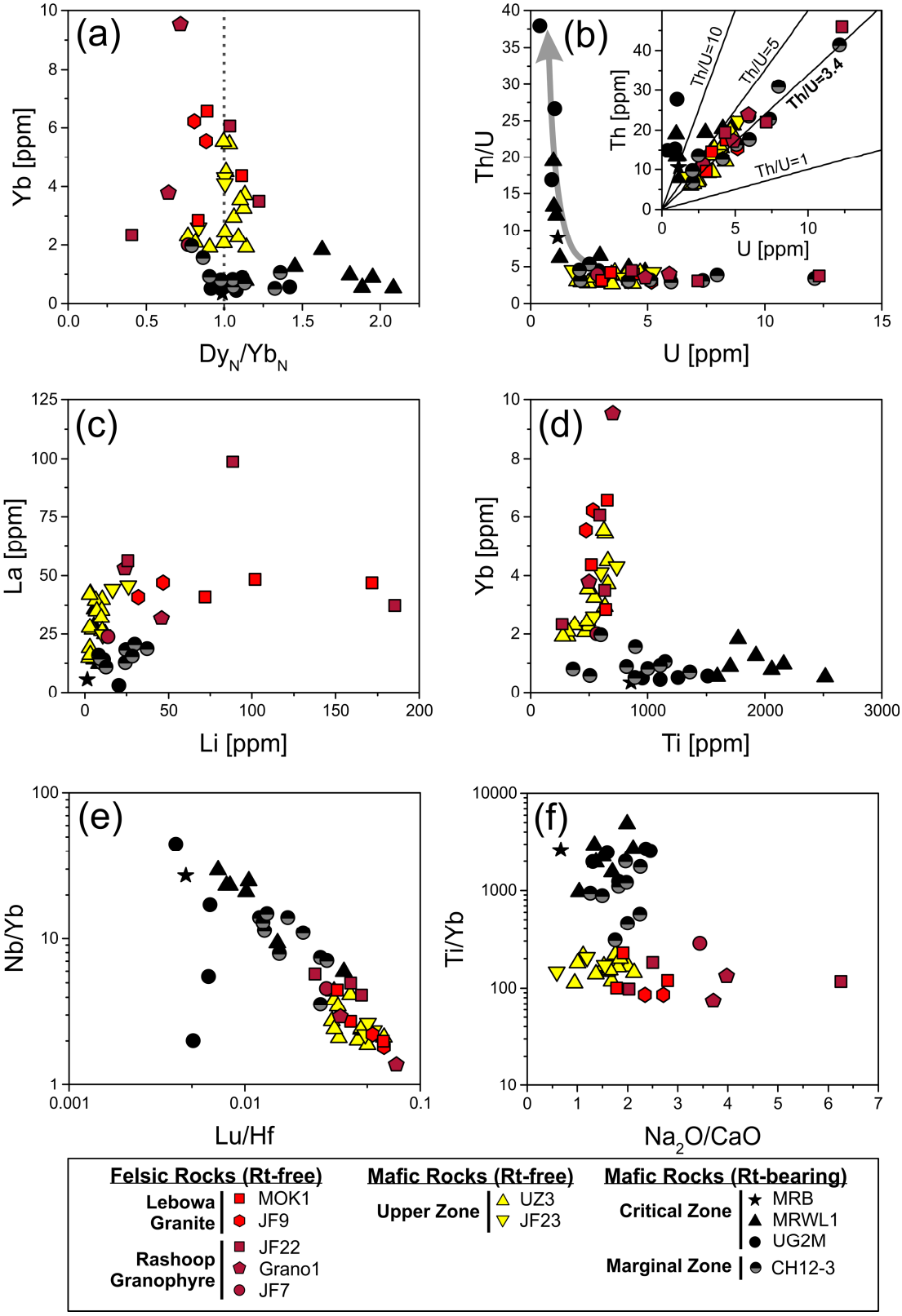

Figure 5.7 - (a-f) Trace element composition of MIZ from different felsic and mafic rocks of the BC shown in covariation diagrams. Note that MIZ of Rt-free rocks (Upper Zone and felsic rocks) display distinctly higher contents in HREE (represented by Yb in a, d), LREE (represented by La in c), higher Lu/Hf ratios (e) but lower Ti contents (d) as well as Nb/Yb and Ti/Yb ratios (e, f) compared to MIZ in Rt-bearing mafic rocks. MIZ in Rt-free mafic rocks (Upper Zone) can only be discriminated from those in felsic rocks by their lower Li contents (c) and Na_2O/CaO ratios (f). (a) and (b) illustrate further trace element fractionation restricted to some MIZ in Rt-bearing mafic cumulates, which show (a) Dy_N/Yb_N >1 at low Yb (i.e. HREE) as well as (b) decoupling from a positive covariation trend in Th and U (Th/U = 3.4) towards significantly higher Th/U (up to 36) at decreasing U contents (gray arrow). Both effects likely indicate HREE and U>Th fractionation due to zircon growth in small intercumulus melt pockets.

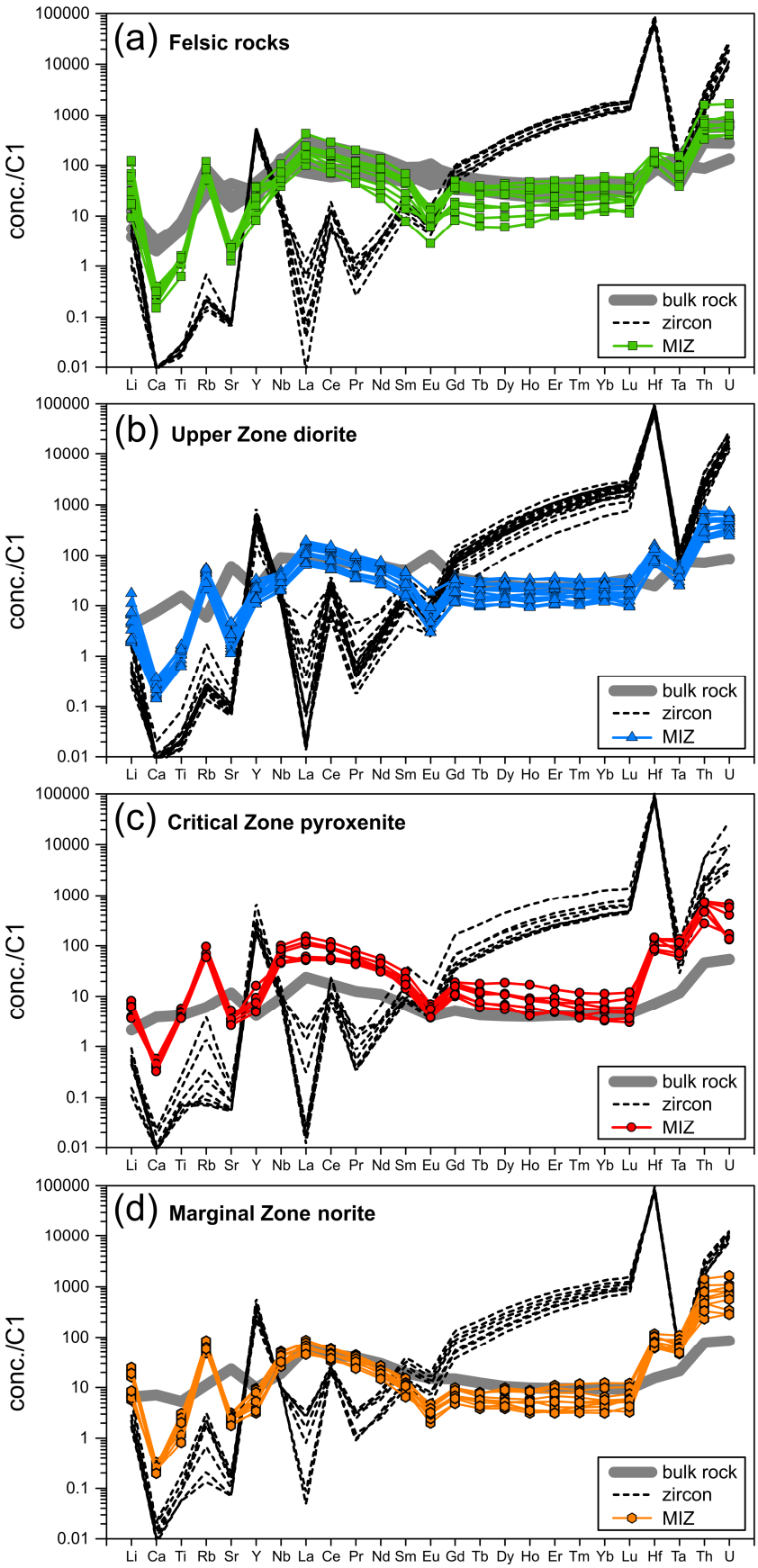

Figure 5.8 - Trace element contents of MIZ, related to those of host zircon and bulk rocks (BR), normalized to C1-chondrite (McDonough and Sun, 1995) for (a) felsic rocks (samples JF9, JF7, Grano1, MOK1, JF22), (b) Upper Zone diorite (samples UZ3, JF23), (c) Critical Zone pyroxenite (sample MR-WL-1), and (d) Marginal Zone norite (sample CH12-3).

5.5.5 Zircon-melt partitioning coefficients

Zircon-melt partitioning coefficients ($D_{Zrc\text{-}melt}$) for all investigated MIZ are within one order of magnitude identical, independent whether they were derived from felsic and mafic samples (Fig. 5.12; Table 5.3). Much larger variation in $D_{Zrc\text{-}melt}$, differing by up to three orders of magnitude, were only obtained for La and Pr, which both have low abundances in host zircon and are most susceptible to zircon alteration and/or contamination by unintentional ablation of LREE-rich inclusions (e.g. monazite). Our results reveal no systematic dependency of $D_{Zrc\text{-}melt}$ with MIZ size, composition, and entrapment temperature. However, $D_{Zrc\text{-}melt}$ derived from MIZ of Rt-bearing mafic cumulate rocks are generally more variable compared to those of Rt-free mafic and felsic rocks, in particular with respect to Ti and REE (Figs. 5.12, 5.13).

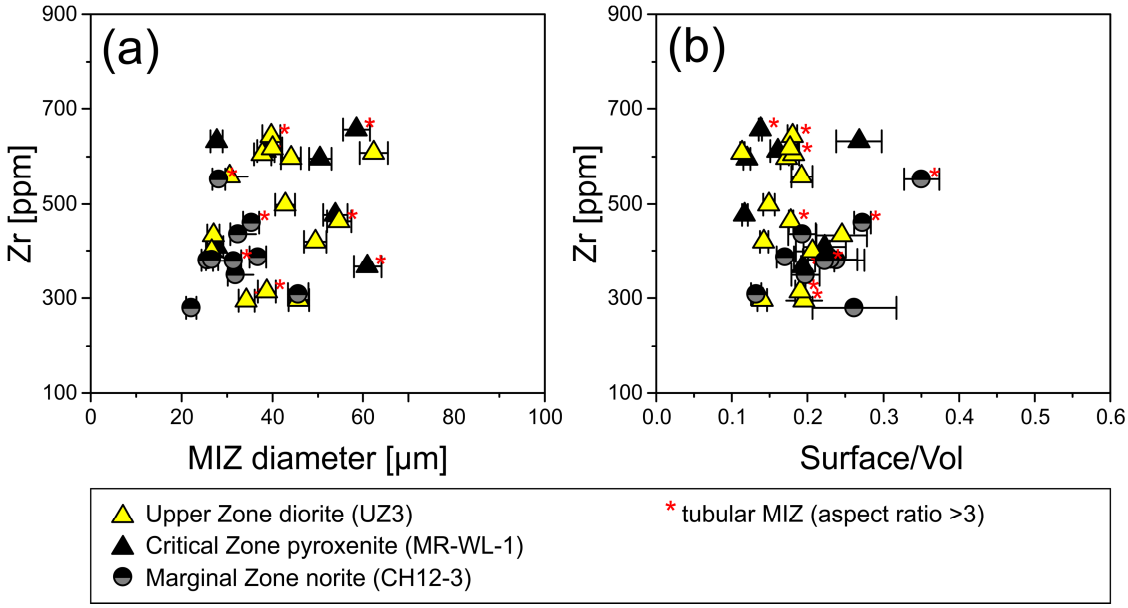

Figure 5.9 - Zr content *versus* geometric parameters of MIZ from different samples of the BC. Note that Zr contents of MIZ are neither correlated with (a) average MIZ diameter nor with (b) MIZ surface/volume ratio. Error bars – error of size measurement (ca. 5%). Red stars indicate tubular MIZ (aspect ratios >3).

5.6 Discussion

5.6.1 Entrapment temperatures of MIZ

In this study, three independent sets of geothermometers are applied to calculate the temperature of MIZ entrapment and host zircon crystallization in mafic and felsic rocks of the BC: (1) liquidus temperatures of MIZ, (2) TiO_2 and zircon saturation temperatures of MIZ, (3) Ti-in-zircon thermometry of host zircon. In the following, the results obtained by these different geothermometric methods are compared and discussed.

Calculation of the liquidus temperatures ($T_{Liq\text{-}QAO}$ and $T_{Liq\text{-}rM}$) is based on major element compositions of the MIZ and the method is largely independent on the occurrence of accessory minerals like rutile, ilmenite, titanite or Ti-magnetite as well as on the homogenization procedure, which may affect certain trace element compositions due to host zircon dissolution (see chapter 6.2 “Zircon saturation thermometry of MIZ”). Results of our study show that MIZ from all samples yield a similar range in liquidus temperature ($T_{Liq\text{-}QAO}$) derived from the Qz-Ab-Or diagram of Tuttle and Bowen (1958), in which MIZ of all samples cluster at 930-850 °C in the Qz field; mainly for mafic samples, temperatures range down to the cotectic line at ~700 °C (Fig. 5.6). We note that for most MIZ, $T_{Liq\text{-}QAO}$ is about 50-100 °C lower than $T_{Liq\text{-}rM}$ calculated by rhyolite-MELTS for H_2O = 2.4 wt.%, which is the average H_2O content measured by SIMS. This difference can be explained by several effects. The Qz-Ab-Or diagram of Tuttle and Bowen (1958) is based on a pure KNASH-system with H_2O in excess (ca. 5.9 wt.% at 200 MPa, see Holtz et al. (1992)), whereas $T_{Liq\text{-}rM}$ includes additional system components (CaO, MgO, FeO, Cl, F) and was calculated for only 2.4 wt.% H_2O. Previous studies have shown that the liquidus temperature will increase (at constant P) with increasing CaO (i.e. normative anorthite content), and decreasing H_2O contents compared to the water-saturated Qz-Ab-Or system (see Wilke et al., 2017 and references therein) - (Fig. 5.11a). To correct for anorthite contents of <20 %, Blundy and Cashman (2001) presented a projection scheme for water-saturated systems. If applied to MIZ of the BC, liquidus temperatures decrease by 20-80 °C and are not consistent with temperatures obtained by other geothermometers applied to MIZ and host zircon (e.g. T_{TiSat}, $T_{Ti\text{-}Zrc}$). We note, that in all investigated MIZ, the amount of CaO, MgO, FeO, Cl and F is minor and that $T_{Liq\text{-}rM}$ and $T_{Liq\text{-}QAO}$ are essentially the same (within ±25°C), if $T_{Liq\text{-}rM}$ is calculated with 4 wt.% H_2O (Fig. 5.11a). Significantly higher $T_{Liq\text{-}rM}$ of 60-150 °C compared to $T_{Liq\text{-}QAO}$ are only obtained for MIZ having normative anorthite contents of >6.5 % (at same pressure and H_2O content). However, $T_{Liq\text{-}rM}$ is strongly dependent on H_2O content. For the investigated MIZ, the H_2O contents measured by SIMS range from 1.6 to 4.0 wt.% (excluding MIZ located along fractures), mostly close to the average of 2.4 wt.%. All these values are much lower than H_2O contents of 5.8-6.7 wt.% (average: 5.9 wt.%) obtained by experiments for water-saturated granitic melts at 200 MPa (Tuttle and Bowen, 1958; Holtz et al., 1992). This difference suggests that all studied MIZ are H_2O-undersaturated. This raises the

question whether the measured H_2O contents still reflect the primary compositions or were biased by post-entrapment alteration and/or during MIZ homogenization. Alteration cannot completely be excluded, but perhaps was minor and incomplete as suggested by the observation of intact aqueous fluid inclusions and hydrous phases (muscovite, amphibole, biotite) in recrystallized MIZ (Fig. 5.2c). Significant H_2O loss during homogenization, e.g. by diffusion through host zircon lattice also seems unlikely, as suggested by relatively high and variable H_2O contents preserved in the investigated MIZ. However, the very low H_2O contents measured by SIMS on MIZ in fractured host zircon suggest that these MIZ underwent H_2O leakage either prior to and/or during homogenization by IHPV (Fig. 5.4d).

In combination, our results suggest that MIZ in all investigated rocks were H_2O-undersaturated by the time of entrapment. For Rt-bearing mafic rocks, the degree of undersaturation can be bracketed by comparing $T_{Liq\text{-}rM}$ (calculated for different H_2O contents) with results of Ti-in-zircon ($T_{Ti\text{-}Zrc}$) geothermometry, which is independent of H_2O content. Host zircon from the Rt-bearing samples (CH12-3, MR-WL-1 and UG2M) yields $T_{Ti\text{-}Zrc}$ between 777 and 916 °C, which only overlap with $T_{Liq\text{-}rM}$ of the respective MIZ if calculated with ca. 3-4 wt.% H_2O (Fig. 5.10). For most MIZ, these H_2O contents are 20-40 % higher than those measured by SIMS, suggesting minor to moderate H_2O loss after entrapment. For all Rt-free felsic and mafic rocks (granites and ferrodiorites), agreement between $T_{Liq\text{-}rM}$ and $T_{Ti\text{-}Zrc}$ is only achieved if a highly reduced TiO_2 activity of aTiO$_2$ = 0.3±0.1 is applied for Ti-in-zircon geothermometry, and H_2O contents of 3.9±0.5 wt.% for rhyolite-MELTS calculations. In that case, the resulting temperatures also overlap with $T_{Liq\text{-}QAO}$ (Fig. 5.11b). In summary, the results indicate that convergence in temperatures for MIZ entrapment and host zircon growth is only achieved for all three geothermometers, if (1) the original H_2O content of the MIZ was 20-40 % higher than measured by SIMS, and (2) aTiO$_2$ = 0.3 is applied for Ti-in-zircon thermometry to Rt-free felsic and mafic rocks. This activity is significantly lower than aTiO$_2$ = 0.7, commonly used for Rt-free rocks in the literature (Hayden and Watson, 2007; Fu et al., 2008). However, it is in good agreement with the most recent results presented by Schiller and Finger (2019), showing that in Rt-free felsic magmas aTiO$_2$ is commonly ≤0.5 during zircon growth. A very similar conclusion was also reached by the study of Gudelius et al. (2020), suggesting that zircons in Rt-free felsic and mafic rocks of the BC crystallized at aTiO$_2$ = 0.3.

The conclusions above are further supported by the results obtained by the TiO_2 saturation geothermometer of Xiong et al. (2011). For Rt-rich mafic rocks of the Critical Zone (MR-WL-1, UG2M) agreement between T_{TiSat}, $T_{Ti\text{-}Zrc}$, and $T_{Liq\text{-}rM}$ for all MIZ-host zircon pairs is only reached if H_2O contents of ca. 4 wt.% H_2O are used for $T_{Liq\text{-}rM}$ (Fig. 5.10), and for all Rt-free rocks, by additionally using a reduced TiO_2^{rutile} of 30±10 wt.% for T_{TiSat} (Figs. 5.10, 5.11c). We note that applying the "30% rule" to both the TiO_2 saturation geothermometer (TiO_2^{rutile} = 30 wt.%) and the Ti-in-zircon geothermometer (aTiO$_2$ = 0.3) yield identical temperatures within

20 °C when applied to most MIZ of Rt-free mafic and felsic rocks (Figs. 5.10, 5.11b, c). Important differences were only obtained for Rt-bearing sample CH12-3 of the Marginal Zone, where $T_{Ti\text{-}Sat}$ is highly variable (671-829 °C) and 40-200°C lower than $T_{Ti\text{-}Zrc}$ and $T_{Liq\text{-}rM}$ (Fig. 5.10). These discrepancies point to a disequilibrium in TiO_2 abundances between MIZ and host zircon, perhaps resulting from kinetic effects due to zircon growth in rapidly evolving intercumulus melt, caused by fast cooling along the contact of the Marginal Zone with quartzitic country rocks with a cooling rate >>500 °C/Ma (Zeh et al., 2015).

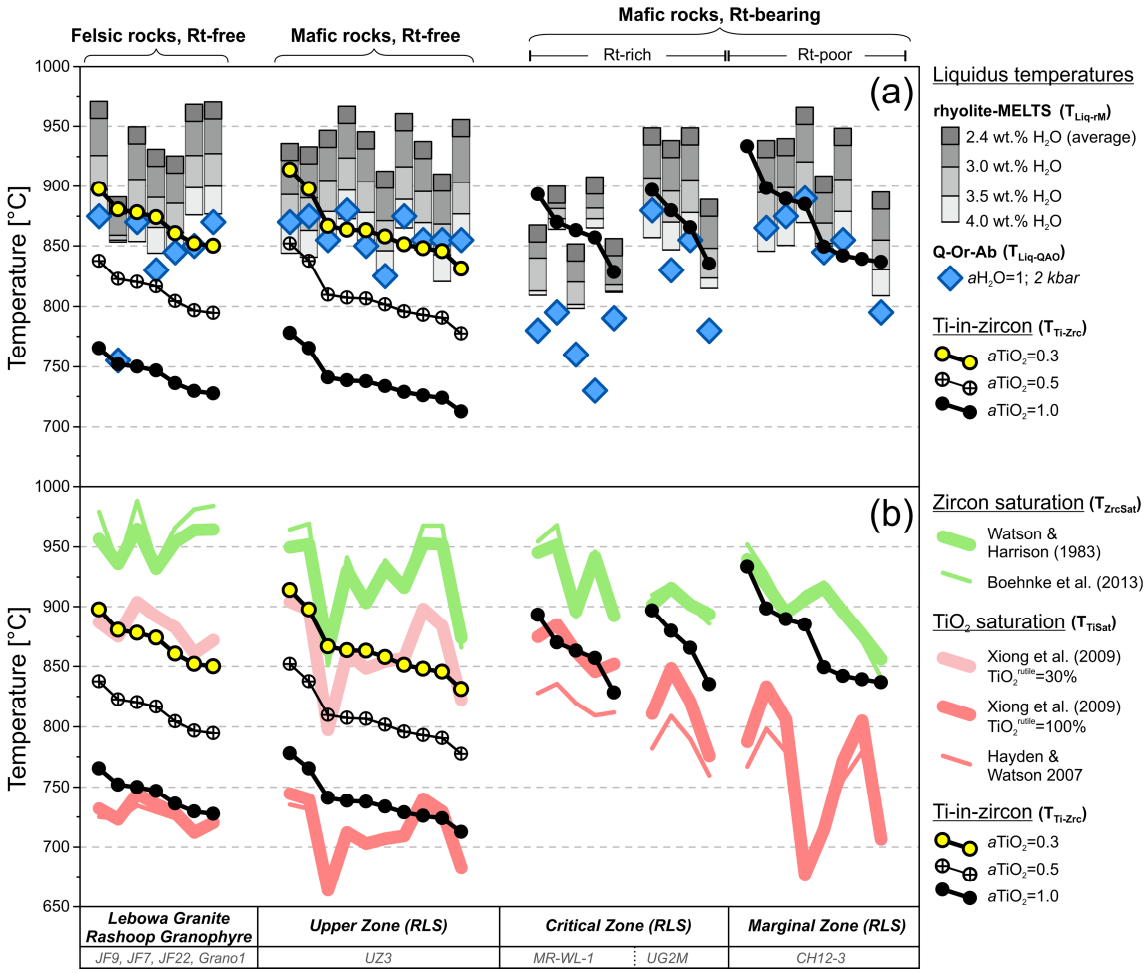

Figure 5.10 - Comparison of temperatures for MIZ entrapment obtained by different geothermometric methods for Rt-bearing and Rt-free rocks of the BC. (a) Comparison of liquidus temperatures ($T_{Liq\text{-}rM}$ and $T_{Liq\text{-}QAO}$) derived from MIZ with Ti-in-zircon temperatures ($T_{Ti\text{-}Zrc}$) derived from host zircon. $T_{Ti\text{-}Zrc}$ was calculated using the calibration of Ferry and Watson (2007) with $aTiO_2 = 1.0$ for Rt-bearing rocks and $aTiO_2 = 0.3$, 0.5 and 1.0 for Rt-free rocks. $T_{Liq\text{-}rM}$ was calculated using rhyolite-MELTS v.1.02 (Gualda et al., 2012) for different H_2O contents ranging from 2.4 wt.% H_2O (average content measured by SIMS) to 4.0 wt.% (maximum content measured by SIMS). $T_{Liq\text{-}QAO}$ was derived from the Qz-Ab-Or diagram of Tuttle and Bowen (1958) - (Fig. 5.6). (b) Comparison of zircon saturation temperatures (T_{ZrcSat}) and TiO_2 saturation temperatures (T_{TiSat}), both based on MIZ compositions, and Ti-in-zircon temperatures ($T_{Ti\text{-}Zrc}$) of host zircon. T_{ZrcSat} was calculated using the calibrations of Watson and Harrison (1983) and Boehnke et al. (2013), and T_{TiSat} with the geothermometer of Xiong et al. (2009) for 200 MPa, 2.4 wt.% H_2O (average value measured by of SIMS) and TiO_2^{rutile} = 100% for Rt-bearing rocks, and TiO_2^{rutile} = 30% for Rt-free rocks. In addition, TiO_2 saturation temperatures after Hayden and Watson (2007) are shown. Note that for Rt-bearing rocks, parity between all geothermometric methods is achieved by applying $aTiO_2 = 1.0$, TiO_2^{rutile} = 100 wt.%, and H_2O contents of 3-4 wt.%, and for all Rt-free rocks by using the same H_2O contents, but a significantly reduced TiO_2 activity of $aTiO_2 = 0.3$, and TiO_2^{rutile} = 30 wt.%.

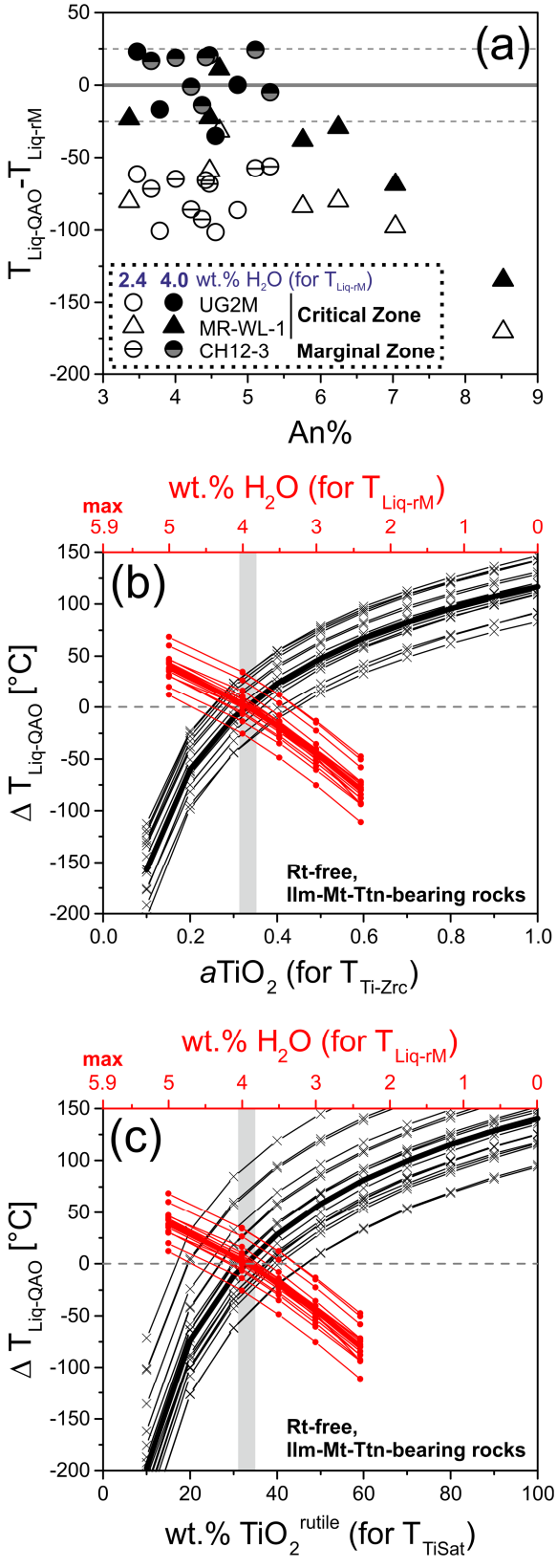

Figure 5.11 - (a) Differences in liquidus temperatures obtained from MIZ using the Qz-Ab-Or diagram of Tuttle and Bowen (1958) ($T_{Liq-QAO}$) and rhyolite-MELTS modelling (T_{Liq-rM}) for H_2O = 2.4 wt.% (average content measured by SIMS) and for H_2O = 4.0 wt.% (maximum content measured by SIMS). Note that for the Rt-bearing mafic rocks of the Critical and Marginal Zones, $T_{Liq-QAO}$ and T_{Liq-rM} are identical within ±25 °C (dotted lines), but only for MIZ having H_2O = 4.0 wt.% and low anorthite contents (An < 5.5%). For MIZ with An > 5.5% and/or H_2O = 2.4 wt.% (average SIMS value) $T_{Liq-QAO}$ is always significantly lower than T_{Liq-rM}. (b) Differences between $T_{Liq-QAO}$ (Tuttle and Bowen, (1958), T_{Liq-rM} (rhyolite-MELTS, Gualda et al., 2012) and T_{Ti-Zrc} (Ti-in-zircon thermometry; Ferry and Watson, 2007) by applying variable H_2O contents for T_{Liq-rM} modelling (2.4-5.0 wt.%), and variable TiO_2 activities for T_{Ti-Zrc} calculations ($aTiO_2$ between 0.1 and 1.0) to MIZ from Rt-free mafic and felsic rocks of the BC. The maximum value of the H_2O axis was defined as 5.9 wt.%, corresponding to the value for water-saturated granitic melts at 200 MPa (Holtz et al., 1992). Note that convergence for all three geothermometers is reached only at H_2O ~ 4.0 wt.% and $aTiO_2$ ~ 0.30. (c) Deviation of $T_{Liq-QAO}$ (Tuttle and Bowen (1958), from T_{Liq-rM} (rhyolite-MELTS, Gualda et al. 2012) and T_{TiSat} (TiO_2 saturation thermometry; Xiong et al. (2009) by applying variable H_2O contents for T_{Liq-rM} modelling (2.5-5.0 wt.%), and variable TiO_2^{rutile} (0-100 wt.% at 200 MPa and 2.4wt.% H_2O) for T_{TiSat} calculations of MIZ in Rt-free mafic and felsic rocks of the BC. Note that convergence of all three geothermometers is reached only at H_2O ~ 4.0 wt.% and TiO_2^{rutile} ~30 wt.%.

Table 5.2 Temperature constraints for melt inclusion entrapment and host zircon crystallization (in °C)

Temperature constraint	melt inclusion in zircon (MIZ)																host zircon				bulk rock
Thermometer	$T_{Liq\text{-}QAO}$				$T_{Liq\text{-}rM}$ (2.4% H_2O)			(4% H_2O)		T_{ZrcSat}				T_{TiSat} *(TiO_2^{rutile} = 30%)				$T_{Ti\text{-}Zrc}$ *($aTiO_2$ = 0.3)				$T_{ZrcSat\ BR}$
Sample	avg	min	max	*n*	avg	min	max	avg	*n*	avg	min	max	*n*	avg	min	max	*n*	avg	min	max	*n*	
Felsic rocks (Rt-free)																						
JF9*	881	855	915	*18*	955	929	981	864	*3*	948	931	965	*2*	842	812	872	*2*	856	831	879	*13*	838
MOK-1*	846	820	865	*5*	938	935	942	854	*3*	956	950	965	*3*	888	862	904	*3*	874	864	888	*9*	845
MOK-2*	855	830	880	*9*	-	-	-	-	-	-	-	-		-	-	-	-	874	843	905	*44*	882
JF7*	884	810	915	*18*	963	-	-	873	*1*	957	-	-	*1*	887	-	-	*1*	860	747	908	*57*	858
Grano1*	877	740	910	*19*	923	884	961	866	*2*	950	936	964	*2*	868	861	875	*2*	868	819	920	*35*	858
JF22*	842	775	930	*7*	933	918	956	843	*3*	939	932	954	*3*	853	783	892	*3*	863	847	874	*10*	853
Rt-free mafic rocks - RLS																						
JF23*	865	730	955	*10*	967	920	1028	827	*3*	943	897	982	*3*	897	860	926	*3*	857	814	900	*25*	-
UZ3*	860	825	880	*14*	933	897	960	849	*14*	918	864	953	*14*	856	785	904	*14*	859	778	925	*29*	-
Rt-bearing mafic rocks - RLS																						
MR-B	851	735	915	*12*	928	978	841	847	*14*	915	-	-	*1*	778	-	-	*1*	841	771	893	*40*	-
MR-WL-1	831	700	925	*29*	871	831	921	829	*7*	930	892	952	*7*	876	846	920	*7*	851	749	933	*37*	-
UG2M	792	720	890	*13*	924	882	942	844	*4*	903	894	915	*4*	814	776	848	*4*	874	738	931	*50*	-
CH12-3	859	795	895	*8*	930	888	967	849	*8*	901	856	940	*10*	765	677	833	*10*	860	831	905	*23*	-

avg = average; $T_{liq\text{-}QAO}$ = liquidus derived from the Qz-Ab-Or diagram of Tuttle and Bowen (1958); $T_{liq\text{-}rM}$ = liquidus temperature calculated by rhyolite-MELTS for 2.4 wt.% and 4 wt.% H_2O (Gualda et al. 2012); T_{ZrSat} = zircon saturation temperature after Watson and Harrison (1983); T_{TiSat} = TiO_2 saturation temperature of Xiong et al. (2009) calculated for 200 MPa and 2.4 wt.% H_2O; $T_{Ti\text{-}Zrc}$ = Ti-in-zircon temperature of Ferry and Watson (2007) calculated with $aSiO_2$=1; $T_{ZcSat\ BR}$ = zircon saturation temperature calculated from bulk rock composition after Watson and Harrison (1983)

* rutile-free, ilmenite-magnetite-titanite-bearing rocks: T_{TiSat} was calculated using TiO_2^{rutile} = 30 % and $T_{Ti\text{-}Zrc}$ using $aTiO_2$ = 0.3. For all other samples TiO_2^{rutile} = 100 % and $aTiO_2$ = 1

5.6.2 Zircon saturation thermometry of MIZ

The results of this study also show that zircon saturation temperatures calculated for the MIZ are always much lower than the laboratory homogenization temperature of 1100 °C. Furthermore, they are highly variable with $T_{ZrcSat\text{-}W}$ ranging from 856 to 982 °C (Watson and Harrison, 1983) and $T_{ZrcSat\text{-}B}$ from 841 to 1023 °C (Boehnke et al., 2013). These results suggest that MIZ compositions were not biased by host zircon melting during the homogenization experiments. For Rt-bearing mafic rocks, T_{ZrcSat} is commonly identical or slightly higher (up to 50 °C) than $T_{Ti\text{-}Zrc}$ and $T_{Liq\text{-}rM}$ calculated for 4.0 wt.% H_2O (Fig. 5.10, Table 5.2). For the Rt-free samples, T_{ZrcSat} are mostly 50-100 °C higher than $T_{Ti\text{-}Zrc}$ (calculated for $a\mathrm{TiO_2}$ = 0.3) and T_{TiSat} (using $\mathrm{TiO_2}^{rutile}$ of 30 wt.%).

Our results suggest that the measured Zr contents of the MIZ are close to those during entrapment and that significant interaction with host zircon, e.g. by dissolution and diffusive exchange, did not occur during our homogenization experiments. This conclusion is supported by two lines of evidence. First, the Zr contents of the MIZ are not correlated with inclusion size, neither with MIZ diameters nor MIZ surface/volume ratios (Fig. 5.9). Second, measured Zr contents of the MIZ are much lower (280-717 ppm) than the 1800 ppm predicted by diffusion modelling, which was calculated for typical MIZ diameters of 40 µm, 6 h heating at 1100°C and published diffusion coefficients for Zr in granitic melts with 2-4 wt.% H_2O and/or elevated F- and Cl-contents (Harrison and Watson, 1983; Baker et al., 2002). For modelling details see supplementary materials 2. The obvious absence of significant host zircon dissolution during our experiments implies that the original MIZ composition remained largely unaltered during our experiments also with respect to all zircon-compatible elements (e.g. Hf, U, Th, and HREE), and that zircon-melt partitioning coefficients of these elements are reliable.

5.6.3 Zircon-melt partitioning coefficients

Zircon-melt partitioning coefficients ($D_{Zrc\text{-}melt}$) derived from all MIZ-host zircon pairs of mafic and felsic rocks are very similar. Variations for most trace elements are commonly less than one order of magnitude. The dataset also reveals no clear correlation between $D_{Zrc\text{-}melt}$ and MIZ size, MIZ composition, entrapment temperature, and host rock composition (Figs. 5.12; 5.13). Partitioning coefficients are essentially the same for all trace elements in MIZ having diameters between 21 and 60 µm, suggesting that $D_{Zrc\text{-}melt}$ was not biased by boundary layer effects. The same conclusion was also been drawn by Thomas et al. (2003) for MIZ of similar size sampled from quartz diorite.

The partitioning coefficients derived in this study for mafic rocks (norite, pyroxenite, diorite) are slightly higher on average and more variable compared to those of felsic rocks (Fig. 5.13; Table 5.3). These differences might be explained by a different degree of magma fractionation at the time of zircon growth, which was at <20% in felsic rocks compared to >75%

in mafic rocks, as indicated by rhyolite-MELTS modelling (Fig. 5.14). These results support the conclusion that zircon crystallization in mafic rocks occurred in highly fractionated intercumulus domains in an assemblage with other accessory and major minerals (Kfs, Pl, Bt, Zrc, Rt, Ap, Mnz). Competitive growth among all these phases caused great variability in trace element contents on a small scale (Gudelius et al., 2020), now reflected by variable $D_{Zrc\text{-}melt}$.

The partitioning coefficients obtained in this study overlap with those derived from granite melt experiments by Rubatto and Hermann (2007) at 900 °C, and those of Thomas et al. (2002) calculated from MIZ entrapped between 725 and 999 °C. However, they are significantly lower by one order of magnitude than those obtained by Rubatto and Hermann (2007) at 800 °C (see Fig. 5.12). As shown in Figure 5.12, our $D_{Zrc\text{-}melt}$ are on average also slightly lower for LREE, and slightly higher for HREE compared to those of Thomas et al. (2002). Significant differences between this study and Thomas et al. (2002) were only found for $D^{Ti}_{Zrc-melt}$ and $D^{Nb}_{Zrc-melt}$, which in our study are 2 to 3 orders of magnitude lower ($D^{Ti}_{Zrc-melt}$= 0.02 *versus* 3.1, $D^{Nb}_{Zrc-melt}$ = 0.2 *versus* 312). We note that the dataset of Thomas et al. (2002) contains very high Ti contents for host zircon, which, when applied to Ti-in-zircon geothermometry, yield unrealistically high temperatures of >2000 °C, suggesting zircon alteration or analytical problems.

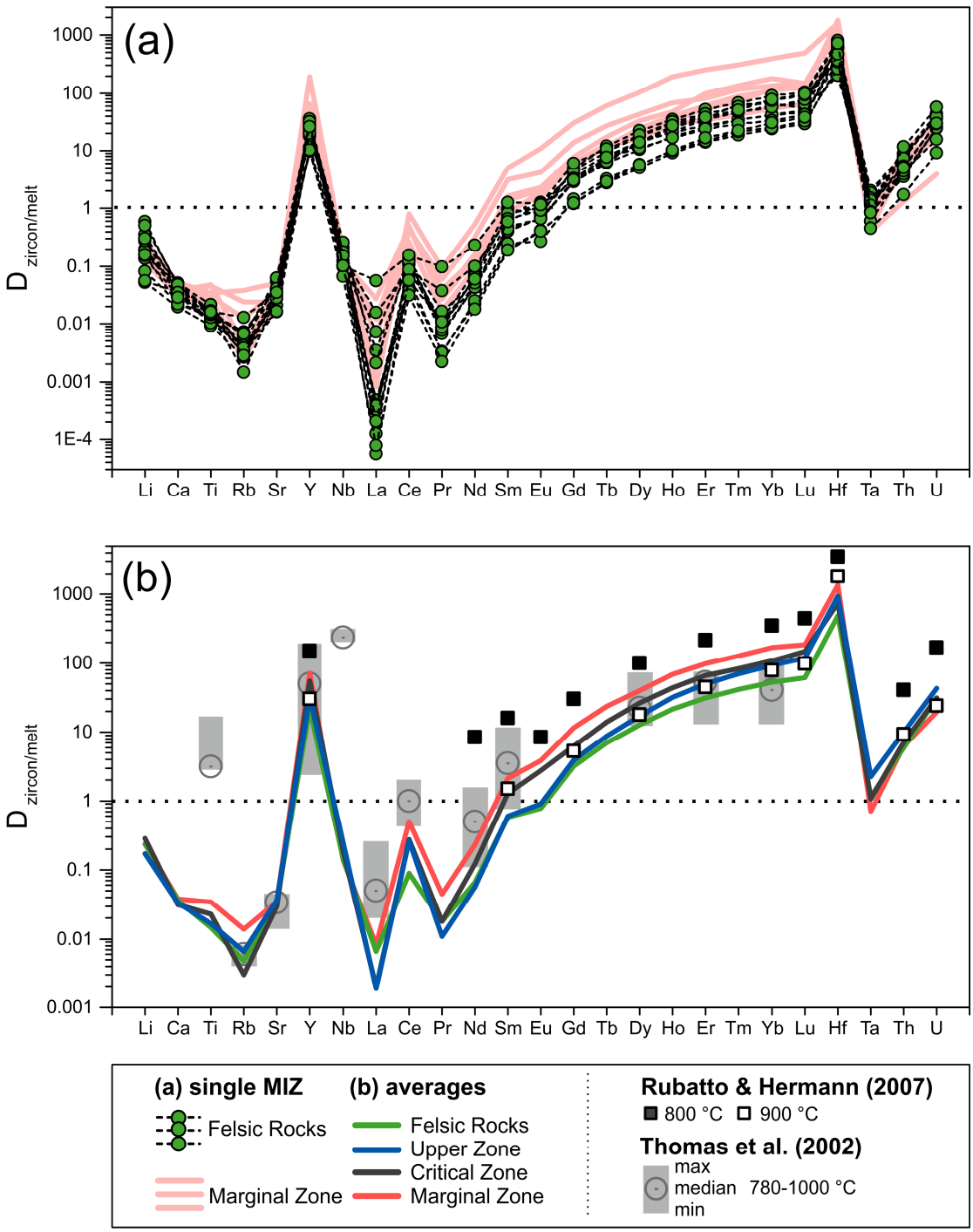

Figure 5.12 - Zircon-melt partitioning coefficients ($D_{Zrc\text{-}melt}$) obtained from melt inclusion - host zircon pairs. (a) Synopsis of $D_{Zrc\text{-}melt}$ values derived from MIZ of several felsic rocks of the BC (samples JF9, JF7, Grano1, MOK1, JF22) and from Marginal Zone norite (sample CH12-3). (b) Average $D_{Zrc\text{-}melt}$ values obtained from all felsic rocks and from different mafic rocks of the BC (Upper Zone, Critical Zone and Marginal Zone), compared to values of the experiments of Rubatto and Hermann (2007) carried out at 800 and 900 °C, and values derived by Thomas et al. (2002) from MIZ formed at temperatures between 780 and 999 °C.

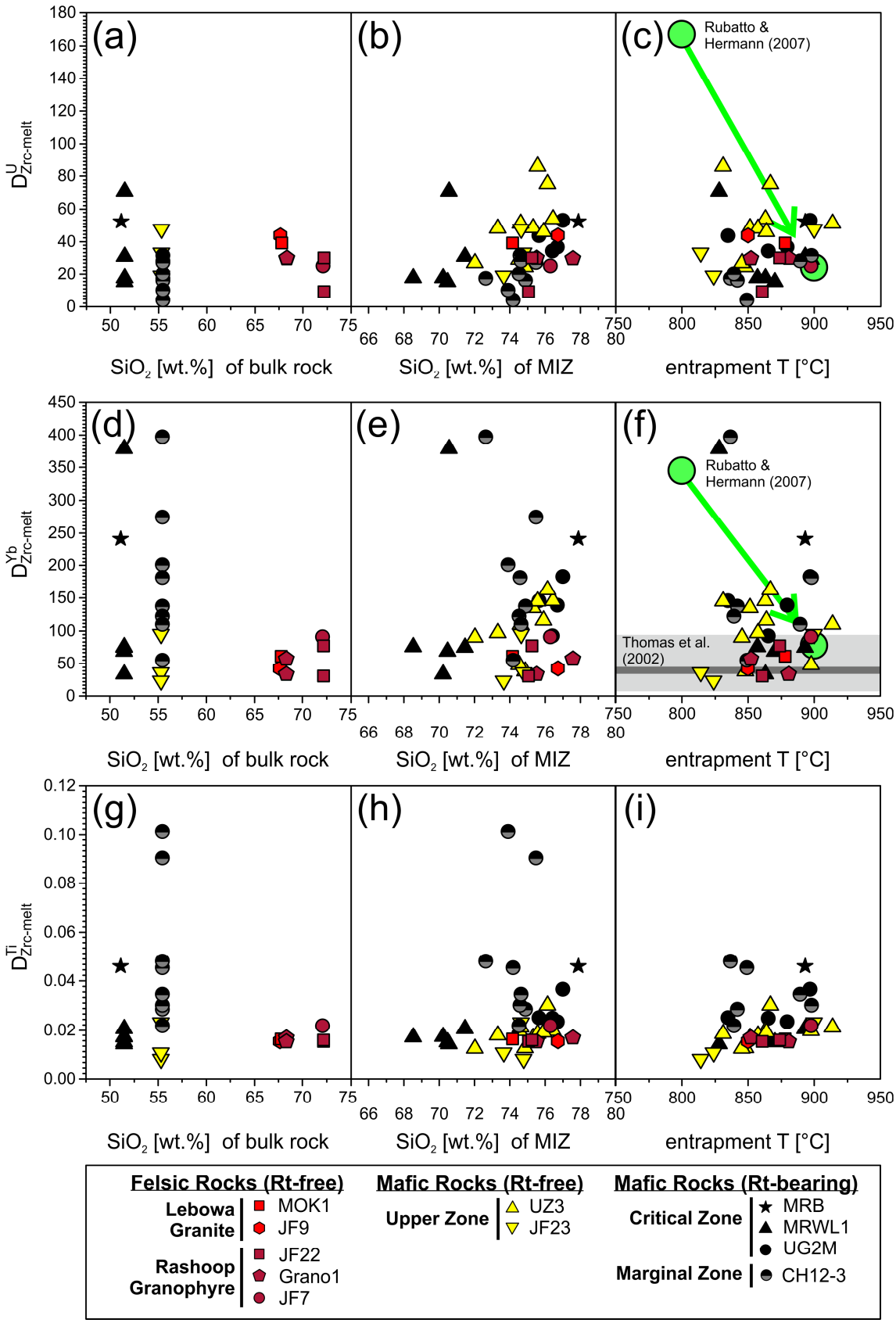

Figure 5.13 - Dependency of $D_{Zrc\text{-}melt}$ (U, Yb, Ti) on SiO_2 content of host rock (a, d, g), SiO_2 content of MIZ (b, e, h), and (c, f, i) MIZ entrapment temperature (which is the Ti-in-zircon temperature of host zircon). In (c) and (f) $D_{Zrc\text{-}melt}$ derived in this study are compared with those presented by Rubatto and Hermann (2007) and Thomas et al. (2002).

Table 5.3 Zircon-melt distribution coefficients derived from melt inclusions in zircon

	All samples		Felsic rocks		Upper Zone diorites		Critical Zone pyroxenites		Marginal Zone norite	
$D_{Zrc\text{-}melt}$	avg	1σ	avg	1σ	avg	1σ	avg	1σ	avg	1σ
n	*39*		*7*		*19*		*15*		*15*	
Li	0.2	*0.2*	0.3	*0.1*	0.22	*0.12*	0.26	*0.36*	0.24	*0.07*
Ti	0.022	*0.009*	0.017	*0.002*	0.017	*0.005*	0.025	*0.010*	0.03	*0.01*
Rb	0.006	*0.007*	0.005	*0.004*	0.0063	*0.0037*	0.0020	*0.0016*	0.014	*0.014*
Sr	0.04	*0.01*	0.04	*0.01*	0.038	*0.013*	0.032	*0.016*	0.03	*0.01*
Y	43	*39*	23	*8*	30	*17*	61	*49*	71	*62*
Nb	0.2	*0.1*	0.15	*0.05*	0.2	*0.1*	0.2	*0.3*	0.14	*0.03*
La	0.003	*0.005*	0.003	*0.006*	0.003	*0.004*	0.001	*0.002*	0.01	*0.01*
Ce	0.3	*0.2*	0.09	*0.03*	0.21	*0.18*	0.30	*0.18*	0.49	*0.18*
Pr	0.02	*0.02*	0.01	*0.01*	0.012	*0.012*	0.020	*0.016*	0.045	*0.028*
Nd	0.1	*0.1*	0.06	*0.03*	0.06	*0.04*	0.14	*0.10*	0.23	*0.17*
Sm	1.0	*1.1*	0.6	*0.3*	0.6	*0.4*	1.5	*1.2*	2.2	*1.6*
Eu	1.9	*2.8*	0.8	*0.3*	0.9	*0.5*	3.3	*4.4*	3.9	*3.6*
Gd	6	*5*	3	*1.2*	3.8	*2.3*	7.0	*5.4*	12	*10*
Tb	12	*11*	7	*3*	9	*5*	15	*12*	24	*19*
Dy	23	*19*	14	*5*	16	*10*	29	*22*	40	*32*
Ho	39	*34*	22	*9*	29	*18*	48	*35*	68	*62*
Er	58	*45*	33	*12*	45	*27*	73	*44*	97	*79*
Tm	76	*57*	43	*16*	61	*36*	91	*57*	128	*96*
Yb	100	*70*	56	*22*	81	*45*	117	*65*	167	*120*
Lu	126	*101*	68	*26*	102	*63*	165	*130*	184	*154*
Hf	913	*349*	622	*122*	843	*308*	911	*230*	1354	*406*
Ta	1.5	*1.0*	1.2	*0.5*	1.9	*1.1*	1.2	*0.8*	0.7	*0.2*
Th	8	*5*	5	*2*	9	*6*	8	*4*	6	*3*
U	33	*17*	29	*11*	39	*19*	34	*15*	19	*10*

avg = average; 1σ = standard deviation; n = number of MIZ - host zircon pairs; granitic rocks: samples JF9, MOK1, JF7, JF22; Upper Zone diorite: samples UZ3, JF23; Critical Zone pyroxenite: samples MR-WL-1, UG2M; Marginal Zone norite: sample CH12-3

5.6.4 Implications for Bushveld magma evolution

Several studies have shown that different stratigraphic units of the BC were formed from different parental magmas, comprising B1 (55.7 wt.% SiO_2; 11.9 wt.% MgO), B1:B2 mixtures (53.8 wt.% SiO_2; 11.6 wt.% MgO), UUMZ (53.8 wt.% SiO_2; 6.5 wt.% MgO) and felsic melts (~68-76 wt.% SiO_2; <0.1 wt.% MgO) (Hill et al., 1996; Barnes et al., 2010; VanTongeren et al., 2010). For mafic rocks of the RLS, these parental magmas are highly different from compositions of the MIZ, which are all rhyolitic (65-78 wt.% SiO_2; <0.8 wt.% MgO). This is in contrast to granitic rocks of the BC, where bulk rock compositions are very close to MIZ compositions, suggesting a highly different magmatic evolution prior to MIZ entrapment compared to the mafic rocks.

In order to better understand the magmatic evolution of the different felsic and mafic rocks of the BC, we compare in the following the compositions (and mineral assemblages) of the MIZ with those calculated with rhyolite-MELTS (Gualda et al., 2012), by using two different calculation modes for (i) fractional crystallization and (ii) equilibrium crystallization. The modelling results indicate that the composition of the MIZ of all felsic and mafic rocks of the BC can be explained by fractional crystallization from their parental magmas, even though there are minor discrepancies between modelled and observed compositions (Fig. 5.14). They

further reveal that MIZ compositions and mineral assemblages (in recrystallized MIZ) are commonly better reproduced by applying the "fractional crystallization" rather than the "equilibrium crystallization" mode in rhyolite-MELTS. This is exemplified in Figure 5.14d for the parental magma B1, where sufficiently high SiO_2, and sufficiently low Al_2O_3 contents, as well as Qz crystallization prior to MIZ entrapment are only achieved by applying the fractional crystallization mode. Nevertheless, even by applying the fractional crystallization mode the modelled SiO_2 contents are always 2-4 wt.% lower than those measured on MIZ at liquidus conditions of 850-930 °C. This deviation remains essentially the same, even if fO_2 (FMQ-1 to FMQ+1), P (from 150 to 300 MPa) and the initial H_2O content of the parental melt (from 0.2 to 2 wt.%) are varied. In felsic rocks, the deficit in modelled SiO_2 content is mostly compensated by higher contents in K_2O, Na_2O, CaO and FeO (up to 2 wt.%), and in mafic rocks by higher modelled CaO and FeO contents (up to 2 wt.%) – (for comparison see Fig. 5.14).

However, there are several other reasons why measured MIZ compositions are not exactly reproduced by modelling results. These include inadequate knowledge of parental magma compositions, complicated fractionation and magma chamber processes, and inappropriate activity models (Gualda et al., 2012). For the Upper Zone diorites and overlying granites, the composition of the parental magmas is not well constrained and mainly based on averages of respective bulk-rock compositions. In Figure 5.14a, consequences of applying different felsic parental magmas compositions are illustrated. The Upper Zone diorites are suggested to have formed from UUMZ parental magma, which according to VanTongeren et al. (2010) originally contained up to 25% of a felsic magma component, similar in composition to the Rashoop Granophyres. We note, that without this felsic component, the difference between modelled and observed MIZ compositions would be even larger (SiO_2 >4 wt.%, K_2O >4 wt.%, Na_2O > 2.5 wt.%, Al_2O_3 >2 wt.%), and that modelling results would not explain the observed apatite inclusions in zircon. We also note that the MIZ provide no evidence for unmixing of felsic and mafic melts as suggested by VanTongeren et al. (2010) and Fischer et al. (2016). Calcium-P-Fe rich melts, as described by Fischer et al. (2016) from Upper Zone apatite, were not found in the MIZ, suggesting MIZ entrapment after liquid immiscibility. We note that the composition of MIZ and host zircon in Upper Zone diorite do not necessarily require magma unmixing, but could also be explained by physical mixing of UUMZ magma with a felsic melt, which was already proposed for the UUMZ in previous studies (Ashwal, 2005; Scoon and Mitchell, 2012; Yuan et al., 2017). Possibly, a felsic melt existed at the roof of the BC during mafic magma injection and was formed by melting of Rooiberg volcanics as suggested by field relationships and thermal modelling (Walraven, 1987), and by Hf isotope constraints (Zeh et al., 2020). Physical mixing is also supported by nearly identical major and trace element compositions of MIZ and host zircon in Upper Zone diorite and overlying granites, which are

significantly different to those found in the mafic cumulate rocks of the lower RLS (Figs. 5.5, 5.7).

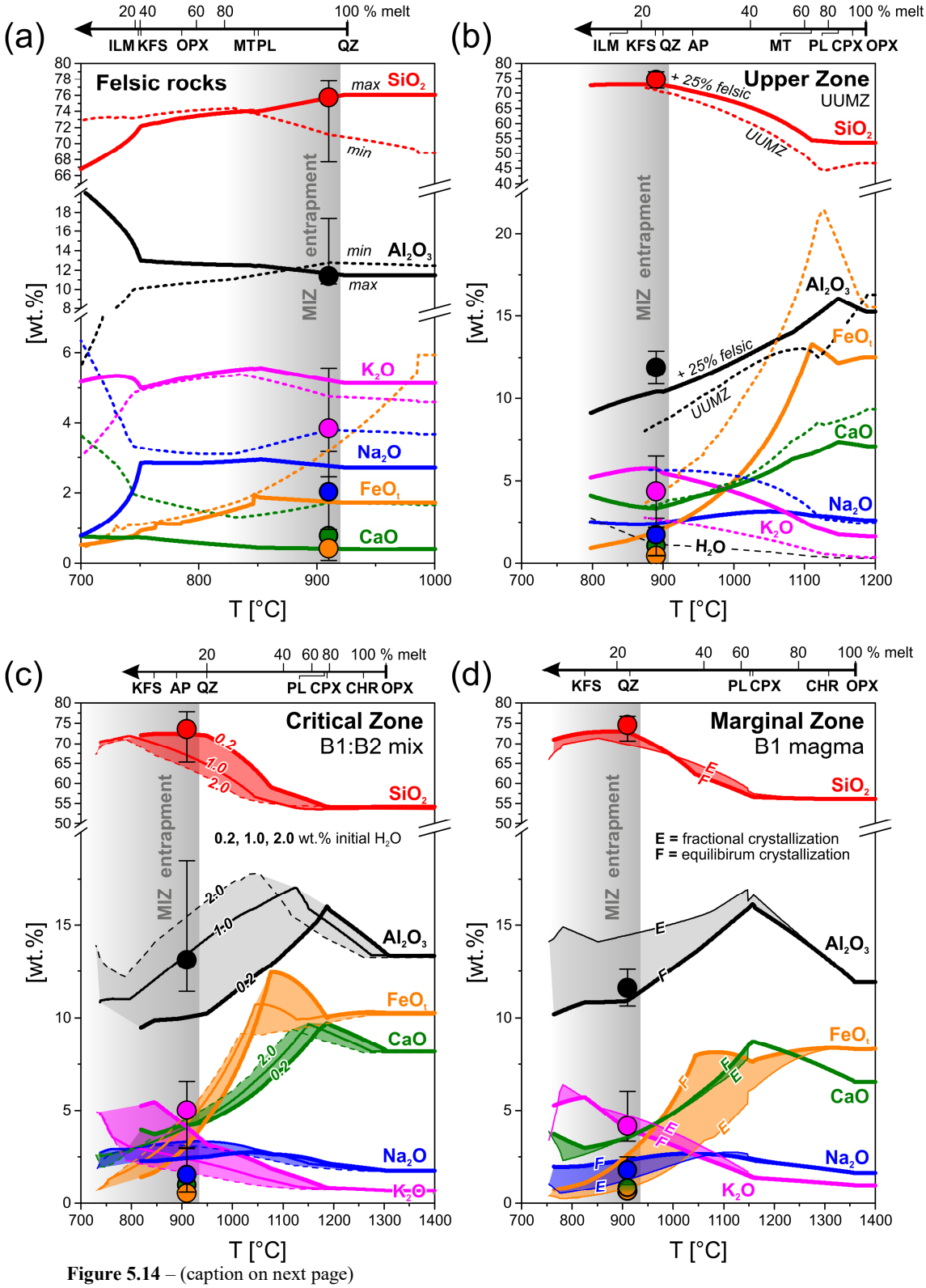

Figure 5.14 – (caption on next page)

Figure 5.14 - Comparison between measured and modelled melt compositions for (a) granite magmas, (b) UUMZ magmas, (c) B1:B2 magma mixture, and (d) B1 magma of the BC. Filled circles represent average MIZ compositions (maximum and minimum values presented by vertical error bars), and solid and dotted lines element evolutionary trends modelled with rhyolite-MELTS v.1.02 (Gualda et al., 2012) for different parameters. MIZ entrapment temperatures are averages of the ten highest liquidus temperatures obtained from the Qz-Ab-Or diagram of Tuttle and Bowen (1958) for the respective rock units. All rhyolite-MELTS models were calculated at 200 MPa and fO_2 = FMQ, using the "fractionate solids" mode (F), except for (d) where additional calculations were carried out using equilibrium crystallization (E). Presented melt fractions (% melt) and crystallization sequence of the minerals Opx, Cpx, Mt, Ap, Ilm, Chr, Pl, Kfs, Qz relate to models represented by thick solid lines. In diagram (a) the evolution of two felsic parental magmas of distinct composition (both for H_2O = 2.2 wt.%) is modelled, based on data of Hill et al. (1996) and Kleemann and Twist (1989) - (thick lines = felsic parental melt with maximum SiO_2 content, dashed lines = felsic parental melt with minimum SiO_2 content). (b) Modelling for a pure UUMZ magma (dashed lines), and UUMZ + 25% felsic component (average Rashoop Granophyre of VanTongeren et al., 2010) - (thick lines), all for H_2O = 0.3 wt.%. (c) Calculation of fractional crystallization of mixed B1-B2 parental magma (B1:B2 = 60:40 as recommended by Barnes et al., 2010) using initial H_2O contents of 0.2 wt.% (thick lines), 1 wt.% (thin lines) and 2 wt.% (dashes lines). (d) Evolutionary trends of B1 parental magma modelled by using equilibrium (E) and fractional crystallization modes (F), at H_2O = 0.4 wt.%. Note that the bulk rock composition of sample CH12-3 overlaps with B1 parental magma (high-Mg andesite), whereas the MIZ composition is rhyolitic.

In mafic cumulate rocks of the RLS differences between observed and modelled MIZ compositions potentially result from three major effects: First, MIZ represent intercumulus melts which were entrapped after >75% fractional crystallization of the parental magmas B1, B2, and UUMZ (as suggested by our modellings; see Fig. 5.14b-d) and therefore, were most likely modified by partial re-equilibration with surrounding cumulus phases and/or by migrating intercumulus melts, two parameters not considered by rhyolite-MELTS modelling. Second, the investigated mafic rocks contain abundant hydrous phases like amphibole and biotite (in assemblage with zircon), the activity-compositions (a-X) relationships of which are not well constrained by rhyolite-MELTS, as discussed by Gualda et al. (2012). Third, initial melt compositions might have been different to parental magma compositions (e.g. B1 and B2) used for modelling, perhaps caused by the cyclic ingression of parental magmas into already evolved resident melts within the RLS magma chamber (e.g. Wilson, 2015; Yuan et al., 2017). This mixing effect perhaps was least for chilled norite from the floor contact of the Marginal Zone (sample CH12-3), having a bulk rock composition identical to B1. We note that for sample CH12-3, very good agreement between modelled and observed MIZ composition is achieved by using an initial H_2O content of 0.4 wt.% for the B1 magma (Fig. 5.14d), close to the LOI value of 0.31 wt.% given by Barnes et al. (2010). In contrast, agreement between modelled and observed MIZ compositions for rocks of the Critical Zone is much poorer, in particular for Al_2O_3, K_2O, Na_2O and CaO contents, independent from the H_2O content used for modelling. The largest deviations are seen for the MIZ of sample MR-WL-1 from the Merensky Reef, containing chromite layers and olivine in an otherwise relatively evolved melt reflected by the occurrence of interstitial biotite, alkali feldspar and quartz. Thus, for samples of the Merensky Reef, the difference between measured and modelled MIZ compositions could be well explained by MIZ entrapment from different batches of heterogeneous intercumulus melt, which originally resulted from the mixing of a parental magma (B1:B2 = 60:40) with an already evolved residual magma.

Our modelling also indicates quartz crystallization prior to alkali feldspar in all rocks independent whether they formed from mafic or felsic parental magmas. This finding is in agreement with the observed linear trends above the cotectic line in the Qz-Or-Ab diagram of Tuttle and Bowen (1958), defined by the MIZ compositions of our samples (Fig. 5.6). For the felsic rocks, Qz-in prior to MIZ entrapment for a model using 2.2 wt.% initial H_2O (as suggested by Kleemann and Twist, 1989) preferentially occurs for a relatively SiO_2-rich parental magma, e.g. the maximum of the dataset of Hill et al. (1996) - (Fig. 5.14a). For the mafic rocks, Qz-in reaction prior to MIZ entrapment is achieved only by using initial H_2O contents of 0.4 wt.% for B1 and B1-B2 parental magmas (similar to 0.45 wt.% H_2O of the Chr-saturated magma forming the Critical Zone proposed by Latypov et al., 2018), as well as 0.3 wt.% for UUMZ magma (Fig. 5.14 c, d). These rather low initial H_2O contents result in still water-undersaturated melts during MIZ entrapment at ca. 900°C (i.e. after ca. 75% of melt fractionation) - (calculated H_2O contents during MIZ entrapment range from 1.3 to 3.0 wt.% H_2O). This finding is in agreement with the H_2O contents measured by SIMS on MIZ (average H_2O = 2.4 wt.%), and those required by our geothermobarometric calculations (3.0-4.0 wt.% H_2O) - (Figs. 5.10, 5.11). In summary, our modelling results suggest that mafic and felsic rocks of the BC were formed mainly by fractional differentiation from parental magmas, which themselves were modified by cyclic ingression into evolved resident magmas, and by heterogeneous fractionation processes prior to MIZ entrapment.

6.7 Conclusions

Results of this study show that melt inclusions in zircon (MIZ) provide detailed information about melt compositions and temperatures during zircon growth in felsic and mafic rocks.

MIZ in mafic and felsic rocks of the BC all have rhyolitic compositions with H_2O contents of 1.6-4.0 wt.% (i.e. water-undersaturated at 200 MPa), and were entrapped mainly at 930-850 °C, tailing down to 700 °C in mafic rocks.

Consistent MIZ entrapment temperatures can be obtained by applying three largely independent methods: (1) liquidus geothermometry (based on experimentally derived Qz-Ab-Or phase diagrams and thermodynamic modelling), (2) TiO_2 saturation geothermometry, (3) Ti-in-zircon geothermometry.

For Rt-bearing mafic rocks of the BC (Marginal and Critical zones), all three geothermometers yield consistent results by applying $a TiO_2 = 1.0$ (for Ti-in-zircon geothermometry), $(TiO_2)^{rutile}$ = 100 wt.% (for TiO_2 saturation geothermometry), and H_2O contents of 3-4 wt.% (for liquidus and TiO_2 saturation geothermometry). These H_2O contents are commonly higher than those

measured by SIMS (1.6 to 4.0 wt.%: average 2.4 wt.%), suggesting minor to moderate H_2O loss from the MIZ after entrapment.

For Rt-free felsic and mafic rocks, agreement between all three geothermometers is only achieved by applying similar H_2O contents (4 wt.%), but a significantly reduced TiO_2 activity of $aTiO_2$ = 0.3 for Ti-in zircon geothermometry, and $(TiO_2)^{rutile}$ = 30 wt.% for TiO_2 saturation geothermometry.

Significantly lower zircon saturation temperatures of 980-880°C derived from MIZ of variable sizes, compared to 1100°C used for homogenization, suggest that in our experiments the MIZ compositions remained unaffected by host zircon dissolution. The results of Zr saturation geothermometry largely overlap with those obtained by all other methods.

Partitioning coefficients derived from MIZ - host zircon pairs are similar for mafic and felsic rocks, and independent from MIZ sizes (20-40 μm), compositions, and entrapment temperatures (700-950°C). They overlap with experimental values obtained at 900 °C and also with those obtained by a previous MIZ study, but are significantly lower for Ti and Nb.

The MIZ compositions of all investigated rocks can generally be explained by fractional crystallization of BC-relevant parental magmas, comprising the mafic parental magmas B1; B1:B2 = 60:40, UUMZ with 25% felsic component (with 0.3-0.4 wt.% H_2O), and a SiO_2-rich felsic magma with 2.2 wt.% H_2O. Differences between measured and modelled MIZ composition can be explained, among others, by mixing effects during cyclic ingression of parental magma with evolved resident magma.

Acknowledgements

DG and AZ thank the Deutsche Forschungsgemeinschaft (DFG grant ZE 424/12-1), and
Linda Marko, Richard Albert Roper and Axel Gerdes (Frankfurt Isotope and Element Research Center (FIERCE), Goethe-University Frankfurt, Germany) for support with sample preparation and LA-ICP-MS analyses. RA thanks DFG for support of the experimental program (DFG grant KO1723/20). We are grateful to Robert Balzer, Stefan Linsler, Florian Pohl and Christian Singer for the help with experiments. All authors are also indebted to late Joe Aphanane (University of the Witwatersrand) for zircon separation and preparation, David Schiller (Salzburg University, Austria) for support during thermodynamic modelling as well as to Samancor Chrome and Bokoni Platinum Mine Proprietary Ltd. for support during sampling.

6. Hafnium Isotopic Composition of the Bushveld Complex requires Mantle Melt - Upper Crust Mixing: New Evidence from Zirconology of Mafic, Felsic and Metasedimentary Rocks

Armin Zeh[1], Allan. H. Wilson[2], **Dominik Gudelius**[1], Axel. Gerdes[3]

[1] Karlsruhe Institute for Technology, Institute for Applied Geosciences, Adenauerring 20b, 76131 Karlsruhe, Germany

[2] University of the Witwatersrand, School of Geosciences, South Africa, 2050 Johannesburg, South Africa

[3] Goethe University Frankfurt, Institute for Geosciences, Altenhöferallee1, 60438, Frankfurt, Germany

Journal of Petrology, Volume 60, Issue 11, pages 2169–2200,

DOI:10.1093/petrology/egaa004

Abstract

The origin of magmas that formed the Bushveld Complex remains highly debated in spite of many decades of intense research. Previous geochemical–petrological studies have shown a strong mantle derivation resulting ultimately in highly economic ore bodies of platinum group elements and chromium. However, geochemistry also points to the contribution of a significant crustal component, which may have been derived singly or in combination from a number of different sources. These include subcontinental lithospheric mantle that was enriched prior to Bushveld magma formation, possibly by subduction, assimilation of lower and upper crust during magma ascent, and contamination during magma chamber accretion within sedimentary rocks of the enclosing Transvaal Supergroup. In this study, the contributions of these various reservoirs will be evaluated by employing Hf isotopic data of well-characterized zircon grains in mafic, felsic and metasedimentary rocks, together with Zr–Hf bulk-rock compositions. The results reveal that magmatic zircon grains in mafic cumulate rocks from the floor to the roof of the *c*. 9 km thick Rustenburg Layered Suite (RLS) show essentially the same variations in $\varepsilon Hf_{2.055\,Ga}$ from −7.5 to −10.2 as those of metamorphic zircon grains and overgrowths in the immediate surrounding quartzite and metapelitic rocks, as well as in granitic melt batches, granophyres, and the upper Rooiberg volcanics. The same values are also obtained by estimating the average Hf isotopic compositions of detrital zircon grains in many quartzite and metapelitic rocks from the surrounding Magaliesberg ($\varepsilon Hf_{2.055\,Ga}$ = −6.2 to −10.8, six samples, maximum deposition age at 2080 Ma) and Houtenbeck formations ($\varepsilon Hf_{2.055\,Ga}$ = −7.1 to −8.9, three samples, maximum deposition age at 2070 Ma), and by a six-point isochron of a garnet-schist from the Silverton Formation ($\varepsilon Hf_t = -6.6 \pm 0.7$; age = 2059.4 ± 2.7 Ma). Zircon morphologies, zoning patterns, Hf isotopic data and petrological constraints furthermore reveal that metamorphic zircon was precipitated from aqueous fluids and/or felsic melts at temperatures between 550 and 900 °C, and that the Hf isotopic composition became

homogenized during fluid transport in the contact aureole. However, results of numerical modelling indicate that fluid infiltration had only a minor effect on the Zr–Hf budget and Hf isotopic composition of the RLS, and that these parameters were mainly controlled by the mixing of melts derived from three major sources: (1) the asthenospheric mantle (>20 %); (2) enriched subcontinental lithospheric mantle (<80 %); (3) assimilation of significant amounts of crust (up to 40 %). The modelling furthermore suggests that assimilation of lower Kaapvaal Craton crust was minor (<15 %) during B1 (high-Mg andesite) magma formation, but up to 40 % during B3 (tholeiite) magma formation. The minor variation in εHf_t of zircon throughout the entire stratigraphy of the RLS resulted from the interplay of three dominant contributing factors: (1) intrusion of hot (>1200 °C) mantle-derived magmas with relatively low Zr–Hf concentrations having a similar $\varepsilon Hf_{2.055\,Ga}$ of -8.5 ± 1.9 to that of upper crust rocks surrounding the RLS; (2) significant assimilation of volcanic and metasedimentary rocks with high Zr–Hf concentration; (3) mingling, mixing and/or diffusive exchange of Zr and Hf between crust and mantle-derived melts and aqueous fluids prior to late-magmatic crystallization of zircon at temperatures between 700 and 900 °C. This study shows that the combination of Zr–Hf bulk-rock data with Hf isotopic data of well-characterized zircon grains provides a powerful tool to quantify various mantle and crustal reservoirs of mafic layered intrusions, and allows new insights into magma chamber and related contact metamorphic processes.

6.1 Introduction

The Rustenburg Layered Suite (RLS) of the Bushveld Complex (BC) in South Africa is the largest mafic layered intrusion on Earth and hosts the world's largest resources of platinum group elements (PGE), Cr and V (Cawthorn, 1999*a*, 1999*b*; Naldrett et al., 2009). Despite intense research over the past 30 years the processes that gave rise to the formation of the BC remain incompletely understood. There is still disagreement on the composition of the parental magmas of the RLS and their sources (Eales and Cawthorn, 1996; Barnes et al., 2010; Wilson, 2012, 2015; Wilson et al., 2017), as well as about the processes that led to magma formation, emplacement and crystallization. The available datasets, comprising a vast number of field and petrographic observations, major and trace element data, as well as isotopic characteristics suggest that the RLS consists of four parental magma types, UM (ultramafic), B1 (high-Mg andesitic), B2 and B3 (tholeiitic), which contributed (on an approximate basis) to the successive accretion of the magma chamber (see detailed discussions by Barnes et al., 2010; Wilson, 2012, 2015; Wilson et al., 2017). The data also suggest that the magma chamber that gave rise to the RLS crystallized from the floor to the roof (e.g. Eales and Cawthorn, 1996), although this is challenged by some researchers [see detailed discussion by Latypov et al. (2017)], and that the crystallization process was accompanied by successive ingressions of mafic magma (e.g. Ashwal et al., 2005; Wilson, 2015). The data also indicate a high degree of crustal

contamination of the parental magmas of about 20 wt%, as suggested by initial Sr isotopic data (Kruger, 1994), oxygen isotope data (Harris et al., 2005), and highly non-radiogenic initial Nd (Maier et al., 2000) and Hf isotopic data (Zirakparvar et al., 2014). However, the source for this crustal contamination, which affected all parental magma types of the RLS, remains a matter of continuing debate. It has been ascribed to the assimilation of (1) wall rocks as currently observed to a shallow-seated magma chamber (e.g. Barnes, 1989; Maier et al., 2000; Barnes et al., 2010), (2) a deep-seated staging magma chamber (e.g. Eales and Costin, 2012) or (3) Kaapvaal Craton crust during magma ascent from the mantle into the present-day magma chamber (Campbell, 1985; Huppert and Sparks, 1985), or considered as (4) entirely due to melting of an enriched subcontinental mantle source (e.g. Hamilton, 1977; Richardson and Shirey, 2008; Zirakparvar et al., 2014) or (5) a combination of these different processes and sources (e.g. Barnes et al., 2010; Wilson et al., 2017).

Hatton (1995) proposed a mantle plume origin for the most primitive Bushveld magmas (UM), and Barnes (1989) considered that the high SiO_2 and MgO contents of the B1 magma result from contamination of komatiite magmas with crustal melts derived from the Kaapvaal Craton. Based on Re–Os isotopic systematics combined with Nd–Sm and Rb–Sr isotopic systems, Richardson and Shirey (2008) demonstrated that it is difficult to model Bushveld magmas by contamination of primary mantle melts with continental crust. Instead, they proposed a source involving both metasomatized (enriched) subcontinental lithospheric mantle (E-SCLM) and primitive convecting, asthenospheric mantle. Building on this, Barnes et al. (2010) suggested that the B1 magmas initially resulted from melting of E-SCLM followed by crustal contamination. The involvement of several crust and mantle reservoirs during RLS formation at 2.06 Ga was also suggested by Wilson et al. (2017), based on a very detailed study on chill and cumulate rocks of the Basal Ultramafic Sequence (BUS), forming the deepest unit of the RLS (up to 800 m thick) beneath the Marginal Zone. By combining the results of detailed borehole logging, petrology, *in situ* Sr isotope analyses, and major and trace element data of more than 100 samples, Wilson et al. (2017) demonstrated that the BUS rocks crystallized within an early embryonic magma chamber (also see Wilson, 2012, 2015), which started as a sill complex and was successively filled by mafic melts (similar to B1) and ultramafic melts (similar to UM) derived from asthenospheric and metasomatized SCLM sources, and modified by crustal melts derived from the Kaapvaal Craton, and overlying Pretoria Group sedimentary rocks. The mixing of melts from four reservoirs is evidenced by, among other features, small-scale variations (centimetres to metres) in initial Sr isotopic ratios within the BUS ranging from 0.7042 to 0.7075 (Wilson et al., 2017). This range overlaps with that obtained by Kruger (1994) and Karykowski et al. (2017) for mafic rocks from the entire RLS above the BUS (Sr_i = 0.7045–0.7085), suggesting that the parental magmas of these rocks underwent similar mixing processes.

In this context, it is pertinent to note that Hf isotopic data of zircon grains in mafic rocks of the RLS and in overlying felsic rocks (Rashoop granophyres, and microgranites) show, within error, identical εHf_t values, reflected by an 'intrusion-wide average' of -8.6 ± 1.2 (Zirakparvar et al., 2014; VanTongeren et al., 2016). Based on these data, in combination with results of two-component mixing modelling, Zirakparvar et al. (2014) suggested that all magmas parental to the RLS resulted exclusively from the melting of a metasomatized mantle source at 2.06 Ga, and that mixing of depleted mantle-derived melts (komatiitic magmas) with Kaapvaal Craton crust was insignificant. This conclusion, however, is speculative for several reasons. First, the 'intrusion-wide εHf_t average' presented by Zirakparvar et al. (2014) and VanTongeren et al. (2016) does not account for the wide scatter of up to 9.5 ε units obtained for zircon grains of individual samples (VanTongeren et al., 2016). Second, it remains unclear in both studies whether this scatter results from inherited xenocryst, as information about internal zoning of the analysed zircon grains was not provided. Third, in the mixing model of Zirakparvar et al. (2014) it was assumed that modification of komatiitic magma was achieved by bulk assimilation of Archean crust or sedimentary rocks of the Kaapvaal Craton and the Limpopo Belt Central Zone, both having highly non-radiogenic $\varepsilon Hf_{2.06\,Ga} < -25$. Such a composition, however, is not representative of Pretoria Group sedimentary rocks forming the wall-rocks of the RLS magma chamber. This is indicated by recent Hf isotopic data of detrital zircon populations in Magaliesberg Group quartzites showing average $\varepsilon Hf_{2.06\,Ga}$ between −16.5 and −6.4 (Zeh et al., 2016), overlapping with the data of the RLS. Fourth, all mixing calculations were based on the assumption that the mantle-derived magmas were modified by bulk-rock assimilation, without consideration that aqueous fluids released by metamorphic processes are also able to dissolve, transport and precipitate large amounts of Zr and Hf (up to several hundred ppm) under sub-solidus conditions (e.g. Ewing et al., 1982; Schmidt et al., 2006; Hay and Dempster, 2009; Zeh et al., 2010a, b; Wilke et al., 2012; Zeh and Gerdes, 2014). In this context we note that several isotope-based studies (Sr, O, H, C) have shown that the BC and its contact aureole were affected by a massive fluid flow during and after its emplacement (e.g. Schiffries and Rye, 1990; Buick et al., 2000; Harris and Chaumba, 2001; Harris et al., 2003).

In this study, we will provide answers to the following three questions identified above. (1) What were the amounts and sources of crustal contamination to RLS parental magmas? (2) Why are Sr isotope compositions within the RLS highly variable, whereas Hf isotopes display only minor variations? (3) How might metamorphic fluid and magma chamber processes relate to the homogenization of the Hf isotope system in the RLS? To address these questions we present a comprehensive set of Hf isotopic data for well-characterized zircon grains in mafic rocks of the RLS, in Bushveld-related felsic rocks, and in surrounding contact metamorphic rocks, along with bulk-rock geochemical analyses. Furthermore, we provide detailed

information about zircon morphologies, internal zoning patterns, and age–Hf isotopic systematics, to constrain the timing of zircon growth, the nature of the homogenization processes, and zircon formation temperatures. Finally, we present results of numerical modelling with the aim of elucidating the influence of fluid infiltration on the Zr–Hf budget and Hf isotopic composition of the RLS, and the amount of the different crust and mantle reservoirs that ultimately contributed to the compositions of the magmas of the BC.

6.2 Geological Setting

The BC is made up by three large igneous provinces: (1) Rooiberg Group volcanics (earliest stage); (2) mafic rocks of the RLS; (3) Lebowa Granite Suite (final stage) (Fig. 6.1). It also incorporates the Rashoop Granophyre Suite, hornfelses and microgranites, all located at the roof of the RLS in the transition zone between the RLS and the Lebowa Granite Suite (e.g. Molyneux, 1970, 1974; Von Gruenewaldt, 1972; Twist and French, 1983; Walraven, 1987; Schweitzer et al., 1997; Mathez et al., 2013; VanTongeren and Mathez, 2015). The Rooiberg volcanics were emplaced on and into the plutonic rocks of the BC as well as the sandstones, shales and carbonates of the uppermost Pretoria Group, forming part of the *c*. 15 km thick 2.64–2.06 Ga Transvaal Supergroup (Eriksson et al., 1995), which rests on *c*. 30 km thick Kaapvaal Craton crust made up of greenstones, tonalite–trondhjemite–granodiorite (TTG) gneisses and granites older than 2.7 Ga [for a detailed summary see Zeh et al. (2016)]. Sedimentary rocks in direct contact with the BC belong to the Magaliesberg and post-Magaliesberg formations (the latter comprising, from floor to top, the Vermont, Lakenvalei, Nederhorst, Steenkampsberg and Houtenbeck formations; Fig. 6.2a). These have an accumulated thickness of more than 2000 m (Eriksson et al., 1995), show maximum deposition ages between 2120 and 2080 Ma (Zeh et al., 2016), and were supplied from at least two distinct sources, on and off the Kaapvaal Craton: (1) from the Pietersburg Block adjacent to the BC (ages mostly between 3.10 and 2.65 Ga) and (2) from the Ophthalmia orogen in NW Australia (ages mostly between 2.45 and 2.11 Ga), as is suggested by U–Pb–Hf isotopic data of detrital zircon grains (Zeh et al., 2016). The RLS and related granites crystallized at pressures between 1.5 and 3.0 ± 0.5 kbar indicative of shallow crustal levels (Kaneko and Miyano, 1990; Pitra and De Waal, 2001; Waters and Lovegrove, 2002). The accretion of the RLS magma chamber, which occurred at temperatures between 1300 and 1150 °C (Cawthorn and Walraven, 1998), led to formation of an extensive contact aureole (>20 km width) in the underlying rocks of the Transvaal Supergroup, and to thermal interaction with Rooiberg volcanics and metasedimentary rocks at the top of the RLS (e.g. Walraven, 1987; VanTongeren and Mathez, 2015).

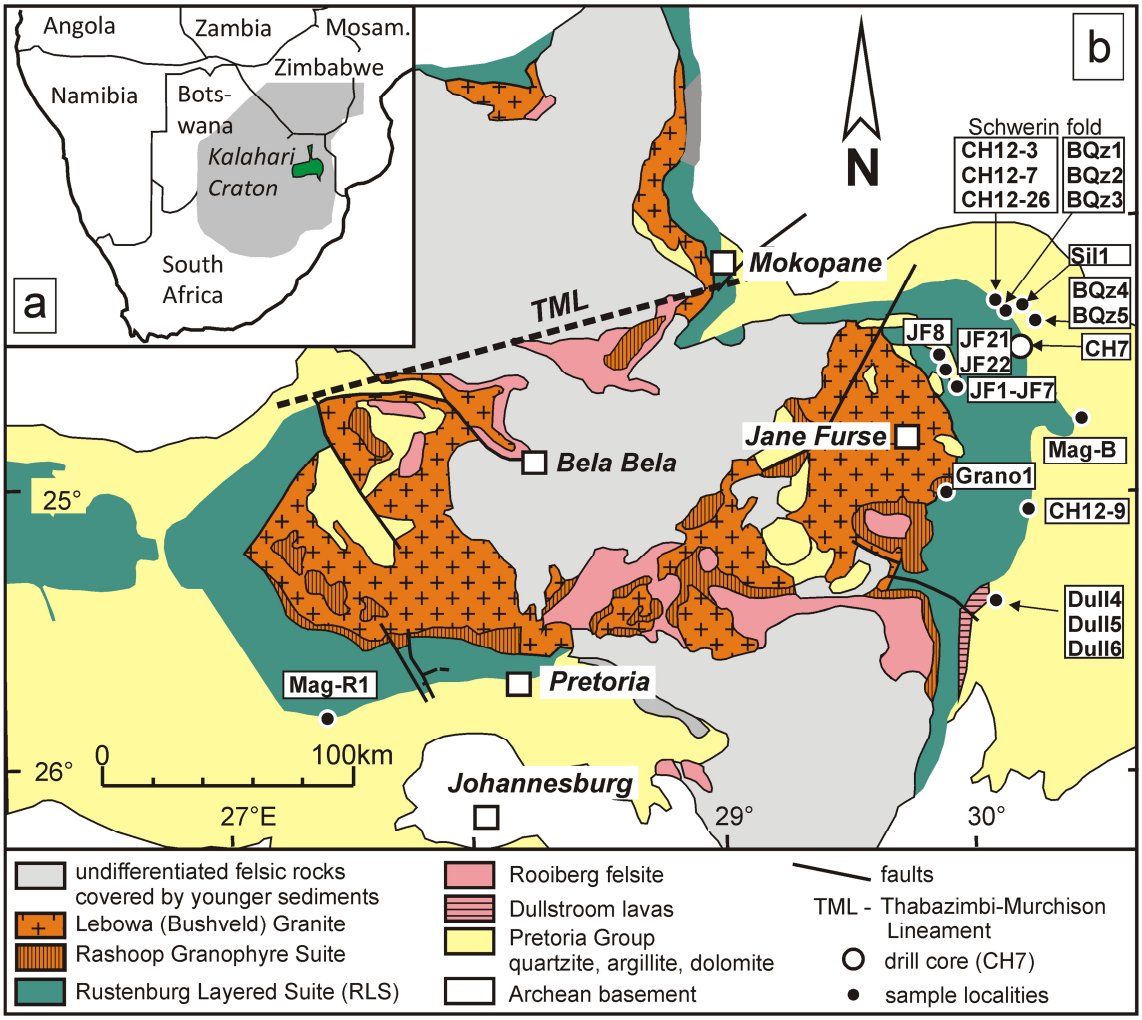

Figure 6.1 - Simplified geological map of the Bushveld Complex (BC) and sample localities (modified after Latypov et al., 2017). (a) Position of the BC in southern Africa; (b) schematic map of the BC.

The Rooiberg Group comprises an up to 5 km thick pile of mostly very fine-grained to glassy lava flows (felsites) and minor pyroclastic rocks (Twist and French, 1983; Twist and Harmer, 1987; Buchanan et al., 1999, 2002, 2004; Lenhardt and Eriksson, 2012; Günther et al., 2018), which are underlain by Magaliesberg and post-Magaliesberg sedimentary rocks (Fig. 2a). The Rooiberg lavas, which have a total volume of *c*. 300 000 km^3 (Twist and French, 1983), can be traced over nearly the entire area of the BC (>67 000 km^2) and comprise from bottom to top the following four formations: Dullstroom, Damwal, Kwaggasnek and Schrikkloof. These were all emplaced prior to the RLS as is supported by field relationships (e.g. Martini, 1998) and radiometric ages of 2061 ± 2 Ma (Pb–Pb zircon evaporation; Walraven, 1997) and 2057.3 ± 2.8 Ma [sensitive high-resolution ion microprobe (SHRIMP) U–Pb zircon; Harmer and Armstrong, 2000]. Some researchers have suggested that the rhyolites of the Kwaggasnek and Schrikkloof formations are synchronous with the RLS (e.g. VanTongeren et al., 2010, 2016; VanTongeren and Mathez, 2012). The Dullstroom lavas, which underlie the RLS, comprise high-Ti and low-Ti basalts, a basal rhyolite, and dacites, all of which are Mg-rich and have a calc-alkaline character. In contrast, lavas of the three upper formations are mostly Mg-poor

(ferroan), and rhyodacitic to rhyolitic in composition. Their compositions overlap with those of the A-type granites forming the Lebowa Granite Suite, and with the Rashoop granophyres (e.g. Twist and French, 1983; Twist and Harmer, 1987; Hatton and Schweitzer, 1995; Hill et al., 1996; Schweitzer et al. 1997; Buchanan et al., 1999, 2002, 2004; Mathez et al., 2013). The Rooiberg felsites are preserved in isolated and widely scattered areas (Fig. 6.1b), where they are intimately associated with the compositionally indistinguishable Rashoop granophyres (Stavoren and Rooikop types; for summary see VanTongeren and Mathez, 2015). Thus, some researchers suggested that the granophyres represent coarse-grained, hypabyssal (plutonic) equivalents to the Rooiberg felsites formed largely by contact metamorphic melting during RLS emplacement (e.g. Walraven, 1987). The stack of Rooiberg volcanics and underlying Transvaal sediments were intruded by mafic magmas of the RLS, whereby the Dullstroom volcanics remained (mostly) at the floor of the expanding RLS magma chamber, and Damwal, Kwaggasnek and Schrikkloof volcanics formed the roof (Fig. 6.2a). An exception is an area in the northeastern part of the BC where the roof is made up of Pretoria Group sedimentary rocks (see profile given by VanTongeren and Mathez, 2015).

The RLS is made up of a 7500–9000 m thick stack of coarse-grained cumulate rocks, covering an area of 67 000 km^2, with a volume of 370 000–670 000 km^3 (Cawthorn and Walraven, 1998). Based on similar stratigraphy, gravimetric data, and xenoliths in kimberlites, it is suggested that the RLS developed in a continuous magma chamber of at least 400 km extent in an east–west direction (Cawthorn and Walraven, 1998). Based on the sequence of different cumulate minerals and marker horizons, the RLS is traditionally subdivided from bottom to top into five zones (Hall, 1932): Marginal Zone, Lower Zone, Critical Zone, Main Zone and Upper Zone (see summary by Cawthorn et al., 2006). However, more recent studies have shown that the Marginal Zone is underlain by significant volumes of (ultra)mafic rocks of the BUS (Wilson, 2012, 2015; Fig. 6.2a), which developed in at least three different compartments (embryonic magma chambers). These started as sill complexes with chilled margins showing spinifex-like textures, and developed into real magma chambers with the Marginal Zone initially forming their differentiated roofs.

Geochemical and petrological data indicate that the cumulate rocks of the RLS result from crystallization of different parental magmas (UM, B1, B2, B3; e.g. Barnes et al., 2010; Wilson, 2012), the compositions of which were estimated from the marginal sills and the BUS (Fig. 6.2a), assumed to represent the undifferentiated magmas. It is suggested that the UM and B1 magmas played a major role during the formation of the BUS, Marginal Zone and Lower Zone, the B1 and B2 magmas for the Critical and lower Main zones, and the B3 magma for the Main and Upper zones. Initial strontium isotopic data (Sr_i) additionally reveal significant variations from $Sr_i = 0.7045$ to 0.7078 for all lower units (from BUS to Critical Zone), but Sr_i remains nearly constant throughout the Main Zone ($Sr_i = 0.7085$), and the Upper Zone (Sr_i =

0.7073), with relatively sharp breaks in between (Kruger and Marsh, 1982; Kruger, 1994; Karykowski et al., 2017; Wilson et al., 2017). The enormous variations in Sr_i within the lower units of the RLS are attributed to mixing of magmas derived from different crust and mantle sources. In contrast, the constant values in the Main and Upper zones result from homogenization processes, which occurred either within the source region of the melts or within the BC magma chamber. In this context, it is pertinent to note that the relatively abrupt increase in Sr_i at the Critical–Main Zone boundary is also highlighted by an abrupt increase in F/Cl ratio in apatite from <0.20 to >0.70 (Willmore et al., 2000). Results of high-precision U–Pb dating, textural–chemical zircon studies and thermal modelling additionally suggest that accretion of the RLS (from Marginal Zone to Upper Zone) occurred within *c*. 70 kyr (Cawthorn and Walraven, 1998), and that subsequent cooling below 700 °C lasted less than 1 Myr, between 2055.91 ± 0.26 Ma and 2054.89 ± 0.37 Ma (Zeh et al., 2015).

The felsic rocks of the BC are diverse, and except for the Dullstroom rhyolites occur at the roof of the RLS, and comprise the Rashoop Granophyre Suite, hornfelses, microgranites and leptites, all of which are cross-cut by granites of the Lebowa Granite Suite (Von Gruenewaldt, 1972; Walraven, 1985, 1987; VanTongeren and Mathez, 2015), having an estimated volume of about 205 000 km^3 (Hill et al., 1996). The Rashoop Granophyre Suite comprises rocks characterized by micrographic intergrowths of quartz and K-feldspar. In general, two types are distinguished: magmatic granophyre (Stavoren, Rooikop granophyres) and metamorphic granophyre (Zwartbank and Diepkloof granophyre). On the basis of geochemistry and detailed fieldwork, Walraven (1985) proposed that the Stavoren granophyre (the most laterally extensive unit) represents intrusive, time-equivalent magmas to the overlying Rooiberg volcanics, whereas Mathez et al. (2013) suggested that its formation was by fractional crystallization from RLS magmas within the BC magma chamber. Metamorphic granophyres are suggested to have been formed by contact metamorphic interaction either between RLS and overlying metasedimentary rocks (Zwartbank pseudogranophyre; Walraven, 1985), or by melting of Rooiberg volcanics (Diepkloof granophyre), which in places were transformed into hornfelses showing a fine-grained granular fabric (VanTongeren and Mathez, 2015). Melting of such hornfelses led to the formation of microgranites, which in the eastern BC originate from Dullstroom and Damwal volcanics (VanTongeren and Mathez, 2015). Such microgranites also occur along the transition zone between the Main and Upper Zone, where they form an extensive layer of up to 40 km in lateral extent. Walraven (1987) modelled the thermal effect of RLS magma emplacement on overlying felsic rocks and concluded that the amount of heat was capable of forming a felsic melt sheet of at least 1000 m thickness (even without considering the effects of convection).

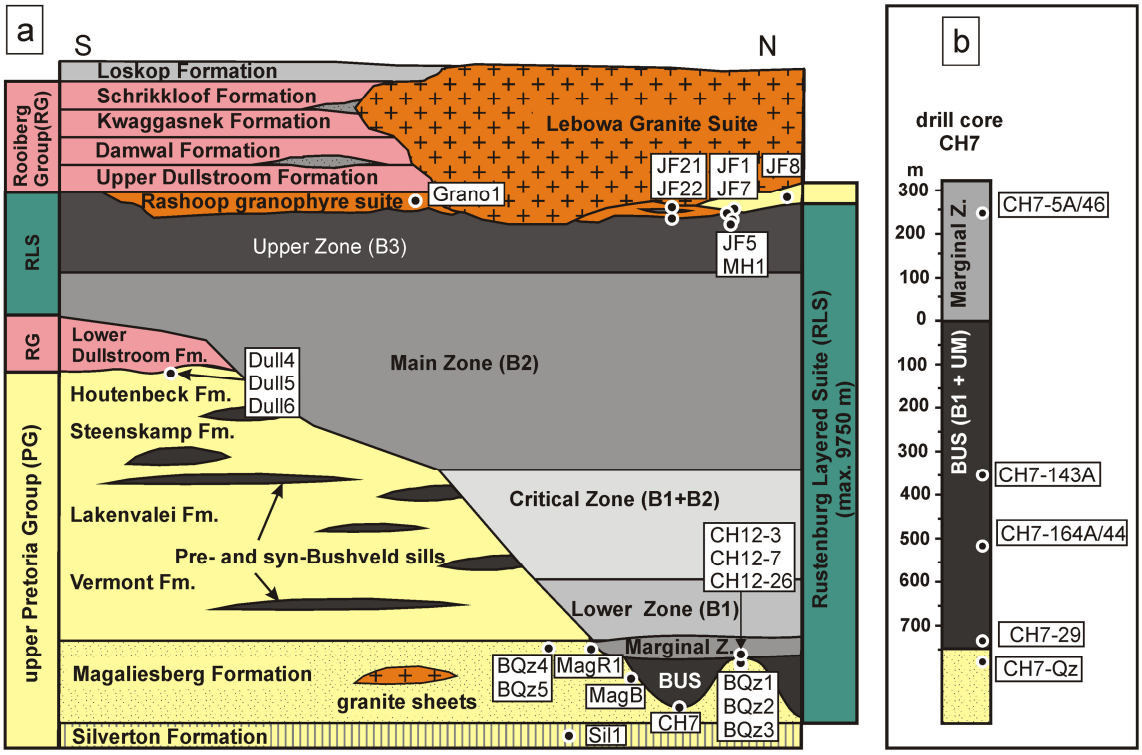

Figure 6.2 - (a) Schematic north–south profile through the eastern BC showing the relationships between the Rustenburg Layered Suite and surrounding rock units [modified after SACS (South African Committee for Stratigraphy), 1980; Schweitzer et al., 1995; Lenhardt and Eriksson, 2012]. (b) Schematic profile through the drill core CH7 with sample positions modified after Wilson (2012) (B1, B2, B3, UM are parental magma compositions).B2, B3, UM are parental magma compositions).

6.3 Samples and field relationships

In this study zircon grains were investigated from 31 rock samples (Figs 6.1b and 6.2a, b), comprising 14 samples from the lowermost and uppermost rock units of the RLS, and 17 from country rocks, including 7 Magaliesberg quartzite samples previously investigated for U–Pb–Hf isotopes by Zeh et al. (2016). From the RLS, zircon grains were separated from cumulate rocks of the BUS (drill core CH7: samples CH7-29, CH7-164/44 and CH7-143 A), from the Marginal Zone (CH12-3, CH12-7, CH12-9, CH12-26 and CH7-5A-46), and from the Upper Zone at Magnet Heights (MH1) and from an outcrop NE of Jane Furse (JF5). From country rocks, zircon grains were selected from the Magaliesberg quartzites at the floor (BQz1, BQz2, BQz3, BQz4, CH7, Mag-R1 and Mag-B) and the roof (JF1a, JF3a, JF3b and JF8) of the RLS, as well as from quartzite (Dull4) and metapelitic rocks (Dull5 and Dull6) of the Houtenbeck Formation beneath the Dullstroom lavas. Zircon grains were furthermore selected from quartz-rich leucogranites associated with quartzite in the roof of the RLS (JF2 and JF4), contact granophyre (JF7), Rashoop granophyre (Grano1), and from a Rooiberg felsite (JF21) grading into a ‘microgranite’ (JF22). The sample coordinates are presented in Supplementary DataTable S1 (supplementary data are available for downloading at http://www.petrology.oxfordjournals.org), and positions are shown in Fig. 6.1b. Furthermore, we estimated the initial Hf-isotopic composition of a garnet–staurolite-bearing schist of the Silverton Formation (Sil1) from the

eastern contact to the BC. From four areas, zircon grains were selected from rock samples of different compositions from either side of the BC–wall-rock contact from (1) an outcrop NE of Jane Furse (Fig. 6.3a and b), (2) the Schwerin fold (Fig. 6.3c and d), (3) the area east of Dullstroom, and (4) drill core CH7 (Fig. 6.2b) described by Wilson (2015).

The outcrop NE of Jane Furse exposes the uppermost contact of the RLS. In the outcrop area, ferrodiorite (JF5 and JF23) occurs in direct contact with irregular layers and occurrences of 'contact' granophyre (0–5 m thickness; JF7), homogeneous, fine-grained leucogranite (JF2, JF4, JF13 and JF16), pure quartzite (JF1a) and impure quartzite (JF3a and JF3b), as well as with fine-grained (JF14) and/or schlieric diorite (JF11; Figs 6.3a and 6.4a–d). Impure quartzite domains commonly consist of amoeboid-shaped bodies of variable size, commonly residing in a quartz–feldspar-rich matrix, representing former melt-rich batches (Fig. 6.4a and b). Such batches locally grade into fine-grained leucogranite. In some places the ferrodiorite contains quartz–feldspar-bearing schlieren, pointing to mixing with felsic material (Fig. 6.4c). In the outcrop area, up to metre-sized rafts of quartzitic country rocks associated with granites of different textures are completely surrounded by ferrodiorite (Fig. 6.3b). About 5 km north of this outcrop, glassy Rooiberg felsite (JF21) occurs in direct contact with medium-grained 'microgranite' (JF22) (Fig. 6.4e and f). The contact is mostly gradational, suggesting felsite assimilation and/or transformation into microgranite. The relationships are similar to those described by VanTongeren and Mathez (2015) for many other locations along the roof of the RLS.

At the Schwerin fold (Fig. 6.1b), feldspathic pyroxenites and norites of the Marginal Zone (samples CH12-3, CH12-7 and CH12-26) occur in direct contact with Magaliesberg quartzite (BQz1, BQz2 and BQz3). In the outcrop, abundant quartzite xenoliths, up to 1 m in size, together with rare blocks of calcsilicate rock occur (Fig. 6.3c and d), suggesting stoping and assimilation of country rocks (Magaliesberg and Silverton formations) prior to crystallization of the Marginal Zone magmas. Similar features are also observed at other Marginal Zone localities; for example, in the Clapham Compartment, and in the drill cores CH6 and CH7 transecting the Marginal Zone (Wilson, 2015; Wilson et al., 2017). Feldspathic pyroxenites at the Schwerin fold show spinifex-like structures with elongated orthopyroxenite crystals (CH12-3), pointing to relatively fast magma cooling (see supplementary material of Zeh et al., 2015). Zircon dated from sample CH12-3 yielded a precise age of 2055.68 ± 0.29 Ma (Zeh et al., 2015), and the bulk-rock composition is identical to typical B1-magma (Supplementary DataTable S2). Detrital zircon populations in the Magaliesberg quartzite at the Schwerin fold were previously investigated by Zeh et al. (2016) and point to a heterogeneous source during sandstone deposition at <2080 Ma.

In the area west of Dullstroom, mature, fine- to coarse-grained sandstones of the Houtenbeck Formation (Dull4) are intercalated with banded metapelitic rocks. This succession occurs below felsic and mafic volcanic rocks of the Dullstroom Formation (lowermost unit of the Rooiberg Group; Fig. 6.2a), comprising basaltic lavas, glassy rhyolitic lavas and tuffites. The investigated pelitic rocks (Dull5 and Dull6) contain the mineral assemblage andalusite + biotite + muscovite + quartz + tourmaline (Fig. 6.4g), pointing to maximum peak metamorphic conditions of 550–600 °C at 1–2 kbar.

Zircon grains from drill core CH7, which transects the deepest part of the RLS in the Clapham Compartment area (for details see Wilson, 2012, 2015), were investigated from five samples: (1) a Magaliesberg quartzite sample (CH7-Qz) from the direct contact with chilled rocks of the BUS (Wilson, 2015; Zeh et al., 2016); (2) relatively fine-grained feldspathic pyroxenites about 10 m (CH7-29), 230 m (CH7-164A-44) and 370 m (CH7-143A) above the contact (Fig. 6.2b); (3) zircon grains from the Marginal Zone norite (CH7-5A/-46) taken about 1200 m above the contact. The Marginal Zone in the drill core also contains abundant quartz bodies, indicating assimilation of country rock from the roof of the evolving magma chamber prior to the intrusion of the Lower Zone magmas (Wilson, 2015; Wilson et al., 2017).

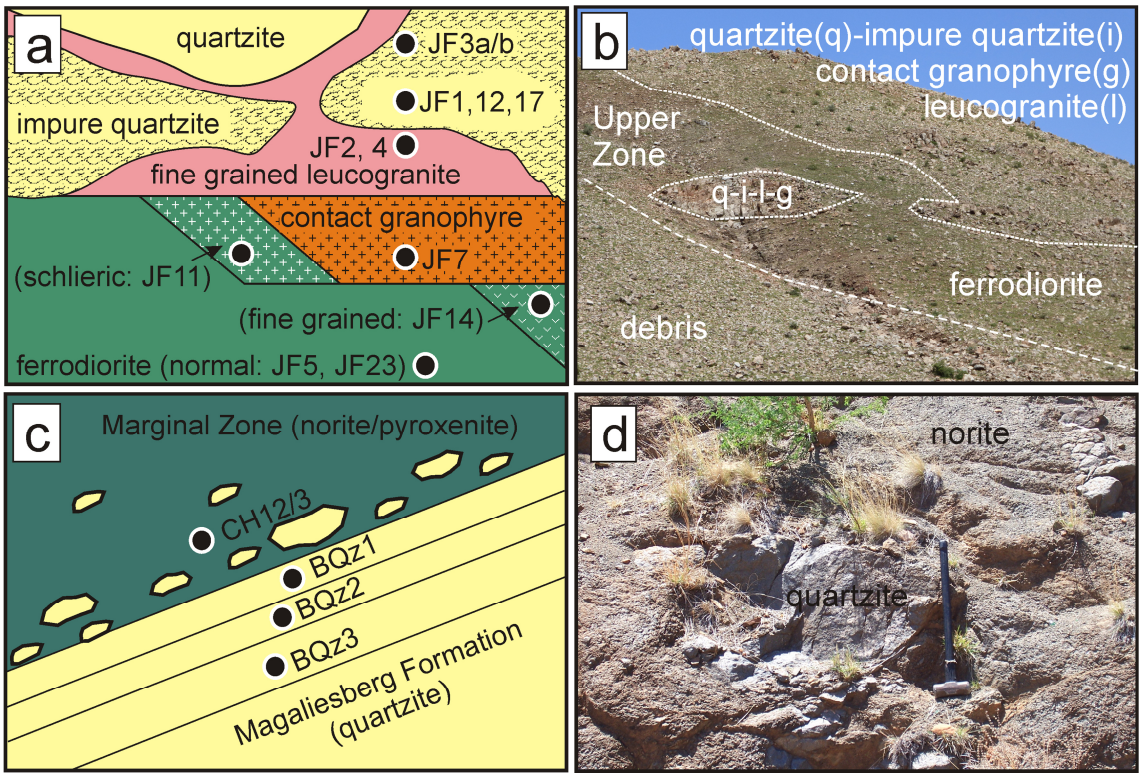

Figure 6.3 - Field relationships at the roof (a, b) and floor (c, d) of the Rustenburg Layered Suite. (a) Schematic overview of the complex lithological relationships observed in an outcrop NE of Jane Furse, with sample positions shown. (b) Exposed contact between metamorphosed sedimentary country rocks (q, pure quartzite; i, impure quartzite), felsic rocks (g, contact granophyre; l, fine-grained leucogranite) and Upper Zone ferrodiorite. (Note the irregular contact and the boulders of different country rock completely surrounded by ferrodiorite.) (c) Schematic contact relationships at the Schwerin fold with sample positions shown. (d) Quartzite xenoliths in norite, indicating assimilation of sedimentary country rocks during Marginal Zone formation.

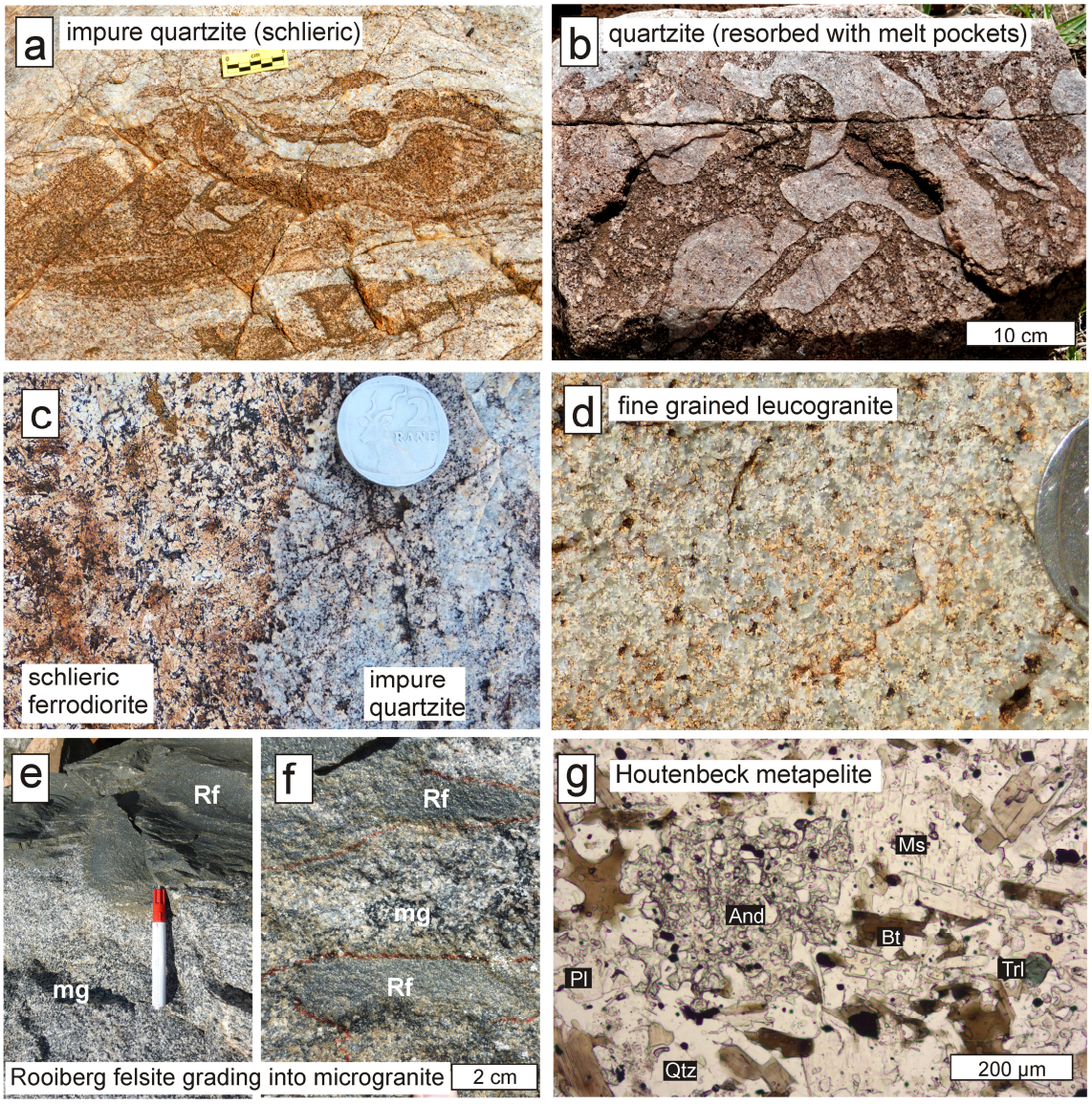

Figure 6.4 - (a–f) Rock types investigated in this study from the area NE of Jane Furse. (a, b) Schlieric impure quartzite of amoeboid shape surrounded by melt pockets grading into fine-grained leucogranite; (c) contact between impure quartzite and schlieric ferrodiorite; (d) fine-grained leucogranite (scale indicated by 2 Rand coin); (e, f) fine-grained, glassy Rooiberg felsite (Rf) grading into hornblende-bearing microgranite (mg); (g) microphotograph of Houtenbeck metapelitic rock (sample Dull5) showing the assemblage andalusite (And)–biotite (Bt)–muscovite (Ms)–plagioclase (Pl)–quartz (Qtz)–tourmaline (Trl) pointing to peak *P*–*T* conditions of 550–600 °C at 1–2 kbar.

6.4 Analytical methods

Bulk-rock composition and trace elements were estimated by means of X-ray fluorescence analysis (XRF) on fusion and powder discs, as well as on dissolved sample aliquots by means of inductively coupled plasma mass spectrometry (ICP-MS), using the method described by Wilson (2012, 2015). The results are shown in Fig. 6.5, and in the Supplementary DataTable S2. For U–Pb dating, Hf isotope analyses and morphology studies, zircon grains were selected under ethanol from heavy mineral concentrates, produced by standard crushing and separation techniques (see Zeh et al., 2009). For morphology studies, a large number of euhedral zircon grains were selected and mounted on double-sided tape, coated with Pt or C, and investigated with a scanning electron microscope (SEM) at Goethe University Frankfurt (JEOL JSM-6490 instrument with Gatan MiniCL). Representative images are shown in Figs 6.6 and 6.7. For quantification of zircon morphologies, the classification scheme of Pupin (1980) was used (Fig. 6.8). Zircon grains analysed for U–Pb dating and Lu–Hf isotopes were mounted in epoxy resin, and ground to expose their approximate centres. Each grain was investigated by cathodoluminescence (CL) and back-scattered electron (BSE) imaging, to obtain detailed information about internal zoning (core–rim relationships), fractures and porosity. Representative images are shown in Figs 6.9 and 6.10. For most Magaliesberg samples, representative images have been presented by Zeh et al. (2016), and for the Marginal and Upper Zone samples CH12-3, CH12-26 and MH1 by Zeh et al. (2015). Zircons from BUS pyroxenites and Rooiberg felsites were investigated in thin sections (Fig. 6.10a–g), and from heavy mineral concentrates (Fig. 6.6h).

Following SEM imaging, U–Pb and Lu–Hf isotopes of zircon grains of quartzite and leucogranite samples (most of which show core–rim relationships) were analysed by means of laser ablation-inductively coupled plasma-sector field-mass spectrometry (LA-ICP-SF-MS). These analyses were carried out with a Resonetics M50 193 nm Excimer laser system, coupled with either a Thermo-Scientific ELEMENT 2 (for U–Pb dating) or a Thermo-Scientific NEPTUNE (for Lu–Hf isotope analyses) at Goethe University, Frankfurt, Germany, using the same methods as described by Gerdes and Zeh (2006, 2009) with modifications given by Zeh and Gerdes (2012). (For instrument and processing parameters see Supplementary DataTable S3.) In most cases, laser spots of 40–50 µm diameter, used for Lu–Hf isotope analyses, were superimposed directly on the U–Pb laser spots of 23–33 µm diameter. Hafnium isotopes for most samples were analysed on polished mounts, except for zoned zircon grains in quartzite sample JF8 (Fig. 6.9d) and tiny grains in Rooiberg felsite JF21. These were measured on grains mounted on double-sided tape. For sample JF8 thin overgrowths around detrital zircon cores were analysed by running a laser line of 60 µm width with a velocity of 3 µm s^{-1}, a frequency of 5 Hz and an energy of *c*. 5 J cm^{-2} over the crystal surface. Subsequently, the cores of the same grains were measured by drilling a spot of 40 µm diameter directly over the line (Fig. 6.9d). The

results of U–Pb dating and Hf isotope analyses are shown in Figs 6.11–6.13 and in Supplementary DataTables S4 and S5, including results of standard measurements. Standard measurements during 12 analytical sessions yielded the following results: GJ1 (always primary standard) = 0.282000 ± 0.000023 [2SD (standard deviation), $n = 290$]; Plešovice: 0.282467 ± 0.000032 ($n = 140$); 91500: 0.282282 ± 0.000035 ($n = 58$); Temora2: 0.282670 ± 0.000038 ($n = 124$); in good agreement with published data (Woodhead and Hergt, 2005; Morel et al., 2008; Sláma et al., 2008). The Lu–Hf isotope compositions of garnet and whole-rock of sample Sil1 were analysed by the isotope dilution technique, using the same procedure as described in detail by Zeh and Gerdes (2014). The results of these analyses are shown in Table 6.1 and Fig. 6.14.

6.5 Results

6.5.1 Bulk rock Zr-SiO_2 compositions

The investigated samples comprise rocks of contrasting compositions, as reflected by highly variable SiO_2 and Zr contents ranging from 52 to 94 wt%, and from 4 to 552 ppm, respectively (Supplementary DataTable S2). The estimated Zr/Hf ratio of most samples is about 38, near the chondritic value of 36.3 ± 0.3 (Jochum et al., 1986). The compositions of the investigated magmatic rocks overlap with those analysed in previous studies of the RLS, Rooiberg Group and the Rashoop granophyres, and the composition of sedimentary rocks with those of the Transvaal Supergroup (for compilation and references see Fig. 6.5 and Supplementary DataTable S2). Here, we note that most rocks from the RLS show significantly lower Zr contents [range 0.4–124 ppm; mean = 27 ± 21 ppm (1σ), $n = 485$] than the surrounding country rocks (Dullstroom pelite: 268–315 ppm; Vermont pelite: 122–225 ppm; Silverton pelite: 150 ± 64 ppm; Magaliesberg quarzite: 81–160 ppm) and the volcanic rocks of the Rooiberg Group (85–600 ppm). The analysed contact granophyre, microgranite and Rooiberg felsites from the roof of the RLS show even higher Zr contents of 418–551 ppm. The ferrodiorite samples from the roof contact of the RLS analysed in this study have significantly higher Zr contents (68–87 ppm) than most other rocks analysed so far from the Upper Zone [range 2.8–159 ppm; mean 43 ± 32 ppm (1σ); $n = 146$]. The schlieric diorite, perhaps a mixture between felsic and mafic magmas, has a Zr content of 202 ppm. The Zr content of the rocks from the BUS and Marginal Zone is highly variable between 4.3 and 63 ppm (also see Wilson et al., 2017). The composition of the spinifex-textured sample CH12-3 (from the Marginal Zone contact at Schwerin fold) has a composition similar to that of the B1 magma (Barnes et al., 2010) (Supplementary DataTable S2).

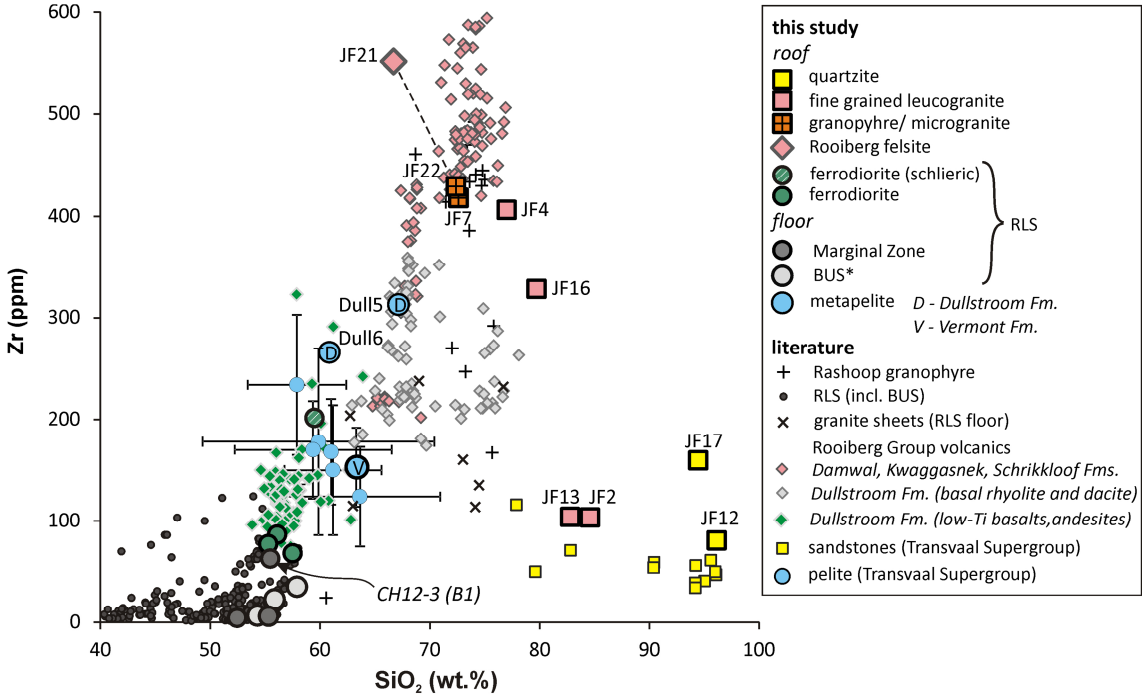

Figure 6.5 - SiO_2 vs Zr diagram of compiled data obtained in this and previous studies from rocks of the Rustenburg Layered Suite (RLS), Bushveld-related granites, Rooiberg Group volcanics and sedimentary rocks of the Transvaal Supergroup. Data sources: RLS (including BUS) from Cawthorn and McCarthy (1985), Cawthorn et al. (1991), Maier et al. (2000), Nex et al. (2002), Arndt et al. (2005), Lundgaard et al. (2006), Wilson and Chunnett (2006), Voordouw et al. (2009), VanTongeren et al. (2010), Godel et al. (2011), Scoon and Mitchell (2012), Wilson (2015) and Wilson et al. (2017); Rashoop granophyre from Kleemann and Twist (1989), Hill et al. (1996) and Mathez et al. (2013); Rooiberg volcanics (Damwal, Kwaggasnek and Schrikkloof) from Schweitzer (1998, compiled by Mathez et al., 2013) and Buchanan et al. (2002, 2003); Rooiberg volcanics (Dullstroom) from Schweitzer (1998, compiled by Mathez et al., 2013) and Buchanan et al. (1999, 2002); granite sheets (RLS floor) from Harris et al. (2003); Transvaal Supergroup sandstones and pelitic rocks from Wronkiewicz and Condie (1990) and Jahn and Condie (1995). Fm., formation.

6.5.2 Zircon morphology and internal zoning

Zircon grains having euhedral shapes were found in most magmatic rocks but also in metasedimentary rocks. In magmatic rocks they occur abundantly in the Upper Zone ferrodiorite (JF5), contact granophyre (JF7), and Marginal Zone feldspathic pyroxenite (sample CH12-3), whereas zircon grains in leucogranite (JF2 and JF4) associated with quartzites are mostly rounded, or show incomplete facets and/or complex morphologies (Figs 6.6 and 6.7). Zircon grains in feldspathic pyroxenites of the BUS are commonly anhedral–irregular (Fig. 6.10b–e), in particular those in the deepest section of the drill core CH7 (Fig. 6.2b), although there are also grains of euhedral shape in each sample (CH7-164A, CH7-143A and CH7-29; Fig. 6.10e–g). Euhedral zircon grains were also found in Rooiberg felsite (JF21), microgranite (JF22) and Rashoop granophyre (JF7) (Fig. 6.6e, h and i). All these grains have very similar morphologies (mostly Pupin-type J5 or D; Fig. 6.8f, i, j and k), dominated by {100} over {110} prisms, and {101} over {211} pyramids (occasionally showing {301} pyramids). However, zircon grains in Rooiberg felsite are much smaller (average width = 27 ± 5 µm, n = 39) than in the immediately surrounding microgranites and granophyres (average width = 81 ± 38 µm, n = 85) (for comparison see Fig. 6.6h and i; Supplementary DataTable S6).

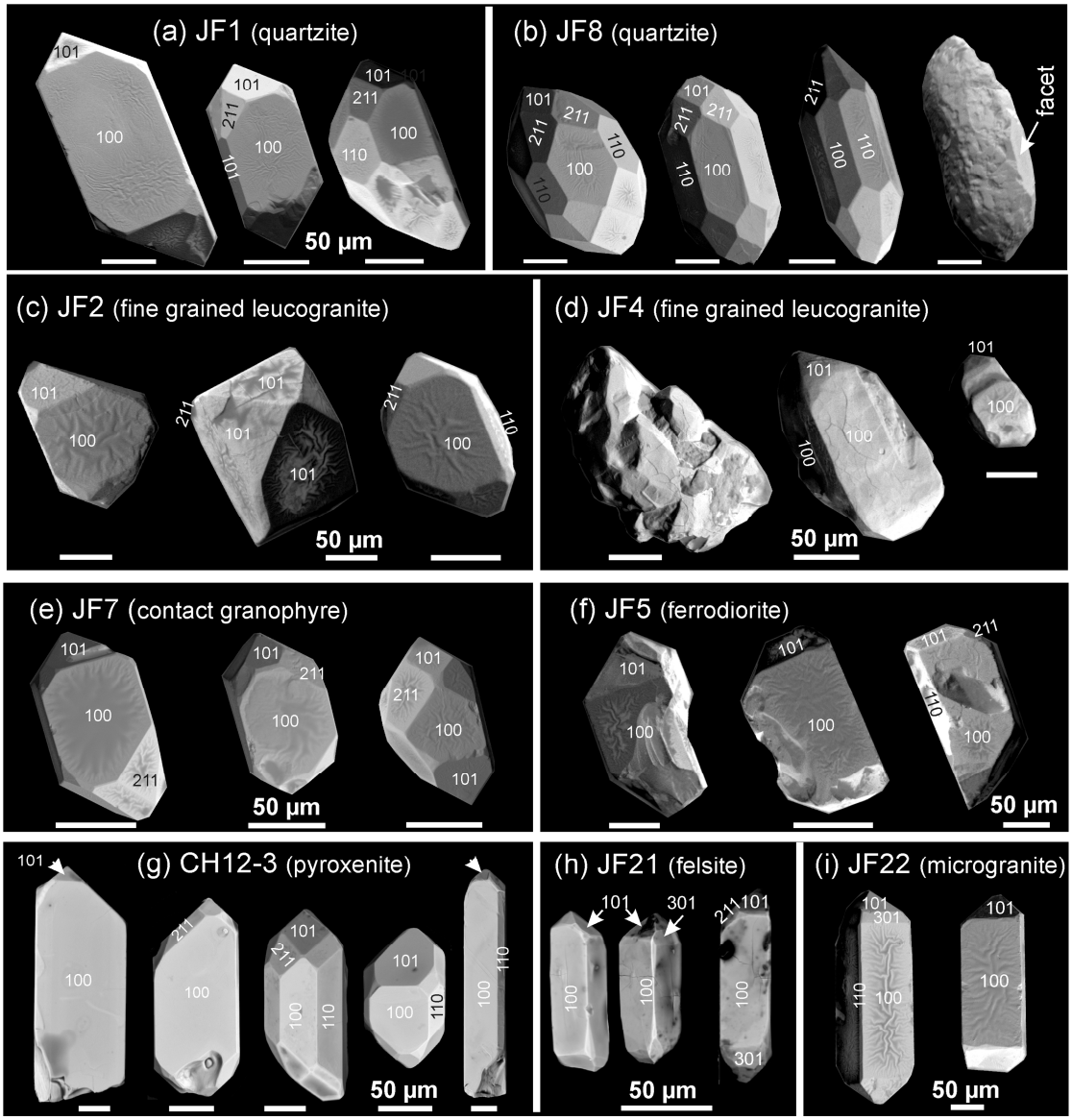

Figure 6.6 - Zircon morphologies in different magmatic and metasedimentary rocks from the roof and floor of the Rustenburg Layered Suite (RLS). It should be noted that magmatic and metamorphic zircons in all rocks from the direct roof contact (JF1, JF2, JF4, JF7, JF5 and JF22) of the RLS and in Rooiberg felsite show similar morphologies dominated by {100} prisms and {101} pyramids, pointing to crystallization temperatures of 900–850 °C, whereas metamorphic zircons in quartzite sample JF8 more remote from the contact show parity between {100 = 110} prisms and {101–211} pyramids or incomplete facets, pointing to lower formation temperatures at 750 °C. Zircon in leucogranite sample JF4 shows complex morphologies resulting from the oriented intergrowth of several crystals parallel to the *c*-axis, and zircon in pyroxenite sample CH12-3 from the direct floor of the RLS shows a wide range in morphologies. All images were obtained by back-scattered electron (BSE) imaging (topographic mode). All scale bars are 50 µm.

Zircon grains of perfect euhedral shape were also found in quartzite samples from the contact aureole of the RLS (*c*. 1–200 m away from the contact: samples JF1, JF8, Mag-R1, BQz1, BQz2 and Mag-B), whereas samples from more remote localities (>1 km: samples Dull4, Dull5 and Dull6) show only a few crystal facets (Fig. 6.7d–h). Here we note that faceted zircon grains from metasedimentary rocks mostly have rounded detrital cores (Fig. 6.9), and the width of the faceted overgrowths and their morphologies are variable (Fig. 6.9a–c). The detrital cores commonly show magmatic zoning patterns, but in each sample there is also a significant number of altered, porous cores pointing to metamictization, leaching and recrystallization

(Fig. 6.9e). Zircon grains in the quartzite sample Mag-B lack inherited cores; therefore all grains were formed during contact metamorphism (for further details see the section ‘Hafnium isotopic composition’).

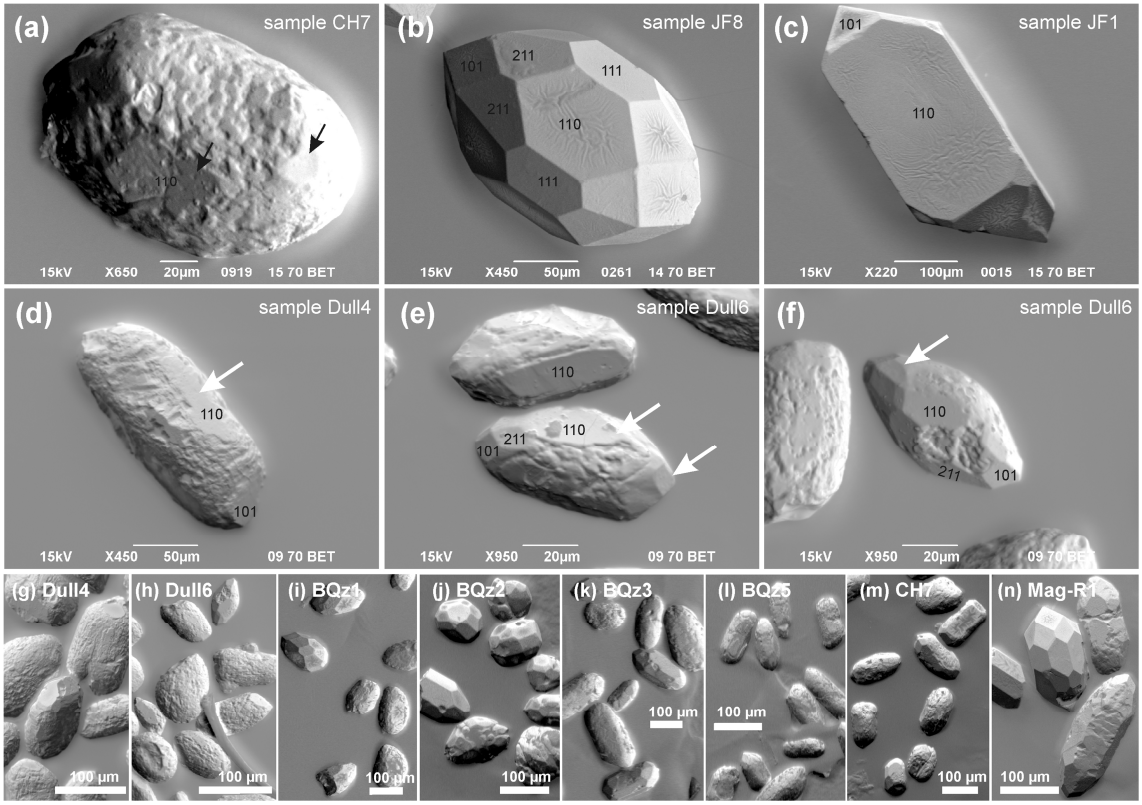

Figure 6.7 - Morphologies of zircon grains in metasedimentary country rocks from the floor (a, d–n) and roof (b, c) of the RLS. It should be noted that zircon grains in all investigated samples (except JF1) show pitted surface structures (a), pointing to dissolution, but also plane facets (b–n), indicating new zircon growth. Planar facets are displayed by zircon grains in quartzite from the direct contact (samples JF1 and Mag-R1), but also in Houtenbeck quartzite and intercalated pelitic schists (d–f) remote from the contact and formed at temperatures as low as 550 °C. In some samples from the direct floor and roof contacts, metamorphic zircon grains of perfect shape are present (JF8, JF1, BQz1, BQz2 and Mag-R1) but with different morphologies. Zircon grains from the direct roof contact are dominated by {100} prisms and {101} pyramids (e.g. JF1), pointing to high temperatures of 900–850 °C, whereas those from the direct floor contact show parity between the prisms {100} and {110} and the pyramids {101} and {211} (e.g. Mag-R1), pointing to lower temperatures at 750 °C. Zircon in quartzite sample CH7 (a, m) from the direct floor contact with the BUS rarely shows perfect facets, indicating incomplete overgrowth.

Zircon grains in quartzite and metapelite samples from the floor of the RLS commonly show incomplete overgrowths of 1–5 µm width, and ‘etching pits’ (Fig. 6.7a and g–n), even in grains taken from the direct contact with the RLS. The morphologies mostly correspond to Pupin-types S12–S13 (Figs 6.6b, 6.7b, i–n and 6.8a, b) and are best developed in sample Mag-R1, and least in samples from the Houtenbeck Formation (Dull4 to Dull6; Fig. 6.7d–h), and in sample CH7-Qz from the direct floor contact with the BUS (Fig. 6.7a and m). Zircon grains of identical characteristics were observed also in a coarse-grained quartzite (JF8) at the roof of the RLS; that is, about 50 m above the contact with the Upper Zone ferrogabbros (Figs 6.6b and 6.9d). In contrast, zircon grains in quartzite from the direct upper contact (samples JF1 and JF3) show very thick overgrowths (up to 50 µm wide) surrounding rounded detrital cores (Fig. 6.9c). Their

morphologies mostly correspond to the Pupin-types J4–J5 and S24–S25 (Fig. 6.8c and d). These morphologies are very similar to those of zircon grains in adjacent fine-grained leucogranite (JF2), contact Rashoop granophyre (Grano1 and JF7), ferrogabbro (JF5), Rooiberg felsite (JF21) and microgranite (JF22) (Figs 6.6 and 6.8), despite significantly different bulk-rock compositions and origins. This suggests that zircon shapes are mainly controlled by temperature, as has been previously suggested by Pupin (1980), rather than by bulk-rock composition or trace element contents of zircon (for detailed discussions see Vavra, 1990; Benisek and Finger, 1993). According to the classification scheme of Pupin (1980), the morphologies of the zircon grains in the RLS, Bushveld-related granites, Rooiberg felsites, and quartzites at the direct upper contact mainly point to formation temperatures of 900–850 °C, whereas those of the lower contact (sample CH12-3) indicate temperatures of 850–750 °C. The morphologies of metamorphic zircon grains in the Magaliesberg quartzite more remote from the contact (Mag-R1 and JF8) point to lower temperatures of 750–700 °C.

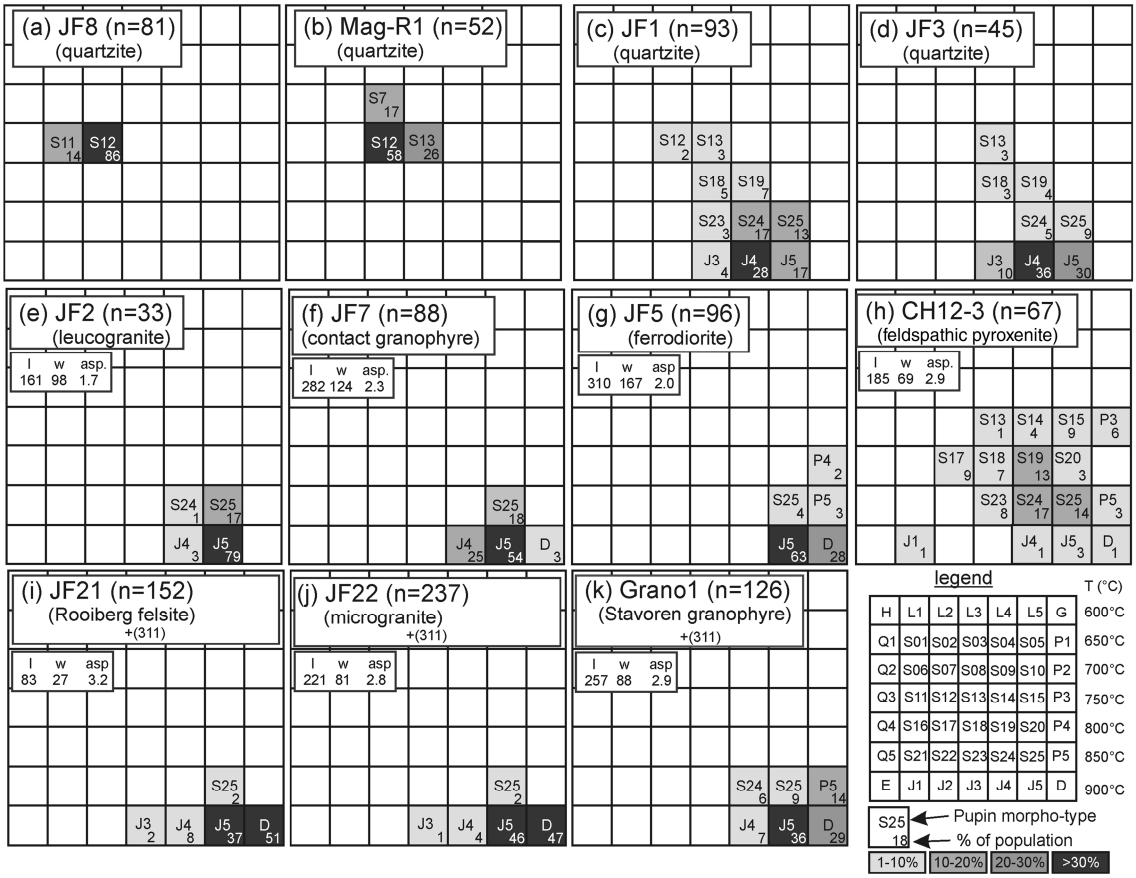

Figure 6.8 - Quantification of zircon morphologies observed in quartzite, different granites, felsite and ferrodiorite presented in the classification diagram of Pupin (1980). Additionally given are average lengths (l), widths (w) and aspect ratios (asp.) for zircon in magmatic rocks (for details see Supplementary Data).

Zircon grains in all mafic and felsic magmatic rocks lack inherited cores, and show significant differences in their zoning patterns. Zircon crystals in ferrodiorite (JF5) reveal a relatively even oscillatory sector zoning, and those in the contact granophyre (JF7) display BSE-dark rims around BSE-bright cores with an oscillatory-sector zoning (Fig. 6.10h and j). Zoning patterns of zircon in leucogranite (JF2 and JF4) are always patchy and irregular, perhaps owing to metamictization followed by recrystallization. The greatest variability in morphology (from Pupin-type S13 to D1; Fig. 6.8h) is shown by zircon grains in the spinifex-structured pyroxenite sample CH12-3 from the Marginal Zone (Fig. 6.6g). These grains also show the largest variation in aspect ratios (from 6.9 to 1.0) of all investigated samples (mostly <4.5 to 1.0; Supplementary DataTable S6). Elongated zircon grains in sample CH12-3 commonly show a banded zoning, whereas more stubby grains display sector zoning (Fig. 6.10k).

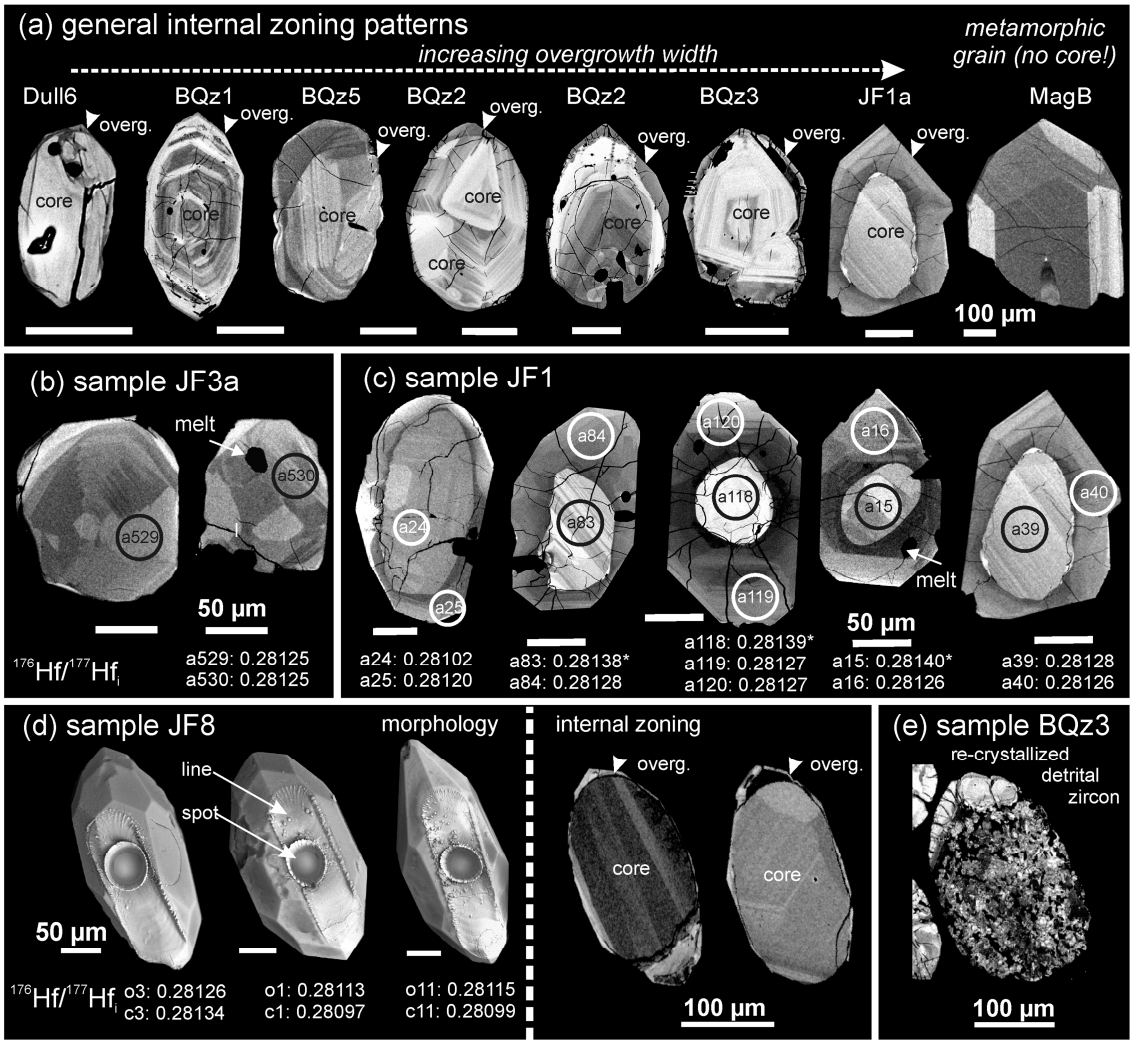

Figure 6.9 - Internal zoning patterns and Hf isotopic compositions of zircon in quartzitic and metapelitic country rocks from the floor and roof of the RLS. (a–d) Zircon grains in most metasedimentary rocks are dominated by rounded detrital cores with magmatic zoning, surrounded by tiny, in some cases perfect overgrowths with thicknesses of a few micrometres (e.g. sample JF8). Only zircon grains in quartzite sample JF1 (c) show broad overgrowths. Zircon grains in quartzite samples MagB (a) and JF3a (b) from floor and roof of the RLS, respectively, are entirely of contact metamorphic origin. Metamorphic zircon grains or domains yield identical initial $^{176}Hf/^{177}Hf_i$, and detrital cores commonly higher or lower $^{176}Hf/^{177}Hf_i$. (e) All metasedimentary samples contain detrital zircon grains showing sponge-like, patchy patterns, pointing to intense alteration and recrystallization.

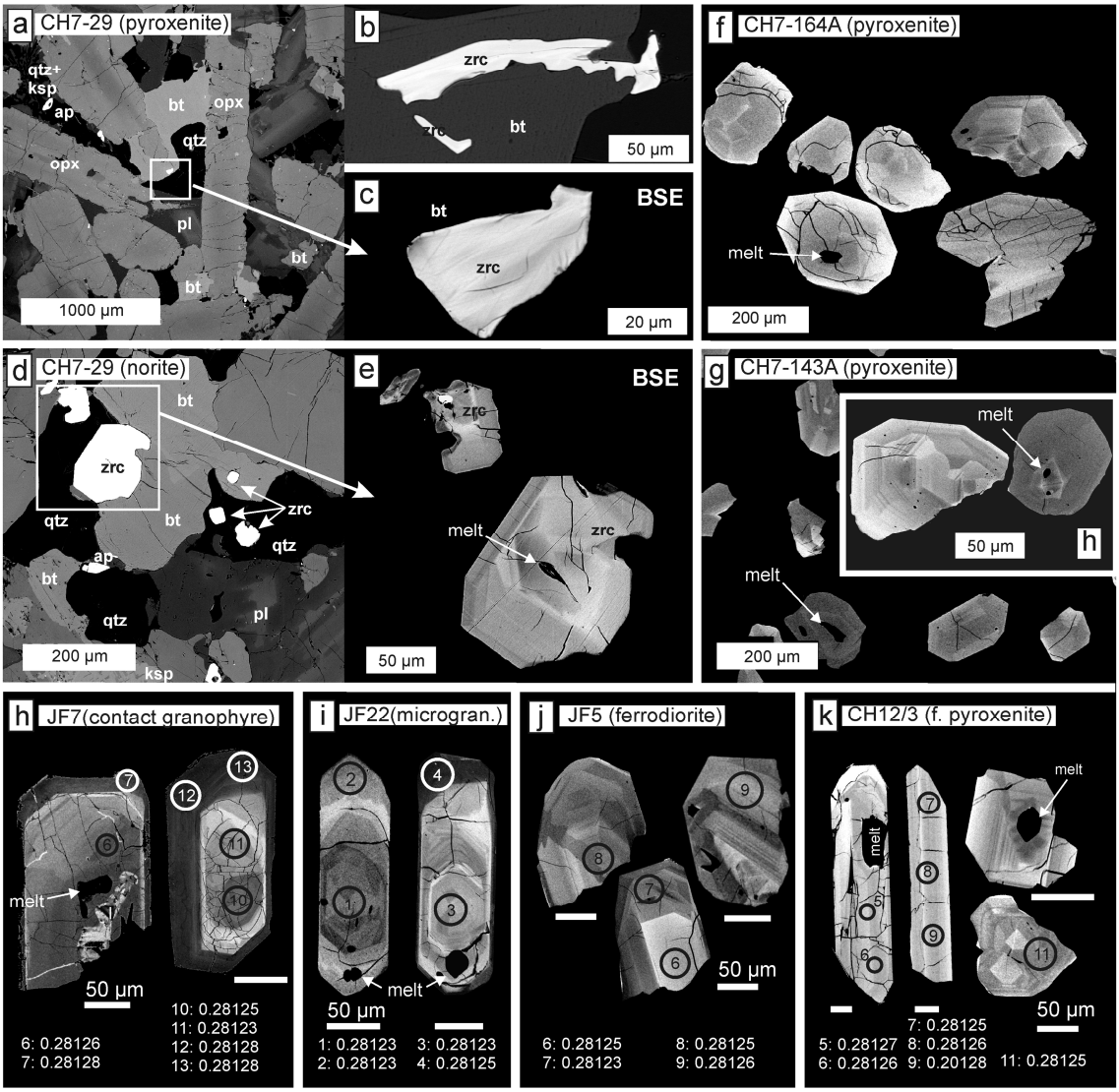

Figure 6.10 - Back-scattered electron images of zircon grains in thin sections (a–e) and grain mounts (f–k) from samples of the (a–g) Basal Ultramafic Suite (BUS), (h) contact granophyre, (i) microgranite, (j) Upper Zone ferrodiorite, and (k) Marginal Zone feldspathic pyroxenite. (a–e) BUS samples contain highly irregular and also euhedral zircon (zrc) grains mostly intergrown with biotite (bt), quartz (qtz), plagioclase (pl), K-feldspar (ksp) and apatite (ap) in intercumulus domains between orthopyroxene (opx). It should be noted that initial $^{176}Hf/^{177}Hf$ ratios obtained from different domains of zoned zircon grains in contact granophyre, microgranite, ferrodiorite and feldspathic pyroxenite are all identical within error. Zircon grains of all samples contain recrystallized melt inclusions.

6.5.3 U-Pb geochronology

A large number of zircon grains from metasedimentary rocks from the floor and roof of the RLS were dated by means of LA-ICP-MS, comprising zircons from five quartzite samples (JF1, JF3a, JF3b, Mag-B, Dull4), two metapelite samples (Dull4, Dull5) and two leucogranite samples (JF2, JF4). The results are shown in Concordia diagrams (Fig. 6.11; and in supplementary materials), and population density diagrams (Fig. 6.12). Detrital zircon cores in the quartzite samples JF1 and JF3a+b yield Archean and Paleoproterozoic ages, overlapping with those obtained for zircon in the Magaliesberg quartzite samples (BQz1, BQz2, BQz3, BQz5, JF8) in a previous study (Zeh et al., 2016). Zircon cores of samples JF1 yield ages of 2864-2561 Ma (n=11), 2126-2116 Ma (n=3), and 2100-2061 Ma (n=14), and sample JF3a+b of 2897-2551 Ma (n=10), 2353-2100 Ma (n=4), and 2090-2061 Ma (n=5) - (Figs. 6.11, 6.12). A minor fraction of Archean zircon grains was also found in the Houtenbeck clastic rocks from the Dullstroom area, but most grains gave Paleoproterozoic ages. The Houtenbeck quartzite (Dull 4) yield two major Paleoproterozoic populations with age peaks at 2250-2220 Ma (n=41) and 2118 ± 4 Ma (n=16), and the metapelitic rocks only one major population peaking at 2113 ± 5 Ma (Dull 5; n=10), and at 2101 ± 5 (Dull 6; n=15), respectively (Fig. 6.12). The youngest concordant ages of detrital zircon grains found in the Houtenbeck samples are at 2072 ± 12 Ma (Dull 4), 2087 ± 9 Ma (Dull 5), and 2068 ± 7 Ma (Dull 6) – (Fig. 6.11f, and Fig. S1, supplementary materials).

Zircon overgrowths in quartzite sample JF1 and JF3a+b mostly gave ages of about 2055 Ma or younger (JF1: Concordia age = 2054 ± 3 Ma, n= 39; sample JF3a: Concordia age = 2057 ± 2 Ma, n= 12; JF3b: upper intercept age: 2051 ± 7 Ma, n=6) - (Fig. 6.11a, b, Table S4), suggesting zircon growth related to formation of the RLS followed by Pb-loss. A similar evolution is also reflected by zircon grains from the two leucogranite samples JF2 and JF4, which either plot on, but in most cases above the reference line between 2055 Ma and present (Fig. 6.11d, supplementary materials). Zircon analyses of samples JF2 and JF4 are mostly discordant and characterized by high contents of common Pb of up to 14.5 % (Table S4). Most zircon grains from quartzite sample Mag-B from the floor contact at the edge of the Burgersfort compartment (Figs. 6.1b, 6.2a) yield concordant ages of 2054.2 ± 3.2 Ma (n=82, Fig. 6.11c).

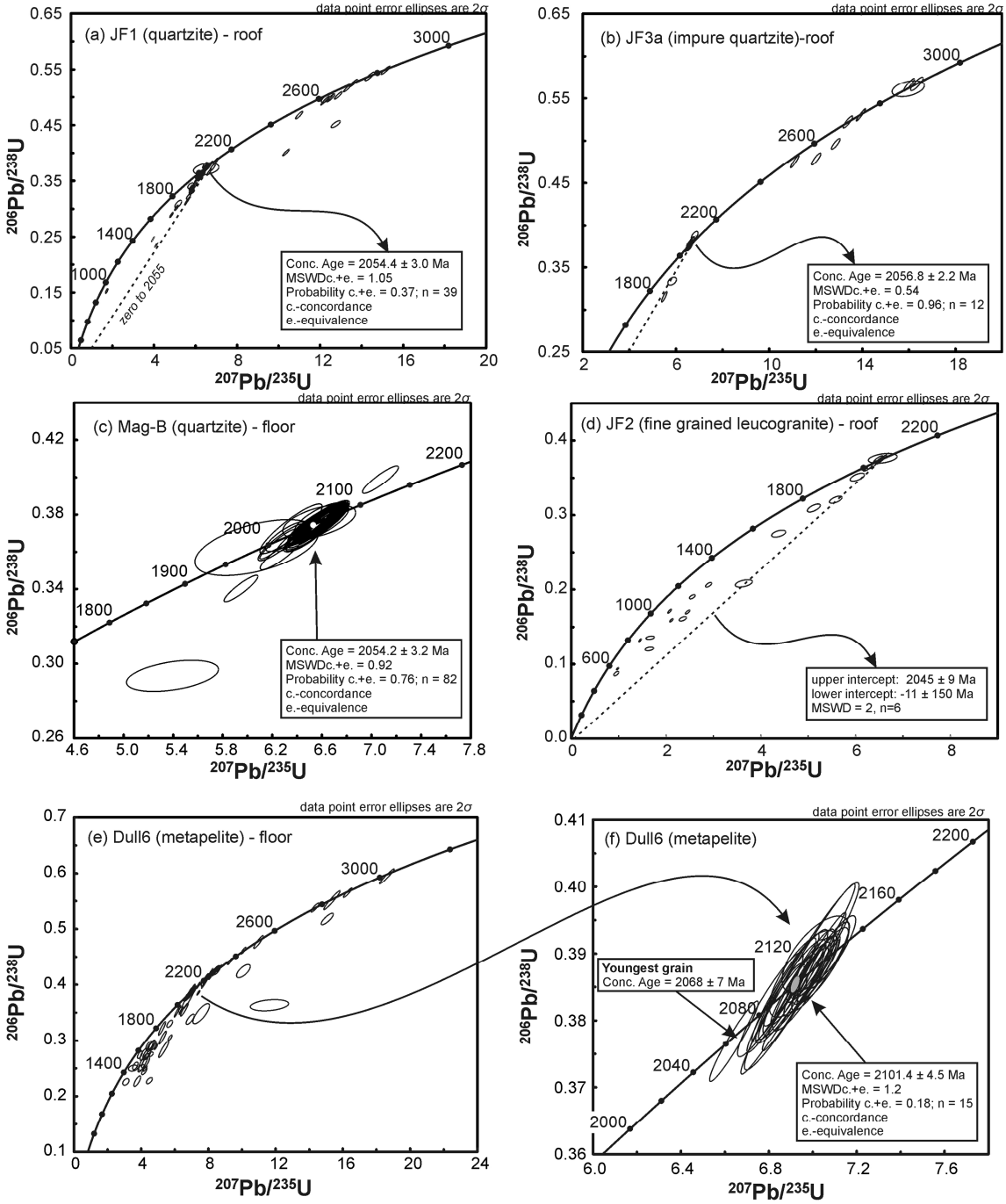

Figure 6.11 - Concordia diagrams showing the results of U–Pb dating of zircon in quartzite and fine-grained leucogranite from the (a, b, d) roof and (c, e, f) floor of the RLS. Concordia ages presented for the samples JF1, JF3a and Mag-B date the time of the contact metamorphic overprint, for leucogranite (JF2) a minimum age for melt formation, and for the metapelitic sample Dull6 the maximum deposition age (youngest grain). Concordia diagrams for samples JF3b, JF4, Dull4 and Dull5 are presented in Supplementary Data.

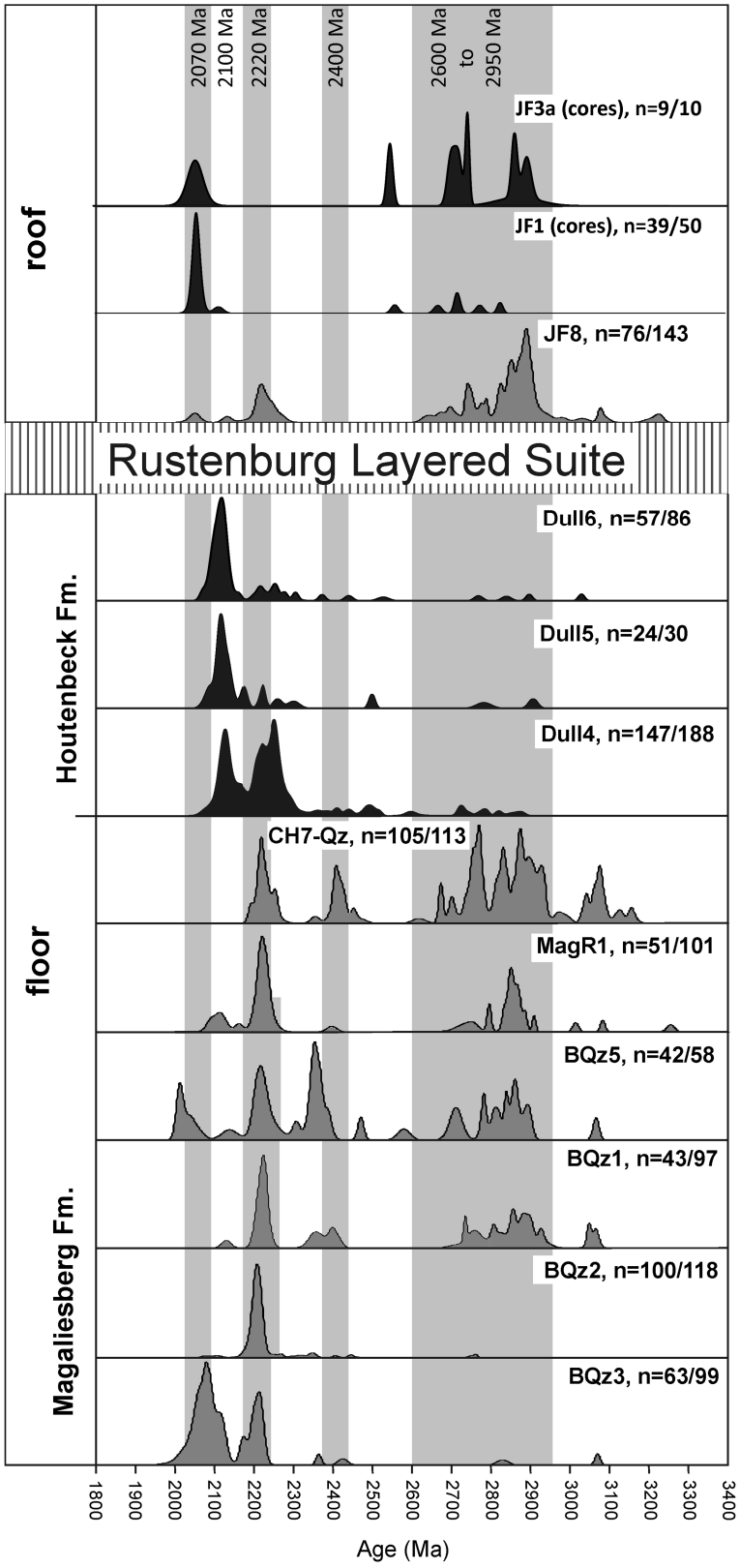

Figure 6.12 - Population density plots showing the age spectra of detrital zircon grains in quartzite and metapelitic rocks of the Magaliesberg and Houtenbeck Formations at the floor and roof of the RLS, obtained in this study and by Zeh et al. (2016) (only data with >95 % concordance). It should be noted that all Magaliesberg quartzites contain a significant age population at 2.22 Ga, and some of them also a significant Archean age population at 2.6–3.1 Ga, whereas Houtenbeck sedimentary rocks are dominated by zircon grains with ages at 2.1 Ga. The youngest age population at <2100 Ma in samples JF1, JF3a and BQz5 perhaps results from Pb loss during the contact metamorphic overprint or from later events.

6.5.4 Hafnium isotopic composition of zircon

Zircons in the following felsic and mafic magmatic rocks from the roof of the RLS yield, within error, identical Hf isotopic compositions (εHf_t; Table 6.2): Rooiberg felsite (JF21: −8.2 ± 1.0, n = 10, 2SD); microgranite (JF22: −8.2 ± 1.0, n = 15); Rashoop granophyre (Grano1: −7.4 ± 1.1, n = 25); contact granophyre (JF7: −7.3 ± 1.0, n = 15); ferrodiorite (JF5: −7.9 ± 1.3, n = 25); ferrogabbro (MH1: −7.5 ± 0.9; n = 22). Overlapping values are also obtained for zircon in mafic rocks of the Marginal Zone (CH7-46: −8.2 ± 0.7, n = 4; CH7-5a: −8.4 ± 1.0, n = 11; CH12-9: −8.1 ± 0.8, n = 16; CH12-3: −8.1 ± 0.7, n = 21; CH12-26: −8.2 ± 0.8, n = 13; CH12-7: −7.8 ± 0.6, n = 10) (Fig. 6.15), as well as for zircon in the leucogranite sample JF2 (−7.5 ± 0.8, n = 16, from concordant to highly discordant zircon domains), and for metamorphic zircon grains or overgrowths in several quartzite samples from the floor (Mag-B: −7.2 ± 1.2, n = 86, all spots) and the roof of the RLS (JF1: −7.3 ± 1.4, n = 45; JF3a: −7.6 ± 1.4, n = 12; JF3b: −7.5 ± 3.0, n = 7). Somewhat lower εHf_t values for zircon were estimated in three out of four cumulate rocks of the BUS (CH7-29: −9.4 ± 1.1, n = 7; CH7-44: −10.2 ± 1.1, n = 9; CH7-164a: −9.1 ± 1.0, n = 15; CH7-143A: −7.6 ± 1.0, n = 10), and from the strongly recrystallized and isotopically discordant zircon grains in the leucogranite sample JF4 from the roof (εHf_t = −10.3 ± 1.7, n = 41) (Supplementary DataTable S5).

Values identical to those of magmatic zircon grains were obtained also by averaging the $\varepsilon Hf_{2.055\,Ga}$ of detrital zircon populations in metapelitic rocks and quartzite of the Houtenbeck Formation (Dull4: −8.7, n = 94; Dull5: −7.2, n = 20; Dull6: −7.1, n = 51), and Magaliesberg quartzite from the floor (BQz3: −6.4, n = 99; BQz2: −7.2, n = 110) and roof of the RLS (JF1: −7.6, n = 50; JF3b: −9.2, n = 22; JF3a: −10.8, n = 4). However, some Magaliesberg samples yield significantly lower average εHf_t (BQz1: −14.9, n = 99; Mag-R1: −14.6, n = 97; CH7: −16.5, n = 110; BQz5: −14.0, n = 41). The ranges in $\varepsilon Hf_{2.055\,Ga}$ of the detrital zircon populations are listed in Table 6.2 and shown in Fig. 6.15. Here we note that metamorphic rims yield either the same εHf_t as the average of the detrital cores (samples JF1, JF3a and JF3b) or higher values (sample JF8). Furthermore, the range in εHf_t of the detrital cores is always much greater (up to 30 ε units) than that of the overgrowths (2.8–8.8 ε units; Fig. 6.15), suggesting Hf transport and Hf isotope homogenization prior to precipitation of metamorphic zircon rims. Homogenization is also supported by the observation that the detrital cores in samples JF1a, JF3a and JF8 show higher and lower εHf_t than respective metamorphic rims (Fig. 6.13c–e).

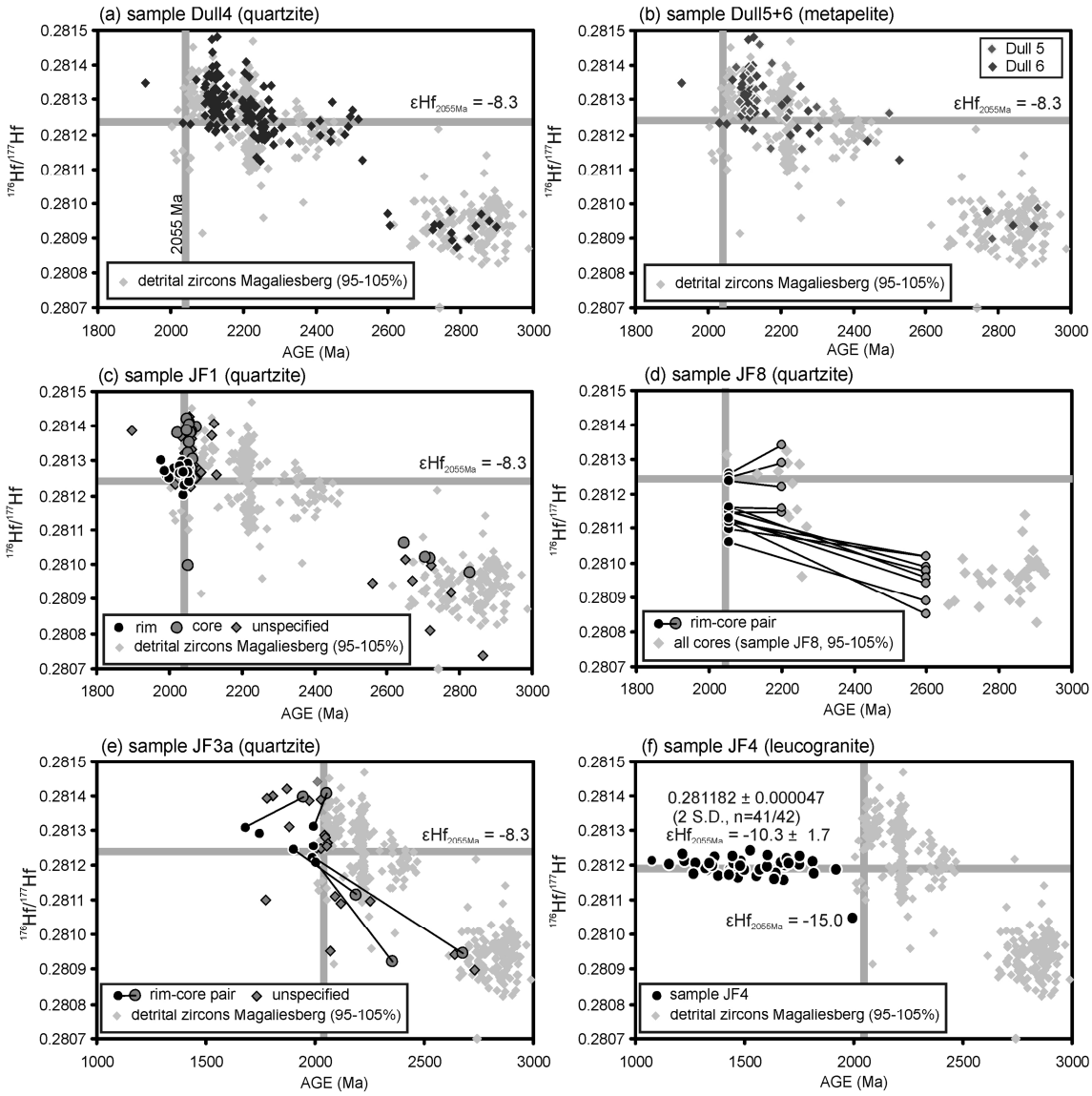

Figure 6.13 - Age versus $^{176}Hf/^{177}Hf$ diagram showing the results of combined U–Pb dating and Hf isotope analyses of detrital zircon grains in (a) quartzite Dull4 and (b) metapelite Dull5 and Dull6, as well as of detrital cores and metamorphic rims in (c) quartzite sample JF1, (d) quartzite sample JF8 and (e) quartzite sample JF3a, and in (f) leucogranite sample JF4. Reference data of detrital zircon in Magliesberg quartzites are from Zeh et al. (2016). In sample JF8, ages for rims and cores were randomly fixed at 2055 Ma (rim), at 2200 Ma (for cores with $^{176}Hf/^{177}Hf$ >0.2811) and at 2600 Ma (for cores with $^{176}Hf/^{177}Hf$ <0.2811). It should be noted that metamorphic rims in JF1, JF8 and JF3a mostly yield lower and higher $^{176}Hf/^{177}Hf$ than related cores, and less scatter. Horizontal line with εHf_t = −8.3 represents the average of all RLS samples investigated in this study.

6.5.5 Results of Lu-Hf isochron dating

Five garnet fractions and one whole-rock fraction of a garnet-bearing schist from the Silverton Formation (sample Sil1) lie on an isochron yielding an age of 2059.7 ± 2.7 Ma (excluding the error of the decay constant, $\lambda = 1.867 \pm 0.015$; Scherer et al., 2001), and an initial $^{176}Hf/^{177}Hf_t$ of 0.281284 ± 0.000021 (Fig. 6.14). This value corresponds to $\varepsilon Hf_{2.06\,Ga} = -6.6 \pm 0.7$, which overlaps with the values estimated for magmatic zircon of the RLS. The low MSWD (mean square weighted deviation) of 0.81 of the six-point isochron hints that Hf isotope homogenization was achieved on hand-specimen scale during contact metamorphic garnet growth under amphibolite-facies conditions, indicated by the assemblage garnet–staurolite–muscovite.

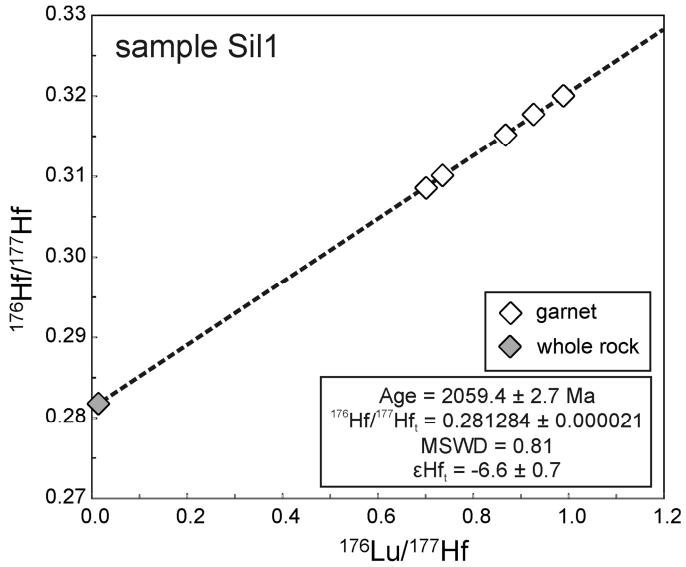

Figure 6.14 - Isochron diagram showing the results of Lu–Hf isotope analyses of five garnet fractions and whole-rock of a garnet schist (sample Sil1) from the Silverton Formation.

Table 6.1 Results of Lu-Hf ID-TIMS isotope analyses of garnet (Grt) and whole rock (wr) of sample Sil1

fraction	weight (g)	Lu ppm	Hf ppm	$^{176}Lu/^{177}Hf$	±2σ (abs)	$^{176}Hf/^{177}Hf$	±2σ (abs)
Grt	0.0851	6.7	1.4	0.6996	0.0017	0.308637	0.000023
Grt	0.1034	6.8	1.3	0.7338	0.0018	0.310008	0.000023
Grt	0.9983	7.6	1.2	0.9285	0.0023	0.317687	0.000023
Grt	0.0786	8.0	1.2	0.9891	0.0025	0.320053	0.000023
Grt	0.1105	7.7	1.3	0.8677	0.0022	0.315238	0.000023
wr	0.1213	0.5	5.2	0.01494	0.00004	0.281870	0.000021

Table 6.2 Summary of hafnium isotopic data and zircon formation temperatures

Sample	Rock	$\varepsilon Hf_{2.05\,Ga}$			$\varepsilon Hf_{2.05\,Ga}$				Temp. of zircon formation (°C)		
		Mean[1]	±2σ	*n*	Mean[2]	Min.	Max.	*n*	Pupin (>80 %)[3]	Zr-sat.[4]	Ti-in-Zrc[5]
Roof of Bushveld Complex											
Felsic rocks		*Magmatic zircon*									
Grano 1	Rashoop granophyre	−7.4	1.1	25					850–900	858	
JF22	microgranite	−8.2	1.0	15					850–900	853	
JF21	Rooiberg felsite	−8.2	1.0	10					850–900	861	
JF4	leucogranite	−10.3	1.7	41							
JF2	leucogranite	−7.5	2.1	16					850–900	(731)	
JF7	contact granophyre	−7.3	1.0	15					850–900	858	
Mafic rocks											
JF5	ferrodiorite (UZ)	−7.9	1.3	25					900		
MH1	ferrodiorite (UZ)	−7.5	0.9	22							760–848
Metasedimentary rocks		*Metamorphic zircon*			*Detrital zircon cores*						
JF84	quartzite	−11.5	4.5	15	−16.1	−26.9	−5.2	102	750		
JF3a	quartzite	−7.6	1.4	12	−10.8	−15.0	−1.6	4	850–900		
JF3b	quartzite	−7.5	3.0	7	−9.2	−20.4	−1.1	22	850–900		
JF1	quartzite	−7.3	1.4	45	−7.6	−26.1	−1.5	50	850–900		

(continued on next page)

Table 6.2 (continued)

Sample	Rock	$\varepsilon Hf_{2.05\,Ga}$			$\varepsilon Hf_{2.05\,Ga}$				Temp. of zircon formation (°C)		
		Mean[1]	±2σ	*n*	Mean[2]	Min.	Max.	*n*	Pupin (>80 %)[3]	Zr-sat.[4]	Ti-in- Zrc[5]
Floor of Bushveld Complex											
Mafic rocks		*Magmatic zircon*									
CH12-7	norite (MZ)	−7.8	0.6	10							
CH12-26	norite (MZ)	−8.2	0.8	13							787–845
CH12-3	norite (MZ)	−8.1	0.7	21					750–850		799–893
CH12-9	norite (MZ)	−8.1	0.8	16							
CH7-5A	norite (MZ)	−8.4	1.0	11							
CH7-46	norite (MZ)	−8.2	0.7	4							
CH7-143A	pyroxenite (BUS)	−7.6	1.0	10							
CH7-164A	pyroxenite (BUS)	−9.1	1.0	15							
CH7-44	norite (BUS)	−10.2	1.1	9							
CH7-29	norite (BUS)	−9.4	1.1	7							
Metasedimentary rocks		*Metamorphic zircon*									
Magaliesberg Formation											
Mag-B	quartzite	−7.2	1.2	86							
BQz36	quartzite				−6.4	−27.8	−0.6	99			
BQz26	quartzite				−7.2	−18.6	−3.5	110			
BQz16	quartzite				−14.9	−25.4	−2.7	99			
Mag-R16	quartzite				−14.6	−27.6	0.0	97	750		
CH76	quartzite				−16.5	−27.4	−3.4	110			
BQz56	quartzite				−14.0	−22.9	−3.5	41			
Houtenbeck Formation											
Dull4	quartzite				−8.7	−20.7	+1.4	94			
Dull5	metapelite				−7.2	−20.0	−0.3	20			
Dull6	metapelite				−7.1	−20.1	+0.4	51			
Silverton Formation		*Initial value of isochron*									
Sil1	metapelite	−6.6	0.7								

UZ, Upper Zone; MZ, Marginal Zone; BUS, Basal Ultramafic Sequence.

[1]Mean of magmatic or metamorphic zircon population.

[2]Mean of detrital zircon populations at 2.05 Ga.

[3]'Zircon morphology temperature' reflected by more than 80 % of zircon population.

[4]Zircon-saturation temperatures.

[5]Ti-in-Zrc indicates Ti-in-zircon temperatures; from Zeh et al. (2015).

[6]Samples and data from Zeh et al. (2016).

6.6 Discussion

6.6.1 Timing and conditions of zircon formation

6.6.1.1 Detrital and magmatic zircon in pre-RLS rocks

Zircon grains investigated in this study were formed either prior to intrusion of the RLS or during crystallization of the RLS and related granites. Pre-RLS zircon comprises detrital grains in the metasedimentary rocks of the Magaliesberg and Houtenbeck formations, and tiny magmatic grains found in Rooiberg felsite (sample JF21). The results indicate that metapelitic rocks and quartzites of the Houtenbeck Formation were deposited after 2070 Ma, as reflected by the youngest detrital zircon grains found in samples Dull4 (2072 ± 12 Ma) and Dull6 (2068 ± 7 Ma). These ages are slightly younger than a maximum deposition age of 2080 ± 7 Ma obtained previously for Magaliesberg quartzite (sample BQz3) by Zeh et al. (2016). All these data suggest that the sedimentary rocks of the uppermost Pretoria Group were deposited less than 25 Myr prior to the intrusion of the RLS. The new datasets, furthermore, reveal that the zircon detritus of the Houtenbeck Formation was supplied mainly from evolved Paleoproterozoic crustal sources ($\varepsilon Hf_{2.3–2.1\ Ga}$ mostly between 0 and −15), affected by magmatic activities mainly at 2.25–2.22 Ga (10–65 %) and 2.12 Ga (30–85 %), whereas evidence for Archean magmatism is scarce (Fig. 6.12). Detrital zircon grains with ages of about 2.12 Ga were found also in Magaliesberg quartzite, although less abundant (11 %), and in clastic sedimentary rocks intercalated with the Dullstroom volcanics (Zeh et al., 2016). The source of Paleoproterozoic detrital zircons is not entirely clear. Zeh et al. (2016) suggested that they derive from the Ophthalmia orogenic belt, which was formed by collision between the southern margin of the Pilbara Craton (present-day western Australia) and the Glenburgh terrane (south of Pilbara) between 2.215 and 2.145 Ga. Further details about the Paleoproterozoic terrane constellation of the Kaapvaal Craton during the Archean to Paleoproterozoic have been given by Zeh et al. (2016). Finally, we note that the detrital zircon population in all Houtenbeck samples, and in many Magaliesberg samples (dominated by Paleoproterozoic zircon grains with ages of 2.22 and 2.12 Ga), yields average $\varepsilon Hf_{2.055\ Ga}$ values between −6.4 and −10.8, which overlap with data obtained for magmatic zircon of the RLS (Fig. 6.15; Table 6.2).

The Rooiberg Group volcanics were formed after deposition of the Houtenbeck sedimentary rocks (<2068 Ma) but prior to the emplacement of the RLS at 2055.9 ± 0.3 Ma (Zeh et al., 2015). This is supported by field relationships (e.g. Martini, 1998) and radiometric ages of 2061 ± 2 Ma (Pb–Pb zircon evaporation; Walraven, 1997) and 2057.3 ± 2.8 Ma (SHRIMP U–Pb zircon; Harmer and Armstrong, 2000). The morphology of tiny zircon grains found in sample JF21 suggests formation temperatures of about 900–850 °C (Pupin, 1980). These temperatures are in good agreement with Zr-saturation temperatures of 861 °C calculated for sample JF21 using the calibration of Watson and Harrison (1983) (Table 6.2), but lower than eruption and

liquidus temperatures between 1045 and 1000 °C calculated for Rooiberg rhyolites by Lenhardt and Eriksson (2012) and Mathez et al. (2013). Based on bulk-rock major and trace element data, Buchanan et al. (2002) suggested that the felsic lavas of the Rooiberg Group (Damwal, Kwaggasnek and Schrikkloof) formed by successive fractionation in a shallow-seated magma chamber. This conclusion is in agreement with the observed increase in contents of incompatible trace elements (e.g. Zr) and SiO_2 (Fig. 6.5), and the A-type character of the rhyolitic volcanics. Here, we note that the Rooiberg volcanic rocks have the same $\varepsilon Hf_{2055\ Ma}$ of -8.2 ± 1.0 as most magmatic zircon grains in the RLS (Fig. 6.15), suggesting a genetic link, although it is pertinent to note that the Hf isotopic composition is constrained so far only by zircon grains from one sample (JF21). Furthermore, it has to be mentioned that all mafic and felsic rocks of the Rooiberg Group have significantly higher Zr contents (200–600 ppm) compared with the RLS (mostly <25 ppm), including the proposed compositions of the parental magmas UM (31 ppm; Wilson, 2012, 2015), B1 (77 ± 20 ppm), B2 (54 ± 28 ppm) and B3 (23 ± 13 ppm) (Barnes et al., 2010). Thus, assimilation of minor amounts of Rooiberg volcanics would have a large impact on the Zr–Hf budget and Hf isotopic composition of the RLS parental magmas (see the section ‘Reservoirs of RLS parental magmas’).

6.6.1.2 Zircon in RLS-rocks

Zircon grains found in cumulate rocks at the floor and roof of the RLS (feldspathic pyroxenite, norite, ferrodiorite and ferrogabbro) are all of magmatic origin, as is indicated by their internal zoning patterns (Fig. 6.10), melt inclusions and morphologies (Fig. 6.6; also see Fig. 3 of Zeh et al., 2015). There is no evidence from CL images, U–Pb ages or Hf isotopic compositions for any inherited component. Most grains crystallized between 2055.91 ± 0.26 and 2054.89 ± 0.37 Ma as suggested by results of high-precision chemical abrasion isotope dilution thermal ionization mass spectrometry (CA-ID-TIMS) dating (Zeh et al., 2015). Field relationships suggest that rocks of the BUS and zircons therein must be somewhat older. However, their exact age is as yet unknown, as results of high-precision CA-ID-TIMS dating are not available. Thin section observations indicate that magmatic zircon throughout the RLS crystallized from intercumulus melts in an assemblage with quartz, K-feldspar, biotite and plagioclase (e.g. Fig. 6.10a and d; also see Yudovskaya et al., 2013; Zeh et al., 2015; Scoates and Wall, 2015). Recrystallized and homogenized melt inclusions in zircon from Marginal and Upper Zone rocks mostly reveal a rhyolitic composition with SiO_2 >73 wt% (Gudelius et al., 2017). At present, it remains unclear whether these rhyolitic melts were formed by fractionation from parental magmas (B1 and B3) and/or by mingling between mafic and felsic melts of distinct viscosity (perhaps droplets of assimilated country rocks; e.g. Rooiberg felsites) prior to the crystallization of cumulus phases.

Based on results of Ti-in-zircon thermometry, Zeh et al. (2015) demonstrated that zircon in cumulate rocks of the Marginal Zone (all buffered by rutile and quartz) formed at temperatures between 895 and 785 °C (Table 6.2). Approximately the same range in temperatures (900–750 °C) is reflected by the zircon morphologies in the spinifex-textured pyroxenite sample CH12-3 (Marginal Zone), occurring in direct contact with Magaliesberg quartzite at the Schwerin fold (Figs 6.6g and 6.8h). Overlapping zircon crystallization temperatures, mainly between 900 and 850 °C, were also obtained by applying the Pupin classification scheme to zircon grains extracted from different rocks exposed at the direct roof contact of the RLS, comprising ferrodiorite (JF5), immediately adjacent granophyre (JF7), leucogranite (JF2) and quartzite (JF1) (Table 6.2). These temperatures are in good agreement with those obtained by applying the Zr-saturation geothermometer (Watson and Harrison, 1983) to Rashoop granophyre, contact granophyre and microgranite, ranging between 858 and 853 °C (Table 6.2). More generally, our dataset supports the interpretation of Pupin (1980) that zircon morphologies, in particular their {100}:{110} prism-face ratios, are controlled mainly by temperature, and only subordinately by melt composition as has been proposed by Vavra (1990) and Benisek and Finger (1993). Nevertheless, a more thorough study on RLS zircon grains, including detailed correlations between internal zoning patterns and trace element compositions, is needed (see Benisek and Finger, 1993) to support this interpretation in more detail.

Zircon grains of nine cumulus rock samples of the Upper Zone and Marginal Zone analysed in this study yield, within error, identical εHf_t between -7.5 ± 0.9 and -8.4 ± 1.0 (mean: 8.0 ± 1.0, 2SD, $n = 121$), and three samples of the BUS unit show somewhat lower εHf_t between -9.1 ± 1.0 and -10.2 ± 1.1. These values overlap with the data estimated by Zirakparvar et al. (2014) for zircon grains in cumulate rocks from the Lower, Critical and Upper zones of the RLS, ranging from -6.9 ± 1.1 to -10.0 ± 0.7, although there are some significant outliers (see Fig. 6.15). In summary, the available dataset indicates that zircon grains in all rocks throughout the RLS formed within late-magmatic, SiO_2–K_2O–H_2O-rich intercumulus melts at temperatures mainly between 900 and 850 °C at the roof and between 900 and 750 °C at the floor, and that variations in Hf isotope composition are minor but significant. A combination of the εHf_t datasets from this study and that of Zirakparvar et al. (2014) indicates that εHf_t values decrease from the Lower Critical Zone (εHf_t at −8.0) towards the Upper Critical Zone–lower Main Zone (εHf_t = −9.0 to −10.0) (Fig. 6.15). This trend, although not very pronounced, is similar to that presented by Maier et al. (2000) for Nd isotopes, showing a decrease in εNd_t from −5.1 to −7.6 along the same stratigraphic profile.

6.6.1.3 Zircon in granitic rocks

Magmatic zircon grains in different granitic rocks of the roof of the RLS, comprising different granophyres (JF7 and Grano) and microgranites (JF22) formed at the expense of Rooiberg

felsite (Fig. 6.4e and f), as well as fine-grained leucogranites (JF2 and JF4) formed by melting of impure quartzite (Fig. 6.4a and b), show the same morphologies as zircon in the adjacent ferrodiorite (JF5; Fig. 6.6), pointing to crystallization temperatures of 900–850 °C (Fig. 6.8e–g and i–k). Only zircon grains in sample JF4 show mostly a complex habit, resulting from the intergrowth of several grains of the same orientation (Fig. 6.6d). The 'zircon morphology temperatures' for most granitic rocks (after Pupin, 1980) are in good agreement with Zr-saturation temperatures (Watson and Harrison, 1983) ranging between 858 and 853 °C (Table 6.3). The only exceptions are leucogranite samples JF2 and JF13, which yield significantly lower Zr-saturation temperature of 731 °C and 765 °C, respectively (Supplementary DataTable S2). These lower temperatures might result from disequilibrium melting (see Watt et al., 1996) of the surrounding impure quartzite. This interpretation is in agreement with field observations, and the very high SiO_2 contents of samples JF2 and JF13 (Figs 6.4a, b and 6.5). BSE or CL images and combined U–Pb–Hf isotopic data of zircon in all granitic rocks provide no evidence for xenocrysts. The only exception is indicated by one grain in sample JF4, showing $\varepsilon Hf_{2.055\,Ga} = -15.0$, whereas all other grains yield $\varepsilon Hf_{2.055\,Ga} = -10.3 \pm 1.7$ (Fig. 6.13f). In summary, formation temperatures of 900–850 °C, and Hf isotopic compositions of zircon in granitic rocks of different origin in the roof of the RLS are identical to those obtained for mafic rocks of the underlying RLS. These results indicate that zircon formation at either side of the roof contact occurred at nearly the same temperatures. They further support the interpretation that the Zr–Hf budget and Hf isotopic composition of the Upper Zone rocks were controlled by assimilation of felsic melts, which were successively formed by contact metamorphic melting of Rooiberg volcanics (microgranites) and/or impure quartzites (leucogranites) at the roof of the progressively expanding RLS magma chamber.

6.6.1.4 Metamorphic zircon in metasedimentary rocks

Zircon grains in all quartzite and metapelitic rocks investigated in this study provide evidence for metamorphic overgrowth around rounded cores, except for sample Mag-B, where the entire population is of contact metamorphic origin, as suggested by a concordia age of 2054 ± 3 Ma and identical $\varepsilon Hf_{2.055\,Ga} = -7.2 \pm 1.2$ of all zircon grains. Apart from sample Mag-B, metamorphic overgrowths of zircon in floor rocks are mostly thin (<5 µm width). Zircons from the direct contact with Marginal Zone rocks (1–20 m away; samples Mag-R1, BQz1 and BQz2) commonly show overgrowths of perfect euhedral shape (Fig. 6.7i, j and n), whereas those in direct contact with chilled rocks of the BUS (CH7-Qz) and away from the contact (BQz5, Dull4–Dull6) are always rounded with only a few facets (Fig. 6.7a, d–f, l and m). The morphologies of the metamorphic zircon overgrowths in floor rocks point to temperatures of 750–700 °C (Pupin-type S12-S13; Fig. 6.8b). These temperatures are in good agreement with near solidus temperatures of 750 ± 50 °C estimated on migmatitic rocks forming the direct floor

of the RLS (Nell, 1985; Kaneko and Miyano, 1990; Harris et al., 2003), and overlap with the lowest temperatures estimated for magmatic zircon in spinifex-textured pyroxenite sample CH12/3 from the direct contact (Fig. 6.8h). Zircon overgrowths in the metasedimentary floor rocks formed in the presence of melt, as is indicated by feldspar grains with low dihedral angles between quartz grains in most quartzite samples (Harris et al., 2003; Zeh et al., 2016). In contrast, the incomplete zircon overgrowths in the Houtenbeck samples (Dull4–Dull6; Fig. 6.7d–h) formed at subsolidus temperatures of about 550–600 °C at 1–2 kbar in the presence of aqueous fluids. This conclusion is supported by the assemblage andalusite–muscovite in samples Dull5 and Dull6 (Fig. 6.4g). In summary, combination of our datasets provides evidence that metamorphic zircon in floor rocks of the RLS was precipitated from aqueous fluids and melts at temperatures between 550 and 800 °C during RLS formation, and that these zircon grains have $\varepsilon Hf_{2.055\,Ga}$ of -7.2 ± 1.2 identical to zircon in adjacent mafic rocks of the BUS and Marginal Zone.

Metamorphic zircon overgrowths and newly formed grains in quartzite at the direct roof contact of the RLS (JF1, JF3a and JF3b) have morphologies that are very similar to those of magmatic zircons in adjacent leucogranite, granophyre and ferrodiorite. However, they are more variable and point to a wider range in crystallization temperatures between 900 and 750 °C (Fig. 6.8c and d). The metamorphic grains or domains show identical $\varepsilon Hf_{2.055\,Ga}$ between -7.3 ± 1.4 and -7.6 ± 1.4, similar to zircon in adjacent granitic and mafic rocks (Fig. 6.15). Metamorphic zircon grains in quartzite more remote from the roof contact (JF8) have only thin overgrowths of perfect euhedral shape (Fig. 6.6b), similar to zircon grains in floor quartzite of the RLS (e.g. Mag-R1; Figs 6.7n and 6.8a, b), pointing to crystallization temperatures of 750–700 °C. Metamorphic rims of zircon in sample JF8 display an average εHf_t of -11.5 ± 4.5, which is higher than the average of -16.1 ± 12 obtained for zircon cores of the same sample (Figs 6.13d and 6.15). This might indicate infiltration of Zr–Hf-bearing fluids from more remote sources (see Zeh and Gerdes, 2014). Zircon crystallization temperatures and feldspar with low dihedral angles between quartz grains in all investigated roof quartzites further suggest zircon formation in the presence of melt. In summary, data of metamorphic zircon (grains and overgrowths) in the floor and roof of the RLS support the conclusion that the Zr–Hf budget of the RLS rocks might have been controlled by the infiltration of aqueous fluids and felsic melts, generated and released during contact metamorphism.

6.6.2 Hafnium isotope homogenization in the RLS and contact aureole

The Hf isotope analyses carried out in this study reveal that zircon grains in different mafic rocks at the floor (BUS, Marginal Zone) and roof (Upper Zone) of the RLS show only slight variations in $\varepsilon Hf_{2.055\,Ga}$ (between −7.5 and −10.2), identical to $\varepsilon Hf_{2.055\,Ga}$ of zircon in different granitic rocks (granophyres, microgranites, fine-grained leucogranites) related to the RLS intrusion, and to metamorphic zircon in country rocks (Fig. 6.15). Identical $\varepsilon Hf_{2.055\,Ga}$ values were also obtained for zircon in the Rooiberg felsite, formed prior to the RLS, as well as by averaging the $\varepsilon Hf_{2.055\,Ga}$ of detrital zircon populations in several Magaliesberg and Houtenbeck formation sedimentary rocks, and by a six-point isochron obtained from a metapelitic schist of the Silverton Formation (Fig. 6.14). This striking overlap in εHf_t suggests that Hf isotopic homogenization was achieved in both the RLS magma chamber and in parts of the contact aureole, and that the Zr–Hf budget in the RLS might have been controlled by bulk assimilation and/or by the infiltration of aqueous fluids and melts from the contact aureole.

A control of the Zr–Hf budget of the RLS by assimilation is, apart from overlapping εHf_t values, also supported by the occurrence of abundant, undigested or partly digested, country rock xenoliths at the floor and roof of the RLS magma chamber (Fig. 6.3; also see VanTongeren, 2015), and by the fact that metasedimentary and volcanic country rocks contain much higher Zr(+Hf) contents (150–550 ppm) than the RLS mafic rocks (mostly <25 ppm; Fig. 6.5). Metamorphic zircon overgrowths in all investigated metasedimentary samples additionally provide evidence for new zircon precipitation from aqueous fluids (e.g. samples Dull4–Dull6) and melts (e.g. sample JF1) at temperatures between 550 and 900 °C. A likely source for the Zr(+Hf) in the fluids is metamict detrital zircon grains, which occur abundantly in all investigated quartzite and metapelitic samples (Fig. 6.9e; also see Fig. 3 of Zeh et al., 2015). During the fluid-assisted transport, the originally large variation in Hf isotopic composition became homogenized, as is reflected by the relatively small scatter in εHf_t of metamorphic zircon grains or rims (2.8–9.0 ε units) compared with detrital zircon cores (up to 30 ε units; Figs 6.13c–e and 6.15) in quartzite (e.g. samples JF1 and Mag-B), and in leucogranites formed in impure quartzite (e.g. samples JF2 and JF4). This deduction is further supported by the low MSWD of the Lu–Hf whole-rock–garnet isochron obtained from sample Sil1. Different volumes of metamorphic zircon (entire zircon population in samples Mag-B and JF3 versus tiny zircon rims in contact samples BQz1 and CH7-Qz; Fig. 6.9a) additionally indicate that the fluid regime was highly heterogeneous throughout the contact aureole, causing spatial variations in the degree of zircon dissolution, transport and re-precipitation. This conclusion is in good agreement with results of Harris et al. (2003), based on detailed studies on quartz textures, and Sr–O-isotope analyses. Considering that accretion and cooling of the RLS below 700 °C occurred in much less than 1 Myr (Zeh et al., 2015), the homogenization process also must have taken place at commensurate rates. Thereby, isotopic heterogeneities resulting from distinct

mafic magma sources in the mantle, as well as from assimilation of different granitic melts, country rocks and fluids in the crust, were smoothed out. The homogenization process very probably comprised magma mixing, mingling and diffusion, and must have terminated prior to zircon formation within intercumulus melts at temperatures between 900 and 700 °C.

Nevertheless, it is pertinent to note that complete homogenization within the RLS magma chamber was not achieved. This is indicated by minor, but still significant, Hf isotope variations ($\varepsilon Hf_{2.055\,Ga}$ = −7.5 to −10.2), in particular within the BUS, as well as by differences in εHf_t values between rocks of the Upper Critical Zone and lowermost Main Zone ($\varepsilon Hf_{2.055\,Ga}$ = −8.9 to −10.0; data of Zirakparvar et al., 2014) and the Marginal Zone and Upper Zone ($\varepsilon Hf_{2.055\,Ga}$ = −8.0; this study) (Fig. 6.15). Here we note that the BUS contains multiple layers of spinifex and fine-grained rocks indicating relatively rapid cooling of this unit (Wilson, 2015) restricting the homogenization process. Furthermore, the RLS still shows pronounced variations in initial Sr isotopic ratios (Sr_i = 0.7045–0.7085; Kruger, 1994; Karykowski et al., 2017; Wilson et al., 2017), and in Nd isotope compositions ($\varepsilon Nd_{2.055\,Ga}$ = −5.3 to −7.9; Maier et al., 2000), indicating the involvement of different reservoirs during RLS magma genesis. The striking difference between Hf and Sr isotopic variations might be explained by the combination of four effects. First, the Zr–Hf budget of the RLS is mainly controlled by the assimilation of country rocks, and the Sr budget by the parental magmas, having higher Sr contents (UM: 85.8 ppm; B1: 198 ppm; B2: 348 ppm; B3: 337 ppm; Barnes et al., 2010) than the country rocks [e.g. Rooiberg volcanics: 67 ppm, n = 85 (compilation of Mathez, et al. 2013); Magaliesberg quartzite: 10 ppm, n = 3 (this study; Wronkiewicz and Condie, 1990); Vermont shale: 77 ppm, n = 11 (this study); Silverton shale: 83 ppm, n = 24 (Wronkiewicz and Condie, 1990)]. Second, Hf isotope homogenization within the RLS magma chamber perhaps was more thorough than Sr isotopic homogenization, owing to the fact that Sr became immobilized early in cumulus and intercumulus clinopyroxene and plagioclase (at T > 1000 °C), whereas Hf remained mobile until its incorporation into zircon late in the magmatic evolution (at T = 900–700 °C). Third, the crust and mantle reservoirs involved in RLS magma genesis perhaps had similar Hf isotopic compositions (see the section ‘Reservoirs of RLS parental magmas’), but highly distinct Sr isotopic compositions (see Wilson et al., 2017). Fourth, Sr and Hf isotopic compositions might have decoupled by fluid-driven processes during devolatilization of RLS country rocks, comprising carbonates and siliciclastic rocks of the Transvaal Supergroup. As Sr is more mobile in aqueous fluids compared with Hf (and Nd), fluid infiltration into RLS magmas, induced by contact metamorphism, might have caused a significant change in Sr isotope composition, but only minor changes in other trace elements and isotopic systems (e.g. Hf and Nd), as has recently been suggested by Karykowski et al. (2017) and Maier et al. (2018). Devolatilization processes of carbonates and siliciclastic sediments, and fluid infiltration into RLS magmas, might be responsible also for the relatively high oxygen isotope signature ($\delta^{18}O$ = 7.07 ± 0.34,

1SD), obtained from cumulate rocks throughout the entire RLS (Harris et al., 2005). Very similar $\delta^{18}O$ values of all RLS rocks also point to a homogenization process that might have occurred at temperatures as low as 850–730 °C (Harris et al., 2005), overlapping with zircon formation temperatures estimated in this study. (For further discussion see the section 'Reservoirs of RLS parental magmas'.)

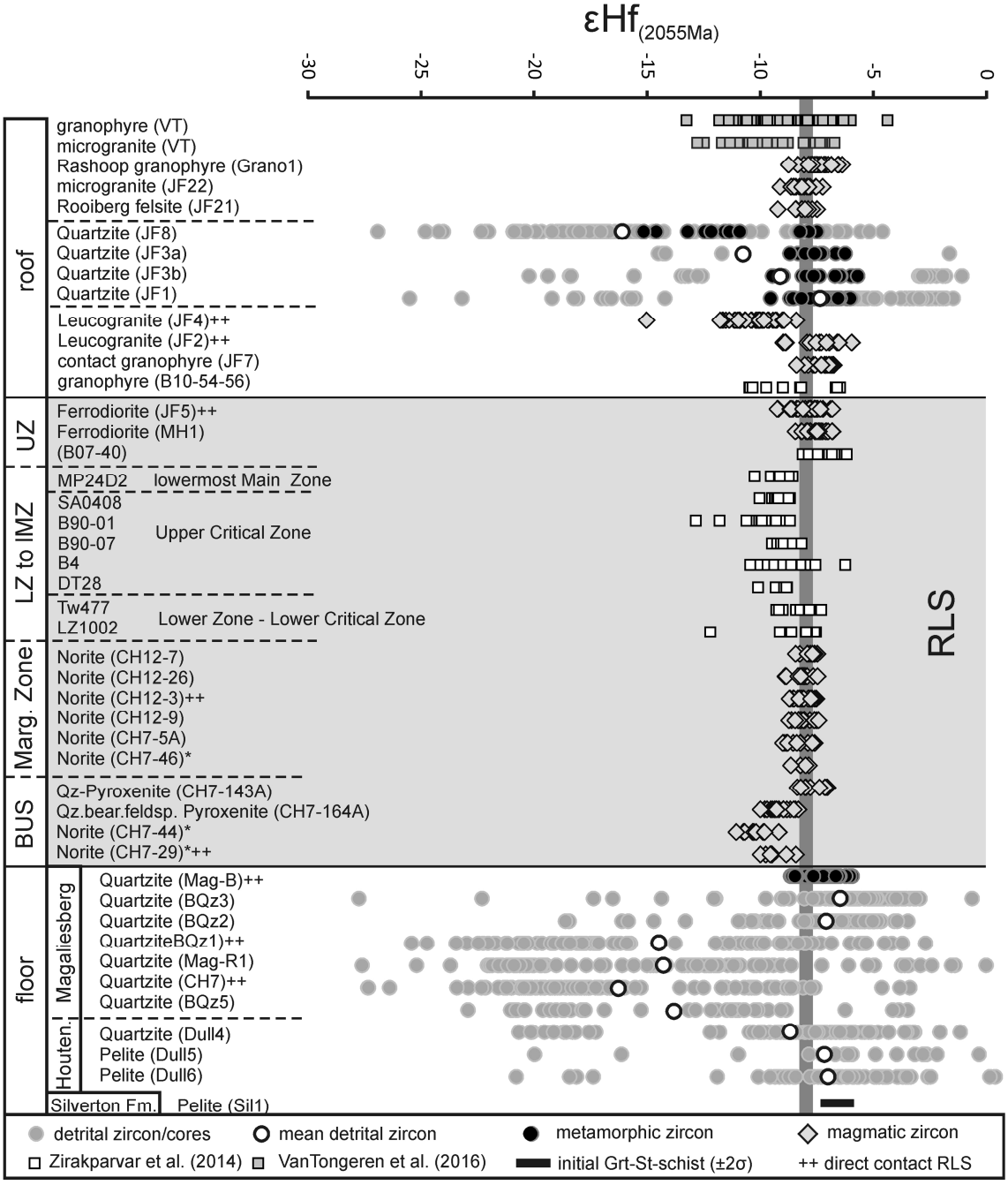

Figure 6.15 - Summary of results of Hf isotope analyses of zircon in mafic rocks from the Rustenburg Layered Suite (RLS), of detrital and metamorphic zircon grains in metasedimentary country rocks, as well as in Rooiberg felsite, granophyre and leucogranite, and results from isochron dating of a Silverton shale (Sil1). The compilation comprises data of this study, and from Zirakparvar et al. (2014) and VanTongeren et al. (2016). All data are calculated for an age of 2055 Ma. It should be noted that the mean εHf_t value obtained for detrital zircon populations in many Magaliesberg and Houtenbeck sedimentary rocks overlaps with the value obtained for zircon in mafic rocks of the RLS and related granites, as well as for metamorphic zircon in the contact aureole.

Table 6.3 Parameters used for modelling

Reservoirs	Zr (ppm)	Hf* (ppm)	$^{176}Hf/^{177}Hf$ (2055 Ma)	εHf_t	$\delta^{18}O$ (‰)	Nd (ppm)	$^{143}Nd/^{144}Nd$ (2055 Ma)	εNd_t	Comments
Av. mantle 1	20.1	0.55	0.28126	−7.5					E-SCLM–komatiite–eclogite 0.6:0.3:0.1
Av. mantle 2	22.1	0.61	0.28146	−0.4	5.9	2.96	0.50997	−0.2	E-SCLM–komatiite–eclogite 0.2:0.5:0.3
Av. mantle 3	17.4	0.48	0.28161[(g)]	5.0	5.7	2.52	0.51010	2.4	Komatiite (depleted)
Komatiite (A; asthenosphere)	17.4[(1)]	0.48	0.28153[(g)]	2.0	5.7[(19)]	2.52[(1)]	0.51010[(1)]	2.4	[(1)]Barberton komatiite
E-SCLM	20[(2)]	0.55	0.28106[§1]	−14.5	5.7[(19)]	4.8[(2)]	0.50968	−5.8	[§1]Pietersburg (websterite)–Phalaborwa (carbonatite) 0.7:0.3
Eclo, eclogite	32[(2)]	0.88	0.28156[(3,4)]	3.2	6.5[(20)]	2.4[(2)]	0.51010[(g)]	2.4	[(3,4)]Rooiwater Complex gabbros or eclogites
MORB	104.2[(5)]	2.9	0.28156[(3,4)]	3.2					
Pietersburg	20[(2)]	0.55	0.28099[(6)]	−17.1			0.50962[(21)]	−7.1	Websterite (Zr–Hf), alkaline rocks (Nd),
Phalaborwa	21[(2)]	0.55	0.28123[(7)]	−8.6			0.50968[(7)]	−5.8	carbonatite
Av. KC-lower crust	118[§2]	3.3	0.28090[§3]	−20.3	9.6	11	0.50929	−13.4	[§2]TTG–av. LCC 1:1, [§3](Witwatersand Block:Pietersburg Block 1:1),
TTG (granitoid) crust	169[(8)]	4.7	0.28090[§3]	−20.3	9.6[(22)]	36[(23,24)]	0.50929[(23,24)]	−13.4	data source: Witwatersrand Block [(9,10)], Pietersburg Block [(6)],
Av. LCC	68[(11)]	1.9	0.28090[§3]	−20.3		11[(11)]			assuming 176Lu/176Hf = 0.0113 (for crustal evolution)
Witwatersrand Gr.	126[(12)]	3.5	0.28082[(13)]	−23.1					[(12)]Av. quartzite (n = 97); [(13)] av. detrital zircon (n = 109)
av. KC-upper crust	240[§4]	6.6	0.28121[§5]	−9.3	12.2[(22)]	37[(15)]	0.50971[(15)]	−5.3	[§4]uPG–RoiV 0.75:0.25
uPG, upper Pretoria Group (av.)	159[§5]	4.4	0.28117[§5]	−10.8					[§5]SS–MH 0.20:0.80 (mlg neglected)
SS, Silverton shale	150[(14)]	4.1	0.281285[(16)]	−6.6					
MH, Magaliesberg to Houtenbeck	161[(14,15,16)]	4.4	0.28114[(16)]	−11.8					[(16)]Av. detrital zircon (n = 913)
mlg, melt sheets/leucogranite	198[(16,17)]	5.5	0.28120[(16)]	−9.6					[(16,17)]Av. melt sheets + leucogranite
RoiV, Rooiberg volcanics	484[(18)]	13.4	0.28125[(16)]	−7.8					[(18)]Av. Damwal, Kwaggasnek and Schrikkloof (n = 87)

KC, Kaapvaal Craton; LCC, lower continental crust; E-SCLM, enriched subcontinental lithospheric mantle; mlg, melt sheets + leucogranites. g, guess; (1) Chavagnac (2004); (2) Aulbach and Jacob (2016); (3) Zeh et al. (2013); (4) Laurent et al. (2018); (5) Hofmann (1988); (6) Laurent and Zeh (2015); (7) Wu et al. (2011); (8) Kamber et al. (2002); (9) Zeh et al. (2009); (10) Frimmel et al. (2009); (11) Rudnick and Fountain (1995); (12) Blane (2013); (13) Koglin et al. (2010); (14) Wronkiewicz and Condie (1990); (15) Jahn and Condie (1995); (16) this study; (17) Harris et al. (2003); (18) compilation of Mathez et al. (2013); (19) Eiler (2001); (20) Riches et al. (2016); (21) Graupner et al. (2018); (22) Harris et al. (2005); (23) Kreissig et al. (2000); (24) Schoene et al. (2009). §1 to §4 - values calculated from basic data (for details see comments).
*Calculated: Zr/36.25.

6.6.3 Effect of aqueous fluid infiltration on Zr-Hf budget of the RLS

Field relationships and petrological data suggest that large amounts of fluids were released by dehydration reactions in the contact aureole of the RLS (e.g. Kaneko and Miyano, 1990; Waters and Lovegrove, 2002; Harris et al., 2003). Strontium–O–C isotopic data additionally point to fluid flow towards and into the RLS (Schiffries and Rye, 1990; Buick et al., 2000; Harris and Chaumba, 2001; Harris et al., 2003, 2005), and the results of this study show that significant amounts of Zr and Hf were dissolved and transported. The estimated dissolution–transport behaviour of Zr(+Hf) is in agreement with experimental data and field-based studies conducted on low-grade to amphibolite-facies metamorphic rocks (e.g. Ewing et al., 1982; Hay and Dempster, 2009; Zeh et al., 2010*b*; Wilke et al., 2012; Zeh and Gerdes, 2014). The experimental results of Wilke et al. (2012) demonstrate that aqueous fluids in feldspar-bearing clastic sedimentary rocks (similar to those in the BC aureole) have a great capacity to transport Zr in the form of Zr–Na–Si complexes. They show that aqueous fluids with $NaSi_3$ contents of 10 wt% (formed by incongruent dissolution of albitic feldspar) can dissolve and transport more than 100 ppm Zr (at 600 °C and 3 kbar), and more than 600 ppm Zr in 18 wt% $NaSi_3$, and that the dissolved Zr content will become even higher at lower pressures and higher temperatures (see Fig. 1 of Wilke et al., 2012). Therefore, it appears likely that metamorphic fluids released from the Bushveld aureole at $T < 800$ °C and $P < 3$ kbar (Kaneko and Miyano, 1990; Waters and Lovegrove, 2002) contained several hundred ppm of Zr.

However, the influence of these fluids on the Zr–Hf budget of the RLS was probably minor, as is suggested by mass-balance constraints. For example, the Zr content and εHf_t value of a 9000 m thick layer of dry, enriched mantle-derived magma (Zr = 18 ppm; $^{176}Hf/^{177}Hf_{2.055\,Ga} = 0.281325$; $\varepsilon Hf_t = -4.2$), would change only slightly (Zr from 18 to 21 ppm; εHf_t from −4.2 to −5.3), if this layer is infiltrated by a Zr-rich aqueous fluid (Zr = 200 ppm), released from a 3 km thick sheet of sedimentary rocks beneath (i.e. vertical distance from the 800 °C to the 500 °C isograd of the BC contact areole; Nell 1985). The released H_2O content would have been 2 wt% on average, and its $^{176}Hf/^{177}Hf_{2.055\,Ga} = 0.281196$ ($\varepsilon Hf_t = -9.8$). The H_2O content is based on the observation that the sedimentary succession beneath the RLS consists of 60 % shale (~3 wt% H_2O release) and 40 % psammitic rocks (~0.5 wt% H_2O release), which is in agreement with the stratigraphy of the upper Pretoria Group in the Transvaal Basin (between the Lydenburg shale member of the Silverton Formation and the Dullstroom Formation; see Eriksson et al., 2006). The $^{176}Hf/^{177}Hf_{2.055\,Ga}$ results from (1) averaging all detrital zircon analyses available from the Upper Pretoria Group (Magaliesberg + post-Magaliesberg rocks: $^{176}Hf/^{177}Hf_{2.055\,Ga} = 0.28114$; $\varepsilon Hf_t = -11.8$, $n = 913$; this study; Zeh et al., 2016), and (2) the value obtained from the Silverton shale ($^{176}Hf/^{177}Hf_{2.055\,Ga} = 0.28128$; $\varepsilon Hf_t = -6.6$; this study), using a ratio of 3:2. The released H_2O content was calculated from loss-on-ignition data estimated on low-grade and high-grade metamorphosed shales of the Vermont and Silverton

formations (this study; Wronkiewicz and Condie, 1990; Harris et al., 2003), and from data of compacted sandstones and quartzites (e.g. Ferdous and Farazi, 2016; this study). Calculations with higher H_2O amounts and Zr-in-fluid contents seem to be unrealistic, as they would be in disagreement with the observations made by Harris et al. (2003) (i.e. quartz textures and O–C isotopes) and with the preservation of abundant detrital zircon grains in most metasedimentary rocks of the Upper Pretoria Group (this study; Zeh et al., 2016).

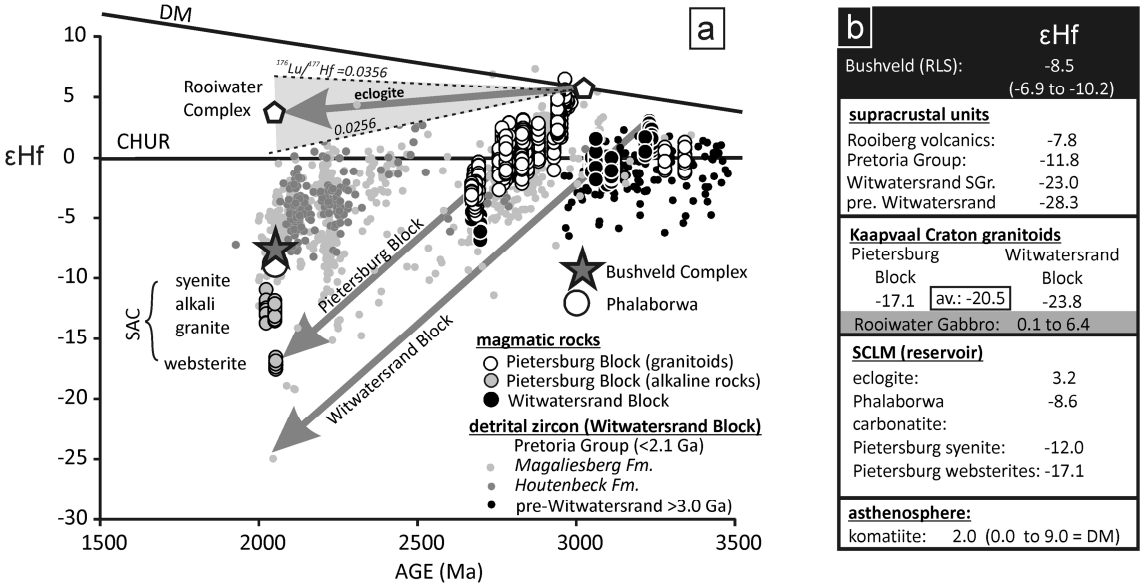

Figure 6.16 - Synopsis of Hf isotopic data of different rock units and reservoirs of the Kaapvaal Craton surrounding the Bushveld Complex. (a) Age vs εHf_t diagram; (b) schematic profile from the Kaapvaal Craton crust down into the asthenosphere, with average εHf_t values used for parental magma modelling; all data in (b) are calculated for 2055 Ma (for details see Table 6.3). Data sources: Rooiberg Group and Pretoria Group from this study and Zeh et al. (2016); Witwatersrand Supergroup from Koglin et al. (2010); pre-Witwatersrand detrital zircons from Zeh et al. (2013); Pietersburg and Witwatersrand block granitoids, and SAC (Schiel Alkaline Complex) syenite and websterite from Frimmel et al. (2009), Zeh et al. (2009) and Laurent and Zeh (2015); Phalaborwa carbonatite from Wu et al. (2011); Rooiwater gabbros and eclogites from Zeh et al. (2013); the $^{176}Lu/^{177}Hf$ was estimated from bulk-rock compositions of Rooiberg gabbros presented by Laurent et al. (2019). CHUR, chondritic uniform reservoir; DM, depleted mantle evolution, straight line between +18 (present) and 0 (at 4.0 Ga).

6.6.4 Reservoirs of RLS parental magmas

In a recent paper, Wilson et al. (2017) postulated that rocks of the deepest units of the RLS (BUS, Marginal Zone and Lower Zone) crystallized from mafic (similar to B1) and ultramafic melts (UM; proposed by Wilson, 2012) derived from at least four major sources: (1) convective asthenospheric mantle (up to 30 %), (2) metasomatized SCLM (up to 90 %), and crustal melts derived from (3) lower Kaapvaal crust (up to 25 %) and (4) Pretoria Group sedimentary rocks (up to 25 %). These four sources are required to simultaneously explain petrological data (e.g. Mg# of olivine and orthopyroxene), major and trace element contents (e.g. SiO_2, Cr and Rb contents) and ratios (e.g. Rb/Sr), and the initial Sr isotope compositions derived from more than 100 samples. In the following, a similar calculation is carried out with the aim of explaining the initial Hf isotopic composition of the RLS magmas estimated from zircon compositions of the BUS, Marginal Zone and Upper Zone of the RLS (Fig. 6.15), along with Zr content of the parental magmas UM, B1, B2 and B3. The isotopic compositions and Zr concentrations used for this calculation are summarized in Table 6.3 and Fig. 6.16b, and results of modelling are shown in Fig. 6.17.

In this study, we identified three major reservoirs (mantle, lower Kaapvaal Craton crust and uppermost Kaapvaal Craton crust), which are most influential and by combination can explain the composition of all parental magmas (UM, B1, B2 and B3; Fig. 6.17). The mantle reservoir is the largest and comprises three sub-reservoirs (A: asthenospheric mantle; E-SCLM: enriched subcontinental lithospheric mantle; Eclo: eclogites). By combining these three sub-reservoirs, mantle melts with a wide range in $\varepsilon Hf_{2055\ Ma}$ but a limited range in Zr contents can be generated. As shown in Fig. 6.17a and b, the addition of crustal components is imperative to explain the composition of parental magmas UM, B1 and B2, whereas B3 could solely be explained by mixing of the three mantle sub-reservoirs. We note that the two crustal reservoirs have highly distinct Hf isotopic compositions, with the lower Kaapvaal Craton crust having $\varepsilon Hf_{2055\ Ma} = -20.5$ (calculated from TTGs, granitoids and granulites exposed in the Pietersburg and Witwatersrand blocks, but also reflected by the average of detrital zircon data of the Witwatersrand Basin with $\varepsilon Hf_{2055\ Ma} = -23.0$), and the uppermost Kaapvaal Craton crust $\varepsilon Hf_{2055\ Ma} = -9.3$ (calculated from detrital zircon data of the Magaliesberg and Houtenbeck formations, Rooiberg felsites and the Silverton shales) (Table 6.3; Figs 6.16 and 6.17a). The involvement of crust in the RLS genesis is also required by $\delta^{18}O$ data to the extent of about 7.1 ‰ (Harris et al., 2005), which is much higher than values typical for mantle rocks (5.5 ± 0.2 ‰; see summary by Eiler, 2001), although mantle eclogites with $\delta^{18}O$ up to 6.5 ‰ (rarely up to 8.0 ‰) were reported from the Kaapvaal Craton (Riches et al., 2016, and references therein). However, the influence of such eclogites on $\delta^{18}O$ on the parental magmas was probably minor, in particular if it is considered that the subcontinental lithospheric mantle beneath the Kaapvaal Craton also hosts eclogite with mantle-like $\delta^{18}O$ of about 5.5 ‰ (e.g.

Schmickler et al., 2004), and that the mantle reservoir consisted of variable amounts of eclogite in addition to enriched harzburgites (see discussion by Richardson and Shirey, 2008).

The simplest way to explain the Zr content and Hf isotopic composition of all Bushveld parental magmas is by mixing mantle- and crust-derived melts that had very similar Hf isotopic compositions of $\varepsilon Hf_{2055\ Ma} = -8.5 \pm 1.5$. For the crust this requirement is fulfilled by the composition of the uppermost Kaapvaal Craton crust ($\varepsilon Hf_{2055\ Ma} = -9.3$; Zr = 240 ppm), and for the mantle by the mixture E-SCLM–Asthenosphere–Eclogite in the relative proportions 0.6:0.3:0.1, resulting in $\varepsilon Hf_{2055\ Ma} = -7.5$ and Zr = 20 ppm (mantle 1; Table 6.3, Fig. 6.17a). In that case, the composition of B1 magma can be explained by adding *c*. 25 % crustal material to mantle-derived magma, for B2 *c*. 15 %, for UM *c*. 7 % and for B3 *c*. 2 %.

For B1 magma genesis the same conclusion is reached, if available $\delta^{18}O$ and Nd isotope data are considered (for parameters see Table 6.3). In that case, the B1 magma composition ($\delta^{18}O$ = 7.1 ‰, Harris et al., 2005; $\varepsilon Nd_t = -5.4$, Maier et al., 2000; Nd = 15 ppm, Barnes et al., 2010) can be reproduced by a binary mixture involving E-SCLM (Phalaborwa-like) and uppermost Kaapvaal Craton crust with a ratio of 0.78:0.22 (Fig. 6.17c). In contrast, at least three reservoirs are required to explain the B3 magma composition ($\delta^{18}O$ = 7.1 ‰, $\varepsilon Nd_t = -7.5$ and Nd= 5.7 ppm), involving *c*. 70 % E-SCLM (Phalaborwa-like), *c*. 20 % of lower Kaapvaal Craton crust and *c*. 10 % upper Kaapvaal Craton crust (Fig. 6.17c). However, the B3 magma composition could also be explained by binary mixing of asthenospheric mantle melt (mantle 3 in Table 6.3) and lower Kaapvaal Craton crust. Using values for Zr and Nd for average lower continental crust (Rudnick and Fountain, 1995), and Hf–Nd–O isotope data compiled for the Kaapvaal Craton in Table 6.3, the required amount of assimilated lower crust would be *c*. 22 % in the Zr–Hf isotope system, and *c*. 30 % in the Nd–O isotope system. The amount of lower crust would become even higher (up to 40 %) if the lower crust was a residue, highly depleted in incompatible trace elements (e.g. Zr, Nd) relative to the average lower continental crust (Fig. 6.17b and d), an option previously discussed by Sharp et al. (1986) and Maier et al. (2000). Depletion perhaps resulted from intense partial melt extraction related to the formation of Rooiberg Group volcanics and B1 magma, both generated prior to B3 magma. In that case, the very low Zr and Nd contents of the B3 magma (Zr = 23 ppm, Nd = 6.3 ppm; Barnes et al., 2010) could be generated by a binary mixture comprising melts from asthenospheric mantle and lower crust residue (with Zr = 30 ppm and Nd = 7 ppm) in the ratio 60:40 (Fig. 6.17b and d).

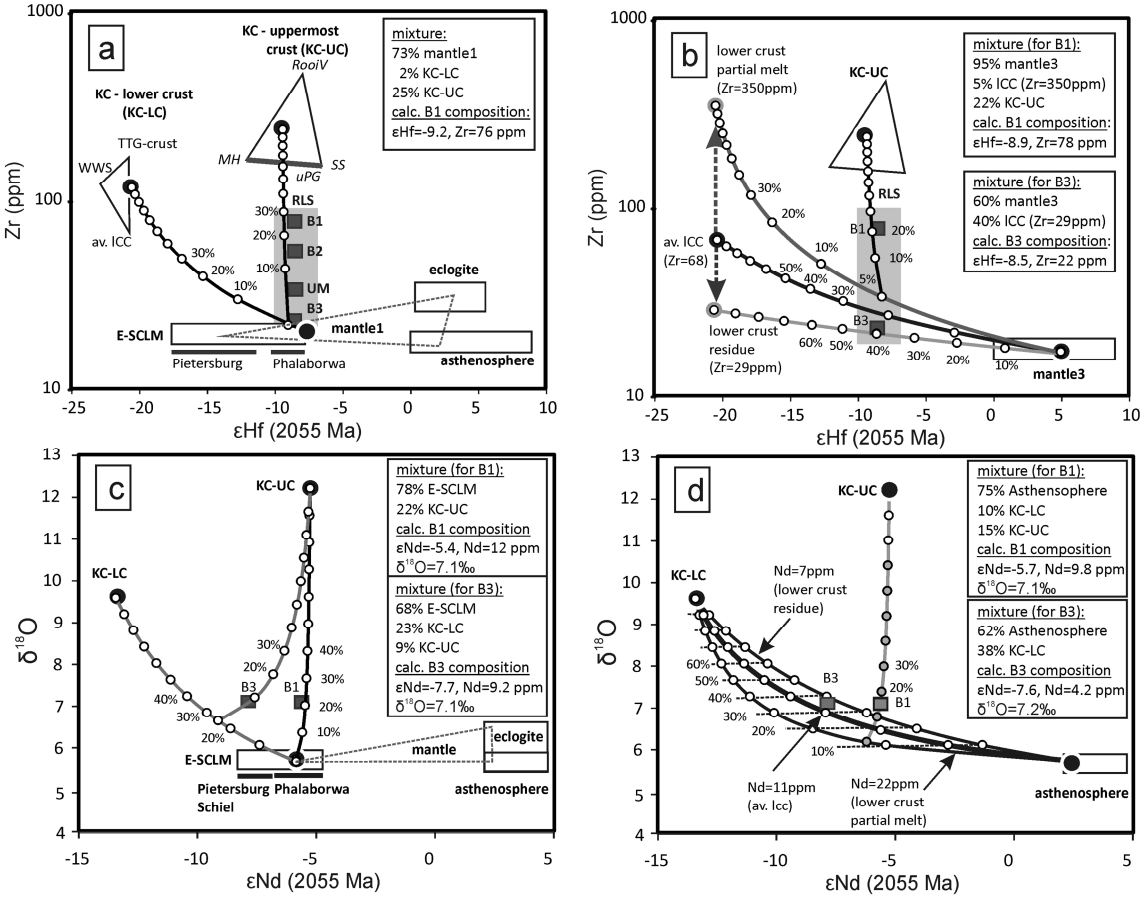

Figure 6.17 - Results of modelling of Rustenburg Layered Suite (RLS) parental magma compositions (UM, B1, B2 and B3) presented in (a, b) εHf_t vs Zr diagrams and (c, d) εNd_t vs $\delta^{18}O$ diagrams. In the modelling three major reservoirs are considered: mantle, lower Kaapvaal Craton crust (KC-LC) and uppermost KC crust (KC-UC). The mantle reservoir comprises three sub-reservoirs: enriched subcontinental lithospheric mantle (E-SCLM), asthenosphere (A) and eclogite; the KC-LC reservoir comprises average lower crust (av. lCC), TTG-crust (tonalite–trondhjemite–granodiorite) and sedimentary rocks of the Witwatersrand Supergroup (WWS); the KC-UC reservoir comprises upper Pretoria Group (uPG), Rooiberg volcanics (RooiV) and melt sheets + leucogranites. The uPG comprises data from Silverton shales (SS) and from Magaliesberg + Houtenbeck (MH) clastic sedimentary rocks. Details and data sources for all reservoirs are presented in Table 6.3. Modelling results assume major involvement of (a, c) an E-SCLM source during RLS parental magma formation, and of (b, d) asthenospheric melts interacting with either (1) average lower continental crust (Zr = 68 ppm, Nd = 11 ppm; Rudnick and Fountain, 1995), (2) a highly depleted lower crustal residue (Zr = 30 ppm; Nd = 7 ppm), or (3) highly enriched partial melts of the lower crust (Zr = 350 ppm; Nd = 22 ppm). It should be noted that in all cases a large amount of upper crust (*c*. 20 %) is required to reproduce the B1 magma composition. Continuous lines represent mixing lines and open circles with numbers the amount of mixing in 10 % steps. Insets show the mixtures used and the results of the modelling.

The modelling carried out above indicates that Hf–Nd–O isotopic composition of the B1 and B3 magmas can be explained for both by binary crust–mantle mixtures involving different reservoirs: E-SCLM–upper Kaapvaal Craton crust 80:20 for the B1 magma and asthenospheric mantle–lower Kaapvaal Craton crust residue 60:40 for the B3 magma. However, more complex scenarios are also possible. For example, a significant amount of lower crust could have been involved in B1 magma genesis, as has previously been suggested by the modelling of Wilson et al. (2017). Based on our Zr–Hf isotopic data, a maximum of 22 % lower crust would be needed, if asthenospheric mantle (mantle 3) contributed significantly to B1 magma formation, and 5 % when the mixture involved partially molten lower crust, highly enriched in incompatible trace elements (Fig. 6.17b). In the case of a complex mantle (most realistic), the amount would be

more intermediate between these two cases; for example, at 10 % if the mantle source was represented by the mixture E-SCLM–Asthenospheric mantle–Eclogite 0.2:0.5:0.3 (mantle 2 in Table 6.3). Irrespective of the detailed model invoked, the involvement of a significant amount of upper crust (*c*. 20 %) is required to explain the B1 magma composition. In contrast, for B3 magma genesis, an upper crust contribution is not necessarily required (Fig. 6.17b and d).

The occurrence of enriched mantle beneath the Kaapvaal Craton at 2055 Ma is indicated by isotopic data from the Phalaborwa carbonatites ($\varepsilon Hf_{2055\ Ma}$ = −7.9 to −10.3; Wu et al., 2011) and from websterites, syenites and sanukitoids from the Pietersburg Block ($\varepsilon Hf_{2055\ Ma}$ = −17.1 to −12.0; Zeh et al., 2009; Laurent and Zeh, 2015; Fig. 6.16a), all occurring spatially adjacent to the Bushveld Complex. However, it remains unclear whether the same mantle source contributed to all parental magmas that were involved in the formation of the RLS. Based on our modelling results it is likely that the crust and mantle reservoirs changed significantly during RLS magma formation, with B1 magma formation mainly controlled by E-SCLM and upper crustal melt (with some addition of asthenospheric mantle, eclogitic mantle and partially molten lower crust), and the B3 magma by asthenospheric mantle and residue lower crust (with variable contributions of E-SCLM and eclogite). A significant change in the mantle reservoirs might also provide an explanation for the abrupt drop in Cl/F ratio of apatite from B1- to B3-related cumulate rocks (Willmore et al., 2000).

6.7 Conclusions

Magmatic zircon in different mafic rocks of the RLS and metamorphic zircon in the contact aureole of the BC, in Bushveld-related granites and Rooiberg felsites show minor variations in $\varepsilon Hf_{2055\ Ma}$ values ranging between −7.5 and −10.2. These data suggest that mafic mantle-derived magmas and the uppermost Kaapvaal Craton crust had, on average, very similar Hf isotopic composition at the time of RLS emplacement, but were distinctly different from the composition of the lower Kaapvaal Craton crust ($\varepsilon Hf_{2055\ Ma} < -20$).

Zircon core–rim relationships provide evidence for Hf isotopic homogenization in the contact aureole owing to Zr–Hf transport by aqueous solutions and melts, which were formed during contact metamorphic heating. However, mass-balance constraints indicate that these fluids did not have a significant influence on the Zr–Hf budget and Hf isotopic composition of the RLS.

Zircon morphologies and overgrowth textures point to heterogeneous fluid flow in the contact aureole, and to maximum contact temperatures of *c*. 800 °C at the floor, and up to *c*. 900 °C at the roof contact of the RLS.

Results of bulk modelling suggest that the B1 magma composition of the RLS is controlled by two major reservoirs—a mantle reservoir dominated by E-SCLM (>60 %) and uppermost Kaapvaal Craton crust (up to 25 %), consisting of sedimentary rocks of the upper

Pretoria Group and Rooiberg volcanics—whereas contribution by lower Kaapvaal Craton crust was minor (<10 %).

In contrast, genesis of B3 parental magma requires the involvement of abundant lower (residue) Kaapvaal Craton crust (up to 40 %), in addition to an asthenospheric and/or mixed mantle source, but only very minor contributions (if any) of upper Kaapvaal Craton crust (<15 %).

Acknowledgements

A.Z. and D.G. thank Linda Marko (University Frankfurt am Main, Germany) for support with sample preparation, scanning electron microscopy and LA-ICP-MS analyses. A.Z. and A.H.W. are indebted to the late Joe Aphane (University of the Witwatersrand) for zircon separation and preparation, to Dominik Weis for editorial handling, and to Alexander Zirakparvar and an anonymous reviewer, who helped to improve a previous version of the paper.

7. Conclusions

Highly different zircon formation conditions are evident within the BC. In felsic rocks (Lebowa Granite, Rashoop Granophyre), zircon is an early magmatic phase forming after ~20% fractional crystallization of a SiO_2-rich felsic parental magma initially having ~2.2 wt.% H_2O. In contrast, zircon in mafic cumulate rocks of the BC (Rustenburg Layered Suite) was formed in felsic intercumulus domains remaining after ≥75% fractional crystallization of RLS-related parental magmas (B1, B1:B2 = 60:40, UUMZ with 25% felsic component; all with ~0.4 wt.% H_2O).

Despite resulting from highly different parental magmas and degrees of fractional crystallization, zircon throughout the BC was formed at generally similar temperatures of mostly 800-900 °C and from rhyolitic melts with similar major element compositions and H_2O contents of 1.6-4.0 wt.%, as suggested by consistent thermometric data and compositions of melt inclusions in zircon.

In contrast to major elements, trace elements in MIZ vary significantly within the BC and reflect the chemical signature inherited from different parental magmas. Here, MIZ from rutile-free felsic and mafic rocks (Upper Zone) can be discriminated from MIZ in rutile-bearing mafic cumulates (Marginal and Critical Zones) by higher Ti contents and Th/U ratios, and lower REE contents.

Zircon formation in the Upper Main and Upper Zones (UUMZ) of the RLS requires admixing of felsic, Zr-rich melts during mafic parental magma injection into a stratified magma chamber. This felsic melt was compositionally similar to felsic rocks of the BC, as suggested by zircon saturation modelling as well as by identical zircon morphologies and trace element contents (ΣREE, Ti, Th/U), as those in overlying felsic rocks.

At the time of RLS emplacement, mantle-derived magmas and the uppermost Kaapvaal Craton crust had very similar average Hf isotopic compositions ($\varepsilon Hf_{2.055\ Ga}$ between -7.5 and -10.2), which were highly different from that of the lower Kaapvaal Craton crust ($\varepsilon Hf_{2.055\ Ga} < -20$).

Hafnium isotope compositions were homogenized in the BC contact aureole due to Zr-Hf transport by aqueous fluids and/or felsic melts formed during contact metamorphic heating. These fluids, however, did not significantly influence the Zr-Hf budget and Hf isotopic composition of the RLS, which is mainly controlled by three main reservoirs (1) the asthenospheric mantle (>20 %), (2) the enriched subcontinental lithospheric mantle (<80 %) and (3) significant assimilation of crust.

B1, the dominant magma for the lower RLS was mostly formed by a mixture of melts derived from the enriched subcontinental lithospheric mantle with re-melted Upper Crust of the Kaapvaal Craton (Pretoria Group Sediments, Rooiberg volcanics). In contrast, B3 magma (Main Zone), was mostly formed by melts derived from the asthenospheric mantle mixed with re-melted Lower Kaapvaal Craton crust.

The trace element contents and zoning patterns of zircon strongly depend on the cogenetic mineral assemblage and the zircon/melt ratio during zircon crystallization. Both depend on the composition of respective parental magmas and their Zr load, which mainly dictates how much fractional crystallization is necessary to reach zircon saturation.

In mafic cumulates of the lower RLS (BUS, Marginal Zone, Critical Zone, and lower Main Zone), zircon grew at high zircon/melt ratios from small volumes of intercumulus melt together with rutile, quartz, alkali feldspar, plagioclase, biotite, and amphibole.

Zircon populations of the Upper Critical Zone are characterized by highly variable zircon crystallization temperatures 690-962 °C (peaking at 850 °C) and trace element contents, indicating melt fractionation within poorly interconnected, compositionally variable intercumulus melt domains resulting from incomplete mixing of parental magma with variably evolved resident melt and compaction of the crystal mush.

For zircon-compatible elements (Th, U, Hf), a strong zircon zoning by Rayleigh fractionation is possible at high zircon/melt: In rutile-bearing mafic cumulates, U<Th depletion of the intercumulus melt caused extremely high Th/U (≤24) in zircon, which is indicated by both modelling results and measured MIZ compositions. This zoning trend was reversed after the onset of the biotite growth and rutile breakdown reaction, causing release of U previously stored in rutile.

In felsic rocks, zircons with low, weakly zoned Th/U indicate that fractionation due to zircon growth is compensated by coeval crystallization of abundant rock-forming minerals, being all highly incompatible for Th, U, Nb and Ta.

Zircon based thermometry strongly depends on the mineral assemblage in which zircon grew. However, melt inclusions in zircon provide largely independent temperature constraints by applying: (1) liquidus geothermometry (based on experimentally derived Qz-Ab-Or phase diagrams and thermodynamic modelling) and (2) TiO_2 saturation geothermometry, which are

consistent with Ti-in-zircon temperatures and temperatures derived from the morphology (Pupin's scheme) of zircon hosts.

For all Rt-free, Mt-Ilm-Ttn-bearing felsic and mafic rocks, thermodynamic modelling indicates a significantly reduced TiO_2 activity of $aTiO_2 = 0.3$ during zircon growth. This is confirmed by respective MIZ compositions, for which agreement between liquidus temperatures, TiO_2 and zircon saturation temperatures as well as Ti-in zircon temperatures obtained from zircon hosts only converge if $aTiO_2 = 0.3$ is used.

Successful homogenization of MIZ requires re-heating in pressurized metal vessels, which hampers a direct observation of the homogenization temperatures. However, this study has shown that MIZ in a large number of zircons, largely irrespective of rock type can be completely homogenized by slightly overheating (1100 °C), without causing detectable sidewall dissolution of host zircon. This is suggested by significantly lower zircon saturation temperatures of 980-880°C (in agreement with other thermometers) and diffusional modelling.

Zircon-melt partitioning coefficients derived from MIZ - host zircon pairs overlap with experimental values and are similar for mafic and felsic rocks, and independent from MIZ sizes (20-40 µm), compositions, and entrapment temperatures (700-950°C). This indicates similar zircon-melt partitioning largely irrespective of the magmatic setting.

7.1 Outlook

Studying melt inclusions in zircon (MIZ) is a new, emerging field in geosciences and this study has demonstrated their great potential as petrogenetic indicators for the zircon crystallization temperature as well as for the generation of zircon-forming melts from different parental magmas. Furthermore, this study has revealed systematically different MIZ compositions for Rt-free felsic and mafic rocks compared to Rt-bearing mafic rocks of the BC, in particular for trace elements (e.g. REE, Ti, Th/U, Li). However, to reliably use MIZ compositions to discriminate between different host rocks, there is a need to extend the database of MIZ compositions (major and trace elements, H_2O contents) including analyses of MIZ derived from various rock types and from different geo-tectonic settings, similar to existing discrimination systematics for zircon trace element compositions presented by Belousova et al. (2002) and Grimes et al. (2015). Although major element contents of MIZ more overlap for the BC, they can be quite easily obtained by EMPA and also offer some discrimination potential, especially for large MIZ populations, which, as demonstrated in our study, can be obtained by IHPV treatment at ~1100 °C of a large number of zircons from different rock types without exact knowledge of the actual entrapment temperature.

The idea to use MIZ as an indicator for the initial growth conditions and respective host rocks of detrital zircons, was already presented in one of the earliest MIZ studies by Chupin et al. (1998). In particular, MIZ in Earth's oldest detrital zircons from the Hadean may provide further information about the earliest stages of crust formation, including crystallization temperatures and host magma compositions. Furthermore, studying MIZ may extend the knowledge about the formation of Earth's oldest silicic rocks comprising tonalite–trondhjemite–granodiorite suites (TTG). For example, Laurent et al. (2020) recently suggested that TTG plutons represent fossil, crystal-rich magma reservoirs tapped by the eruption of silicic melts. Here, K_2O-rich, Na_2O-poor and low Sr/Y melts residual to Pl accumulation are included in TTG quartz grains. Provided that zircon crystallizes after quartz, it would be elusive to see, whether MIZ compositions continue this fractionation trend, which would further support the model presented by Laurent et al. (2020). In advantage to melt inclusions in quartz, those in zircon would additionally provide temperature constraints, as done in this study using several independent MIZ- and host zircon-based thermometers.

With respect to the BC and other layered intrusions, further data is needed for MIZ compositions combined with analyses of melt inclusions in other minerals of the crystallization sequence (e.g. chromite, orthopyroxene, rutile, apatite), which would provide a more complete picture of the liquid line of descent and close the gap between parental magma compositions and highly fractionated, zircon-forming melts.

The evaluation of zircon morphologies using Pupin's classification scheme is a largely independent thermometer for zircon crystallization. Although this study has shown that temperatures derived from zircon morphology generally agree with results obtained from other thermometers (Ti-in-zircon, liquidus temperature and TiO_2 saturation temperature of MIZ, bulk-rock zircon saturation temperature), further work is needed to better constrain the chemical controls on the growth rate of different zircon sectors, giving rise to its morphology. This can be done by the acquisition of trace element profiles along zircon growth sectors towards the outermost rim (e.g. by SIMS or LA-ICP-MS with small spot sizes). Zircons of the BC would be suited for this approach as many of them exhibit euhedral shapes and are strongly zoned in Th/U, U, Ti and Nb.

This study has extended the knowledge about how geothermometers based on Ti contents in zircon and melt can be applied on rutile-free, hence TiO_2-undersaturated rocks, which is a large fraction of magmatic rocks including most granites. Further work is needed to test whether $a\mathrm{TiO_2}$ estimates based on MIZ compositions and thermodynamic modelling (rhyolite-MELTS and/or Perple_X) would also provide robust Ti-in-zircon temperatures for other rock types.

As outlined in this study, zircon zoning patterns strongly depend on zircon/melt ratios as well as on the cogenetic mineral assemblage and mineral reactions associated with it. However, zircon zoning mechanisms still offer some open questions. For example, not all zircon populations from the Critical Zone of the BC display two zoning trends marked by Th/U increase along with U decrease, which is reversed following U release due to rutile breakdown and biotite growth. Modelling results indicate that this reaction mostly occurs at 825-850 °C, but also depends on the H_2O and major element contents of the melt. Further work is needed to test whether this mechanism also accounts for the high variability in Th/U observed for zircon in magmatic rocks from other settings, as well as in zircon from rutile-, biotite-bearing metamorphic rocks (Kirkland et al., 2015; Yakymchuk et al., 2018).

Based on the results presented in this study, further work regarding the Hf isotope systematics of the BC is needed. For, example, the Hf isotope composition of zircon-poor or zircon-free BC units is largely unconstrained, including the Lower Zone and basal chilled rocks of the RLS as well as most of the Rooiberg Group volcanics. The latter are critical for the magma evolution of the BC, in particular regarding the generation of large volumes of felsic magma that formed the Lebowa Granite and Rashoop Granophyre Suites. Furthermore, to test the hypothesis that different parental magmas of the RLS had essentially the same Hf isotope composition at 2.055 Ga, parts of the RLS in which a mixing of magmas is proposed should be investigated in more detail. For example, assuming that B1 and B2 magmas had different Hf isotope compositions, zircon populations in the Upper Critical Zone should display some systematic excursions in zircon Hf isotope composition, indicative of variable mixtures of B1 and B2 (Barnes et al., 2010).

References

Akin L., Aydar E., Schmitt A. K. and Çubukçu H. E. (2019) Application of zircon typology method to felsic rocks (Cappadocia, Central Anatolia, Turkey): A zircon crystallization temperature perspective. *Turkish Journal of Earth Sciences* **28**, 351–371.

Arndt N., Jenner G., Ohnenstetter M., Deloule E. and Wilson A. H. (2005) Trace elements in the Merensky Reef and adjacent norites Bushveld Complex South Africa. *Mineralium Deposita* **40**, 550–575.

Ashwal L. D. (2005) Magmatic stratigraphy in the Bushveld Northern Lobe: Continuous geophysical and mineralogical data from the 2950 m Bellevue drillcore. *South African Journal of Geology* **108**, 199–232.

Audétat A. and Lowenstern J. B. (2014) Melt Inclusions. In: *Treatise on Geochemistry.* Elsevier, pp. 143–173.

Aulbach S. and Jacob D. E. (2016) Major- and trace-elements in cratonic mantle eclogites and pyroxenites reveal heterogeneous sources and metamorphic processing of low-pressure protoliths. *Lithos* **262**, 586–605.

Baker D. R., Conte A., Freda C. and Ottolini L. (2002) The effect of halogens on Zr diffusion and zircon dissolution in hydrous metaluminous granitic melts. *Contributions to Mineralogy and Petrology* **142**, 666–678.

Barnes S.-J., Maier W. D. and Curl E. A. (2010) Composition of the Marginal Rocks and Sills of the Rustenburg Layered Suite, Bushveld Complex, South Africa: Implications for the Formation of the Platinum-Group Element Deposits. *Economic Geology* **105**, 1491–1511.

Barnes S.-J. and Maier W. D. (2002) Platinum-group Elements and Microstructures of Normal Merensky Reef from Impala Platinum Mines, Bushveld Complex. *Journal of Petrology* **43**, 103–128.

Barnes S. J. (1989) Are Bushveld U-type parent magmas boninites or contaminated komatiites? *Contributions to Mineralogy and Petrology* **101**, 447–457.

Belousova E., Griffin W., O'Reilly S. Y. and Fisher N. (2002) Igneous zircon: Trace element composition as an indicator of source rock type. *Contributions to Mineralogy and Petrology* **143**, 602–622.

Belousova E. A., Griffin W. L. and O'Reilly S. Y. (2006) Zircon Crystal Morphology, Trace Element Signatures and Hf Isotope Composition as a Tool for Petrogenetic Modelling: Examples From Eastern Australian Granitoids. *Journal of Petrology* **47**, 329–353.

Benisek A. and Finger F. (1993) Factors controlling the development of prism faces in granite zircons: A microprobe study. *Contributions to Mineralogy and Petrology* **114**, 441–451.

Blane C. H. (2013) Composition and provenance of quartzites of the Mesoarchean Witwatersrand supergroup, South Africa. Dissertation, University of Johannesburg.

Blundy J. and Cashman K. (2001) Ascent-driven crystallisation of dacite magmas at Mount St Helens, 1980–1986. *Contributions to Mineralogy and Petrology* **140**, 631–650.

Blundy J. and Wood B. (1994) Prediction of crystal–melt partition coefficients from elastic moduli. *Nature* **372**, 452–454.

Boehnke P., Watson E. B., Trail D., Harrison T. M. and Schmitt A. K. (2013) Zircon saturation re-revisited. *Chemical Geology* **351**, 324–334.

Borisov A. and Aranovich L. (2019) Zircon solubility in silicate melts: New experiments and probability of zircon crystallization in deeply evolved basic melts. *Chemical Geology* **510**, 103–112.

Boudreau A. E. (1995) Crystal aging and the formation of fine-scale igneous layering. *Mineralogy and Petrology* **54**, 55–69.

Brätz H. and Klemd R. (2002) *Analysis of Rare Earth Elements in Geological Samples by Laser Ablation – Inductively Coupled Plasma Mass Spectrometry (LA-ICP-MS).* 5988-6305EN, Agilent Technology, Inc.

Buchanan P. C. (2006) The Rooiberg Group. In: *Geology of South Africa* (eds. M. R. Johnson, C. R. Anhausser and R. J. Thomas). Geological Society of South Africa. Johannesburg, pp. 283–289.

Buchanan P. C., Koeberl C. and Reimold W. U. (1999) Petrogenesis of the Dullstroom Formation, Bushveld Magmatic Province, South Africa. *Contributions to Mineralogy and Petrology* **137**, 133–146.

Buchanan P. C., Reimold W. U., Koeberl C. and Kruger F. J. (2002) Geochemistry of intermediate to siliceous volcanic rocks of the Rooiberg Group, Bushveld Magmatic Province, South Africa. *Contributions to Mineralogy and Petrology* **144**, 131–143.

Buchanan P. C., Reimold W. U., Koeberl C. and Kruger F. J. (2004) Rb-Sr and Sm-Nd isotopic compositions of the Rooiberg Group, South Africa: early Bushveld-related volcanism. *Lithos* **75**, 373–388.

Buick I. S., Gibson R., Wallmach T. and Metz J. (2000) The occurrence of cuspidine, foshagite and hillebrandite in calc-silicate xenoliths from the Bushveld Complex, South Africa. *South African Journal of Geology* **103**, 249–254.

Campbell I. H. (1985) The difference between oceanic and continental tholeiites: A fluid dynamic explanation. *Contributions to Mineralogy and Petrology* **91**, 37–43.

Campbell I. H., Roeder P. L. and Dixon J. M. (1978) Plagioclase buoyancy in basaltic liquids as determined with a centrifuge furnace. *Contributions to Mineralogy and Petrology* **67**, 369–377.

Campbell I.H. (1978) Some problems with the cumulus theory. *Lithos* **11**, 311–323.

Carley T. L., Miller C. F., Wooden J. L., Padilla A. J., Schmitt A. K., Economos R. C., Bindeman I. N. and Jordan B. T. (2014) Iceland is not a magmatic analog for the Hadean: Evidence from the zircon record. *Earth and Planetary Science Letters* **405**, 85–97.

Carlson R. W., Boyd F. R., Shirey S. B., Janney P. E., Grove T. L., Bowring S. A., Schmitz M. D., Dann J. C., Bell D. R., Gurney J. J., Richardson S. H., Tredoux M., Menzies A. H., Pearson D. G., Hart R. J., Wilson A. H. and Moser D. (2000) Continental growth, preservation, and modification in Southern Africa. *GSA Today* **10**, 1–7.

Cawthorn R. G. (1999b) Platinum-group element mineralization in the Bushveld Complex - a critical reassessment of geochemical models. *South African Journal of Geology* **102**, 268–281.

Cawthorn R. G. (2015) The Bushveld Complex, South Africa. In: *Layered intrusions* (eds. B. Charlier, O. Namur, R. Latypov and C. Tegner). Springer. Dordrecht, pp. 517–587.

Cawthorn R. G. and Davies G. (1983) Experimental data at 3 kbars pressure on parental magma to the Bushveld Complex. *Contributions to Mineralogy and Petrology* **83**, 128–135.

Cawthorn R. G., Eales H. V., Walraven F., Uken R. and Watkeys M. K. (2006) The Bushveld Complex. In: *Geology of South Africa* (eds. M. R. Johnson, C. R. Anhausser and R. J. Thomas). Geological Society of South Africa. Johannesburg, pp. 261–281.

Cawthorn R. G., Meyer P. S. and Kruger F. J. (1991) Major Addition of Magma at the Pyroxenite Marker in the Western Bushveld Complex, South Africa. *Journal of Petrology* **32**, 739–763.

Cawthorn R. G. and Walraven F. (1998) Emplacement and Crystallization Time for the Bushveld Complex. *Journal of Petrology* **39**, 1669–1687.

Cawthorn R. G. and Webb S. J. (2001) Connectivity between the western and eastern limbs of the Bushveld Complex. *Tectonophysics* **330**, 195–209.

Cawthorn R. G. and McCarthy T. S. (1985) Incompatible trace element behavior in the Bushveld Complex. *Economic Geology* **80**, 1016–1026.

Chavagnac V. (2004) A geochemical and Nd isotopic study of Barberton komatiites (South Africa): Implication for the Archean mantle. *Lithos* **75**, 253–281.

Cherniak D. J. and Watson E. B. (2003) Diffusion in Zircon. In: *Zircon* (eds. J. M. Hanchar and P. W. O. Hoskin). Mineralogical Society of America and The Geochemical Society. Chantilly, VA, pp. 113–143.

Cherniak D. J. and Watson E. B. (2007) Ti diffusion in zircon. *Chemical Geology* **242**, 470–483.

Chupin S. V., Chupin V. P., Barton Jr. J. M. and Barton E. S. (1998) Archean melt inclusions in zircon from quartzite and granitic orthogneiss from South Africa: Magma compositions and probable sources of protoliths. *European Journal of Mineralogy* **10**, 1241–1252.

Chupin V. P., Titov A. V., Stepanyuk L. M. and Goryainov S. V. (1992) Melt inclusions in zircons from precambrian rocks of the Anabar Shield. *Rossiiskaia Akademiia Nauk, Doklady* **323**, 545–548.

Chupin V. P., Vetrin V. R., Rodionov N. V., Matukov D. I., Berezhnaya N. G., Sergeev S. A., Mitrofanov F. P. and Smirnov Y. P. (2006) Composition of melt inclusions and age of zircons from plagiogneisses of the archean complex in the Kola superdeep borehole, Baltic Shield. *Doklady Earth Sciences* **406**, 153–157.

Claiborne L. L., Miller C. F., Walker B. A., Wooden J. L., Mazdab F. K. and Bea F. (2006) Tracking magmatic processes through Zr/Hf ratios in rocks and Hf and Ti zoning in zircons: An example from the Spirit Mountain batholith, Nevada. *Mineralogical Magazine* **70**, 517–543.

Claiborne L. L., Miller C. F. and Wooden J. L. (2010) Trace element composition of igneous zircon: A thermal and compositional record of the accumulation and evolution of a large silicic batholith, Spirit Mountain, Nevada. *Contributions to Mineralogy and Petrology* **160**, 511–531.

Clarke B., Uken R. and Reinhardt J. (2009) Structural and compositional constraints on the emplacement of the Bushveld Complex, South Africa. *Lithos* **111**, 21–36.

Connolly J. A. D. (2009) The geodynamic equation of state: What and how. *Geochemistry, Geophysics, Geosystems* **10**.

Coogan L. A. and Hinton R. W. (2006) Do the trace element compositions of detrital zircons require Hadean continental crust? *Geology* **34**, 633.

Corfu F., Hanchar J. M., Hoskin P. W. O. and Kinny P. (2003) Atlas of zircon textures. In: *Zircon* (eds. J. M. Hanchar and P. W. O. Hoskin). Mineralogical Society of America and The Geochemical Society. Chantilly, VA, pp. 469–500.

Davis D. W. (2003) Historical Development of Zircon Geochronology. *Reviews in Mineralogy and Geochemistry* **53**, 145–181.

Deer W. A., Howie R. A. and Zussman J. (2013) *An Introduction to the Rock-Forming Minerals.* Mineralogical Society of Great Britain and Ireland.

Diener J. F. A., Powell R., White R. W. and Holland T. J. B. (2007) A new thermodynamic model for clino- and orthoamphiboles in the system Na_2O-CaO-FeO-MgO-Al_2O_3-SiO_2-H_2O-O. *Journal of Metamorphic Geology* **25**, 631–656.

Eales H. V. and Cawthorn R. G. (1996) The Bushveld Complex. In: *Layered Intrusions* (ed. R. G. Cawthorn). Elsevier, pp. 181–229.

Eales H. V. and Costin G. (2012) Crustally Contaminated Komatiite: Primary Source of the Chromitites and Marginal, Lower, and Critical Zone Magmas in a Staging Chamber Beneath the Bushveld Complex. *Economic Geology* **107**, 645–665.

Eriksson K. A., Simpson E. L. and Mueller W. (2006) An unusual fluvial to tidal transition in the mesoarchean Moodies Group, South Africa: A response to high tidal range and active tectonics. *Sedimentary Geology* **190**, 13–24.

Eriksson P. G., Schreiber U. M., Reczko B. F. F. and Snyman C. P. (1994) Petrography and Geochemistry of Sandstones Interbedded with the Rooiberg Felsite Group (Transvaal Sequence, South Africa): Implications for Provenance and Tectonic Setting. *Journal of Sedimentary Research* **64**, 836–846.

Eriksson P. G., Hattingh P. J. and Altermann W. (1995) An overview of the geology of the Transvaal Sequence and Bushveld Complex, South Africa. *Mineralium Deposita* **30**.

Ewing R. C., Haaker R. F. and Lutze W. (1982) Leachability of Zircon as a Function of Alpha Dose. In: *Scientific Basis for Radioactive Waste Manage-* (ed. W. Lutze). Elsevier. Amsterdam, pp. 389–397.

Ferdous N. and Farazi A. H. (2016) Geochemistry of Tertiary sandstones from southwest Sarawak, Malaysia: Implications for provenance and tectonic setting. *Acta Geochimica* **35**, 294–308.

Ferriss E. D., Essene E. J. and Becker U. (2008) Computational study of the effect of pressure on the Ti-in-zircon geothermometer. *European Journal of Mineralogy* **20**, 745–755.

Ferry J. M. and Watson E. B. (2007) New thermodynamic models and revised calibrations for the Ti-in-zircon and Zr-in-rutile thermometers. *Contributions to Mineralogy and Petrology* **154**, 429–437.

Finch R. J. and Hanchar J. M. (2003) Structure and Chemistry of Zircon and Zircon-Group Minerals. In: *Zircon* (eds. J. M. Hanchar and P. W. O. Hoskin). Mineralogical Society of America and The Geochemical Society. Chantilly, VA, pp. 1–25.

Fischer L. A., Wang M., Charlier B., Namur O., Roberts R. J., Veksler I. V., Cawthorn R. G. and Holtz F. (2016) Immiscible iron- and silica-rich liquids in the Upper Zone of the Bushveld Complex. *Earth and Planetary Science Letters* **443**, 108–117.

Frimmel H. E., Zeh A., Lehrmann B., Hallbauer D. and Frank W. (2009) Geochemical and Geochronological Constraints on the Nature of the Immediate Basement next to the Mesoarchaean Auriferous Witwatersrand Basin, South Africa. *Journal of Petrology* **50**, 2187–2220.

Fu B., Page F. Z., Cavosie A. J., Fournelle J., Kita N. T., Lackey J. S., Wilde S. A. and Valley J. W. (2008) Ti-in-zircon thermometry: Applications and limitations. *Contributions to Mineralogy and Petrology* **156**, 197–215.

Fuhrman M. L. and Lindsley D. H. (1988) Ternary-feldspar modeling and thermometry. *American Mineralogist*, 201–215.

Gaetani G. A. and Watson E.B. (2000) Open system behavior of olivine-hosted melt inclusions. *Earth and Planetary Science Letters* **183**, 27–41.

Geisler T., Schaltegger U. and Tomaschek F. (2007) Re-equilibration of Zircon in Aqueous Fluids and Melts. *Elements* **3**, 43–50.

Gerdes A. and Zeh A. (2006) Combined U–Pb and Hf isotope LA-(MC-)ICP-MS analyses of detrital zircons: Comparison with SHRIMP and new constraints for the provenance and age of an Armorican metasediment in Central Germany. *Earth and Planetary Science Letters* **249**, 47–61.

Gerdes A. and Zeh A. (2009) Zircon formation versus zircon alteration — New insights from combined U–Pb and Lu–Hf in-situ LA-ICP-MS analyses, and consequences for the interpretation of Archean zircon from the Central Zone of the Limpopo Belt. *Chemical Geology* **261**, 230–243.

Gervasoni F., Klemme S., Rocha-Júnior E. R.V. and Berndt J. (2016) Zircon saturation in silicate melts: A new and improved model for aluminous and alkaline melts. *Contributions to Mineralogy and Petrology* **171**, 725.

Ghiorso M. S. and Gualda G. A. R. (2015) An H_2O–CO_2 mixed fluid saturation model compatible with rhyolite-MELTS. *Contributions to Mineralogy and Petrology* **169**, 1245.

Godel B., Barnes S. J. and Maier W. D. (2011) Parental magma composition inferred from trace element in cumulus and intercumulus silicate minerals: An example from the Lower and Lower Critical Zones of the Bushveld Complex, South-Africa. *Lithos* **125**, 537–552.

Graupner T., Klemd R., Henjes-Kunst F., Goldmann S., Behnsen H., Gerdes A., Dohrmann R., Barton J. M. and Opperman R. (2018) Formation conditions and REY enrichment of the 2060 Ma phosphorus mineralization at Schiel (South Africa): Geochemical and geochronological constraints. *Mineralium Deposita* **53**, 1117–1142.

Griffin W. L., Belousova E. A., Shee S. R., Pearson N. J. and O'Reilly S. Y. (2004) Archean crustal evolution in the northern Yilgarn Craton: U–Pb and Hf-isotope evidence from detrital zircons. *Precambrian Research* **131**, 231–282.

Grimes C. B., John B. E., Kelemen P. B., Mazdab F. K., Wooden J. L., Cheadle M. J., Hanghøj K. and Schwartz J. J. (2007) Trace element chemistry of zircons from oceanic crust: A method for distinguishing detrital zircon provenance. *Geology* **35**, 643.

Grimes C. B., Wooden J. L., Cheadle M. J. and John B. E. (2015) "Fingerprinting" tectono-magmatic provenance using trace elements in igneous zircon. *Contributions to Mineralogy and Petrology* **170**, 341.

Grimes C. B., John B. E., Cheadle M. J., Mazdab F. K., Wooden J. L., Swapp S. and Schwartz J. J. (2009) On the occurrence, trace element geochemistry, and crystallization history of zircon from in situ ocean lithosphere. *Contributions to Mineralogy and Petrology* **158**, 757–783.

Gualda G. A. R., Ghiorso M. S., Lemons R. V. and Carley T. L. (2012) Rhyolite-MELTS: A Modified Calibration of MELTS Optimized for Silica-rich, Fluid-bearing Magmatic Systems. *Journal of Petrology* **53**, 875–890.

Gudelius D., Zeh A., Wilson A. H. and Almeev R. (2017) Liquid Immiscibility at <850°C: Evidence from Melt Inclusions in Zircon of the Basal Bushveld Complex. *Goldschmidt Abstracts* **2017**, 1454.

Gudelius D., Zeh A. and Wilson A. H. (2020) Zircon formation in mafic and felsic rocks of the Bushveld Complex, South Africa: constraints from composition, zoning, Th/U ratios, morphology, and modelling. *Chemical Geology* **546**.

Günther T., Haase K. M., Klemd R. and Teschner C. (2018) Mantle sources and magma evolution of the Rooiberg lavas, Bushveld Large Igneous Province, South Africa. *Contributions to Mineralogy and Petrology* **173**, 1953.

Hall A. L. (1932) The Bushveld igneous complex in the central Transvaal, Pretoria.

Hamilton J. (1977) Sr Isotope and Trace Element Studies of the Great Dyke and Bushveld Mafic Phase and their Relation to Early Proterozoic Magma Genesis in Southern Africa. *Journal of Petrology* **18**, 24–52.

Hanchar J. M. and van Westrenen W. (2007) Rare Earth Element Behavior in Zircon-Melt Systems. *Elements* **3**, 37–42.

Hanchar J. M. and Watson E. B. (2003) Zircon Saturation Thermometry. *Reviews in Mineralogy and Geochemistry* **53**, 89–112.

Harley S. L. and Kelly N. M. (2007) Zircon Tiny but Timely. *Elements* **3**, 13–18.

Harmer R. E. and Armstrong R. A. (2000) Duration of Bushveld Complex (sensu lato) magmatism: constraints from new SHRIMP zircon chronology. Workshop on the Bushveld Complex. *Abstracts, National Research Foundation, Bushveld Complex Workshop, Gethlane Lodge, South Africa*.

Harris C., Pronost J. J. M., Ashwal L. D. and Cawthorn R. G. (2005) Oxygen and Hydrogen Isotope Stratigraphy of the Rustenburg Layered Suite, Bushveld Complex: Constraints on Crustal Contamination. *Journal of Petrology* **46**, 579–601.

Harris N., McMillan A., Holness M., Uken R., Watkeys M., Rogers N. and Fallick A. (2003) Melt Generation and Fluid Flow in the Thermal Aureole of the Bushveld Complex. *Journal of Petrology* **44**, 1031–1054.

Harrison T. M. and Watson E. B. (1983) Kinetics of zircon dissolution and zirconium diffusion in granitic melts of variable water content. *Contributions to Mineralogy and Petrology* **84**, 66–72.

Harrison T. M., Watson E. B. and Aikman A. B. (2007) Temperature spectra of zircon crystallization in plutonic rocks. *Geology* **35**, 635.

Hatton C. J. (1995) Mantle plume origin for the Bushveld and Ventersdorp magmatic provinces. *Journal of African Earth Sciences* **21**, 571–577.

Hatton C. J. and Schweitzer J. K. (1995) Evidence for synchronous extrusive and intrusive Bushveld magmatism. *Journal of African Earth Sciences* **21**, 579–594.

Hay D. C. and Dempster T. J. (2009) Zircon Behaviour during Low-temperature Metamorphism. *Journal of Petrology* **50**, 571–589.

Hayden L. A. and Watson E. B. (2007) Rutile saturation in hydrous siliceous melts and its bearing on Ti-thermometry of quartz and zircon. *Earth and Planetary Science Letters* **258**, 561–568.

Hill M., Barker F., Hunter D. and Knight R. (1996) Geochemical Characteristics and Origin of the Lebowa Granite Suite, Bushveld Complex. *International Geology Review*, 195–227.

Hofmann A. W. (1988) Chemical differentiation of the Earth: The relationship between mantle, continental crust, and oceanic crust. *Earth and Planetary Science Letters* **90**, 297–314.

Holland T. J. B. and Powell R. (1996) Thermodynamics of order-disorder in minerals .2. Symmetric formalism applied to solid solutions. *American Mineralogist* **81**, 11–12.

Holland T. J. B. and Powell R. (1998) An internally consistent thermodynamic data set for phases of petrological interest. *Journal of Metamorphic Geology* **16**, 309–343.

Holland T. J. B. and Powell R. (2001) Calculation of Phase Relations Involving Haplogranitic Melts Using an Internally Consistent Thermodynamic Dataset. *Journal of Petrology* **42**, 673–683.

Holland T. and Powell R. (2003) Activity-composition relations for phases in petrological calculations: an asymmetric multicomponent formulation. *Contributions to Mineralogy and Petrology* **145**, 492–501.

Holtz F., Pichavant M., Barbey P. and Johannes W. (1992) Effects of H_2O on liquidus phase relations in the haplogranite system at 2 and 5 kbar. *American Mineralogist* **77**, 1223–1241.

Hopkins M., Harrison T. M. and Manning C. E. (2008) Low heat flow inferred from 4 Gyr zircons suggests Hadean plate boundary interactions. *Nature* **456**, 493–496.

Hoskin P. W. O. and Schaltegger U. (2003) The Composition of Zircon and Igneous and Metamorphic Petrogenesis. *Reviews in Mineralogy and Geochemistry* **53**, 27–62.

Huppert H. E. and Sparks R. S. J. (1985) Cooling and contamination of mafic and ultramafic magmas during ascent through continental crust. *Earth and Planetary Science Letters* **74**, 371–386.

Ickert R. B., Williams I. S. and Wyborn D. (2011) Ti in zircon from the Boggy Plain zoned pluton: Implications for zircon petrology and Hadean tectonics. *Contributions to Mineralogy and Petrology* **162**, 447–461.

Irvine T. N. (1982) Terminology for Layered Intrusions. *Journal of Petrology* **23**, 127–162.

Jahn B.-M. and Condie K. C. (1995) Evolution of the Kaapvaal Craton as viewed from geochemical and Sm-Nd isotopic analyses of intracratonic pelites. *Geochimica et Cosmochimica Acta* **59**, 2239–2258.

Jakobsen J. K., Tegner C., Brooks C. K., Kent A. J. R., Lesher C. E., Nielsen T. F. D. and Wiedenbeck M. (2010) Parental magma of the Skaergaard intrusion: Constraints from melt

inclusions in primitive troctolite blocks and FG-1 dykes. *Contributions to Mineralogy and Petrology* **159**, 61–79.

Jakobsen J. K., Veksler I. V., Tegner C. and Brooks C. K. (2005) Immiscible iron- and silica-rich melts in basalt petrogenesis documented in the Skaergaard intrusion. *Geology* **33**, 885.

Jakobsen J. K., Veksler I. V., Tegner C. and Brooks C. K. (2011) Crystallization of the Skaergaard Intrusion from an Emulsion of Immiscible Iron- and Silica-rich Liquids: Evidence from Melt Inclusions in Plagioclase. *Journal of Petrology* **52**, 345–373.

James D. E., Fouch M. J., VanDecar J. C. and van der Lee S. (2001) Tectospheric structure beneath southern Africa. *Geophysical Research Letters* **28**, 2485–2488.

Jochum K.P., Seufert H.M., Spettel B. and Palme H. (1986) The solar-system abundances of Nb, Ta, and Y, and the relative abundances of refractory lithophile elements in differentiated planetary bodies. *Geochimica et Cosmochimica Acta* **50**, 1173–1183.

Johnson M. R. and Wolmarans L. G. (2008) Simplified geological map of the Republic of South Africa and the kingdoms of Lesotho and Swaziland. *Council for Geoscience*.

Kaavera J., Rajesh H. M., Tsunogae T. and Belyanin G. A. (2018) Marginal facies and compositional equivalents of Bushveld parental sills from the Molopo Farms Complex layered intrusion, Botswana: Petrogenetic and mineralization implications. *Ore Geology Reviews* **92**, 506–528.

Kamber B. S., Ewart A., Collerson K. D., Bruce M. C. and McDonald G. D. (2002) Fluid-mobile trace element constraints on the role of slab melting and implications for Archaean crustal growth models. *Contributions to Mineralogy and Petrology* **144**, 38–56.

Kamenetsky V. S. and Kamenetsky M. B. (2011) Magmatic fluids immiscible with silicate melts: examples from inclusions in phenocrysts and glasses, and implications for magma evolution and metal transport. In: *Frontiers in geofluids* (eds. B. W. D. Yardley, C. Manning and G. Garven). Wiley-Blackwell. Oxford, Hoboken, N.J, pp. 293–311.

Kaneko Y. and Miyano T. (1990) Contact metamorphism by the bushveld complex in the northeastern Transvaal, south Africa. *Journal of Mineralogy, Petrology and Economic Geology* **85**, 66–81.

Karykowski B. T. and Maier W. D. (2017) Microtextural characterisation of the Lower Zone in the western limb of the Bushveld Complex, South Africa: Evidence for extensive melt migration within a sill complex. *Contributions to Mineralogy and Petrology* **172**, 1126.

Kelsey D. E. and Hand M. (2015) On ultrahigh temperature crustal metamorphism: Phase equilibria, trace element thermometry, bulk composition, heat sources, timescales and tectonic settings. *Geoscience Frontiers* **6**, 311–356.

Kent A. J.R. (2008) Melt Inclusions in Basaltic and Related Volcanic Rocks. *Reviews in Mineralogy and Geochemistry* **69**, 273–331.

Kinny P. D. and Maas R. (2003) Lu-Hf and Sm-Nd isotope systems in zircon. *Reviews in Mineralogy and Geochemistry* **53**, 327–341.

Kirkland C. L., Smithies R. H., Taylor R.J.M., Evans N. and McDonald B. (2015) Zircon Th/U ratios in magmatic environs. *Lithos* **212-215**, 397–414.

Kleemann G. J. and Twist D. (1989) The Compositionally-zoned Sheet-like Granite Pluton of the Bushveld Complex: Evidence Bearing on the Nature of A-type Magmatism. *Journal of Petrology* **30**, 1383–1414.

Klemme S., Prowatke S., Hametner K. and Günther D. (2005) Partitioning of trace elements between rutile and silicate melts: Implications for subduction zones. *Geochimica et Cosmochimica Acta* **69**, 2361–2371.

Koglin N., Zeh A., Frimmel H. E. and Gerdes A. (2010) New constraints on the auriferous Witwatersrand sediment provenance from combined detrital zircon U–Pb and Lu–Hf isotope data for the Eldorado Reef (Central Rand Group, South Africa). *Precambrian Research* **183**, 817–824.

Köksal S., Cemal Göncüoglu M., Toksoy-Köksal F., Möller A. and Kemnitz H. (2008) Zircon typologies and internal structures as petrogenetic indicators in contrasting granitoid types from central Anatolia, Turkey. *Mineralogy and Petrology* **93**, 185–211.

Kreissig K., Nägler T. F., Kramers J. D., van Reenen D. D. and Smit C.A. (2000) An isotopic and geochemical study of the northern Kaapvaal Craton and the Southern Marginal Zone of the Limpopo Belt: Are they juxtaposed terranes? *Lithos* **50**, 1–25.

Kruger F. J. (1994) The Sr-isotopic stratigraphy of the Western Bushveld Complex. *South African Journal of Geology* **97**, 393–398.

Kruger F. J. (2005) Filling the Bushveld Complex magma chamber: lateral expansion, roof and floor interaction, magmatic unconformities, and the formation of giant chromitite, PGE and Ti-V-magnetitite deposits. *Mineralium Deposita* **40**, 451–472.

Kruger F. J. and Marsh J. S. (1982) Significance of $^{87}Sr/^{86}Sr$ ratios in the Merensky cyclic unit of the Bushveld Complex. *Nature* **298**, 53–55.

Latypov R., Chistyakova S. and Mukherjee R. (2017) A Novel Hypothesis for Origin of Massive Chromitites in the Bushveld Igneous Complex. *Journal of Petrology* **58**, 1899–1940.

Latypov R., Costin G., Chistyakova S., Hunt E. J., Mukherjee R. and Naldrett T. (2018) Platinum-bearing chromite layers are caused by pressure reduction during magma ascent. *Nature communications* **9**, 462.

Laurent O., Zeh A., Brandl G., Vezinet A. and Wilson A. H. Granitoids and Greenstone Belts of the Pietersburg Block—Witnesses of an Archaean Accretionary Orogen Along the Northern Edge of the Kaapvaal Craton. In: *The Archaean Geology of the Kaapvaal Craton, Southern Africa* (eds. A. Kröner and A. Hofmann). Springer, pp. 83–107.

Laurent O., Björnsen J., Wotzlaw J.-F., Bretscher S., Pimenta Silva M., Moyen J.-F., Ulmer P. and Bachmann O. (2020) Earth's earliest granitoids are crystal-rich magma reservoirs tapped by silicic eruptions. *Nature Geoscience* **13**, 163–169.

Laurent O. and Zeh A. (2015) A linear Hf isotope-age array despite different granitoid sources and complex Archean geodynamics: Example from the Pietersburg block (South Africa). *Earth and Planetary Science Letters* **430**, 326–338.

Laurent O., Zeh A., Gerdes A., Villaros A., Gros K. and Słaby E. (2017) How do granitoid magmas mix with each other?: Insights from textures, trace element and Sr–Nd isotopic composition of apatite and titanite from the Matok pluton (South Africa). *Contributions to Mineralogy and Petrology* **172**, 60.

Lenhardt N. and Eriksson P. G. (2012) Volcanism of the Palaeoproterozoic Bushveld Large Igneous Province: the Rooiberg Group, Kaapvaal Craton, South Africa. *Precambrian Research* **214-215**, 82–94.

Li Z. (1994) The silicate melt inclusions in igneous rocks. In: *Fluid Inclusions in Minerals: Methods and Applications Virginia* (eds. B. De Vivo and M. L. Frezzotti). Virginia Tech. Virginia, pp. 73–94.

Liu Y., Hu Z., Zong K., Gao C., Gao S., Xu J. and Chen H. (2010) Reappraisement and refinement of zircon U-Pb isotope and trace element analyses by LA-ICP-MS. *Chinese Science Bulletin* **55**, 1535–1546.

Lundgaard K. L., Tegner C., Cawthorn R. G., Kruger F. J. and Wilson J. R. (2006) Trapped intercumulus liquid in the Main Zone of the eastern Bushveld Complex, South Africa. *Contributions to Mineralogy and Petrology* **151**, 352–369.

Maier W. D., Barnes S.-J. and Groves D. I. (2013) The Bushveld Complex, South Africa: Formation of platinum–palladium, chrome- and vanadium-rich layers via hydrodynamic sorting of a mobilized cumulate slurry in a large, relatively slowly cooling, subsiding magma chamber. *Mineralium Deposita* **48**, 1–56.

Maier W. D., Prevec S. A., Scoates J. S., Wall C. J., Barnes S.-J. and Gomwe T. (2018) The Uitkomst intrusion and Nkomati Ni-Cu-Cr-PGE deposit, South Africa: Trace element geochemistry, Nd isotopes and high-precision geochronology. *Mineralium Deposita* **53**, 67–88.

Maier W. D., Arndt N. T. and Curl E. A. (2000) Progressive crustal contamination of the Bushveld Complex: evidence from Nd isotopic analyses of the cumulate rocks. *Contributions to Mineralogy and Petrology* **140**, 316–327.

Martini J.E.J. (1998) The Loskop Formation and its relationship to the Bushveld Complex, South Africa. *Journal of African Earth Sciences* **27**, 193–222.

Marxer F. and Ulmer P. (2019) Crystallisation and zircon saturation of calc-alkaline tonalite from the Adamello Batholith at upper crustal conditions: An experimental study. *Contributions to Mineralogy and Petrology* **174**, 616.

Mathez E. A., VanTongeren J. A. and Schweitzer J. K. (2013) On the relationships between the Bushveld Complex and its felsic roof rocks, part 1: petrogenesis of Rooiberg and related felsites. *Contributions to Mineralogy and Petrology* **166**, 435–449.

McBirney A. R. and Noyes R. M. (1979) Crystallization and Layering of the Skaergaard Intrusion. *Journal of Petrology* **20**, 487–554.

McDonough W. F. and Sun S.-s. (1995) The composition of the Earth. *Chemical Geology* **120**, 223–253.

Miles A. J., Graham C. M., Hawkesworth C. J., Gillespie M. R. and Hinton R. W. (2013) Evidence for distinct stages of magma history recorded by the compositions of accessory apatite and zircon. *Contributions to Mineralogy and Petrology* **166**, 1–19.

Molyneux T. G. (1970) The geology of the area in the vicinity of Magnet Heights, Eastern Transvaal, with special reference to the magnetic iron ore. *Geological Society of South Africa Special Publication* **1**, 228–241.

Molyneux T. G. (1974) A geological investigation of the Bushveld Complex in Sekhukhuneland and part of the Steelpoort Valley. *Transactions Geological Society of South Africa* **77**, 329–338.

Morel M.L.A., Nebel O., Nebel-Jacobsen Y. J., Miller J. S. and Vroon P. Z. (2008) Hafnium isotope characterization of the GJ-1 zircon reference material by solution and laser-ablation MC-ICPMS. *Chemical Geology* **255**, 231–235.

Mungall J. E., Kamo S. L. and McQuade S. (2016) U-Pb geochronology documents out-of-sequence emplacement of ultramafic layers in the Bushveld Igneous Complex of South Africa. *Nature communications* **7**, 13385.

Naldrett A. J., Wilson A., Kinnaird J. and Chunnett G. (2009) PGE Tenor and Metal Ratios within and below the Merensky Reef, Bushveld Complex: Implications for its Genesis. *Journal of Petrology* **50**, 625–659.

Naldrett A. J., Wilson A. H., Kinnaird J. A., Yudovskaya M. and Chunnett G. (2012) The origin of chromitites and related PGE mineralization in the Bushveld Complex: new mineralogical and petrological constraints. *Mineralium Deposita* **47**, 209–232.

Namur O., Abily B., Boudreau A. E., Blanchette F., Bush J. W. M., Ceuleneer G., Charlier B., Donaldson C. H., Duchesne J.-C., Higgins M. D., Morata D., Nielsen T. F. D., O'Driscoll B., Pang K. N., Peacock T., Spandler C. J., Toramaru A. and Veksler I. V. (2015) Igneous Layering in Basaltic Magma Chambers. In: *Layered Intrusions* (eds. B. Charlier, O. Namur, R. Latypov and C. Tegner). Springer Netherlands. Dordrecht, pp. 75–152.

Namur O., Charlier B., Pirard C., Hermann J., Liégeois J.-P. and Auwera J. V. (2011) Anorthosite formation by plagioclase flotation in ferrobasalt and implications for the lunar crust. *Geochimica et Cosmochimica Acta* **75**, 4998–5018.

Namur O., Charlier B., Toplis M. J., Higgins M. D., Liégeois J.-P. and Vander Auwera J. (2010) Crystallization Sequence and Magma Chamber Processes in the Ferrobasaltic Sept Iles Layered Intrusion, Canada. *Journal of Petrology* **51**, 1203–1236.

Nell J. (1985) The Bushveld metamorphic aureole in the Potgietersrus area; evidence for a two-stage metamorphic event. *Economic Geology* **80**, 1129–1152.

Nex P. A. M., Cawthorn R. G. and Kinnaird J. A. (2002) Geochemical effects of magma addition: Compositional reversals and decoupling of trends in the Main Zone of the western Bushveld Complex. *Mineralogical Magazine* **66**, 833–856.

Nutman A. P. and Hiess J. (2009) A granitic inclusion suite within igneous zircons from a 3.81 Ga tonalite (W. Greenland): Restrictions for Hadean crustal evolution studies using detrital zircons. *Chemical Geology* **261**, 77–82.

O'Driscoll B. and VanTongeren J. A. (2017) Layered Intrusions: From Petrological Paradigms to Precious Metal Repositories. *Elements* **13**, 383–389.

Olsson J. R., Söderlund U., Hamilton M. A., Klausen M. B. and Helffrich G. R. (2011) A late Archaean radiating dyke swarm as possible clue to the origin of the Bushveld Complex. *Nature Geoscience* **4**, 865–869.

Parrish R. R. and Noble S. R. (2003) Zircon U-Th-Pb Geochronology by Isotope Dilution -- Thermal Ionization Mass Spectrometry (ID-TIMS). *Reviews in Mineralogy and Geochemistry* **53**, 183–213.

Pitra P. and De Waal S. A. (2001) High-temperature, low-pressure metamorphism and development of prograde symplectites, Marble Hall Fragment, Bushveld Complex (South Africa). *Journal of Metamorphic Geology* **19**, 311–325.

Portnyagin M., Almeev R., Matveev S. and Holtz F. (2008) Experimental evidence for rapid water exchange between melt inclusions in olivine and host magma. *Earth and Planetary Science Letters* **272**, 541–552.

Poujol M., Robb L. J., Anhaeusser C. R. and Gericke B. (2003) A review of the geochronological constraints on the evolution of the Kaapvaal Craton, South Africa. *Precambrian Research* **127**, 181–213.

Prendergast M. D. (2012) The Molopo Farms Complex, Southern Botswana - A Reconsideration of Structure, Evolution, and the Bushveld Connection. *South African Journal of Geology* **115**, 77–90.

Pupin J. P. (1980) Zircon and granite petrology. *Contributions to Mineralogy and Petrology* **73**, 207–220.

Richardson S. H. and Shirey S. B. (2008) Continental mantle signature of Bushveld magmas and coeval diamonds. *Nature* **453**, 910–913.

Riches A.J.V., Ickert R. B., Pearson D. G., Stern R. A., Jackson S. E., Ishikawa A., Kjarsgaard B. A. and Gurney J. J. (2016) In situ oxygen-isotope, major-, and trace-element constraints on the metasomatic modification and crustal origin of a diamondiferous eclogite from Roberts Victor, Kaapvaal Craton. *Geochimica et Cosmochimica Acta* **174**, 345–359.

Roedder E. (1979) Origin and significance of magmatic inclusions. *Bulletin de Mineralogie* **102**, 487–510.

Roedder E. (ed.) (1984) *Fluid Inclusions.* Mineralogical Society of America and The Geochemical Society, Chantilly, VA.

Rubatto D. (2002) Zircon trace element geochemistry: Partitioning with garnet and the link between U–Pb ages and metamorphism. *Chemical Geology* **184**, 123–138.

Rubatto D. and Hermann J. (2007) Experimental zircon/melt and zircon/garnet trace element partitioning and implications for the geochronology of crustal rocks. *Chemical Geology* **241**, 38–61.

Rudnick R. L. and Fountain D. M. (1995) Nature and composition of the continental crust: A lower crustal perspective. *Reviews of Geophysics* **33**, 267.

SACS (South African Committee for Stratigraphy) (1980) Stratigraphy of South Africa. Part 1: Lithostratigraphy of the Republic of South Africa, South West Africa/Namibia and the Republics of Bophuthatswana, Transkei, and Venda. In: *Handbook 8* (ed. L. E. Kent). Geological Survey of South Africa. Pretoria.

Scherer E., Munker C. and Mezger K. (2001) Calibration of the lutetium-hafnium clock. *Science* **293**, 683–687.

Schiffries C. M. and Rye D. M. (1990) Stable isotopic systematics of the Bushveld Complex; II, Constraints on hydrothermal processes in layered intrusions. *American Journal of Science* **290**, 209–245.

Schiller D. and Finger F. (2019) Application of Ti-in-zircon thermometry to granite studies: Problems and possible solutions. *Contributions to Mineralogy and Petrology* **174**, 51.

Schmickler B., Jacob D. E. and Foley S. F. (2004) Eclogite xenoliths from the Kuruman kimberlites, South Africa: Geochemical fingerprinting of deep subduction and cumulate processes☆. *Lithos* **75**, 173–207.

Schmidt C., Rickers K., Wirth R., Nasdala L. and Hanchar J. M. (2006) Low-temperature Zr mobility: An in situ synchrotron-radiation XRF study of the effect of radiation damage in zircon on the element release in H_2O + HCl SiO_2 fluids. *American Mineralogist* **91**, 1211–1215.

Schmitt A. K. (2001) Gas-saturated crystallization and degassing in large-volume, crystal-rich dacitic magmas from the Altiplano-Puna, northern Chile. *Journal of Geophysical Research* **106**, 30561–30578.

Schoene B. (2014) U–Th–Pb Geochronology. In: *Treatise on Geochemistry.* Elsevier, pp. 341–378.

Schoene B., Dudas F. O. L., Bowring S. A. and Wit M. de (2009) Sm-Nd isotopic mapping of lithospheric growth and stabilization in the eastern Kaapvaal craton. *Terra Nova* **21**, 219–228.

Schweitzer J. K., Hatton C. J. and de Waal S. A. (1995) Regional lithochemical stratigraphy of the Rooiberg Group, upper Transvaal Supergroup: a proposed new subdivision. *South African Journal of Geology* **98**, 245–255.

Schweitzer J. K. (1998) The Dullstroom Basalt Formation and the Rooiberg Group: volcanic rocks associated with the Bushveld Complex. Dissertation.

Schweitzer J. K., Hatton C. J. and Waal S. A. de (1997) Link between the granitic and volcanic rocks of the Bushveld Complex, South Africa. *Journal of African Earth Sciences* **24**, 95–104.

Scoates J. S. and Friedman R. M. (2008) Precise age of the platiniferous Merensky Reef, Bushveld Complex, South Africa, by the U-Pb zircon chemical abrasion ID-TIMS technique. *Economic Geology* **103**, 465–471.

Scoates J. S. and Wall C. J. (2015) Geochronology of Layered Intrusions. In: *Layered intrusions* (eds. B. Charlier, O. Namur, R. Latypov and C. Tegner). Springer. Dordrecht, pp. 3–74.

Scoon R. N. and Mitchell A. A. (2012) The Upper Zone of the Bushveld Complex at Roossenekal, South Afrca: Geochemical stratigraphy and evidence of multiple episodes of magma replenishment. *South African Journal of Geology* **115.4**, 515–534.

Scoon R. N. and Viljoen M. J. (2019) Geoheritage of the Eastern Limb of the Bushveld Igneous Complex, South Africa: A Uniquely Exposed Layered Igneous Intrusion. *Geoheritage* **11**, 1723–1748.

Setera J. B., VanTongeren J. A., Turrin B. D. and Swisher C. C. (2020) Rapid cooling of the Rustenburg Layered Suite of the Bushveld Complex (South Africa): Insights from biotite 40Ar/39Ar geochronology. *Geology*.

Sharpe M. R., Evensen N. M. and Naldrett A. J. (1986) Sm/Nd and Rb/Sr evidence for liquid mixing, magma generation and contamination in the Eastern Bushveld Complex. *Geocongress, Conference Abstract, University of the Witwatersrand, Johannesburg*, 621–624.

Sharpe M. R. (1981) The chronology of magma influxes to the eastern compartment of the Bushveld Complex as exemplified by its marginal border groups. *Journal of the Geological Society* **138**, 307–326.

Sharpe M. R. and Hulbert L. J. (1985) Ultramafic sills beneath the eastern Bushveld Complex; mobilized suspensions of early lower zone cumulates in a parental magma with boninitic affinities. *Economic Geology* **80**, 849–871.

Siégel C., Bryan S. E., Allen C. M. and Gust D. A. (2018) Use and abuse of zircon-based thermometers: A critical review and a recommended approach to identify antecrystic zircons. *Earth-Science Reviews* **176**, 87–116.

Silver P. G. (2004) Seismic anisotropy, mantle fabric, and the magmatic evolution of Precambrian southern Africa. *South African Journal of Geology* **107**, 45–58.

Sláma J., Košler J., Condon D. J., Crowley J. L., Gerdes A., Hanchar J. M., Horstwood M. S.A., Morris G. A., Nasdala L., Norberg N., Schaltegger U., Schoene B., Tubrett M. N. and Whitehouse M. J. (2008) Plešovice zircon — A new natural reference material for U–Pb and Hf isotopic microanalysis. *Chemical Geology* **249**, 1–35.

Sobolev V. S. and Kostyuk V. P. (1975) Magmatic crystallization based on a study of melt inclusions. *Fluid Inclusion Research* **9**, 182–253.

Spandler C. J., Mavrogenes J. and Arculus R. (2005) Origin of chromitites in layered intrusions: Evidence from chromite-hosted melt inclusions from the Stillwater Complex. *Geology* **33**, 893–896.

Sparks R. S. J., Huppert H. E., Kerr R. C., McKenzie D. P. and Tait S. R. (1985) Postcumulus processes in layered intrusions. *Geological Magazine* **122**, 555–568.

Stepanov A. S. and Hermann J. (2013) Fractionation of Nb and Ta by biotite and phengite: Implications for the "missing Nb paradox". *Geology* **41**, 303–306.

Szymanowski D., Fehr M. A., Guillong M., Coble M. A., Wotzlaw J.-F., Nasdala L., Ellis B. S., Bachmann O. and Schönbächler M. (2018) Isotope-dilution anchoring of zircon reference materials for accurate Ti-in-zircon thermometry. *Chemical Geology* **481**, 146–154.

Tajčmanová L., Connolly J. A. D. and Cesare B. (2009) A thermodynamic model for titanium and ferric iron solution in biotite. *Journal of Metamorphic Geology* **27**, 153–165.

Tegner C., Cawthorn R. G. and Kruger F. J. (2006) Cyclicity in the Main and Upper Zones of the Bushveld Complex, South Africa: Crystallization from a Zoned Magma Sheet. *Journal of Petrology* **47**, 2257–2279.

Thomas J. B., Bodnar R. J., Shimizu N. and Chesner C. A. (2003) Melt inclusions in zircon. In: *Zircon* (eds. J. M. Hanchar and P. W. O. Hoskin). Mineralogical Society of America and The Geochemical Society. Chantilly, VA, pp. 63–88.

Thomas J. B., Bodnar R. J., Shimizu N. and Sinha A.K. (2002) Determination of zircon/melt trace element partition coefficients from SIMS analysis of melt inclusions in zircon. *Geochimica et Cosmochimica Acta* **66**, 2887–2901.

Trail D., Mojzsis S. J., Harrison T. M., Schmitt A. K., Watson E. B. and Young E. D. (2007) Constraints on Hadean zircon protoliths from oxygen isotopes, Ti-thermometry, and rare earth elements. *Geochemistry, Geophysics, Geosystems* **8**, 1-22.

Trail D., Watson B. E. and Tailby N. D. (2012) Ce and Eu anomalies in zircon as proxies for the oxidation state of magmas. *Geochimica et Cosmochimica Acta* **97**, 70–87.

Tuttle O. F. and Bowen N. L. (1958) *Origin of Granite in the Light of Experimental Studies in the System $NaAlSi_3O_8$–$KAlSi_3O_8$–SiO_2–H_2O.* Geological Society of America Memoirs.

Twist D. and French B. M. (1983) Voluminous acid volcanism in the Bushveld Complex: A review of the Rooiberg Felsite. *Bulletin Volcanologique* **46**, 225–242.

Twist D. and Harmer R. E. (1987) Geochemistry of contrasting siliceous magmatic suites in the Bushveld Complex: Genetic aspects and implications for tectonic discrimination diagrams. *Journal of Volcanology and Geothermal Research* **32**, 83–98.

Van den Kerkhof A. M. and Hein U. F. (2001) Fluid inclusion petrography. *Lithos* **55**, 27–47.

VanTongeren J. A. and Mathez E. A. (2012) Large-scale liquid immiscibility at the top of the Bushveld Complex, South Africa. *Geology* **40**, 491–494.

VanTongeren J. A. and Mathez E. A. (2015) On the relationship between the Bushveld Complex and its felsic roof rocks, part 2: the immediate roof. *Contributions to Mineralogy and Petrology* **170**.

VanTongeren J. A., Mathez E. A. and Kelemen P. B. (2010) A Felsic End to Bushveld Differentiation. *Journal of Petrology* **51**, 1891–1912.

VanTongeren J. A., Zirakparvar N. A. and Mathez E. A. (2016) Hf isotopic evidence for a cogenetic magma source for the Bushveld Complex and associated felsic magmas. *Lithos* **248-251**, 469–477.

Vavra G. (1990) On the kinematics of zircon growth and its petrogenetic significance: A cathodoluminescence study. *Contributions to Mineralogy and Petrology* **106**, 90–99.

Ver Hoeve T. J., Scoates J. S., Wall C. J., Weis D. and Amini M. (2018) A Temperature-Composition Framework for Crystallization of Fractionated Interstitial Melt in the Bushveld Complex from Trace Element Systematics of Zircon and Rutile. *Journal of Petrology* **59**, 1383–1416.

Viljoen M. (2016) The Bushveld Complex -Host to the World's Largest Platinum, Chromium and Vanadium Resources. *IUGS Episodes* **39**, 238–268.

Von Gruenewaldt G. (1972) The origin of the roof rocks of the Bushveld Complex between tauteshoogte and paardekop in the eastern Transvaal. *South African Journal of Geology* **75**, 121–134.

Voordouw R., Gutzmer J. and Beukes N. J. (2009) Intrusive origin for Upper Group (UG1, UG2) stratiform chromitite seams in the Dwars River area, Bushveld Complex, South Africa. *Mineralogy and Petrology* **97**, 75–94.

Wall C. J., Scoates J. S., Weis D., Friedman R. M., Amini M. and Meurer W. P. (2018) The Stillwater Complex: Integrating Zircon Geochronological and Geochemical Constraints on the Age, Emplacement History and Crystallization of a Large, Open-System Layered Intrusion. *Journal of Petrology* **59**, 153–190.

Walraven F. (1985) Genetic aspects of the granophyric rocks of the Bushveld Complex. *Economic Geology* **80**, 1166–1180.

Walraven F. (1987) *Textural, geochemical and genetic aspects of the granophyric rocks of the Bushveld complex.* Gov. Print, Pretoria.

Walraven F. (1997) *Geochronology of the Rooiberg Group, Transvaal Supergroup, South Africa,* Economic Geology Research Unit, University of the Witwatersrand, Johannesburg, South Africa.

Waters D. J. and Lovegrove D. P. (2002) Assessing the extent of disequilibrium and overstepping of prograde metamorphic reactions in metapelites from the Bushveld Complex aureole, South Africa. *Journal of Metamorphic Geology* **20**, 135–149.

Watson E. B. and Harrison T. M. (2005) Zircon thermometer reveals minimum melting conditions on earliest Earth. *Science* **308**, 841–844.

Watson E. B., Wark D. A. and Thomas J. B. (2006) Crystallization thermometers for zircon and rutile. *Contributions to Mineralogy and Petrology* **151**, 413–433.

Watson E. B. and Harrison T. M. (1983) Zircon saturation revisited: Temperature and composition effects in a variety of crustal magma types. *Earth and Planetary Science Letters* **64**, 295–304.

Watt G. R., Burns I. M. and Graham G. A. (1996) Chemical characteristics of migmatites: Accessory phase distribution and evidence for fast melt segregation rates. *Contributions to Mineralogy and Petrology* **125**, 100–111.

Watts K. E. and Mercer C. N. (2020) Zircon-hosted melt inclusion record of silicic magmatism in the Mesoproterozoic St. Francois Mountains terrane, Missouri: Origin of the Pea Ridge iron oxide-apatite-rare earth element deposit and implications for regional crustal pathways of mineralization. *Geochimica et Cosmochimica Acta* **272**, 54–77.

Webb S. J. (2004) Gravity modeling of Bushveld Complex connectivity supported by Southern African Seismic Experiment results. *South African Journal of Geology* **107**, 207–218.

Webb S. J., Ashwal L. D. and Cawthorn R. G. (2011) Continuity between eastern and western Bushveld Complex, South Africa, confirmed by xenoliths from kimberlite. *Contributions to Mineralogy and Petrology* **162**, 101–107.

Wetherill G. W. (1956) Discordant uranium-lead ages. *Transactions of the American Geophysical Union*, 320–326.

White R. W., Powell R. and Clarke G. L. (2002) The interpretation of reaction textures in Fe-rich metapelitic granulites of the Musgrave Block, central Australia: Constraints from mineral equilibria calculations in the system K_2O-FeO-MgO-Al_2O_3-SiO_2-H_2O-TiO_2-Fe_2O_3. *Journal of Metamorphic Geology* **20**, 41–55.

Whitehouse M. J. and Kamber B. S. (2002) On the overabundance of light rare earth elements in terrestrial zircons and its implication for Earth's earliest magmatic differentiation. *Earth and Planetary Science Letters* **204**, 333–346.

Whitney D. L. and Evans B. W. (2009) Abbreviations for names of rock-forming minerals. *American Mineralogist* **95**, 185–187.

Wiedenbeck M., Hanchar J. M., Peck W. H., Sylvester P., Valley J., Whitehouse M., Kronz A., Morishita Y., Nasdala L., Fiebig J., Franchi I., Girard J.-P., Greenwood R. C., Hinton R., Kita N., Mason P.R.D., Norman M., Ogasawara M., Piccoli P. M., Rhede D., Satoh H., Schulz-Dobrick B., Skår O., Spicuzza M., Terada K., Tindle A., Togashi S., Vennemann T., Xie Q. and Zheng Y.-F. (2004) Further Characterisation of the 91500 Zircon Crystal. *Geostandards and Geoanalytical Research* **28**, 9–39.

Wilke M., Schmidt C., Dubrail J., Appel K., Borchert M., Kvashnina K. and Manning C. E. (2012) Zircon solubility and zirconium complexation in H_2O+Na_2O+SiO_2±Al_2O_3 fluids at high pressure and temperature. *Earth and Planetary Science Letters* **349-350**, 15–25.

Wilke S., Holtz F., Neave D. A. and Almeev R. (2017) The Effect of Anorthite Content and Water on Quartz–Feldspar Cotectic Compositions in the Rhyolitic System and Implications for Geobarometry. *Journal of Petrology* **58**, 789–818.

Williams I. S. and Claesson S. (1987) Isotopic evidence for the Precambrian provenance and Caledonian metamorphism of high grade paragneisses from the Seve Nappes, Scandinavian Caledonides. *Contributions to Mineralogy and Petrology* **97**, 205–217.

Willmore C. C., Boudreau A. E. and Kruger F. J. (2000) The Halogen Geochemistry of the Bushveld Complex, Republic of South Africa: Implications for Chalcophile Element Distribution in the Lower and Critical Zones. *Journal of Petrology* **41**, 1517–1539.

Wilson A. H. (2012) A Chill Sequence to the Bushveld Complex: Insight into the First Stage of Emplacement and Implications for the Parental Magmas. *Journal of Petrology* **53**, 1123–1168.

Wilson A. H. (2015) The Earliest Stages of Emplacement of the Eastern Bushveld Complex: Development of the Lower Zone, Marginal Zone and Basal Ultramafic Sequence. *Journal of Petrology* **56**, 347–388.

Wilson A. H. and Chunnett G. (2006) Trace Element and Platinum Group Element Distributions and the Genesis of the Merensky Reef, Western Bushveld Complex, South Africa. *Journal of Petrology* **47**, 2369–2403.

Wilson A. H., Zeh A. and Gerdes A. (2017) In Situ Sr isotopes in Plagioclase and Trace Element Systematics in the Lowest Part of the Eastern Bushveld Complex: Dynamic Processes in an Evolving Magma Chamber. *Journal of Petrology* **58**, 327–360.

Wilson J., Ferré E. C. and Lespinasse P. (2000) Repeated tabular injection of high-level alkaline granites in the eastern Bushveld, South Africa. *Journal of the Geological Society* **157**, 1077–1088.

Woodhead J. D. and Hergt J. M. (2005) A Preliminary Appraisal of Seven Natural Zircon Reference Materials for In Situ Hf Isotope Determination. *Geostandards and Geoanalytical Research* **29**, 183–195.

Wronkiewicz D. J. and Condie K. C. (1990) Geochemistry and mineralogy of sediments from the Ventersdorp and Transvaal Supergroups, South Africa: Cratonic evolution during the early Proterozoic. *Geochimica et Cosmochimica Acta* **54**, 343–354.

Wu F.-Y., Yang Y.-H., Li Q.-L., Mitchell R. H., Dawson J. B., Brandl G. and Yuhara M. (2011) In situ determination of U–Pb ages and Sr–Nd–Hf isotopic constraints on the petrogenesis of the Phalaborwa carbonatite Complex, South Africa. *Lithos* **127**, 309–322.

Xiong X., Keppler H., Audetat A., Gudfinnsson G., Sun W., Song M., Xiao W. and Yuan L. (2009) Experimental constraints on rutile saturation during partial melting of metabasalt at the amphibolite to eclogite transition, with applications to TTG genesis. *American Mineralogist* **94**, 1175–1186.

Yakymchuk C., Kirkland C. L. and Clark C. (2018) Th/U ratios in metamorphic zircon. *Journal of Metamorphic Geology* **51**, 785.

Yardley B. W. D., Manning C. and Garven G. (eds.) (2011) *Frontiers in geofluids.* Wiley-Blackwell, Oxford, Hoboken, N.J.

Yuan Q., Namur O., Fischer L. A., Roberts R. J., Lü X. and Charlier B. (2017) Pulses of Plagioclase-laden Magmas and Stratigraphic Evolution in the Upper Zone of the Bushveld Complex, South Africa. *Journal of Petrology* **58**, 1619–1643.

Yudovskaya M., Kinnaird J. A., Naldrett A. J., Rodionov N., Antonov A., Simakin S. and Kuzmin D. (2013) Trace-element study and age dating of zircon from chromitites of the Bushveld Complex (South Africa). *Mineralogy and Petrology* **107**, 915–942.

Zeh A. and Gerdes A. (2014) HFSE (High Field Strength Elements)-transport and U–Pb–Hf isotope homogenization mediated by Ca-bearing aqueous fluids at 2.04Ga: Constraints from zircon, monazite, and garnet of the Venetia Klippe, Limpopo Belt, South Africa. *Geochimica et Cosmochimica Acta* **138**, 81–100.

Zeh A., Wilson A. H., Gudelius D. and Gerdes A. (2020) Hafnium Isotopic Composition of the Bushveld Complex requires Mantle Melt - Upper Crust Mixing: New Evidence from Zirconology of Mafic, Felsic and Metasedimentary Rocks. *Journal of Petrology* **60**, 2169–2200.

Zeh A. and Gerdes A. (2012) U–Pb and Hf isotope record of detrital zircons from gold-bearing sediments of the Pietersburg Greenstone Belt (South Africa)—Is there a common provenance with the Witwatersrand Basin? *Precambrian Research* **204-205**, 46–56.

Zeh A., Gerdes A. and Barton J. M. (2009) Archean Accretion and Crustal Evolution of the Kalahari Craton—the Zircon Age and Hf Isotope Record of Granitic Rocks from Barberton/Swaziland to the Francistown Arc. *Journal of Petrology* **50**, 933–966.

Zeh A., Gerdes A., Barton J. and Klemd R. (2010b) U–Th–Pb and Lu–Hf systematics of zircon from TTG's, leucosomes, meta-anorthosites and quartzites of the Limpopo Belt (South Africa): Constraints for the formation, recycling and metamorphism of Palaeoarchaean crust. *Precambrian Research* **179**, 50–68.

Zeh A., Gerdes A., Will T. M. and Frimmel H. E. (2010a) Hafnium isotope homogenization during metamorphic zircon growth in amphibolite-facies rocks: Examples from the Shackleton Range (Antarctica). *Geochimica et Cosmochimica Acta* **74**, 4740–4758.

Zeh A., Jaguin J., Poujol M., Boulvais P., Block S. and Paquette J.-L. (2013) Juvenile crust formation in the northeastern Kaapvaal Craton at 2.97Ga—Implications for Archean terrane accretion, and the source of the Pietersburg gold. *Precambrian Research* **233**, 20–43.

Zeh A., Ovtcharova M., Wilson A. H. and Schaltegger U. (2015) The Bushveld Complex was emplaced and cooled in less than one million years – results of zirconology, and geotectonic implications. *Earth and Planetary Science Letters* **418**, 103–114.

Zeh A., Wilson A. H. and Ovtcharova M. (2016) Source and age of upper Transvaal Supergroup, South Africa: Age-Hf isotope record of zircons in Magaliesberg quartzite and Dullstroom lava, and implications for Paleoproterozoic (2.5–2.0 Ga) continent reconstruction. *Precambrian Research* **278**, 1–21.

Zeh A., Wilson A. H. and Ovtcharova M. (2020) Zircon U-Pb-Hf isotope systematics of Transvaal Supergroup – Constraints for the geodynamic evolution of the Kaapvaal Craton and its hinterland between 2.65 and 2.06 Ga. *Precambrian Research* **345**.

Zeng X., Joy K. H., Li S., Lin Y., Wang N., Li X., Li Y., Hao J., Liu J. and Wang S. (2020) Oldest Immiscible Silica-rich Melt on the Moon Recorded in a ~4.38 Ga Zircon. *Geophysical Research Letters* **47**, 328.

Zirakparvar N. A., Mathez E. A., Scoates J. S. and Wall C. J. (2014) Zircon Hf isotope evidence for an enriched mantle source for the Bushveld Igneous Complex. *Contributions to Mineralogy and Petrology* **168**, 409.

Declaration of Authorship

Chapter 4: Zircon formation in mafic and felsic rocks of the Bushveld Complex, South Africa: constraints from composition, zoning, Th/U ratios, morphology, and modelling

Gudelius D., Zeh A. and Wilson A. H. (2020) Zircon formation in mafic and felsic rocks of the Bushveld Complex, South Africa: constraints from composition, zoning, Th/U ratios, morphology, and modelling. *Chemical Geology* **546**

As first author, I extended, combined, and re-evaluated an existing dataset of zircon trace element and bulk-rock major and trace element compositions previously obtained by the co-authors Armin Zeh and Allan H. Wilson. Together with both co-authors, I was involved in fieldwork and sample collection in South Africa. I did all SEM imaging and thermodynamic modelling, which greatly benefited from assistance by David Schiller (Salzburg University) and Armin Zeh. I evaluated all data, visualized them, and did the interpretation and discussion with inputs from Armin Zeh and Allan H. Wilson. Finally, I wrote the article.

Chapter 5: Zircon melt inclusions in mafic and felsic rocks of the Bushveld Complex – constraints for zircon crystallization temperatures and partitioning coefficients

Gudelius D., Zeh A., Almeev R. R., Wilson A. H., Fischer L. A., Schmitt, A. K. (2020) Zircon melt inclusions in mafic and felsic rocks of the Bushveld Complex – constraints for zircon crystallization temperatures and partitioning coefficients. *Geochimica et Cosmochimica Acta (submitted 05/2020)*

As first author, I acquired a new dataset of major and trace element compositions as well as H_2O contents of melt inclusions in zircon, using samples investigated in chapter 4. Re-homogenization of all investigated melt inclusions was done by co-author Renat R. Almeev, which is highly appreciated. I set up the method of preparing and polishing zircons with melt inclusions and did all imaging by polarization microscopy and SEM. Trace element analysis of melt inclusions and zircon hosts was performed by LA-ICP-MS at Frankfurt University with assistance of Richard Albert Roper and Armin Zeh. H_2O was analyzed using SIMS at Heidelberg University by co-author Axel K. Schmitt. Major element analysis by EPMA was done at Freiburg University with assistance of co-author Lennart A. Fischer. I evaluated all data, visualized them, and did the interpretation and discussion with inputs from Armin Zeh, Renat R. Almeev, Allan H. Wilson, Lennart A. Fischer and Axel K. Schmitt. Finally, I wrote the article.

Chapter 6: Hafnium Isotopic Composition of the Bushveld Complex requires Mantle Melt - Upper Crust Mixing: New Evidence from Zirconology of Mafic, Felsic and Metasedimentary Rocks

Zeh A., Wilson A. H., **Gudelius D.** and Gerdes A. (2020) Hafnium Isotopic Composition of the Bushveld Complex requires Mantle Melt - Upper Crust Mixing: New Evidence from Zirconology of Mafic, Felsic and Metasedimentary Rocks. *Journal of Petrology* **60**, 2169–2200

As a co-author, I was involved in sampling and fieldwork in South Africa as well as in sample preparation. Furthermore, I extended the dataset of zircon morphologies and corresponding crystallization temperatures using Pupin's scheme and contributed to the SEM imaging. I was involved in Hf isotope analysis by LA-ICP-MS at Frankfurt University, which greatly benefited from assistance by Linda Marko and Axel Gerdes. I further contributed to the data evaluation and visualization as well as to the interpretation and discussion. Finally, Armin Zeh wrote the article.